Title

Electrocatalytic carbon dioxide reduction by bipyridine based complexes and their derivatives

Permalink

https://escholarship.org/uc/item/5828t5hb

Author

Helm, Melissa Lynn

Publication Date

2017

Peer reviewed|Thesis/dissertation

UNIVERSITY OF CALIFORNIA, SAN DIEGO

Electrocatalytic carbon dioxide reduction by bipyridine based complexes and their derivatives

A dissertation submitted in partial satisfaction of the requirements for the degree of Doctor of Philosophy

in

Chemistry

by

Melissa Lynn Helm

Committee in charge:

Professor Clifford P. Kubiak, Chair
Professor Joshua Figueroa
Professor Michael Gilson
Professor William Trogler
Professor John Weare

2017

This Dissertation of Melissa Lynn Helm is approved, and it is acceptable in quality and form for publication on microfilm and electronically:

Chair

University of California, San Diego

2017

EPIGRAPH

The true delight is in the finding out rather than in the knowing.

Issac Asimov

TABLE OF CONTENTS

LIST OF FIGURES

LIST OF TABLES

ACKNOWLEDGEMENTS

When I started by PhD studies I had no idea how many people would be there to help and support me throughout the way. I am extremely greatful for all of my friends, family, mentors, and coworkers that encouraged me over the past five years so that I am able to write this acknowledgement in my PhD dissertation.

The first person I have to thank is my husband, Cameron. I am so happy he came with me to San Diego. Cameron embraced the graduate school experience with me so well that many people think he are also a chemistry PhD student. He have cheered me up and cheered me on for so many years, and I cannot thank him enough for being so supportive. I am so lucky to be married to him. I love you.

I also want to give a big thanks to my family. Their loving support made it all the way from the east coast every day, and I am extremely thankful for the many phone calls and fun adventures when they have visited. To Mom, Dad, Jenna, and Josh: thank you. I also have to thank Cameron's family. It means a lot that they are proud of me and I am very happy to be a Helm.

Graduate school would have been absolutely terrible without my terrific friends that I have made in San Diego. Thank you to Vivi, Jessie, Sarah, Mike, Lewis, and Cory for creating the closest group of friends I have ever had. Karaoke, hot tubbing, brewery hopping, wedding shenanegans, Sunday watch parties, and many dinners with way too much food are some hallmarks of the great times we have all had here. I hope we can continue the good times for years to come.

Ok, onto the science folks. I have to thank all of the Kubiak lab members that I overlapped with, because every single person taught me something during my graduate studies and made lab a fun place to work. I will miss the days of late mornings, two hours lunches, loud music in lab, and early trips to the pub. Special thanks to Prof. Kyle Grice, Dr. Candance Seu, Dr. Matt Sampson, Prof. Charles Machan, and Dr. Mark Reineke, who helped me get started in lab and supported my research the most during my graduate career. I also need to thank Chris Miller, who allowed me to mentor him for his first year, accepted all my half-baked ideas as good ones, and continueously encouraged me to push through the final six months of graduate school.

There are so many great people in the department that I have crossed paths with that it would be impossible to name them all. I certainly want to thank everyone that helped make SWIGS (the Society for Women in Graduate Studies in Chemistry & Biochemistry) such a great community, especially Alissa, Lisa, Katherine, Jessie Moreton, and Joey. Thank you to the professors that I interacted with more than most, including Prof. Charlie Perrin, Prof. Nathan Gianneschi, Prof. Josh Figueroa, Prof. Seth Cohen, and Prof. Stacey Brydges. I also have to give a shout out to the great people who run all the facilities here at UCSD, from safety to crystallography to the stockroom and everything in between. The department would not survive without all their hard work.

I also need to thank all of my collaborators. Thank you to those in the Yale-Emory collaboration (especially Prof. Tim Lian, Prof. Victor Batista, Dr. Aimin Ge, and Benjamin Rudshteyn), the MURI (Prof. Emily Carter, Dr. Martina Lessio), and the 2D SFG collaboration (Prof. Wei Xiong and Jiaxi Wang). I’d like to also thank the labs that trained me in specific techniques. Prof. Jeanne Pemberton and Dr. Dallas Matz at the University of Arizona for training me in PM-IRRAS and everyone at CVIS who taught me all there is to know about cyclic voltammetry.

Last but probably most important, I have to thank Cliff. Thanks to Cliff for letting me rearrange his lab and backing me up when I forced my fellow labmates through arduous projects like writing a new website and creating SOPs. I am very thankful that he allowed me to go to so many conferences and traning programs, which really helped me be a part of the scientific community. Thank you for letting me persue my own projects and giving me honest feedback on them. Cliff’s understanding of chemistry and his ability to remember so much of it has always amazed me and I will forever look up to him.

I cannot think of a better city to be in for graduate school. The consistent weather and endless things to do in San Diego have made this place an ideal escape from lab. Here is a sampling of the things I will miss in San Diego, and since you (yes you) are reading this, I encourage you to enjoy these things as I did: Modern Times, Green Flash, North County brewery hopping, San Diego Zoo, San Diego symphony orchestra, Old Globe productions, burritos, La Jolla Shores, watching paragliders from lab, acai bowls from the Juice Kaboose, Oscar’s tacos, and in general exploring the food an drink options of Hillcrest and North Park.

CHAPTER SPECIFIC ACKNOWLEDGEMENTS

Chapter 2 is unpublished work that is a culmination in persistence in learning molecular electrochemistry during my time in graduate school. I would like to acknowledge all those who participated in Cyclic Voltammetry International School in 2015, where I really cultivated my interest and understanding of cyclic voltammetry. In particular the instructors Prof. Jean-Michel Savéant, Prof. Cyrille Costentin, Prof. Marc Robert, and Prof. Benoît Limoges, and those who helped me better understand what we learned during instruction, especially Dr. Cédric Tard, Prof. Jillian Dempsey, Michael Pegis, and Dominik Halter. Special thanks to Prof. Clifford P. Kubiak for introducing me to electrochemistry and for supporting my trip to Paris, France for this workshop.

Chapter 3, in part, is currently being prepared for submission for publication of the material, entitled "Kinetic and Mechanistic Effects of Substituent, Labile Ligand, and Brønsted Acid on Electrocatalytic CO_2 Reduction by Re(bpy) Complexes" by Melissa L. Clark, Martina Lessio, Po Ling Cheung, Emily A. Carter, and Clifford P. Kubiak. The dissertation author is the primary author of this manuscript.

This work was supported by the Air Force Office of Scientific Research through the MURI program under AFOSR Award No. FA9550-10-1-0572. Dr. Mark Reineke, Dr. Matthew D. Sampson, Prof. Cyrille Costentin, Prof. Charles Machan,

and Dr. Jonathan M. Smieja are acknowledged for valuable discussions and assistance.

Chapter 4, in full, comes directly from a manuscript entitled: "Electrocatalytic CO_2 Reduction by $M(bpy\text{-}R)(CO)_4$ (M = Mo, W; R = H, *t*Bu) Complexes. Electrochemical, Spectroscopic, and Computational Studies and Comparison with Group 7 Catalysts." by Melissa L. Clark, Kyle A. Grice, Curtis E. Moore, Arnold L. Rheingold, and Clifford P. Kubiak, which has been published in *Chemical Science*, **2014**, 5, 1894-1900. http://dx.doi.org/10.1039/c3sc53470g. The dissertation author is a primary co-author of this manuscript.

This work was supported by the Air Force Office of Scientific Research through the MURI program under AFOSR Award No. FA9550-10-1-0572. Dr. Candace Sue, Dr. Jonathan M. Smieja, Dr. Eric E. Benson, Dr. Jesse Froehlich, and Dr. Matthew D. Sampson are acknowledged for valuable discussions and assistance.

Chapter 5, in full, comes directly from a manuscript entitled: "Orientation of Cyano-Substituted Bipyridine Re(I) *fac*-Tricarbonyl Electrocatalysts Bound to Conducting Au Surfaces" by Melissa L. Clark, Benjamin Rudshteyn, Aimin Ge, Steven A. Chabolla, Charles W. Machan, Brain T. Psciuk, Jia Song, Gabriele Canzi, Tianquan Lian, Victor S. Batista, and Clifford P. Kubiak, which has been published in *The Journal of Physical Chemistry C*, **2016**, *120(3)*, 1657-1665.

http://dx.doi.org/10. 1021/acs.jpcc.5b10912. The dissertation author is the primary author of this manuscript.

This work was supported by the Air Force Office of Scientific Research Grant No. FA9550-13-1-0020. This research was carried out in collaboration with Prof. Tianquan Lian at Emory University, whose lab provided spectroscopic characterization, and Prof. Victor Batista at Yale Univeristy, whose lab provided computational modeling for the manuscript. I would like to thank all researchers that attended our weekly video conferences for their help and support. Prof. Charles W. Machan and Tram Dang are acknowledged for their insight and helpful discussions.

Chapter 6, in part, is currently being prepared for submission for publication of the material by Melissa L. Clark, Aimin Ge, Benjamin Rudshteyn, Christopher Miller, Tianquan Lian, Victor S. Batista, and Clifford P. Kubiak. The dissertation author is the primary author of this manuscript.

This work was supported by the Air Force Office of Scientific Research Grant No. FA9550-17-0198 under the same collaboration as Chapter 6. Gwendolynne Lee and Alma Zhanaidarova are acknowledged for their support and helpful discussions.

Chapter 7, in part, is currently being prepared for submission for publication of the material, entitled "Kinetic and Mechanistic Effects of Substituent, Labile Ligand, and Brønsted Acid on Electrocatalytic CO_2 Reduction by Re(bpy)

Complexes" by Melissa L. Clark, Martina Lessio, Po Ling Cheung, Emily A. Carter, and Clifford P. Kubiak, where Dr. Martina Lessio contributed the computational studies for this chapter. The dissertation author is the primary author of this manuscript.This work was supported by the Air Force Office of Scientific Research through the MURI program under AFOSR Award No. FA9550-10-1-0572. Prof. Charles Machan and Prof. Seth Cohen are acknowledged for valuable discussions and assistance.

VITA

2017	Doctor of Philosophy, University of California, San Diego
2014	Master of Science, University of California, San Diego
2012	Bachelor of Science, Rensselaer Polytechnic Institute

PUBLICATIONS

Sheik, D.A.; Chamberlain, J.M.; Brooks, L.R.; Clark, M.L.; Kim, Y.H.; Leriche, G.; Kubiak, C.P.; Dewhurst, S.; Yang, J. "Hydrophobic Nanoparticles Reduce the β-sheet content of SEVI Amyloid Fibrils and Inhibit SEVI-Enhanced HIV Infectivity" *Langmuir* **2017** *33 (10)*, 2596-2602.

Li, Y.; Wang, J. Clark, M.L.; Kubiak, C.P.; Xiong, W. "Characterizing Interstate Vibrational Coherent Dynamics of Surface Adsorbed Catalysts by Fourth-Order 3D SFG Spectroscopy" *Chem. Phys. Lett.* **2016** *650*, 1-6.

Clark, M.L.; Rudshteyn, B.; Ge, A.; Chabolla, S.A.; Machan, C.A.; Psciuk, B.T.; Song, J.; Canzi, G.; Lian, T.; Batista, V.S.; Kubiak, C.P. "Orientation of Cyano-Substituted Bipyridine Re(I) *fac*-Tricarbonyl Electrocatalysts Bound to Conducting Au Surfaces" *J. Phys. Chem. C.* **2016** *120 (3),* 1657-1665.

Wang, J.; Clark, M.L.; Li, Y.; Kaslan, C.L.; Kubiak, C.P.; Xiong, W. "Short Range Catalyst-Surface Interactions Revealed by Heterodyne Two Dimensional Sum Frequency Generation Spectroscopy" *J. Phys. Chem. Lett.* **2015** *6*, 4204-4209.

Vollmer, M.W.; Machan, C.W.; Clark, M.L.; Antholine, W.E.; Agarwal, J.; Schaefer III, H.F.; Kubiak, C.P.; Walensky, J.R. "Synthesis, Spectroscopy, and Electrochemistry of (α-Diimine)M(CO)$_3$Br, M = Mn, Re, Complexes: Ligands Isoelectronic to Bipyridyl Show Differences in CO$_2$ Reduction" *Organometallics* **2015**, *34 (1)*, 3-12.

Khetubol, A.; Van Snick, S.; Clark, M.L.; Fron, E.; Coutiño-González, E.; Cloet, A.; Kennes, K.; Firdaus, Y.; Vlasselaer, M.; Leen, V.; Dehaen, W.; Van der Auweraer, M. "Improved Spectral Coverage and Fluorescence Quenching in Donor–acceptor Systems Involving Indolo[3,2-*b*]carbazole and Boron-dipyrromethene or Diketopyrrolopyrrole" *Photochem. Photobiol.* **2015**, *91(3)*, 637-653.

Clark, M.L.; Grice, K.A.; Moore, C.E.; Rheingold, A.L.; Kubiak, C.P.; "Electrocatalytic CO_2 reduction by $M(bpy\text{-}R)(CO)_4$ (M = Mo, W; R = H,*t*Bu) complexes. Electrochemical, spectroscopic, and computational studies and comparison with group 7 catalysts." *Chem. Sci.*, **2014**, *5*, 1894-1900.

ABSTRACT OF THE DISSERTATION

Electrocatalytic carbon dioxide reduction by bipyridine based complexes and their derivatives

by

Melissa Lynn Helm
Doctor of Philosophy in Chemistry
University of California, San Diego, 2017
Professor Clifford P. Kubiak, Chair

As global anthropogenic carbon dioxide (CO_2) emissions continue to rise, there is a need not only to reduce production of CO_2, but also an opportunity to use it as a substrate for value-added products. One viable solution is to reduce CO_2 in the two proton, two electron coupled process to produce carbon monoxide (CO), which can in turn be utilized to recreate hydrocarbon fuels. One of the most active and selective molecular electrocatalysts for the reduction of CO_2 to CO is Re(2,2′-bipyridine)$(CO)_3Cl$ (Re-bpy) and derivatives thereof. The best method to study electrocatalysts is cyclic voltammetry (CV), which affords both kinetic and thermodynamic information about catalysis. CV is the main technique used to characterize substituent, labile ligand, and Brønsted acid effects on Re-bpy based catalysts, which show increased activity with electron donating 4,4′-substituents and moderate Brønsted acids such as 2,2,2-trifluoroethanol and phenol. The Re-bpy catalyst motif is also extended to Group 6 Mo and W metals, which are not as active as their Group 7 counterparts due to high overpotentials and product poisoning of the catalyst.

To build a fundamental understanding of how molecular catalysts interact with surfaces, Re-bpy derivatives were bound to Au substrates and studied by sum frequency generation spectroscopy (SFG). While cyano substituents deactivated the molecular catalyst, they adsorbed onto Au surfaces, allowing for determination of molecular orientation on the surface as well as characterization of surface-molecule vibratinal communication. Thiol groups were subsequently employed on the bpy ligand for both Re and Mn catalysts to create a covalent attachment to Au surfaces. These groups did not deactivate the molecular catalysts and reproducibly create monolayers on Au surfaces. Further studies are needed in order to fully understand the implications of surface bound Re-bpy based catalysis as well as apply the design principles learned from Re-bpy systems to future molecular electrocatalysts.

Chapter 1

Carbon Dioxide: Reduce, Reuse, Recycle

1.1 Reduce CO_2 Emissions

The development and implementation of a renewable, clean energy infrastructure to support modern day society across the globe is one of the biggest challenges currently facing humanity. Since the industrial revolution, mankind has relied on mining oil, coal, and natural gas (termed ‘fossil fuels’) to provide the energy needed to drive economic progress. As of 2015, an estimated 78.3% of the world’s energy still come from these sources (Figure 1.1),[1-2] which are estimated to be near depleted by the end of the century. Considering the extremely unbalanced distribution of fossil fuel reserves across the globe, tension between political parties will continue to escalate as demand for fossil fuels surpasses the remaining supply.

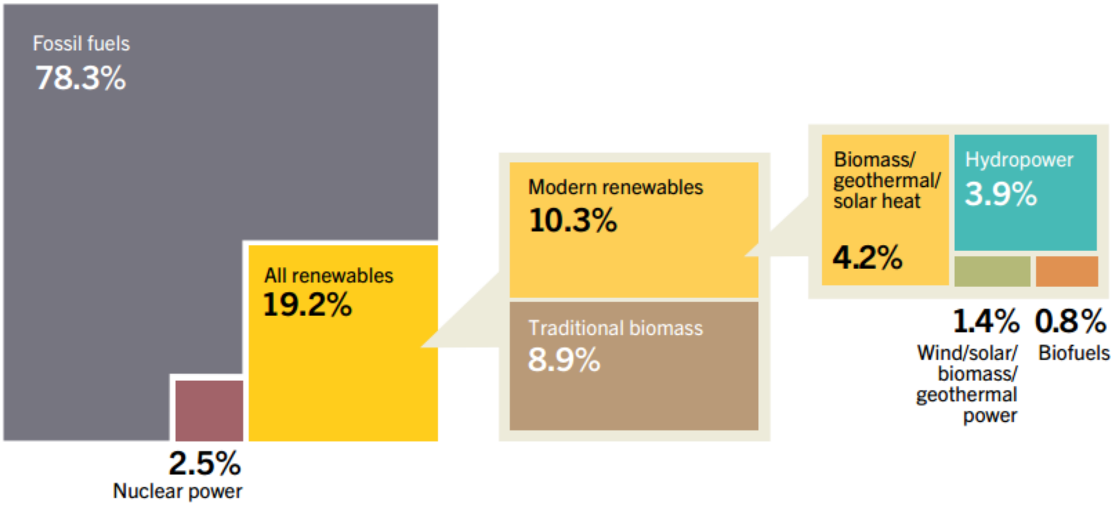

Figure 1.1 Estimated Renewable Energy Share of Global Final Energy Consumption, 2014. Figure reproduced in full from Reference 2.

Not only are fossil fuels a finite resource, but the procurement of these energy sources cause significant damage to the environment. The extraction of fossil fuels through mountaintop removal or mining creates a plethora of environmental rists including landslides, flashfloods, and sinkholes due to the removal of natural vegetation, as well as pollution of public water supply.[3] Extraction from the sea floor has high risks as well because of the potential of an oil spill, like the *Deepwater Horizon* BP oil spill in 2010, which discharged an estimated 210 million gallons of oil in the Gulf of Mexico.[4] The environmental impacts of fossil fuel consumption has even higher negative impacts than their extraction. The main waste products from fossil fuel combustion are carbon dioxide (CO_2), carbon monoxide (CO), sulfur dioxide (SO_2), nitrogen oxides (NO_x), and particulate matter (including lead).[5] All but CO_2 are damaging to human health, harming the lungs and putting strain on the cardiovascular system. Sulfur dioxide and nitrogen oxides also cause acid rain, which leads to acidification of the land and waterways, creating toxic environments for fish and plants. Acid rain causes significant damage to buildings and monuments through the increased corrosion of limestone and marble. Furthermore, these emissions create significant air pollution, which decrease visibility (as witnessed during the 2008 Summer Olympics in Beijing).

The principal and most damaging product from fossil fuel combustion is carbon dioxide. Carbon dioxide accounts for roughly 78% of all emissions,[6] and the increased level of CO_2 in the environment is having an alarming impact. While the Earth has a natural CO_2 cycle between the plants, ocean, and atmosphere, anthropogenic CO_2 emissions are adding an extra *ca.* 3% of CO_2 to the atmosphere a year (based on emissions data from 2000-2005).[7] This impacts every part of the natural cycle. Increased levels of CO_2 in the ocean are causing pH levels to lower ($CO_2 + H_2O \leftrightarrow H_2CO_3 \leftrightarrow HCO_3^- + H^+ \leftrightarrow CO_3^{2-} + 2H^+$), causing problems like coral bleaching, decreased growth of organisms that rely on calcification, and general disruption of ecosystems.[8] The 2014 concentration of CO_2 in the atmosphere (397 ppm) was about 40% higher than that in the 1880s, with an average growth of 2 ppm/year over the last ten years.[1] Increased CO_2 in the atmosphere contributes to the “greenhouse effect,” where gases trap infrared radiation from the Earth’s surface and cause the planet to warm. This ‘global warming’ leads to warming of the ocean, melting glaciers and causing sea level rise. The ocean has a large impact on weather patterns, and as a result extreme weather events such as droughts, hurricanes, flooding, and tornados are becoming more frequent and deadly.[6] Mankind's land, food sources, and health are at risk and the need to reduce CO_2 emissions is dire.

Eliminating the use of fossil fuels would greatly decrease the amount of anthropogenic CO_2 emissions, thus helping to mitigate these harmful effects. Significant advances in technology have already allowed for the implementation of a variety of non-fossil fuel energy resources. These include wind, solar, geothermal, hydropower, and biomass, which currently cover 19.2% of global energy consumption (Figure 1.1).[2] While these technologies should continue to be developed and implemented, the one area that they all fall short in is storage and transport.[9] The convenience of oil comes from its ease of transport and high energy density, and batteries have yet to match its energy storage capacity (airplanes and rockets cannot run off of batteries, for example).[10] Further technologies need to be developed.

1.2 Reuse CO_2

Until solutions are found that fit into our current oil-based infrastructure, action needs to be taken to limit how much CO_2 escapes into our atmosphere. The first step would be in CO_2 capture. Carbon capture and sequestration (CCS) is the concept of capturing waste CO_2 from power and manufacturing plants, cars, or other producers and store it so that it will not enter the atmosphere.[6] Various technologies are being developed to adsorb CO_2 and some with commercial use, however the increased cost of implementing current systems far outweigh the benefits. The second step would be in the consumption and utilization of CO_2. CO_2 has a variety of uses in our modern day society;[11-12] it is most often used as a liquid by the oil industry (e.g. enhanced oil recovery), food industry (e.g. wine making, food preservation, beverage carbonation), steel manufacturing, and waste water treatment. Chemicals such as aspirin, urea, and polycarbamates are manufactured using CO_2 as a reactant. Even with these uses, the supply of CO_2 from fossil fuel combustion (*ca.* 49 $GtCO_2$ equivalents/yr)[6] is inordinately larger than the industrial demand (80 $MtCO_2$/yr).[13]

1.3 Recycle CO_2

The dependence on fossil fuels for the foreseeable future as well as the lack of industry to completely consume manufactured CO_2 leads to an idea of recycling CO_2 to recreate energy dense fuels.[14] There are no commercially viable ways to do this yet, however there are many proposed approaches (Figure 1.2). One method could be to directly convert CO_2 into a liquid fuel such as methanol. However, the kinetic and thermodynamic barriers to complete this $6H^+$, $6e^-$ coupled process limits its feasibility.[15] A second idea is tandem catalysis, where a specific catalyst is used for each step of the process in order to make a chemical fuel. This has been demonstrated by using three different homogeneous catalysts for the hydrogenation of CO_2 to methanol.[16] Here, CO_2 is hydrogenated to formic acid, followed by esterification to a formate ester, which is then hydrogenated to create methanol. This strategy shows promise, however the scalability has yet to be determined.

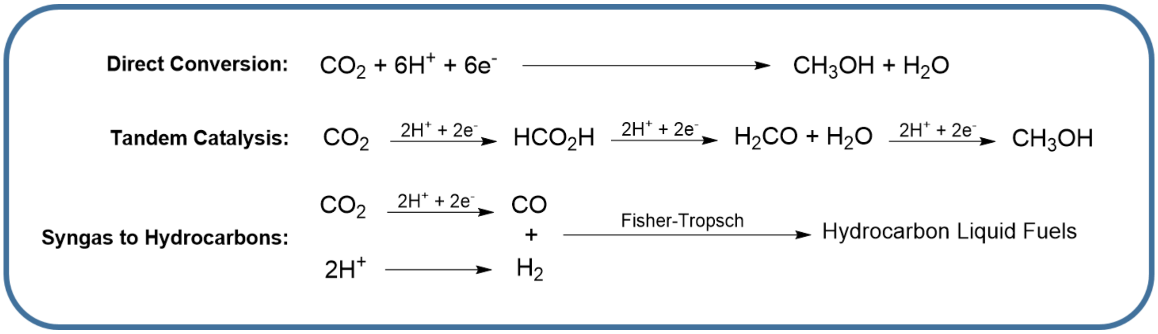

Figure 1.2 Schemes showing the three main strategies for converting CO_2 into liquid fuels.

A third strategy to produce liquid fuels from CO_2 is to reduce CO_2 to CO to help produce syngas (a mixture of CO and H_2). The produced syngas can then be used in already commercialized Fischer-Tröpsch reactions. Fischer-Tröpsch technologies utilize high temperatures (300-350ºC) and pressures (2 MPa) with iron-based catalysts to produce linear chain hydrocarbons, including gasoline.[17] The largest scale implementation of the Fischer-Tröpsch technology is operated by Sasol in South Africa, where it produces the majority of the country's diesel fuel.[18]

These strategies are dependent on the facile activation of CO_2. A quite stable molecule, CO_2 is nonpolar and has a high thermodynamic barrier for the addition of one electron ($CO_2 + 1e^- \rightarrow CO_2^{\bullet-}$ takes –1.90 V vs. NHE).[14] This primarily has to do with the large reorganizational energy required to bend the linear CO_2 molecule. Proton-coupled reactions or the presence of reducing agents help decrease this barrier. This includes the base-assisted H_2 activation to make formate, insertion into metal bonds to make carbamates, or electrocatalytic reduction to make CO, formate, or carbonates.[19] To drive these chemical reactions, organometallic catalysts are often employed. Transition metal complexes can polarize CO_2 to activate it by most commonly attacking the carbon — η^1 nucleophilic activation, where η^x signifies the number of bonds between the metal and coordinated CO_2 — or activating the double bond, η^2 activation (Figure 1.3).[20] CO_2 can also bind between two metal centers, and structures have been reported where three or four metal centers are involved.[21] The characterization of these CO_2-adducts is important in better understanding activation to help drive discovery of catalysts.

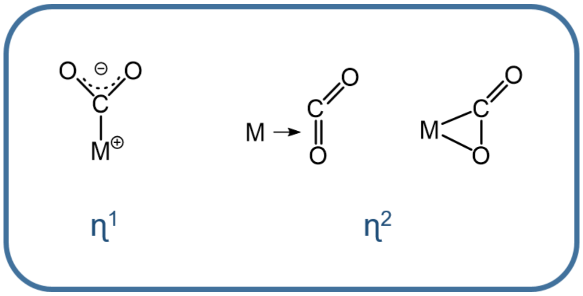

Figure 1.3 Depiction of common binding modes between a CO_2 ligand and metal center.

1.4 Re(bpy)(CO)$_3$Cl – An electrocatalyst for recycling CO$_2$

In 1984 Hawecker, Lehn, and Ziessel reported the electrochemical reduction of CO_2 to CO by Re(bpy)(CO)$_3$Cl (bpy = 2,2′-bipyridine, referred to as Re(bpy)).[22] In this report, it is shown that the catalyst selectively reduces CO_2 to CO in a 9:1 DMF:H_2O solution with 98% Faradaic efficiency. This Re(bpy) catalyst and derivatives thereof are still among the most active and selective molecular electrocatalysts for the reduction of CO_2.[23]

The Re(bpy) catalyst undergoes two reductions to create a catalytically active state capable of the proton coupled 2-electron process of converting CO_2

into CO (Figure 1.4). The first reduction has been found to be a ligand centered, where the electron density presides in the π^* orbital of the bpy. This is observed through a quasi-reversible wave in the cyclic voltammetry (CV) as well as in infrared-spectroelectrochemistry (IR-SEC) where the carbonyl stretching frequencies shift by about 20 cm^{-1}.[24-25] The singly reduced state will undergo a ligand to metal charge transfer (LMCT), yielding Re^0 and subsequent loss of chloride. Dimerization is known to occur, which is both spectroscopically observed and structurally characterized.[26] If the complex is held at a potential akin to the first reduction under catalytic conditions, the main products observed are CO and carbonate (CO_3^{2-}). This has been termed the “one-electron pathway.”[27] Re(bpy) is also photochemically active at the singly reduced state, where carbonate is thought to form via a bimolecular pathway.[28-30]

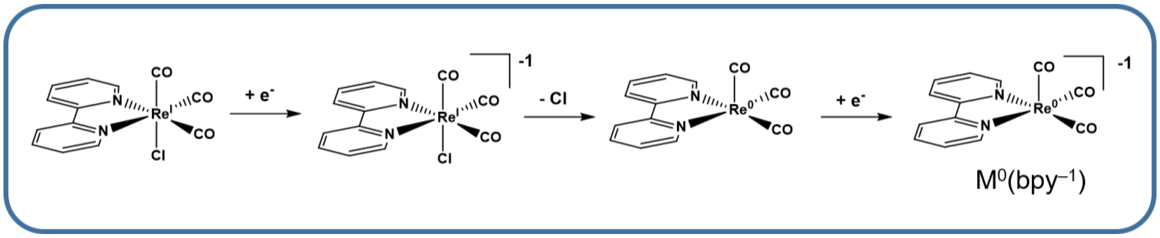

Figure 1.4 Reductions of Re(bpy) leading to the catalytically active state of the complex. Under CV conditions, the second reduction is metal based which happens concurrently with the loss of chloride.

The second reduction of Re(bpy) under CV conditions is metal based, coupled with the loss of the halide ligand to form the catalytically active state. The crystal structure of this doubly reduced complex exhibits a 5-coordinate distorted square pyramidal arrangement, where the bpy C_{py}-C_{py} is shortened compared to the neutral ligand indicating significant electron density on the bpy.[26, 31] The oxidation state of rhenium was confirmed by X-ray absorption spectroscopy (XAS) at the Re L_3 absorption edge, where the white-line region matched that of the Re^0 dimer [$\{Re(bpy)(CO)_3\}_2$] and showed increased electron density compared to the singly reduced state.[32]

This $Re^0(bpy)^{-1}$ catalytically active state is thought to be a main reason why the catalyst is so selective for CO_2 reduction over proton reduction to produce H_2.[32] The delocalized highest occupied molecular orbital (HOMO) across the metal and ligand allow for both σ and π interactions for activation of CO_2 (Figure 1.5). A $Re^{-1}(bpy)^0$ state would have a doubly occupied $d_z{}^2$ orbital, which is predicted to more easily form the metal hydride for H_2 production.[32] Density functional theory (DFT) calculations of the reactivity of the catalytically active state show that it is more thermodynamically favorable for protons to bind to the catalyst over CO_2, however the reaction barrier is higher.[33] Through stopped-flow spectroscopy it was found that CO_2 reacts 35 times faster than water with the catalyst.[34] This points to a kinetic over thermodynamic reasoning for catalyst selectivity. It has been calculated that the catalyst would favor proton reduction at a pK_a below that of 16.5,[33] although this has not been experimentally verified.

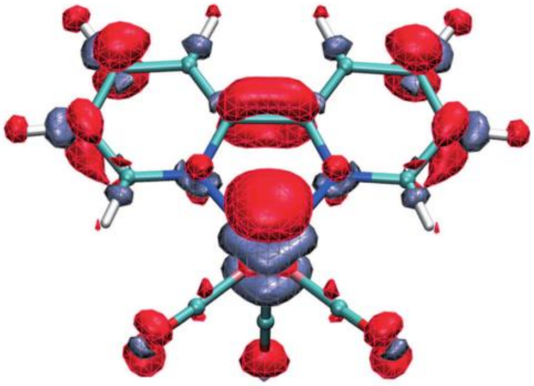

Figure 1.5 Density difference plots showing the polarization that occurs upon adding two electrons to the LUMO of the $[Re(bpy)(CO)_3]^+$ cation to form the HOMO of the $[Re(bpy)(CO)_3]^-$ anion. The isosurface depicts contour values of 0.005; red is increased charge density; purple is decreased charge density. Reproduced in full from Reference 32.

Progressing past CO_2 binding, the mechanism for CO_2 reduction involves the addition of two protons and the breaking of a C=O bond to create CO and H_2O (Figure 1.6). In the current understanding of the mechanism, the bound and now bent CO_2 molecule immediately abstracts a proton from solution in a thermodynamically neutral step to create a bound hydroxycarbonyl.[35] The molecule then undergoes a bpy-based reduction followed by the rate limiting step, which is the abstraction of another proton and cleavage of the C-O bond to liberate water. Another reduction of the complex occurs to expel the produced CO and regenerate the catalytically active state.[36-37]

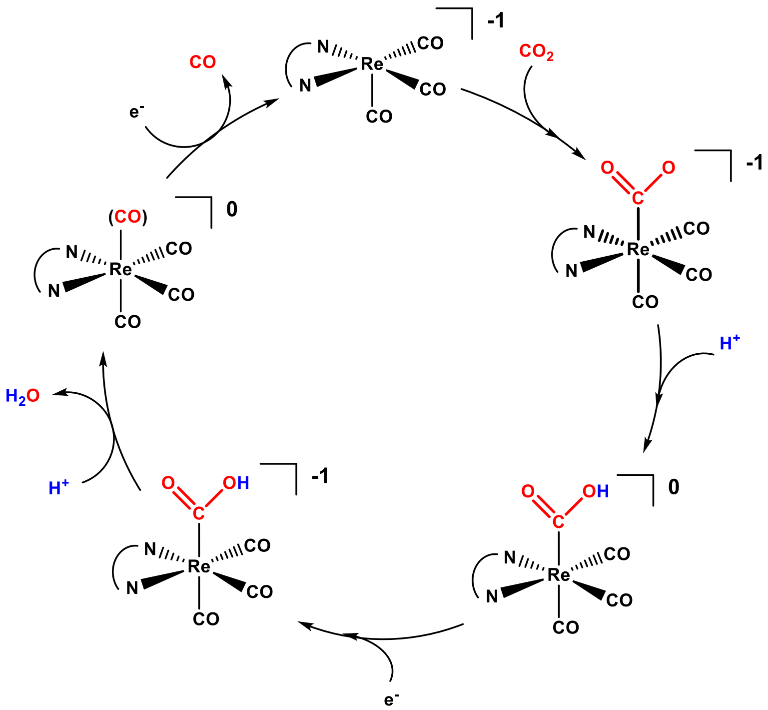

Figure 1.6 Proposed electrocatalytic mechanism for the reduction of CO_2 to CO by $Re(bpy)(CO)_3Cl$. N∩N represents the 2,2′-bipyridine ligand.

Along with the interest in understanding how the catalyst operates, significant efforts have been made to increase activity while maintaining catalyst selectivity. One factor is proton concentration. Re(bpy) has a second order rate dependence on protons,[34] and in the first report of Re(bpy) it was shown that adding 10% water increased the activity of the catalyst.[22] The effect of added Brønsted acids was expanded to trifluoroethanol (TFE), methanol (MeOH), and phenol with $Re(bpy)(CO)_3(py)$ (py = pyridine),[38] where it was noted that the efficiency of the catalyst increases with the acidity of the acid used (TFE > MeOH > H_2O at turnover frequencies of 410, 94, and 5.7 s^{-1}, respectively).[39] This trend has also been computationally verified, where decreasing the pKa of solution lowers the reaction free energy for CO_2 reduction, allowing for higher turnover frequencies.[40]

The synthetic ability to functionalize bpy[41] has also led to extensive studies of the effect of ligand modification on catalysis. In 1986, Sullivan and Meyer reported a kinetic study of the effect of 4,4′-substituted bpys on the rate of CO_2 insertion into a Re-H bond. They found that electron donating groups (OMe, tBu, and CH_3) increased the rate of insertion.[42] This idea of changing the electronic character of the bpy by adding electron donating or withdrawing substituents at the 4,4′-position was directly applied to electrocatalysis in 2010, where it was found that electron donating substituents, particularly *tert*-butyl groups, enhanced catalytic activity without affecting selectivity.[24, 43] Biology-inspired substituents have also been applied that encourage hydrogen-bonding between complexes to promote a bimetallic pathway that resulted in increased production of carbonate.[44-45] Positional effects are also noted to effect catalysis. In a study using methyl substituents, it was found that 5,5′-substituents increase catalytic activity while 3,3′-substituents decrease catalytic current response.[46]

The success of Re(bpy) as a molecular catalyst has inspired work into incorporating the complex into heterogeneous structures. Using 4-vinyl-bpy, Re complexes have been made into polymerized films on platinum,[47-49] silicon, tungsten selenide,[50] titanium oxide (TiO_2),[51] and carbon[48, 52-53] electrodes, where catalysis is still observed but selectivity is decreased (products such as oxalate, hydrogen or formate are also detected).[53-54] Re(bpy) has been incorporated into a Nafion membranes where water could be used as the solvent, however selectivity dropped to 23% for CO production, as H_2 and formate were also produced.[55] Re(bpy) has also been incorporated into a bio-inspired polymeric structure, where overpotential was decreased by 300 mV without affecting the selectivity of the parent homogeneous catalyst.[56] Extending to substrate-surface interactions, Re(4,4′-dicarboxy-bpy)$(CO)_3Cl$ covalently attached to TiO_2 has been extensively studied using sum frequency generation spectroscopy (SFG), where information about electron transfer and orientation of the complexes on the surface are scrutinized.[57-64] All of these methods demonstrate the potential versatility of catalysts like Re(bpy) and the many viable ways to incorporate homogeneous catalysts into industrially viable systems.

1.5 Outlook

The dire need for solutions to mankind's dependence on fossil fuels for energy generation puts a large emphasis on research and development of all promising sustainable technologies. Implementation of stationary power sources from wind, geothermal, hydropower, and solar are all necessary to help provide energy to our existing electric grid. The continued advancement of battery technology will also help to alleviate the need for transportable consumable energy sources. Larger transportation needs such as airplanes and rockets will still need combustible fuel, and finding ways to sustainably meet this need is a key factor still missing for a sustainable energy economy.

Returning produced CO_2 to an energetically useful state is a promising route to create the transportable liquid fuels needed, but currently the thermodynamic and kinetic barriers for any product are too high. Better understanding of how to activate CO_2 and the mechanisms behind these transformations is needed in order to help develop more deployable solutions. The research that has been put into developing and understanding the Re(bpy) family of catalysts has laid important groundwork to help achieve these goals. Further research into the discovery of homogeneous or heterogeneous catalysts for CO_2 reduction is of great importance to help accelerate the adoption of renewable energy practices before the environmental damages from our current energy practices become completely irreversible.

With all of these issues in mind, the work described in this dissertation focuses on further developing our understanding of the Re(bpy) system to help contribute to the knowledge of how to reduce CO_2. The activity of substituted Re(bpy) systems is expanded to fully understand the effects of substituent and acid co-substrate. Group 6 metals (W and Mo) are investigated to identify how these more Earth-abundant metals behave as electrocatalysts.[65] Cyano[66] and thiol substituents are also explored because of their ability to attach to gold substrates so that surface-complex interactions can be measured. Finally, non-bpy α-diimines are considered for their ability to electrocatalytically reduce CO_2 using the same Re tricarbonyl framework, and their inability to stand up to the activity and selectivity of Re(bpy) is scrutinized.

1.6 References

(1) CO_2 Emissions From Fuel Combustion. Highlights 2015 Edition *IEA Statisitcs* [Online], 2015. (accessed May 28, 2017).

(2) Renewables 2016 Global Status Report *Key Findings 2016* [Online], 2016. (accessed May 28, 2017).

(3) Holzman, D. C., *Environ. Health Perspect.* **2011**, *119*, a476.

(4) On Scene Coordinator Report: Deepwater Horizon Oil Spill 2011, p. 244. (accessed May 28, 2017).

(5) Pisupati, S. Products of Combustion *EGEE 102: Energy Conservation and Environmental Protection* [Online], 2017. (accessed May 28, 2017).

(6) Climate Change 2014 Synthesis Report *Summary for Policymakers* [Online], 2014. (accessed May 28, 2017).

(7) Raupach, M. R.; Marland, G.; Ciais, P.; Le Quere, C.; Canadell, J. G.; Klepper, G.; Field, C. B., *Proc. Nat. Acad. Sci. USA* **2007**, *104*, 10288.

(8) Orr, J. C.; Fabry, V. J.; Aumont, O.; Bopp, L.; Doney, S. C.; Feely, R. A.; Gnanadesikan, A.; Gruber, N.; Ishida, A.; Joos, F.; Key, R. M.; Lindsay, K.; Maier-Reimer, E.; Matear, R.; Monfray, P.; Mouchet, A.; Najjar, R. G.; Plattner, G. K.; Rodgers, K. B.; Sabine, C. L.; Sarmiento, J. L.; Schlitzer, R.; Slater, R. D.; Totterdell, I. J.; Weirig, M. F.; Yamanaka, Y.; Yool, A., *Nature* **2005**, *437*, 681.

(9) Cook, T. R.; Dogutan, D. K.; Reece, S. Y.; Surendranath, Y.; Teets, T. S.; Nocera, D. G., *Chem. Rev.* **2010**, *110*, 6474.

(10) Luo, X.; Wang, J.; Dooner, M.; Clarke, J., *Appl. Energy* **2015**, *137*, 511.

(11) Liu, Q.; Wu, L.; Jackstell, R.; Beller, M., *Nat. Commun.* **2015**, *6*, 5933.

(12) Maeda, C.; Miyazaki, Y.; Ema, T., *Catal. Sci. Tech.* **2014**, *4*, 1482.

(13) Jochem, E., *Improving the efficiency of R&D and the market diffusion of energy technologies*. Physica: Dordrecht; London, 2009; 33.

(14) Benson, E. E.; Kubiak, C. P.; Sathrum, A. J.; Smieja, J. M., *Chem. Soc. Rev.* **2009**, *38*, 89.

(15) Alberico, E.; Nielsen, M., *Chem. Commun.* **2015**, *51*, 6714.

(16) Huff, C. A.; Sanford, M. S., *J. Am. Chem. Soc.* **2011**, *133*, 18122.

(17) Dry, M. E., *Catal. Today* **2002**, *71*, 227.

(18) Sasol. www.sasol.com (accessed May 27, 2017).

(19) Grice, K. A., *Coord. Chem. Rev.* **2017**, *336*, 78.

(20) Aresta, M.; Dibenedetto, A.; Quaranta, E., *Reaction Mechanisms in Carbon Dioxide Conversion*. 1 ed.; Springer-Verlag Berlin Heidelberg: 2016.

(21) Paparo, A.; Okuda, J., *Coord. Chem. Rev.* **2017**, *334*, 136.

(22) Hawecker, J.; Lehn, J.-M.; Ziessel, R., *J. Chem. Soc., Chem. Commun.* **1984**, 328.

(23) Grice, K. A.; Kubiak, C. P., Chapter five - Recent studies of rhenium and manganese bipyridine carbonyl catalysts for the electrochemical reduction of CO_2. In *Advances in Inorganic Chemistry*, Michele, A.; Rudi van, E., Eds. Academic Press: 2014; Vol. 66, 163-188.

(24) Smieja, J. M.; Kubiak, C. P., *Inorg. Chem.* **2010**, *49*, 9283.

(25) Machan, C. W.; Sampson, M. D.; Chabolla, S. A.; Dang, T.; Kubiak, C. P., *Organometallics* **2014**, *33*, 4550.

(26) Benson, E. E.; Kubiak, C. P., *Chem. Commun.* **2012**, *48*, 7374.

(27) Sullivan, B. P.; Bolinger, C. M.; Conrad, D.; Vining, W. J.; Meyer, T. J., *J. Chem. Soc., Chem. Commun.* **1985**, 1414.

(28) Agarwal, J.; Fujita, E.; Schaefer, H. F., 3rd; Muckerman, J. T., *J. Am. Chem. Soc.* **2012**, *134*, 5180.

(29) Hawecker, J.; Lehn, J.-M.; Ziessel, R., *J. Chem. Soc., Chem. Commun.* **1983**, 536.

(30) Morris, A. J.; Meyer, G. J.; Fujita, E., *Acc. Chem. Res.* **2009**, *42*, 1983.

(31) Kallane, S. I.; van Gastel, M., *J. Phys. Chem. A* **2016**, *120*, 7465.

(32) Benson, E. E.; Sampson, M. D.; Grice, K. A.; Smieja, J. M.; Froehlich, J. D.; Friebel, D.; Keith, J. A.; Carter, E. A.; Nilsson, A.; Kubiak, C. P., *Angew. Chem. Intl. Ed.* **2013**, *52*, 4841.

(33) Keith, J. A.; Grice, K. A.; Kubiak, C. P.; Carter, E. A., *J. Am. Chem. Soc.* **2013**, *135*, 15823.

(34) Smieja, J. M.; Benson, E. E.; Kumar, B.; Grice, K. A.; Seu, C. S.; Miller, A. J.; Mayer, J. M.; Kubiak, C. P., *Proc. Nat. Acad. Sci. USA* **2012**, *109*, 15646.

(35) Sampson, M. D.; Froehlich, J. D.; Smieja, J. M.; Benson, E. E.; Sharp, I. D.; Kubiak, C. P., *Energy Environ. Sci.* **2013**, *6*, 3748.

(36) Grice, K. A.; Gu, N. X.; Sampson, M. D.; Kubiak, C. P., *Dalton Trans.* **2013**, *42*, 8498.

(37) Riplinger, C.; Sampson, M. D.; Ritzmann, A. M.; Kubiak, C. P.; Carter, E. A., *J. Am. Chem. Soc.* **2014**, *136*, 16285.

(38) Wong, K.-Y.; Chung, W.-H.; Lau, C.-P., *J. Electroanal. Chem.* **1998**, *453*, 161.

(39) Smieja, J. M.; Sampson, M. D.; Grice, K. A.; Benson, E. E.; Froehlich, J. D.; Kubiak, C. P., *Inorg. Chem.* **2013**, *52*, 2484.

(40) Riplinger, C.; Carter, E. A., *ACS Catal.* **2015**, *5*, 900.

(41) Smith, A. P.; Fraser, C. L., Bipyridine Ligands. In *Comprehensive Coordination Chemistry II*, Elsevier Ltd.: 2004; Vol. 1, 1-23.

(42) Sullivan, B. P.; Meyer, T. J., *Organometallics* **1986**, *5*, 1500.

(43) Benson, E. E.; Grice, K. A.; Smieja, J. M.; Kubiak, C. P., *Polyhedron* **2013**, *58*, 229.

(44) Machan, C. W.; Chabolla, S. A.; Yin, J.; Gilson, M. K.; Tezcan, F. A.; Kubiak, C. P., *J. Am. Chem. Soc.* **2014**, *136*, 14598.

(45) Machan, C. W.; Yin, J.; Chabolla, S. A.; Gilson, M. K.; Kubiak, C. P., *J. Am. Chem. Soc.* **2016**, *138*, 8184.

(46) Chabolla, S. A.; Dellamary, E. A.; Machan, C. W.; Tezcan, F. A.; Kubiak, C. P., *Inorg. Chim. Acta* **2014**, *422*, 109.

(47) Cosnier, S.; Deronzier, A.; Moutet, J.-C., *J. Electroanal. Chem.* **1986**, *207*, 315.

(48) Cosnier, S.; Deronzier, A.; Moutet, J.-C., *J. Mol. Catal.* **1988**, *45*, 381.

(49) O'Toole, T. R.; Margerum, L. D.; Westmoreland, T. D.; Vining, W. J.; Murray, R. W.; Meyer, T. J., *J. Chem. Soc., Chem. Commun.* **1985**, 1416.

(50) Cabrera, C. R.; Abruña, H. D., *J. Electroanal. Chem.* **1986**, *209*, 101.

(51) Cecchet, F.; Alebbi, M.; Bignozzi, C. A.; Paolucci, F., *Inorg. Chim. Acta* **2006**, *359*, 3871.

(52) Blakemore, J. D.; Gupta, A.; Warren, J. J.; Brunschwig, B. S.; Gray, H. B., *J. Am. Chem. Soc.* **2013**, *135*, 18288.

(53) O'Toole, T. R.; Sullivan, B. P.; Bruce, M. R. M.; Margerum, L. D.; Murray, R. W.; Meyer, T. J., *J. Electroanal. Chem.* **1989**, *259*, 217.

(54) Cosnier, S.; Deronzier, A.; Moutet, J. C., *New J. Chem.* **1990**, *14*, 831.

(55) Yoshida, T.; Tsutsumida, K.; Teratani, S.; Yasufuku, K.; Kaneko, M., *J. Chem. Soc., Chem. Commun.* **1993**, 631.

(56) Gianneschi, N. C.; Sahu, S.; Cheung, P. L.; Machan, C.; Chabolla, S.; Kubiak, C., *Chemistry* **2017**, *Just Accepted*.

(57) Paoprasert, P.; Laaser, J. E.; Xiong, W.; Franking, R. A.; Hamers, R. J.; Zanni, M. T.; Schmidt, J. R.; Gopalan, P., *J. Phys. Chem. C* **2010**, *114*, 9898.

(58) Anfuso, C. L.; Snoeberger, R. C., 3rd; Ricks, A. M.; Liu, W.; Xiao, D.; Batista, V. S.; Lian, T., *J. Am. Chem. Soc.* **2011**, *133*, 6922.

(59) Xiong, W.; Laaser, J. E.; Mehlenbacher, R. D.; Zanni, M. T., *Proc. Nat. Acad. Sci. USA* **2011**, *108*, 20902.

(60) Anfuso, C. L.; Ricks, A. M.; Rodríguez-Córdoba, W.; Lian, T., *J. Phys. Chem. C* **2012**, *116*, 26377.

(61) Anfuso, C. L.; Xiao, D. Q.; Ricks, A. M.; Negre, C. F. A.; Batista, V. S.; Lian, T. Q., *J. Phys. Chem. C* **2012**, *116*, 24107.

(62) Liu, C.; Dubois, K. D.; Louis, M. E.; Vorushilov, A. S.; Li, G., *ACS Catal.* **2013**, *3*, 655.

(63) Laaser, J. E.; Christianson, J. R.; Oudenhoven, T. A.; Joo, Y.; Gopalan, P.; Schmidt, J. R.; Zanni, M. T., *J. Phys. Chem. C* **2014**, *118*, 5854.

(64) Ge, A.; Rudshteyn, B.; Psciuk, B. T.; Xiao, D.; Song, J.; Anfuso, C. L.; Ricks, A. M.; Batista, V. S.; Lian, T., *J. Phys. Chem. C* **2016**, *120*, 20970.

(65) Clark, M. L.; Grice, K. A.; Moore, C. E.; Rheingold, A. L.; Kubiak, C. P., *Chem. Sci.* **2014**, *5*, 1894.

(66) Clark, M. L.; Rudshteyn, B.; Ge, A.; Chabolla, S. A.; Machan, C. W.; Psciuk, B. T.; Song, J.; Canzi, G.; Lian, T.; Batista, V. S.; Kubiak, C. P., *J. Phys. Chem. C* **2016**, *120*, 1657.

Chapter 2

Careful Cyclic Voltammetry as a Means for Understanding Electrocatalysis

2.1 Introduction

Electrochemistry is the study of the interconversion between chemical and electrical energy. It is typically investigated using electrochemical cells composed two half reactions, one occurring at the anode (negatively charged electrode) and one at the cathode (positively charged electrode). If the reaction taking place at the anode is more thermodynamically favored than the one at the cathode, the reactions will occur spontaneously and a current (flow of electrons) is measured between the two half cells. This is called a galvanic cell. Batteries are a type galvanic cell; for example, in alkaline batteries a zinc anode is oxidized while a manganese dioxide cathode is reduced, giving the overall reaction in Equation E2.1.[1] This reaction results in a positive voltage of 1.5 V, typical of a household AA battery.

$$Zn(s) + 2MnO_2(s) \rightleftharpoons ZnO(s) + Mn_2O_3(s) \qquad E^\circ = +1.50\ V \qquad (\textbf{E2.1})$$

If the reaction is non-spontaneous, a voltage is applied to the cell to drive the reaction and is classified as an electrolytic cell. Electroplating is an example of this.

In systems that are thermodynamically driven, the voltage from the cell is related to the Gibbs free energy of the reaction as determined by Equation E2.2

$$\Delta G = -nFE^{o}_{cell} \qquad (\textbf{E2.2})$$

where n is the number of electrons involved in the overall reaction, F is Faraday's constant, and E^{o}_{cell} is the potential at which the overall reaction takes place. This relationship only applies when the cell is in its standard state. When the cell components are at non-equilibrium, the cell potential (E_{cell}) is related to E^{o}_{cell} via the Nernst equation (E2.3),

$$E_{cell} = E^{\circ}_{cell} - \frac{RT}{nF}\log Q \qquad (\textbf{E2.3})$$

where R is the universal gas constant, T is temperature, and Q is the reaction quotient. The Nernst equation is applied when looking at the redox processes of one analyte at one electrode (Equation E2.4)

$$O + ne^- \rightleftharpoons R \qquad (\textbf{E2.4})$$

where O and R are the oxidized and reduced forms of the redox couple, respectively. Therefore, Q is the relationship of the concentrations of each (i.e. C_O/C_R). The resulting current from this redox reaction (described by the Nernst equation) is often termed *Faradaic current*, as it behaves according to Faraday's Law (n×F).[2] In the case of an electrolytic cell, a voltammogram is drawn to relate the voltage input (x-axis, thermodynamic) to the resulting current (y-axis, kinetic). The shape and magnitude of the current response is governed by all the kinetic processes involved in that electrochemical reaction. These include mass transfer (to and from the electrode surface), electron transfer at the electrode surface, chemical reactions involved with electron transfer, electrodeposition, and adsorption/desorption of matter on the electrode.[3]

This chapter will focus on cyclic voltammetry, where voltage is cycled to and from a chosen potential in order to look at both oxidative and reductive current responses of an analyte as a function of applied potential.[2-7] The approach here is to look at CVs through the eyes of an experimentalist, covering the basics as they relate to understanding a CV taken in the laboratory. This includes the many experimental components (and common pitfalls) to consider when trying to perform cyclic voltammetry, understanding electrocatalysis finding ways to benchmark electrocatalysis via CV, and a consideration of other experiments used to substantiate results from cyclic voltammetry.

2.2 Cyclic Voltammetry – The Experiment

Cyclic voltammetry is a commonly used non-destructive electroanalytical technique for studying redox active complexes and molecular electrocatalysts. In a cyclic voltammetry experiment, charge is applied to the cell at a fixed rate to and from a certain voltage, and any resulting current that flows between the two electrodes is measured on both the forward and reverse scan. Here, the terms anode and cathode are not strictly correct because both positive and negative bias can be applied to the cell, thus the two electrodes are called the working (WE) and counter electrode (CE). The current of the cell is measured at the WE. A third electrode, the reference electrode (RE), is also employed in a CV experiment. The RE is typically a stable redox couple which serves as a known half-cell so that the potential being applied between the WE and CE can be determined. All of this occurs in a single compartment cell (Figure 2.1). To aid in the transfer of charge between the electrodes, the solution must contain an appreciable number of charged ions, or electrolyte.

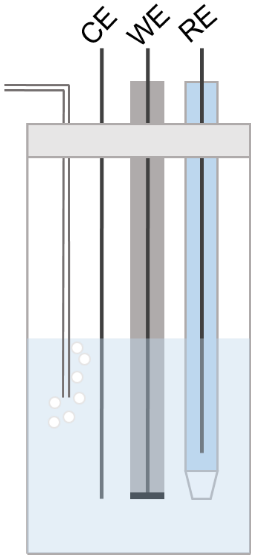

Figure 2.1 Schematic of a typical electrochemical cell containing a degassed solution of analyte, electrolyte, and internal reference (if applicable). The cell consists of a working electrode (WE), counter electrode (CE), reference electrode (RE), and gas sparging needle. Current flows between the WE and CE while the potential is controlled between the RE and WE.

The best way to understand how CV works is to take a step-by-step approach to a typical CV scan. Take for example ferrocene (Fc), which has a reversible redox couple defined by Equation E2.5 and CV in Figure 2.2.

$$\mathrm{Fc}^{+} + 1\mathrm{e}^{-} \rightleftharpoons \mathrm{Fc}^{0} \qquad E^{o} = 0.40 \text{ V vs. SCE(MeCN)} \qquad (\mathbf{E2.5})$$

In the CV experiment, let us say the experimentalist chose to sweep from 0 V to 0.6 V vs. SCE at a scan rate of 100 mV/s (Figure 2.2, left side). This means the CV scan will take 12 seconds.

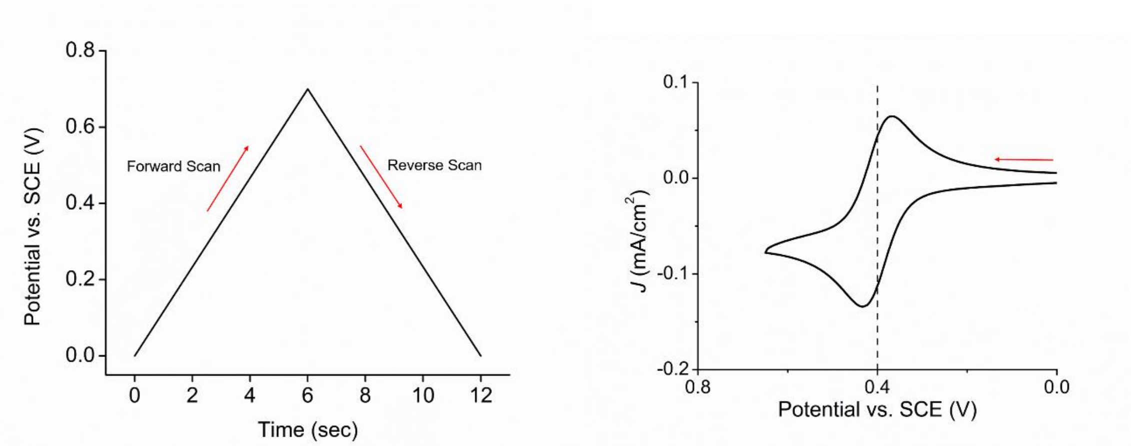

Figure 2.2 Left: Potential vs. time signal corresponding to the input values for a CV. Right: Resulting CV of ferrocene taken at 100 mV/s.

The current is measured at the WE, therefore the current response is dictated by the environment around the WE (Figure 2.3). When any potential is applied to the WE, oppositely charged particles are attracted to its surface. A layer of these charged particles, made up of solvent and/or electrolyte, adsorbes onto the surface and is referred to as the *inner Helmholtz plane*. The next layer, the *outer Helmholtz plane*, consists of ions and solvated ions still of opposing charge to the electrode that are not adsorbed but still attracted to the surface via long range coulombic forces.[2] Together these two areas make up the *electrical double layer*, which exists on all charged electrodes. Past the electrical double layer is the *diffuse layer*, which contains solvent, electrolyte, and analyte that is still within the electric field of the WE. This is the layer in which the redox processes of interest are measured. The *diffuse layer* extends out to the bulk solution, which is not affected by the processes going on at the electrode. However, mass transport occurs between the bulk solution and the diffuse layer, ideally by diffusion only (as opposed to convection or migration). The electrical double layer and diffuse layer act as a capacitor, and this *double layer capacitance* cannot be eliminated, resulting in background current observed in all electrochemical experiments (Figure 2.2 between 0.0 V and 0.2 V). This current is referred to with many names, including *charging current*, *capacitive current* or *non-Faradaic current* since it is not related to electron transfer to the analyte.[2] This capacitive current is controlled by the rate of electron transfer, which is described by the Butler-Volmer equation.[3] The magnitude of capacitive current is directly proportional to the concentration of electrolyte in solution, the diffusion coefficients of the analyte and electrolyte, and the scan rate.

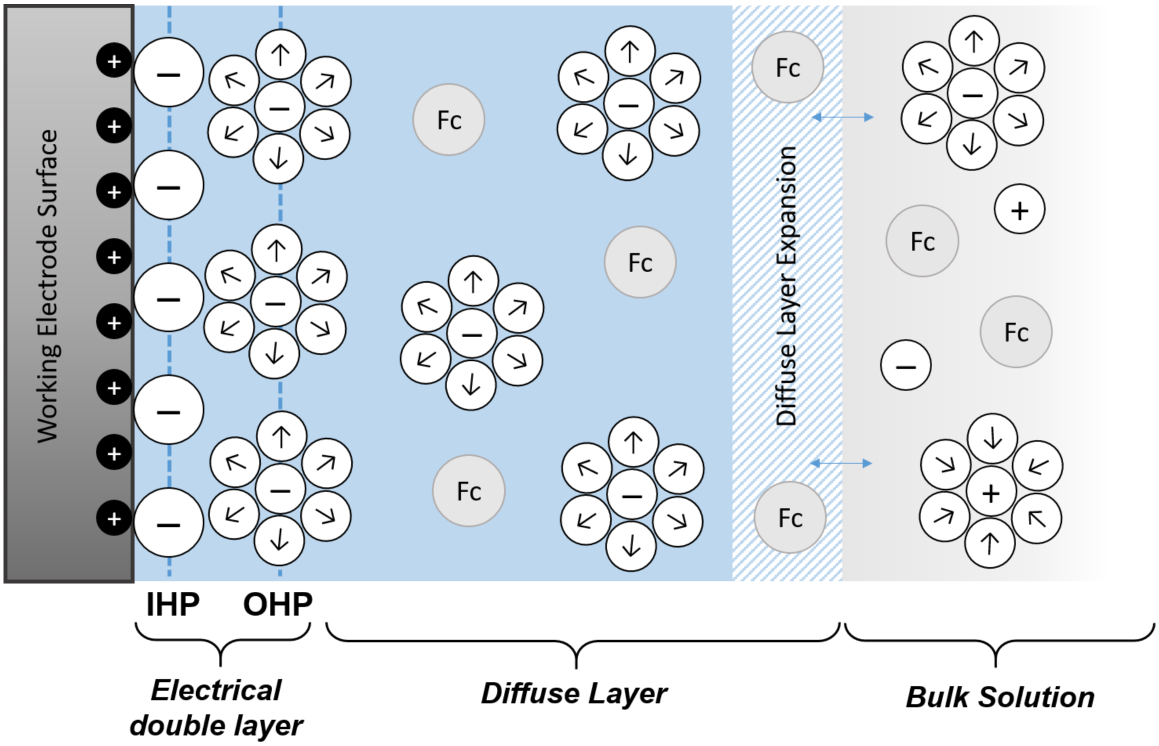

Figure 2.3 Schematic representation of the layers near the electrode surface that are effected during a CV experiment. From left to right: Positively charged working electrode (grey), negatively charged inner Helmholtz plane (IHP) outer Helmholtz plane (OHP), which make up the electrical double layer. This is followed by the diffuse layer, which expands when current is passed, followed by the (neutrally charged) bulk solution, which interacts with the other layers through diffusion.

Looking at the forward CV scan in Figure 2.2, current starts to increase slightly before and through the potential corresponding to E^o (0.4 V), where there are equal concentrations of O and R as described by the Nernst equation. In this example, the current corresponds to the oxidation of Fc^0 to Fc^+ in the diffusion layer. During this part of the scan the diffusion layer thickness increases (Figure 2.3 shaded area) until a maximum thickness is achieved and a peak is seen in the CV. After the peak, the current drops, but to a level above that of the capacitive current. This resulting current, known as the *diffusional current*, represents the continuous mass transport (and therefore continuous oxidation) of Fc^0 between the diffusion layer and bulk solution. In the reverse scan these reduced species are reduced back in the same steps described above, therefore the forward scan is identical to the reverse but opposite in charge.

There is a variety of thermodynamic and kinetic information that can be gleamed from a reversible couple like the one seen for Fc. As a Nernstian process, the peak potentials (E_p) are related to E^o by Equation E2.6

$$E^{\circ} = \frac{E_{p,O} + E_{p,R}}{2} \qquad \textbf{(E2.6)}$$

and the separation between the peak potentials is given by Equation E2.7

$$\Delta E_p = E_{p,O} - E_{p,R} = \frac{0.059\ V}{n} \qquad \textbf{(E2.7)}$$

where 0.059 is the value obtained by finding RT/F in the Nernst equation (Equation E2.3). A one electron reversible couple seen in a CV would then have an ideal peak-to-peak splitting of 59 mV, whereas the peak splitting of a 2-electron reversible process would be 29.5 mV. The peak potentials are independent of scan rate, but the peak current (i_p) is dependent on scan rate (v) as described by the Randles-Sevcik Equation (Equation E2.8)[3]

$$i_p = (2.69 \times 10^5) n^{3/2} A C D^{1/2} \nu^{1/2} \qquad \textbf{(E2.8)}$$

where A is the electrode area (in cm^2), C is the concentration (mol/L), and D is the diffusion coefficient (cm^2/s), assuming standard conditions. Thus, for a freely diffusion species (i.e. a molecular analyte that does not physically interact with the electrode), i_p is proportional to the square root of the scan rate.

When slow electron transfer or a chemical change occurs, the resulting peak shape in the CV is no longer symmetrical and the Nernstian relationships described for fast reversible redox couples no longer apply. These waves are referred to as quasi-reversible or irreversible depending on the presence of the type of return (oxidative) wave. Without knowing the rate constant, transfer coefficient (α), or diffusion coefficient of the analyte, E^o cannot be obtained from the CV.[2] There are many different ways in which electronic (E) and chemical (C) steps can be coupled to give an irreversible wave in a CV, which are described in a variety of resources[4-5, 8] and will not be detailed here.

A CV can also be taken of an electroactive species that has been attached or electroactively adsorbed onto the WE. Nernstian behavior of a of a surface-confined species results in a CV where both the anodic and cathodic peak current aligns with E^o (remember that peak splitting is caused by diffusional processes). The number of electrons in the process is determined by a peak half-width of 90.6/n mV.[2] The peak current will be proportional to the scan rate and the surface coverage (Γ) as described by Equation E2.9

$$i_p = \frac{n^2F^2\Gamma Av}{4RT} \quad \textbf{(E2.9)}$$

Many experimental issues arise when looking at heterogeneous systems via CV (increase in capacitive current, decrease in electrolyte mobility, blocking effects) that may result in peak splitting, even for reversible electron transfer processes. Care must be taken in analyzing these CVs to maintain data integrity.

2.3 Experimental Aspects of Cyclic Voltammetry

Moving from theory to practice, there are a whole host of experimental conditions to consider when conducting electrochemical measurements. Each will be considered in turn, followed by some common problems and general practices to adhere to.

Electrodes. Electrodes chosen for a CV experiment must be of a conducting material that is inert to the conditions and substrates in the electrochemical cell in the potential range of interest. WE are typically flat with a small surface area to enhance concentration polarization. One of the most common WE materials is glassy (or vitreous) carbon (Figure 2.4). The same substrates can also be used as the CE; however, platinum wire is a common choice. Shape of the CE is inconsequential; the important factor is that the surface area of the CE is equal to or larger than that of the WE so that it does not limit current flow.

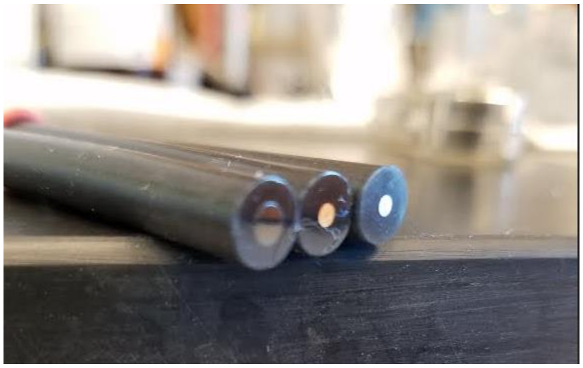

Figure 2.4 Photo of (left to right), 3.0 mm diameter glassy carbon, 1.6 mm gold and 1.6 mm platinum disc working electrodes, which are manufactured in a solvent resistant plastic body (BASi).

Having a clean electrode surface is immensely important to recording CV data that is only of the substrate of interest. Dirty electrodes can substantially change the current response of the substrate, both in shape of the wave and intensity.[9] The most common way to clean a working electrode is to polish it with either diamond or alumina paste of varying sizes. Care must be taken to make sure all the polishing paste is removed from the surface before use. This can be done by either washing copiously with methanol and wiping dry, or sonicating for 30 seconds in methanol. Companies that sell electrodes will often have instructions on how best to polish them. Bare wires are often used for the CE, and in the case of platinum the easiest cleaning method is to flame-treat the wire with a butane torch before use. A CV sweep of a solution only containing electrolyte will help identify how clean the electrodes are and if further cleaning is necessary.

References electrodes are treated much differently than the WE and CE. Since the RE is its own half reaction, the electrode is typically separated from bulk solution via a glass tube with a porous glass tip (Figure 2.5). The type of reference electrode used is dependent on the solvent choice for the electrochemical experiment. In aqueous electrochemistry, the saturated calomel electrode (SCE) and standard hydrogen electrode (SHE) are often employed. Another common RE couple is silver/silver chloride (Ag/AgCl). A Ag/AgCl RE is prepared either by employing an Ag wire in a solution of silver nitrate or electrodepositing AgCl onto a Ag wire (see Appendix). Bare silver wire as a Ag/Ag^+ couple can also be employed.[5] An important factor is to keep the solvent and electrolyte of the reference the same as that used for the measurements to decrease solvent contamination and unwanted potential junctions in the cell.

Figure 2.5 Photo of two types of non-aqueous Ag/AgCl reference electrodes (RE) being stored between experiments. Care must be taken to keep the porous tip saturated in the same solvent and electrolyte as is used in the CV experiment.

While textbooks may lead some to believe that SCE and SHE are the primary standards for referencing redox couples, in non-aqueous electrochemistry it is recommended to use an internal reference. The variance in conditions in which a RE such as Ag/AgCl can be made (concentration, solvent, electrolyte), can cause significant potential drift. Therefore, having a stable known redox couple in solution to reference to is most ideal. Ferrocene is most frequently used ($Fc^{0/+}$), however decamethylcolbaltocene and bis(biphenyl)chromium(0) are also common. Redox couples measured in solution are then reported against the ferrocene couple (i.e. $Fc^{+/0}$ = 0.00 V). Ferrocene or an analogous internal reference can be added directly to the analyte solution for the duration of the analysis or after analysis if it has the possibility to influence the measurements.

Proper storage of electrodes is important to maintain their usability. Working and counter electrodes should be kept clean and away from any objects that might scratch their surfaces. Reference electrode tips are made of a porous plastic material such as Vycor or CoralPor, which must be kept solvent saturated (Figure 2.5). These tips should be replaced periodically, as they will get clogged over time. The easiest way to tell if a tip should be replaced is if it is visibly contaminated (i.e. colored) or if the measured resistance of the cell is very high. Properly stored RE will also help to prevent Ag from entering the analyte solution. Electrodeposited Ag^0 on a glassy carbon electrode can be detected by the irreversible reduction of Ag^I around –0.53 V and –0.77 V as well as an oxidative feature ca. –0.14 V vs. $Fc^{+/0}$.[5]

Solvent. The first criteria for choice of solvent is the solubility and stability of the analyte. Further criteria include solvent stability under potential and solvent window. The solvent window refers to the potentials at which the system exhibits a current response that is not associated with the analyte of interest. The solvent window is defined by the working electrode, solvent, electrolyte, substrate, and atmosphere under which the CV is taken. An example of the difference in solvent window per working electrode, co-substrate, and atmosphere is shown in Figure 2.6, where a gold working electrode has a smaller solvent window than glassy carbon by 500 mV in a 0.1 M solution of $TBAPF_6$ in MeCN under Ar, which decreases under an CO_2 and when 0.5 M phenol is added.[9]

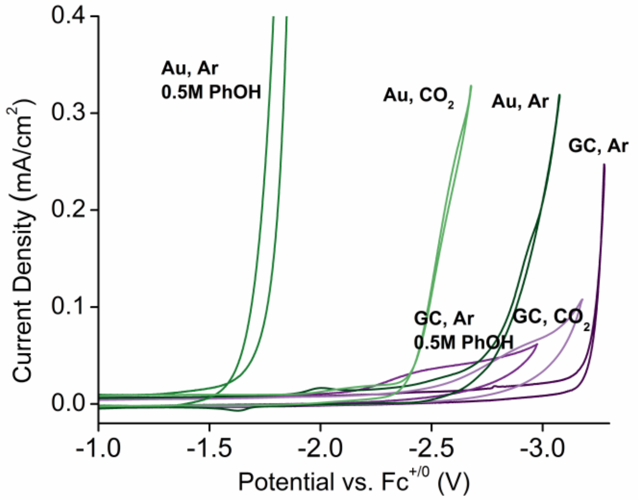

Figure 2.6 Solvent windows using a glassy carbon WE (purple) and gold WE (green) under three different experimental conditions. Taken in 0.1 M $TBAPF_6$ solution in MeCN with Pt CE and Ag/AgCl RE at 100 mV/s.

Care should be taken to keep the solvent used for electrochemistry oxygen (i.e. air) and water free (unless of course the solvent of chose is water, then only oxygen need be eliminated). This prevents any errant current responses or unwanted reactivity of the substrates. The drying process used depends on the solvent, but typical methods include using solvent from a dry box or solvent system, drying over molecular sieves (3Å or 4Å), or freeze-pump-thaw.[10] Oxygen has a prominent redox couple, while water will limit the solvent window (Figure 2.18). While it is believed that water is never truly eradicated from most solvents used in CV experiments, care should be taken to remove as much as possible.

Electrolyte. The electrolyte chosen should be inert and soluble in the solvent of choice. Depending on the analyte, ion size may also be important. Common electrolytes for non-aqueous electrochemistry include tetrabutylammonium hexafluorophosphate ($TBAPF_6$), tetrabutylammonium tetrafluoroborate ($TBABF_4$), lithium perchlorate ($LiClO_4$, not used in the Kubiak laboratory due to the explosive nature of perchlorate salts), and non-aqueous buffers. Aqueous electrolytes include potassium chloride (KCl), ammonium chloride (NH_4Cl), sodium hydroxide (NaOH), sulfuric acid (H_2SO_4), and aqueous buffers. The concentration of electrolyte is usually quite high (≥0.1 M) to minimize cell resistance. Again, care should be taken to minimize contamination and moisture in the electrolyte. In the Kubiak lab where $TBAPF_6$ is most often used, the salt is recrystallized from methanol and dried in a vacuum oven at 80°C before use in electrochemical experiments.

Atmosphere. The best way to perform rigorous CV experiments is in a dry box, where oxygen and water are all but eliminated from the atmosphere. For most systems, there is little difference between using a nitrogen (N_2) versus an argon (Ar) atmosphere, and thus the atmosphere used has more to do with availability than preference. If CV experiments are done outside of a dry box, CV experiments are performed under a constant stream of N_2 or Ar. The gas being used (Ar or N_2)

is first sparged through the CV solution for at least 5 minutes before the first scan is taken to eliminate as much air (oxygen) as possible. Care must be taken that this influx of gas is not perturbing the solution during the experiment, but it is often recommended to sparge the solution periodically throughout the experiment.

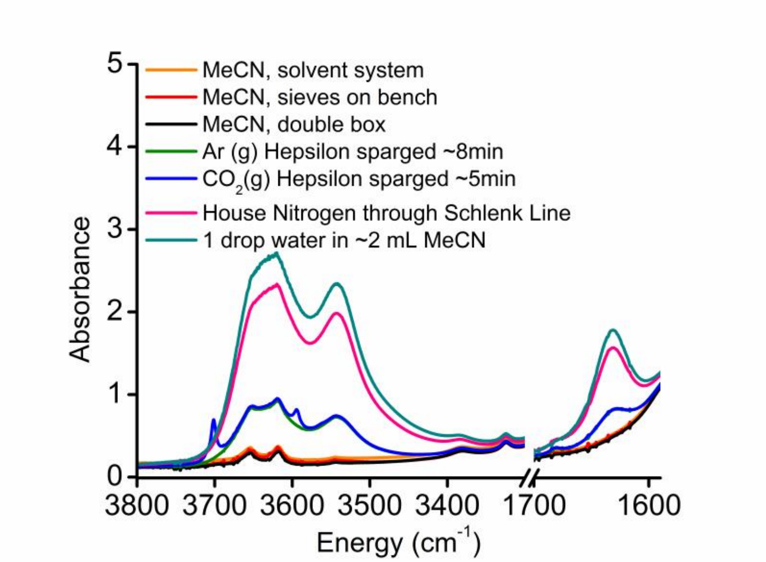

Figure 2.7 FT-IR spectra of the water OH stretches (3540 and 1631 cm^{-1}) in a solution of 0.1 M $TBAPF_6$ MeCN under various conditions. Yellow, red, and blue represent solutions that have not been sparged with any gas. Green and blue show the increase in water in solution due to sparging using the gas tanks at the Hepsilon hood (Hood 6) in the Kubiak lab. Pink shows the increase in water from using the house nitrogen, which is almost equivalent to adding a drop of water to the solution (green).

There are two major issues that arise when doing CV experiments outside of a dry box. First is that continual sparging of the solution with Ar/N_2 leads to solvent loss over time. The second issue being that even ″bone dry″ gases out of a new cylinder will still contain some moisture, which will quickly accumulate in the CV cell. This is demonstrated in Figure 2.7, which has FT-IR spectra of 5 mL of 0.1 M $TBAPF_6$ MeCN solutions that have been prepared with various gas sources in the Kubiak laboratory. While the drying procedure does not change the amount of water in solution, the source of the sparging gas greatly increases the amount of water in solution in all cases.

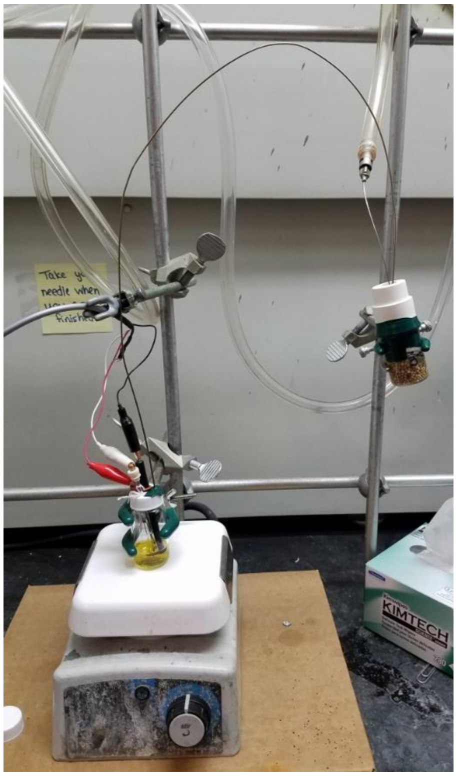

Figure 2.8 A CV experimental setup where a sparging chamber is used to limit oxygen and water from entering the CV cell as well as provide solvent saturated gas to prevent solvent loss from sparging.

The best way to overcome the issues associated with performing CV experiments outside of the glove box is to utilize additional drying methods. First is to set up a Drierite drying unit, which will remove the bulk of the water coming from the gas cylinder. Gas should then pass through a sparging chamber (Figure 2.8). Here, the gas passes through a sealed vial filled with molecular sieves and the solvent used in experiment. This will help remove any residual water as well as saturate the gas with the solvent, thus preventing loss of solvent from the CV cell. As seen in the FT-IR spectra (Figure 2.9), this results in the lowest amount of water entering the cell.

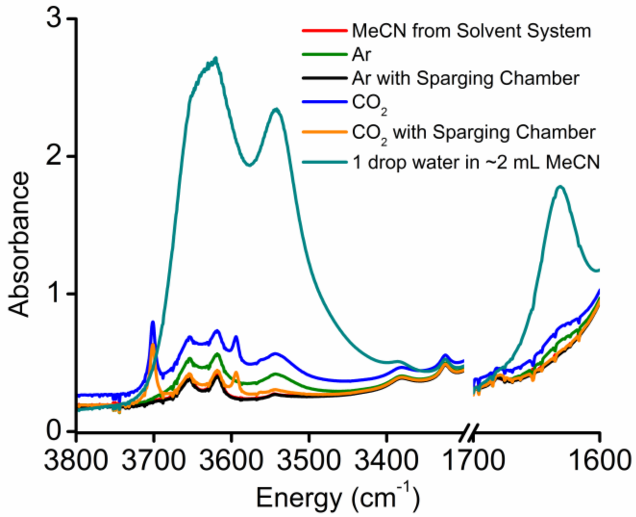

Figure 2.9 FT-IR spectra of the water OH stretches (3540 and 1631 cm^{-1}) in a solution of 0.1 M $TBAPF_6$ MeCN to demonstrate the efficacy of using a sparging chamber (photo in Figure 2.8). Gas was from the tanks at the Hepsilon Hood (Hood 6) in the Kubiak Laboratory, which was first passed through a Drierite column and sparged through solution for 6 minutes.

Compensating for Uncompensated Resistance. As stated in Section 2.2, the reference electrode is utilized by the potentiostat as a point of reference to determine the potential between the WE and CE. What is not considered is the resistance between the reference electrode and working electrode, which is referred to as Ohmic drop (E_{OD}). Thus, the potential measured at the electrode surface is given by $E_{actual} = E_{measured} – E_{OD}$.[11] The Ohmic drop is defined by Ohm's law, ($E_{OD} = i_{measured}R$); the magnitude of the Ohmic drop is directly related to the current measured and thus can change throughout the experiment.

The cell resistance causing Ohmic drop comes from the capacitive current (*vide supra*) and the bulk solution (solvent/electrolyte) between the WE and CE.

To prevent the capacitive current from overpowering the Faradaic current response from the analyte, the capacitive current should be reduced as much as possible. This can be done in a variety of ways. First, the electrodes should be positioned as close as possible to each other, limiting the physical distance current must travel. Second is to ensure maximum conductivity of the solvent and electrolyte of choice. This could mean choosing a more conductive solvent or increasing electrolyte concentration.[5] Decreasing the size of the WE is also a possibility, as less current would be passed. Finally, when all physical possibilities have been exhausted, any remaining resistance is accounted for using active positive feedback on the potentiostat. This is often an option when entering the experimental parameters, where the instrument will allow for the measurement and compensation of Ohmic drop. On a BASi Eplison potentiostat, this is done through the "IR Comp" tool. In a typical setup like Figure 2.8 where a 0.1 M $TBAPF_6$ MeCN solution is used with a 3 mm glassy carbon working electrode, the calculated Ohmic drop (R) should be under 300Ω. Correcting for 100% of the Ohmic drop will cause an oscillatory circuit response,[4] thus correcting for 80-90% of the Ohmic drop (depending on the amount of measured current) is recommended. The effect of Ohmic drop correction on the catalytic response of Fe(tetraphenylporphyrin) can be seen in Figure 2.10, where the line-shape is drastically different, which would result in incorrect reporting of catalysis.

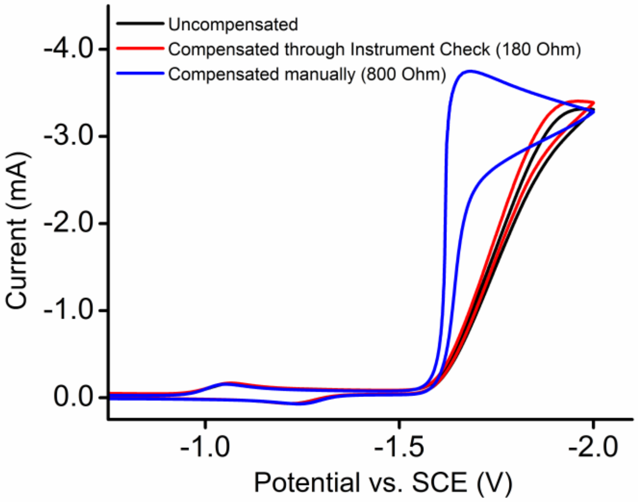

Figure 2.10 Electrocatalytic CV response of 1 mM Fe(tetraphenylporphyrin) in 0.1 M $TBABF_4$ DMF solution under an atmosphere of CO_2 (g) with (blue) and without (black and red) proper Ohmic drop compensation. Conditions: Glassy carbon WE, platinum CE, SCE RE, 100 mV/s.

Common Experimental Issues. No matter how careful one is when setting up a CV experiment, invariably something will go wrong. The most notable outcomes are high cell resistance, contamination noted in a CV of the blank solution (CV of just solution/analyte or solution/analyte/internal reference), and change in current response over the course of the CV experiment. Possible reasons (in order of most common to least common) for each of these issues are listed in Table 2.1.

Table 2.1 Most common experimental issues when performing CV experiments with probable causes.

Issue	**High Cell Resistance**	**Non-Ideal Voltammogram of Blank Solution**	**Change in Current Response Over Course of Experiment**
Reasons	• Leads not properly connected to electrodes • All three electrodes are not in solution • Electrodes are touching the bottom of the vessel • Electrodes too far apart • Reference electrode tip is clogged • A gas bubble is on the surface of an electrode • Poor Ohmic drop correction • Leads to potentiostat are broken	• Solution is stirred or disturbed by gas flow • Water in solution • Oxygen in solution • Solvent or electrolyte impurity • Electrodes not clean	• Oxygen is entering CV cell • Water is entering CV cell • WE surface is contaminated • Analyte is clogging RE • Reaction happening at CE • Degradation of analyte

2.4 A Typical CV Experiment

When analyzing a molecule electrochemically for the first time, there are several CV experiments that will yield kinetic and thermodynamic data. Considering CV is a non-destructive analytical tool, it saves the researcher’s time and the lab’s valuable resources to start a CV experiment prepared to do many scans so that the most amount of information is gained from a single CV setup. This section will go over the most common CV experiments and the information learned from them (freely diffusing species only). Typical CV cells in the Kubiak laboratory can be seen in Figure 2.11, and a setup that utilizes a sparging chamber as seen in Figure 2.8 is highly recommended. It is prudent to make sure that solvent, analyte, electrolyte, any co-substrates, and electrodes are clean, dry and of high purity before starting any experiment electrochemical experiment. If an internal reference is being used, its redox couple should be present in every scan taken. If taking CVs for the first time (especially if interested in catalytic systems), it is good practice to study a known complex first. The examples in this section are of Re(4,4′-*tert*-butyl-2,2′-bipyridine)$(CO)_3$Cl (**Re(*t*Bu-bpy)**).[12] Reproducibility is important for the validity of CV findings, and therefore any CV experiments should be repeated with fresh solution and analyte at least 2-3 times.

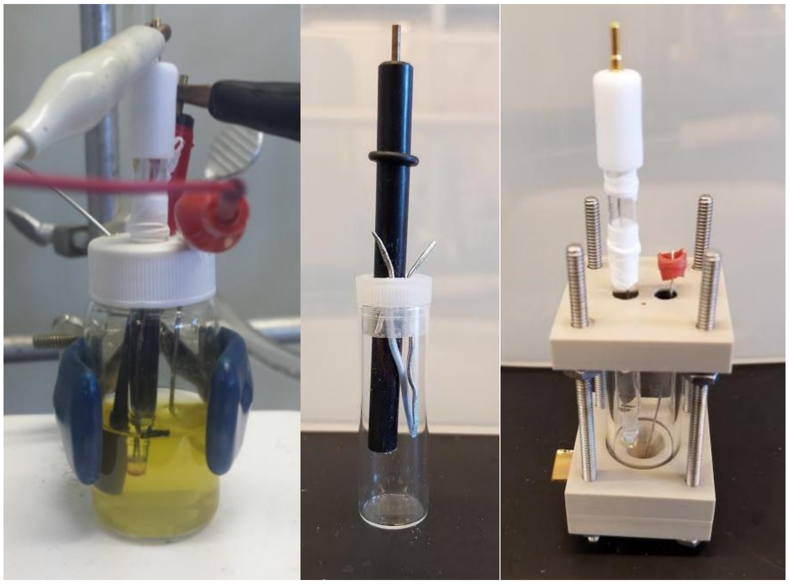

Figure 2.11 Examples of CV cells used in the Kubiak laboratory. Left: Disposable 20 mL scintillation vial with a drilled cap to fit the electrodes; 5-10 mL of solution is used. Middle: Disposable 5 mL vial with drilled cap for 2-3 mL solution. Right: Custom cell for use with cut microscope slides with conductive coating as the working electrode (bottom left of photo).

Full Window Scans. A scan of the entire solvent window will help determine the potentials an analyte can be studied at without interference from electrode-based reactions. These are taken before the analyte and of all conditions that will be used (i.e. Ar(g), CO_2(g), addition of any co-substrates). These ‘blank’ scans ensure the solution is clean, the capacitive current is low, and no oxygen or water is present. A full window scan of the analyte will show all the redox processes available to monitor via CV. If an internal reference such as ferrocene is being used, the peak-to-peak splitting can be checked to ensure proper Ohmic drop correction. The most widely used scan rate is 100 mV/s and should be used for most experiments.

Partial Window Scans. CV scans that isolate each feature in the CV will help to identify if redox processes before or after effect on the reversibility of earlier waves. These different window scans are also useful during data workup, when there are a variety of windows to choose from to present the most interesting redox processes of the analyte. It is revealed for **Re(*t*Bu-bpy)** that if the second reduction in Figure 2.12 is not included in the CV, the first reduction becomes a reversible redox couple (fast a reversible electron transfer redox process), indicating that a chemical step is happening at the second reduction potential.

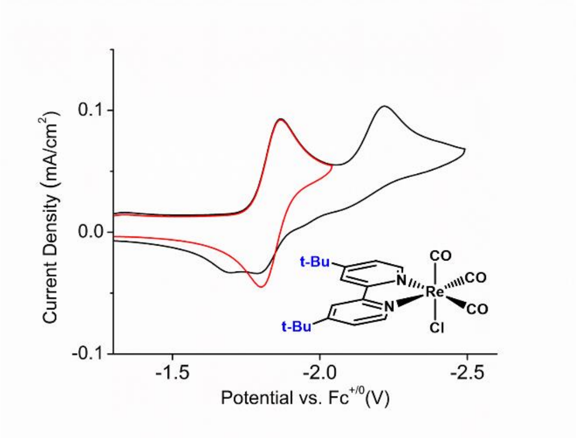

Figure 2.12 CV of **Re(*t*Bu-bpy)** (structure inset) under Ar(g) showing the increased reversibility of the first reduction when the 2nd reduction is not reached.

Scan Rate Dependence. Scan rate dependence (SRD) will help to determine if the analyte is freely diffusing in solution (*vide supra*) and gives more information about the reversibility of redox features. Typically, the scan rate is increased over one or two orders of magnitude. Truly irreversible features will not change per scan rate, while slow chemical steps may become more reversible at higher scan rates. In the SRD study of **Re(*t*Bu-bpy)** in Figure 2.13, the second reduction remains irreversible even at high scan rates (3200 mV/s), while the first reduction becomes more reversible. A plot of the peak current versus the square root of the scan rate yields a linear line. Using the Randles-Sevcik Equation (Equation 2.9), the diffusion coefficient is determined to be 2.01×10^{-11} cm^2/s.

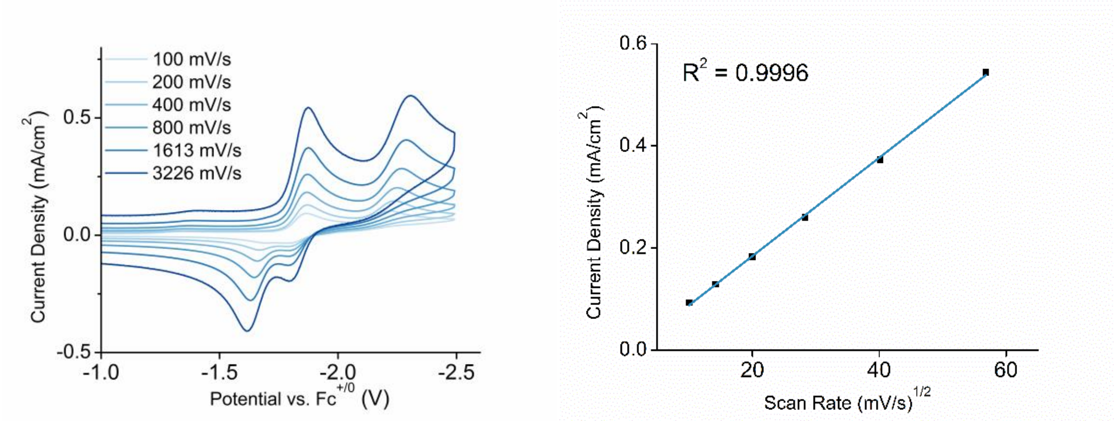

Figure 2.13 Scan rate dependence CVs for **Re(*t*Bu-bpy)** (left) and corresponding plot for the 1st reduction potential (right) to show that the complex is freely diffusing in solution as described by the Randles-Sevcik equation.

Differential Pulse Voltammetry. Differential pulse voltammetry (DPV) is not a CV technique, however it utilizes the same set up as CV and can be done in addition to CV experiments. DPV is most useful for determining the number of electrons involved in a reversible redox process. This may be needed if there are overlap in redox processes in a CV or if poor Ohmic drop correction makes determination via peak-to-peak splitting difficult. The electron count is determined by the peak width at half height, which is typically 90.4 mV for 1e$^-$ and 45.2 mV for a 2e$^-$ process. Bard and Faulkner[3] is a good resource to learn more about DPV and other pulse voltammetry experiments.

Catalytic Conditions. In the example of **Re(*t*Bu-bpy)**, catalytic conditions include the addition of CO_2 gas, which at saturation is ~0.28 M in MeCN.[13] The electrochemical cell is sparged with the new atmosphere for 5-8 minutes before any scans are taken. Catalysis is observed in a CV by an increase in current at the redox process that creates the catalytically active species. In the catalytic CV of **Re(*t*Bu-bpy)** (Figure 2.14, left panel), a large increase in current is seen at the second reduction. These scans should be repeated a few times, sparging CO_2 (g) for ~30 seconds between scans. It is often essential to polish the working electrode between scans to maintain reproducibility. An ideal catalytic wave is 'S-shaped' and scan rate independent (*vide infra*), however a peak shape is much more common. One way to attempt to gain a catalytic S-shape is to increase the scan rate until the catalytic current approaches plateau[14] (Figure 2.14, right panel).

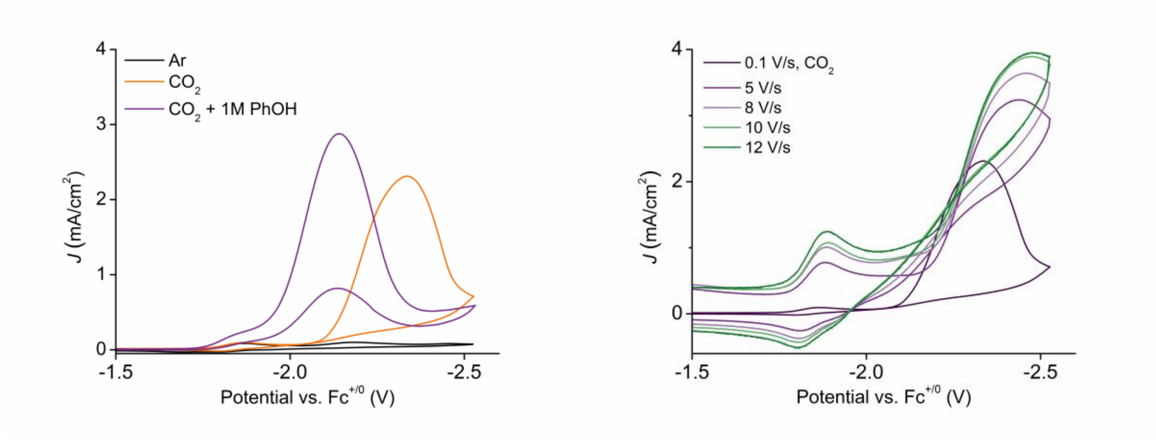

Figure 2.14 Left: CV of 1 mM **Re(*t*Bu-bpy)** in 0.1 M TBAPF$_6$ MeCN solution under inert atmosphere (Ar, black), CO$_2$ (orange), and CO$_2$ with 1 M phenol (purple) at 0.1 V/s. Right: Scan rate dependence of the catalytic current of **Re(*t*Bu-bpy)**, showing that a plateau current is reached around 10 V/s. GC working, Pt counter, and Ag/AgCl reference electrodes.

Addition of Co-substrates. The catalyst of interest may have a dependence on co-substrates. For example, **Re(*t*Bu-bpy)** has a second order dependence on protons ($CO_2 + 2e^- + 2H^+ \rightarrow CO + H_2O$; rate = $k_{obs}[CO_2][H^+]^2$),[15] and an increase in catalytic response can be seen in Figure 2.14 with the addition of 1 M phenol. Again, care should be taken that scans are reproducible.

Variable Concentration Studies. CV can also be used to determine the order of a reaction. Variable concentration studies of catalyst, substrate, co-substrate can help to determine the reaction order of each by using textbook kinetic analysis of the resulting data.[16]

2.5 Reporting Catalysis using Cyclic Voltammetry

Catalysis is an inner sphere reaction between the catalyst and substrate which lowers the activation barrier of a chemical transformation. How well a catalyst works can be described by a variety of metrics obtained from a CV. These include turn over frequency (TOF), overpotential (ɳ), and intrinsic catalytic rate constants (k). In the literature, these values are often found using very different (and sometimes inaccurate) methods and conditions. In response, there has been a push to find common ground in which valid catalyst benchmarking can be obtained.[5, 8, 17-22] Here we will go over how to properly obtain these values as well as the pitfalls of each method. It should be stressed that equations used for determination of k and other kinetic parameters are specific to a certain mechanism and must be derived for each catalyst type to which it is applied.[5, 8, 23]

Overpotential. Overpotential (ɳ) is defined as "the additional potential (beyond the thermodynamic requirement) needed to drive a reaction at a certain rate."[3] While being seemingly straightforward, both the standard reduction potential (E^o) for the reaction of interest as well as the catalytic potential are dependent on reaction conditions, thus making determination of ɳ much more ambiguous. Taking into account the presence of solvent (S) and acid (AH), the electrochemical reduction of CO_2 to CO is defined by Equation E2.10

$$CO_{2(S)} + 2HA_{(S)} + 2e^- \rightleftharpoons CO_{(S)} + H_2O_{(S)} + 2A^-_{(S)} \qquad \textbf{(E2.10)}$$

Depending on the calculation method, values of $E^o_{CO2/CO(MeCN)}$ have been found to be –0.541 V[24] or –0.12 V[25] vs. $Fc^{+/0}$. If a strong acid is present such as phenol ($pK_{a,MeCN}$ = 29.14),[26] its conjugate acid (phenolate) will be re-protonated by the strongest acid in solution, which is still CO_2 in the presence of water ($pK_{a,CO2,MeCN}$ = 17.03), which results in the formation of bicarbonate in solution[27] (Equation E2.11).

$$CO_{2(S)} + 3CO_{2(S)} + 2H_2O_{(S)} + 2e^- \rightleftharpoons CO_{(S)} + H_2O_{(S)} + 2HCO_3^-{}_{(S)} \qquad \textbf{(E2.11)}$$

This results in a $E^o_{CO2/CO(MeCN)}$ of –1.36 V vs. $Fc^{+/0}$.[24]

Determination of the catalytic potential is equally indefinite. One way could be to choose the E° of the catalytic redox couple under inert conditions, however many catalysts have irreversible redox features. Additionally, catalytic waves often plateau or peak substantially after the redox event seen under inert conditions. One recommendation is to estimate E_{cat} from the potential corresponding to the value at half of the catalytic current ($E_{cat/2}$), which occurs at or near the steepest part of the catalytic wave.[28] While this could involve some variation in instances of non-ideal (i.e. not S-shaped) catalytic behavior, the variation in $E_{cat/2}$ would be smaller than if the potential at peak i_{cat} was used. Applying these concepts to **Re(*t*Bu-bpy)** (Figure 2.15) gives a $E_{cat/2}$ of –2.20 V vs. $Fc^{+/0}$ and an η of 1.66 V vs. $Fc^{+/0}$ (using $E^o_{CO2/CO(MeCN)}$ of –0.541 V vs. $Fc^{+/0}$).

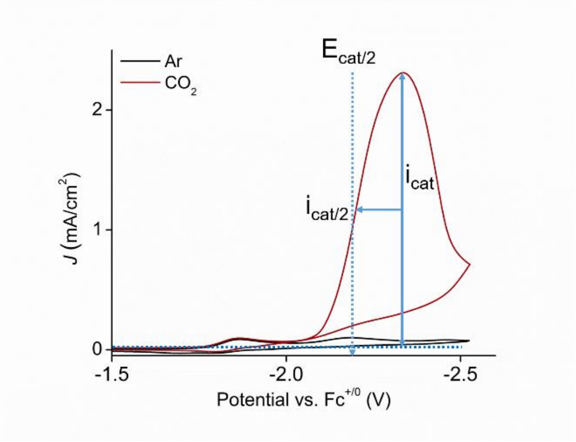

Figure 2.15 Catalytic CV of 0.1 mM **Re(*t*Bu-bpy)** in 0.1 M $TBAPF_6$ MeCN solution illustrating the selection of peak catalytic current (i_{cat}), half catalytic current ($i_{cat/2}$), and catalytic potential from $i_{cat/2}$ ($E_{cat/2}$) to aid in determining overpotential for the catalyst. Taken at 0.1 V/s with GC working, Pt counter, and Ag/AgCl reference electrodes.

Intrinsic Catalytic Rate Constants: Using 'S-shaped' Current Responses and Foot of the Wave Analysis. The techniques to gain kinetic and thermodynamic information from catalytic CVs have been pioneering by Savéant and co-workers over the past several decades.[4, 29-33] Through careful electrochemical techniques and the right mathematical relationships, intrinsic catalytic activity values (i.e. values not affected by external parameters such as experimental environment or deactivation pathways) can be obtained for almost all mechanisms (granted one knows which equations to use). There are two main drawbacks to using these approaches. First is the barrier to entry for all electrochemists when faced with the high-level math involved in calculating these parameters for their catalyst. Secondly and more importantly, this approach most rigorously applies only to well behaved catalysts. Most systems however suffer from what has been termed 'side-phenomena,' which include events such as deactivation of the catalyst, consumption of the substrate, or inhibition by products.[19-20] While Savéant and co-workers have found other ways to determine kinetic for non-ideal catalytic responses, these methods can still be inhibited by other redox events or very poor catalysis. **Re(*t*Bu-bpy)** will be used as an example complex to demonstrate the two ways to determine kinetic data from a CV: S-Shaped current response via increased scan rate and foot of the wave analysis (FOWA).

An ideal catalytic CV response is one that increased until it reached a plateau current that was scan rate independent and was retraced on the return wave. This 'S-shaped' waveform comes from a complex that has no immediate degradation pathways and has a gross excess of substrate available in the diffuse layer. Most catalysts, however, suffer from the various ‘side-phenomena.’ This leads to the many different catalytic waveforms as seen in Figure 2.16.[5, 34] As noted in the legend, experimental factors such as scan rate (v), initial catalyst concentration (C^o_P), and initial substrate concentration (C^o_A) can be varied to ‘traverse’ the zone diagram to get an S-shaped voltammogram.

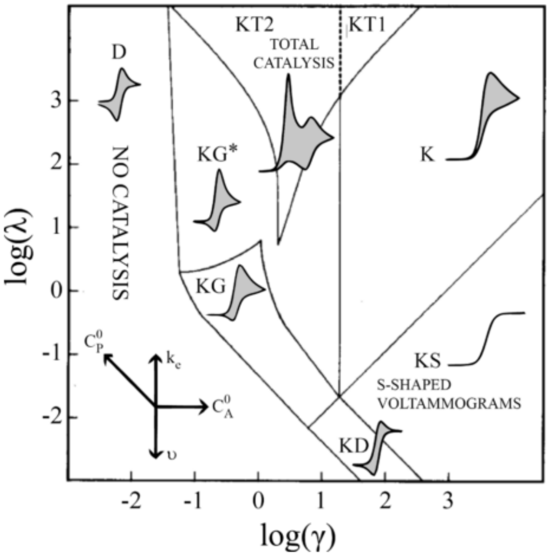

Figure 2.16 Catalytic zone diagram and simulated CV waveforms for an EC′ catalytic reaction. Figure is reproduced from Reference 5.

As seen in Figure 2.14, **Re(*t*Bu-bpy)** has a peaked shaped response at 0.1 V/s, but as the scan rate is increased a more plateaued current response is reached. As a 2-electron EC′ mechanism (where the prime indicates a catalytic reaction), the catalytic rate constant (k_{cat}) can be determined from the plateau current using the relationship between i_{cat} (Equation E2.13) and i_p (Equation E2.14, which is the Randles-Sevcik equation (E2.8) not assuming standard conditions).

Dividing Equation E2.12 by E2.13 (assuming the diffusion coefficient does not change dramatically under Ar versus CO_2) yields Equation E2.14.

$$i_{cat}=n_{cat}FAC_P^{\circ}(Dk_{cat})^{1/2} \quad \textbf{(E2.12)}$$

$$i_p=0.4463n_p^{3/2}FAC_P^{\circ}\left(\frac{F}{RT}\right)^{1/2}\nu^{1/2}D^{1/2} \quad \textbf{(E2.13)}$$

$$\frac{i_{cat}}{i_p}=2.24\sqrt{\frac{RT}{F}\frac{2k_{cat}}{\nu}} \quad \textbf{(E2.14)}$$

k_{cat} can also be described as the maximum turnover frequency (TOF_{max}), which is the theoretical number of times a catalyst can convert substrate to product per unit of time (Equation E2.15).

$$TOF_{max}=k_{cat} \quad \textbf{(E2.15)}$$

It is noted that k_{cat} is a global rate constant and does not apply to a particular step in the catalytic mechanism. Applying Equation 2.15, **Re(*t*Bu-bpy)** has a k_{cat} of 593 s^{-1} (where i_{cat}/i_p at 0.1 V/s was 30 and k_{cat} was determined at a scan rate of 10 V/s). In this case, the overall rate cannot be determined because the exact concentration of protons in solution is not known. If we consider the case where 1 M phenol is added to the solution, a plateau current cannot be reached even at 25 V/s (highest scan rate available with our potentiostat, Figure 2.19). If we estimate that 25 V/s is near the scan rate for the plateau current, then **Re(*t*Bu-bpy)** with 1 M phenol has a k_{cat} of 1099 s^{-1}. At this time, there are no rate values to compare to in the literature from other methods to corroborate these results.

When an S-shaped catalytic response cannot be reached, foot of the wave analysis (FOWA) can be used determine k_{cat}. FOWA uses the onset catalytic current, which has not yet been affected by 'side-phenomena'. Again, in consideration of **Re(*t*Bu-bpy)**, the foot of the wave is described by Equation E2.16

$$\frac{i_{cat}}{i_p} = \frac{2.24n_{cat}\sqrt{\left(\frac{RT}{Fv}\right)k_{cat}}}{1+\exp\left[\left(\frac{F}{RT}\right)(E-E°_{cat})\right]} \qquad \textbf{(E2.16)}$$

where n_{cat} is the number of electrons involved in the catalytic process, E the potential (V) corresponding to i_{cat}, and $E°_{cat}$ the standard potential of the active catalyst recorded under non-catalytic conditions. k_{cat} is obtained by plotting i_{cat}/i_p vs. $1/(1+\exp[(F/RT)(E - E°_{cat}])$, where the slope is defined by $2.24n_{cat}[(Fv/RT) k_{cat}]^{1/2}$ (Figure 2.21). Using FOWA, k_{cat} is determined to be 405 s^{-1}. Comparing to the value obtained from catalytic SRD (593 s^{-1}), while not significantly different, still has a 32% decrease in rate. This points in part to the fact that **Re(*t*Bu-bpy)** is a 'non-ideal' catalyst, and therefore these approaches are not strictly valid. A more ideal catalyst is Fe(tetraphenylporphyrin) and its derivatives, which is the complex used by Savéant and co-workers to demonstrate these methods.[24] In this case, the validity of FOWA has been independently verified for the catalytic reduction of oxygen to water by Fe(tetraphenylporphyrin), where identical rate constants to FOWA was determined by stopped-flow UV-vis spectroscopy.[35] FOWA could not be used for the catalytic reduction of CO_2 by **Re(*t*Bu-bpy)** in the presence of 1 M phenol because the foot of the wave overlaps with the first reduction feature of the complex.

Catalytic Tafel Plots. There has been a recent push in the literature for more standard practices so that catalysts can be accurately compared across research laboratories.[17, 36-37] One answer to this call are Savéant and Costentin's ‘catalytic Tafel plots’, which relates the catalyst’s TOF and ɳ (named in honor of Julius Tafel and not to be confused with Tafel plots themselves).[29] An ideal catalyst would have both high TOF and low ɳ. Catalytic Tafel plots work to illustrate the interplay between the two values in spirit of rational catalyst benchmarking.[24, 38]

To create the catalytic Tafel plot, a TOF needs to be calculated for each ɳ value. This is done using Equation E2.17.

$$\mathrm{TOF} = \frac{\mathrm{TOF_{max}}}{1+\exp\left[\frac{F}{RT}\left(E^{\circ}_{\mathrm{CO2/CO(MeCN)}}-E^{\circ}_{\mathrm{cat}}\right)\right]\exp\left(-\frac{F}{RT}\eta\right)} \qquad (\mathbf{E2.17})$$

The log(TOF) values are then plotted against the overpotential to get a catalytic Tafel plot as seen in Figure 2.17 (see Appendix for further details). While the log(TOF)-ɳ relationship can be applied to any complex (granted all the values needed are obtained), the differences in experimental conditions (And E°) should be noted.[39]

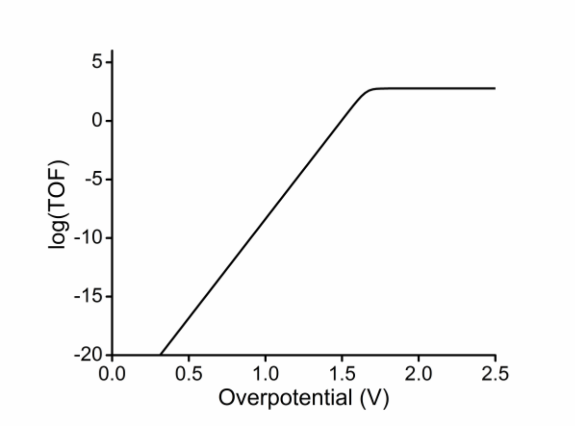

Figure 2.17 Catalytic Tafel plot of **Re(tBu-bpy)** using $\mathrm{TOF_{max}} = 593\ \mathrm{s^{-1}}$, $E^{\circ}_{\mathrm{CO2/CO(MeCN)}}$ of –0.541 V and $E_{\mathrm{cat}} = -2.20$ V vs $\mathrm{Fc^{+/0}}$. Plotted values can be found in Table 2.3.

2.6 Supporting Experiments for Understanding Catalysis

Cyclic voltammetry can provide a vast amount of information about a redox active complex, however additional experiments may be needed to substantiate claims based on CV experiments. Common supporting evidence experiments include controlled potential electrolysis (CPE), infrared or ultraviolet-visible spectroelectrochemistry (IR-SEC or UV-vis-SEC), chemical reductions of the complex and subsequent characterization of the reduced states, and computational modeling. Nuclear magnetic resonance (NMR), fluorescence, electron paramagnetic/spin resonance (EPR/ESR) can also be useful. Briefly, CPE uses a set up similar to that of CV (but usually more volume) where the catalytic potential is held constant in solution so that the catalytic products and stability of the catalyst over time can be measured. The product distribution is reported in terms of Faradaic efficiency (%FE), which the percentage of the charge passed that directly resulted in product. IR-SEC or UV-vis-SEC is another bulk electrolysis technique; however, a thin layer of the solution is used so that an IR or UV-Vis signal can be obtained through the solution. The potential applied to the cell step-wise so that changes to the spectra can be related to the redox events in the CV. The same data is often obtained from chemical reductions, although resulting species will only show the most stable species of each reduction. Nonetheless, isolation of these chemically (or catalytically) relevant species and obtaining crystal structures are invaluable pieces of data in understanding the mechanism and stable states of otherwise transient species. Finally, CVs can be computationally modeled using software such as DigiSim or DigiElch to help quantitatively understand mechanisms and kinetics seen in a CV experiment. These experiments, when brought together, help to portray a more complete picture of the electrical and chemical transformations surrounding redox active species and electrochemical catalysts, and there are many great examples of this in the literature.[40-42]

2.7 Conclusion

Cyclic voltammetry is a powerful and non-destructive analytical technique for better understanding redox active complexes and electrocatalysis. Through manipulations such as changing the scan rate, potential window, solvent, atmosphere, substrates or co-substrates, CV experiments can provide a wide range of kinetic and thermodynamic descriptors, both qualitative and quantitative. The experimental conditions and preparation of a clean electrocatalytic cell are vital to obtaining reliable data, and care must be taken to ensure reproducibility and accuracy of results. Recent trends have pushed the ability to gain catalytic rate constants from CV data, and the application of such techniques is vital to better understanding electrocatalysis through consistency and benchmarking.

2.8 References

(1) Silberberg, M. S.; Weberg, E. B., *Chemistry : The Molecular Nature of Matter and Change*. 5th ed.; McGraw-Hill: Boston, 2009; 923-969.

(2) Wang, J., *Analytical Electrochemistry*. 3rd ed.; Wiley-VCH: Hoboken, N.J., 2006; 1-41.

(3) Bard, A. J.; Faulkner, L. R., *Electrochemical Methods: Fundamentals and Applications*. 2001.

(4) Savéant, J.-M., *Elements of molecular and biomolecular electrochemistry : an electrochemical approach to electron transfer chemistry*. Wiley-Interscience: Hoboken, N.J., 2006.

(5) Rountree, E. S.; McCarthy, B. D.; Eisenhart, T. T.; Dempsey, J. L., *Inorg. Chem.* **2014**, *53*, 9983.

(6) Savéant, J.-M., *ChemElectroChem* **2016**, *3*, 1967.

(7) Hendel, S. J.; Young, E. R., *J. Chem. Ed.* **2016**.

(8) Costentin, C.; Savéant, J.-M., *ChemElectroChem* **2014**, *1*, 1226.

(9) McCarthy, B. D.; Martin, D. J.; Rountree, E. S.; Ullman, A. C.; Dempsey, J. L., *Inorg. Chem.* **2014**, *53*, 8350.

(10) Armarego, W. L. F.; Chai, C. L. L., *Purification of laboratory chemicals*. 5th ed.; Butterworth-Heinemann: Amsterdam ; Boston, 2003.

(11) Myland, J. C.; Oldham, K. B., *Anal. Chem.* **2000**, *72*, 3972.

(12) Smieja, J. M.; Kubiak, C. P., *Inorg. Chem.* **2010**, *49*, 9283.

(13) Wong, K.-Y.; Chung, W.-H.; Lau, C.-P., *J. Electroanal. Chem.* **1998**, *453*, 161.

(14) Costentin, C.; Passard, G.; Robert, M.; Savéant, J.-M., *J. Am. Chem. Soc.* **2014**, *136*, 11821.

(15) Smieja, J. M.; Benson, E. E.; Kumar, B.; Grice, K. A.; Seu, C. S.; Miller, A. J.; Mayer, J. M.; Kubiak, C. P., *Proc. Nat. Acad. Sci. USA* **2012**, *109*, 15646.

(16) Anslyn, E. V.; Dougherty, D. A., *Modern Physical Organic Chemistry*. University Science: Sausalito, CA, 2006.

(17) Bligaard, T.; Bullock, R. M.; Campbell, C. T.; Chen, J. G.; Gates, B. C.; Gorte, R. J.; Jones, C. W.; Jones, W. D.; Kitchin, J. R.; Scott, S. L., *ACS Catal.* **2016**, *6*, 2590.

(18) Costentin, C.; Passard, G.; Savéant, J.-M., *J. Am. Chem. Soc.* **2015**, *137*, 5461.

(19) Costentin, C.; Drouet, S.; Robert, M.; Savéant, J.-M., *J. Am. Chem. Soc.* **2012**, *134*, 11235.

(20) Costentin, C.; Drouet, S.; Robert, M.; Savéant, J.-M., *J. Am. Chem. Soc.* **2012**, *134*, 19949.

(21) Aresta, M.; Dibenedetto, A.; Quaranta, E., One- and Multi-electron Pathways for the Reduction of CO_2 into C1 and C1+ Energy-Richer Molecules: Some Thermodynamic and Kinetic Facts. In *Reaction Mechanisms in Carbon Dioxide Conversion*, 2016; 311-345.

(22) Matheu, R.; Neudeck, S.; Meyer, F.; Sala, X.; Llobet, A., *ChemSusChem* **2016**, *9*, 3361.

(23) Savéant, J.-M., *Chem. Rev.* **2008**, *108*, 2348.

(24) Azcarate, I.; Costentin, C.; Robert, M.; Savéant, J.-M., *J. Am. Chem. Soc.* **2016**, *138*, 16639.

(25) Pegis, M. L.; Roberts, J. A.; Wasylenko, D. J.; Mader, E. A.; Appel, A. M.; Mayer, J. M., *Inorg. Chem.* **2015**, *54*, 11883.

(26) Raamat, E.; Kaupmees, K.; Ovsjannikov, G.; Trummal, A.; Kütt, A.; Saame, J.; Koppel, I.; Kaljurand, I.; Lipping, L.; Rodima, T.; Pihl, V.; Koppel, I. A.; Leito, I., *J. Phys. Org. Chem.* **2013**, *26*, 162.

(27) Riplinger, C.; Carter, E. A., *ACS Catal.* **2015**, *5*, 900.

(28) Appel, A. M.; Helm, M. L., *ACS Catal.* **2014**, *4*, 630.

(29) Costentin, C.; Robert, M.; Savéant, J.-M., *Chem. Soc. Rev.* **2013**, *42*, 2423.

(30) Bhugun, I.; Lexa, D.; Savéant, J.-M., *J. Am. Chem. Soc.* **1994**, *116*, 5015.

(31) Savéant, J. M.; Vianello, E., *Electrochimica Acta* **1963**, *8*, 905.

(32) Nadjo, L.; Savéant, J. M., *J. Electroanal. Chem.* **1973**, *48*, 113.

(33) Andrieux, C. P.; Blocman, C.; Dumas-Bouchiat, J. M.; M'Halla, F.; Savéant, J. M., *J. Electroanal. Chem.* **1980**, *113*, 19.

(34) Martin, D. J.; McCarthy, B. D.; Rountree, E. S.; Dempsey, J. L., *Dalton Trans.* **2016**, *45*, 9970.

(35) Wasylenko, D. J.; Rodriguez, C.; Pegis, M. L.; Mayer, J. M., *J. Am. Chem. Soc.* **2014**, *136*, 12544.

(36) Costentin, C.; Savéant, J.-M., *J. Am. Chem. Soc.* **2017**.

(37) Sampson, M. D.; Kubiak, C. P., *J. Am. Chem. Soc.* **2016**, *138*, 1386.

(38) Costentin, C.; Robert, M.; Savéant, J.-M.; Tatin, A., *Proc. Nat. Acad. Sci. USA* **2015**, *112*, 6882.

(39) Azcarate, I.; Costentin, C.; Robert, M.; Savéant, J.-M., *J. Phys. Chem. C* **2016**, *120*, 28951.

(40) Sieh, D.; Lacy, D. C.; Peters, J. C.; Kubiak, C. P., *Chem. Eur. J.* **2015**, *21*, 8497.

(41) Clark, M. L.; Grice, K. A.; Moore, C. E.; Rheingold, A. L.; Kubiak, C. P., *Chem. Sci.* **2014**, *5*, 1894.

(42) Wilson, A. D.; Newell, R. H.; McNevin, M. J.; Muckerman, J. T.; Rakowski DuBois, M.; DuBois, D. L., *J. Am. Chem. Soc.* **2006**, *128*, 358.

2.9 Appendix

Experimental Considerations. Solvents were obtained from Fisher Scientific and were dried over alumina, dispensed from a custom made solvent dispensing system and degassed with Ar(g) prior to use. Reagents were obtained from commercially available sources. Tetrabutylammonium hexafluorophosphate ($TBAPF_6$, Aldrich, 98%) was recrystallized twice from methanol and dried at 90°C overnight before use in electrochemistry experiments. Re(4,4′-*tert*-butyl-2,2′-bipyridine)$(CO)_3Cl$ was synthesized according to literature procedure.[12]

Cyclic Voltammetry. Cyclic voltammetry was performed on a BASi Epsilon potentiostat. Experiments were typically run in 0.1 M TBAPF6 in 5 mL of MeCN with 1 mM catalyst. Ferrocene was used as an internal standard (~1 mM) for all scans. Cell set up is that seen in Figure 2.8, where the incoming sparging gas is run through a Drierite column and a sparging solution of MeCN before entering the cell. Electrodes used were a 3 mm diameter glassy carbon working electrode, bare Pt wire counter electrode, and an Ag/AgCl reference electrode that separated from solution in by a glass tube filled with 0.1 M $TBAPF_6$ solution in MeCN fitted with a CoralPor tip. The platinum wire was flame treated with a butane torch prior to use. The glassy carbon working electrode was polished with 15, 3, and 1 micron diamond paste successively, thoroughly rinsed with methanol and dried under a stream of nitrogen prior to experiments and polished with 1 micron diamond polishing paste between scans. Ohmic drop of the cell was corrected for by using the potentiostat’s iR-compensation tool, correcting for 80-90% of the measured resistance. This resulted in a ferrocene peak splitting typically between 61-67 mV.

Preparing a Ag/AgCl Reference Electrode. To make an Ag/AgCl RE, find a silver wire that is longer than the glass sheath it will be housed in. Using fine grade sandpaper, sand the wire to ensure it is clean. To electrochemically coat the wire in AgCl, make a 3 M solution of HCl (aq). Set up an electrochemical cell with the silver wire as the working electrode, a Pt counter and a Pt reference. Make sure the silver wire is submerged in the HCl solution as far as possible to coat most the wire. Run an oxidative CV from 0 to 1 V 2-3 times until the wire looks well coated. Attached a CoralPor tip (BASi) to the end of the glass sheath with heat shrink wrap, being careful to not melt the tip or have the heat shrink wrap extend beyond the CoralPor (this would trap gas bubbles during use). Store the electrode housing (glass sheath with tip) in the same solution that will be used in the electrochemical experiments at least 24 hours before first use and between experiments. Replace the CoralPor tip and recoat the silver wire periodically to maintain a well-behaved Ag/AgCl RE.

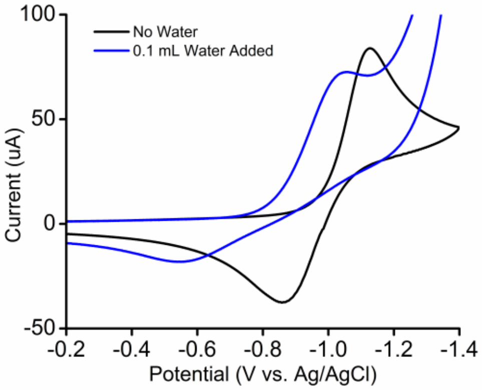

Figure 2.18 CV of the oxygen couple in 0.1 M $TBAPF_6$ MeCN solution that has not been sparged with any gas. Black: before addition of any water. Blue: Addition of 0.1 mL of water, which changed both the Ohmic drop and solvent window.

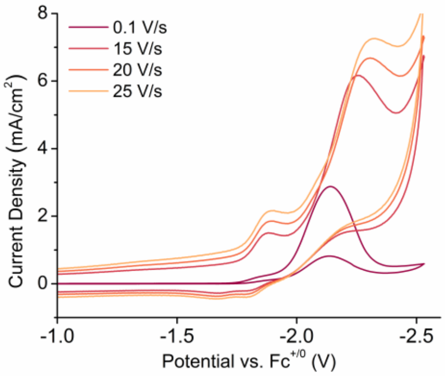

Figure 2.19 Catalytic SRD CV of **Re(tBu-bpy)** (1 mM) under CO_2(g) with 1 M phenol added. Peak data from 25 V/s was used to calculate k_{cat} using Equation 2.14.

Use of FOWA for Re(tBu-bpy). The steps for using FOWA are as follows:

1. CV under Ar to determine:
    a. Peak current when no catalysis is occurring (i_p)
    b. Standard Reduction Potential for the catalytic wave (E_{cat}) (for **Re(tBu-bpy)** this is currently being taken from DPV)
    c. Capacitive current (i_c)
2. Subtract i_c from the foot of the wave area of catalysis and from i_p
3. Plot i_{cat}/i_p vs. $1/(1+\exp[(F/RT)(E – E°_{cat}])$
4. Use the slope linear region of the graph to determine k_{obs} from $2.24(n_{cat})[(RT/Fv)(k_{cat})]^{1/2}$

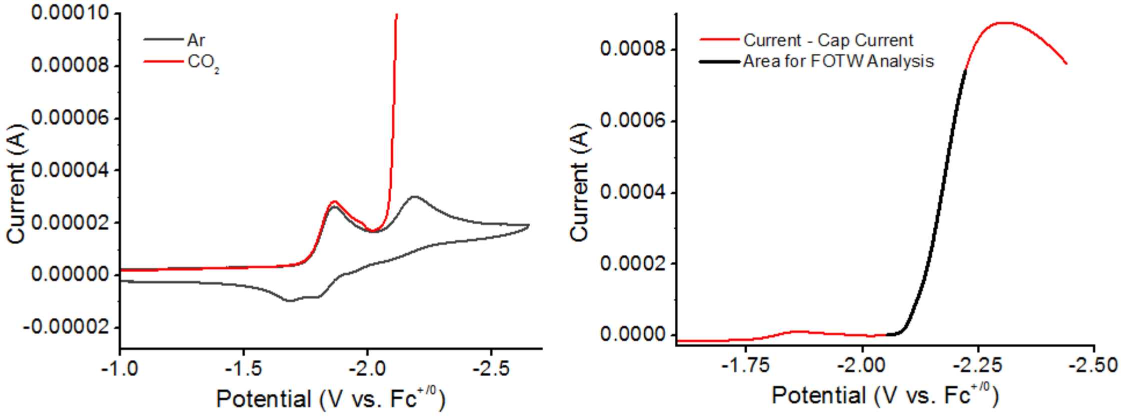

Figure 2.20 Left: Zoom in of the Ar CV of **Re(tBu-bpy)** under Ar and CO_2. i_c = 1.73037×10^{-5} A and uncorrected peak current i_{p*} = 2.63614×10^{-5} A to give i_p = 9.0577×10^{-6} A. Right: Catalytic CO_2 forward scan of **Re(tBu-bpy)** where i_c has been correction for. The region used for FOWA is shaded in black.

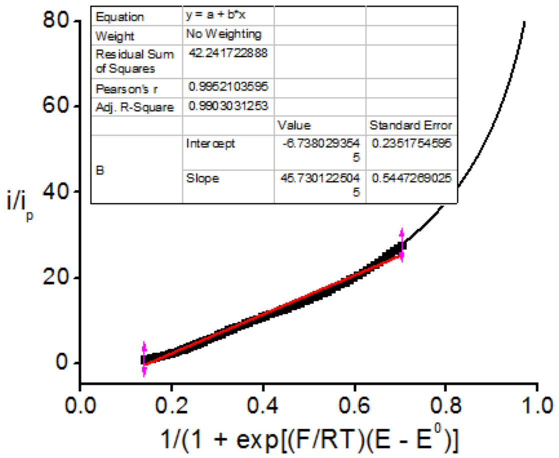

Equation	y = a + b*x		
Weight	No Weighting		
Residual Sum of Squares	42.241722888		
Pearson's r	0.9952103595		
Adj. R-Square	0.9903031253		
		Value	Standard Error
B	Intercept	-6.7380293545	0.2351754595
	Slope	45.7301225045	0.5447269025

Figure 2.21 FOWA plot using E^o_{cat} = –2.128 V vs. $Fc^{+/0}$ and the data points from Figure 2.20 starting at a i_{cat}/i_p of 1 (indicating the start of a catalytic response). The fit included data points only up to $R^2 > 0.99$.[35]

Table 2.2 Values used to create the catalytic Tafel plot of **Re(tBu-bpy)** in Figure 2.17.

Overpotential	**TOF**	**log (TOF)**
0	5.3877E-26	-25.268593
0.025	1.4255E-25	-24.8460245
0.05	3.7718E-25	-24.423456
0.075	9.9796E-25	-24.0008874
0.1	2.6405E-24	-23.5783189
0.125	6.9863E-24	-23.1557504
0.15	1.8485E-23	-22.7331818
0.175	4.8909E-23	-22.3106133
0.2	1.2941E-22	-21.8880448
0.225	3.4239E-22	-21.4654762
0.25	9.0593E-22	-21.0429077
0.275	2.397E-21	-20.6203392
0.3	6.342E-21	-20.1977706
0.325	1.678E-20	-19.7752021
0.35	4.4398E-20	-19.3526336
0.375	1.1747E-19	-18.9300651
0.4	3.1082E-19	-18.5074965
0.425	8.2238E-19	-18.084928
0.45	2.1759E-18	-17.6623595
0.475	5.7572E-18	-17.2397909
0.5	1.5233E-17	-16.8172224
0.525	4.0304E-17	-16.3946539
0.55	1.0664E-16	-15.9720853
0.575	2.8215E-16	-15.5495168
0.6	7.4654E-16	-15.1269483
0.625	1.9752E-15	-14.7043797
0.65	5.2262E-15	-14.2818112
0.675	1.3828E-14	-13.8592427
0.7	3.6587E-14	-13.4366742
0.725	9.6804E-14	-13.0141056
0.75	2.5613E-13	-12.5915371
0.775	6.7769E-13	-12.1689686
0.8	1.7931E-12	-11.7464
0.825	4.7443E-12	-11.3238315
0.85	1.2553E-11	-10.901263
0.875	3.3213E-11	-10.4786944
0.9	8.7877E-11	-10.0561259

Table 2.2 Values used to create the catalytic Tafel plot of **Re(tBu-bpy)** in Figure 2.17, continued.

Overpotential	**TOF**	**log (TOF)**
0.925	2.3251E-10	-9.63355737
0.95	6.1519E-10	-9.21098884
0.975	1.6277E-09	-8.78842031
1	4.3067E-09	-8.36585178
1.025	1.1395E-08	-7.94328325
1.05	3.015E-08	-7.52071472
1.075	7.9773E-08	-7.09814619
1.1	2.1107E-07	-6.67557766
1.125	5.5846E-07	-6.25300913
1.15	1.4776E-06	-5.8304406
1.175	3.9096E-06	-5.40787207
1.2	1.0344E-05	-4.98530354
1.225	2.7369E-05	-4.56273502
1.25	7.2416E-05	-4.14016653
1.275	0.0001916	-3.71759808
1.3	0.00050696	-3.29502978
1.325	0.00134134	-2.87246186
1.35	0.00354899	-2.44989495
1.375	0.00939008	-2.02733069
1.4	0.02484429	-1.60477348
1.425	0.06573022	-1.1822349
1.45	0.17388191	-0.75974559
1.475	0.45984704	-0.3373866
1.5	1.21514468	0.08462799
1.525	3.20430812	0.50573427
1.55	8.40344681	0.924457456
1.575	21.7276589	1.337012934
1.6	54.2188906	1.734150627
1.625	124.691951	2.09583842
1.65	245.095512	2.38933536
1.675	385.946292	2.586526873
1.7	493.031672	2.692874819
1.725	550.790923	2.740986775
1.75	576.308119	2.760654738
1.775	586.578914	2.768326447
1.8	590.55671	2.771261608
1.825	592.074192	2.772376131

Table 2.2 Values used to create the catalytic Tafel plot of **Re(tBu-bpy)** in Figure 2.17, continued.

Overpotential	**TOF**	**log (TOF)**
1.85	592.649753	2.772798108
1.875	592.867576	2.7729577
1.9	592.949944	2.773018032
1.925	592.98108	2.773040837
1.95	592.992849	2.773049456
1.975	592.997297	2.773052714
2	592.998979	2.773053945
2.025	592.999614	2.773054411
2.05	592.999854	2.773054587
2.075	592.999945	2.773054653
2.1	592.999979	2.773054678
2.125	592.999992	2.773054688
2.15	592.999997	2.773054691
2.175	592.999999	2.773054693
2.2	593	2.773054693
2.225	593	2.773054693
2.25	593	2.773054693
2.275	593	2.773054693
2.3	593	2.773054693
2.325	593	2.773054693
2.35	593	2.773054693
2.375	593	2.773054693
2.4	593	2.773054693
2.425	593	2.773054693
2.45	593	2.773054693
2.475	593	2.773054693
2.5	593	2.773054693

Chapter 3

Kinetic and Mechanistic Effects of Substituent, Labile Ligand, and Brønsted Acid on Electrocatalytic CO_2 Reduction by Re(bpy) Complexes

3.1 Introduction

The activation of carbon dioxide to use as a chemical feedstock for synthetic liquid fuels is a tremendous modern day energy challenge. The simplest commercial fuel that could be made from CO_2 is methanol, however the kinetic and thermodynamic barriers to complete this $6H^+$, $6e^-$ coupled process limits its feasibility.[1] Even the direct reduction of CO_2 to create the active anion radical $CO_2^{\bullet-}$ has a high-energy cost (CO_2/ $CO_2^{\bullet-}$ couple is –1.97 V vs. NHE in DMF)[2] due to the large reorganization energy required to bend the linear CO_2 molecule.[3] To side step these issues, catalysts are used to help lower these energy barriers and simpler fuel precursors are often the targets of these reactions.[4-9] One such target is carbon monoxide (CO), which can in turn be used as a feedstock for alkanes through the Fischer-Tröpsch process.[10] An organometallic catalyst family that has been demonstrated to be selective and active towards the reduction of CO_2 to CO are those based on the *fac*-Re(2,2′-bipyridine)$(CO)_3$Cl (Re-bpy) motif.[11-15] This catalyst and derivatives thereof have been investigated for their electrochemical[16] and photochemical[17-19] catalytic properties, as well as incorporated into higher order systems[20-21] and attached to surfaces.[22-23] Most of these studies involve tailoring the Re-bpy system,[24] although the variance in experimental conditions and measurements make it hard to compare catalysts across reports.

A recent push in the literature has been to find common ground by which catalysts for the same reaction can be compared.[25-26] Savéant and co-workers have shown how cyclic voltammetry (CV) can be utilized to gain kinetic and thermodynamic parameters that are intrinsic to the catalytic activity of a complex, thus finding a common ground for comparison. Ideally, a catalytic CV would show a “S-shape” wave that is independent of scan rate, where the plateau current can be used to determine in intrinsic catalytic rate constants. More common however is a peak-shaped response, which occurs due to events such as deactivation of the catalyst, consumption of substrate, or inhibition by products.[27] An S-shaped wave can sometimes still be obtained by traversing the kinetic zone diagram by increasing the scan rate, decreasing catalyst concentration, or increasing the substrate,[28] but this is not always the case. In such instances a foot-of-the-wave analysis (FOWA) is more favorable, which utilizes onset catalytic current not yet affected by side-phenomena.[29] FOWA has given identical rate constants to stopped-flow UV-vis spectroscopy for catalytic reduction of oxygen by iron-tetraphenylporphyrin chloride, demonstrating the validity of a CV approach to obtain kinetic information.[30] Coupled with the overpotential of the catalytic reaction, these CO_2-to-CO catalysts can be directly compared with catalytic Tafel plots, which relate the intrinsic catalytic rate constant to the overpotential to visually demonstrate the relationship between the two.[2]

These CV techniques have not been applied toward Re-bpy systems, despite cyclic voltammetry being a primary characterization tool for these complexes. Herein, the descriptors of intrinsic catalytic rate constant and overpotential are used to report the effects of 4,4′-substituent (OCH_3, CH_3, *t*Bu, H, CN, CF_3), labile ligand (pyridine, acetonitrile, chlorine, bromine), and Brønsted acid (phenol, 2,2,2-trifluoroethanol, acetic acid) on Re-bpy based catalysis (Figure 3.1). While these modifications to the complex have been previously reported,[11, 16, 31] full comparisons, especially with respect to the electrocatalytic mechanism, have not been made. To this end, DFT calcu-lations are used to describe how modifications to the cata-lyst effect the mechanism and affinity for CO_2 binding. These descriptors, coupled with careful analysis by CV techniques, allow for the comparison of Re-bpy with other CO_2 reduction electrocatalysts using catalytic

Tafel plots, revealing the unique nature of the Re-bpy system for selec-tive and active catalysis.

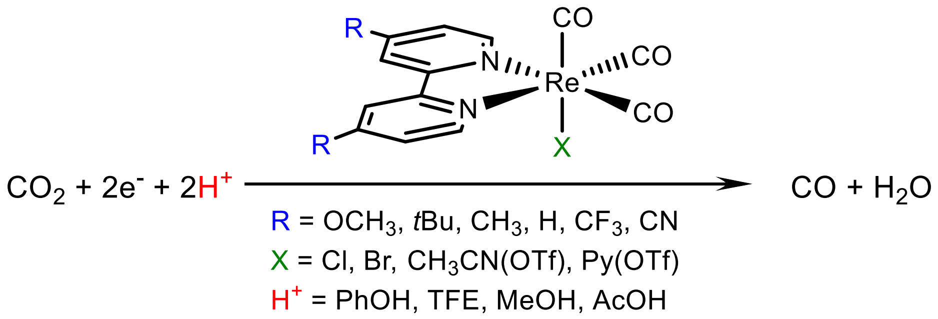

Figure 3.1 Variants of Re(4,4′-R-2,2′-bipyridine)$(CO)_3X$ studied in this work.

3.2 Results

Cyclic Voltammetry under Ar. To investigate the thermodynamic effect of the electron donating nature of the bpy substituents as well as the labile ligand, the complexes were first examined via CV under inert atmosphere. Six complexes were chosen with varying electron donating/withdrawing substituents in the 4,4′-position of the bpy: **OCH$_3$**, *t*Bu (**tBu-Cl**), **CH$_3$**, H (**bpy-H**), **CF$_3$**, and **CN** (Figure 3.1). The above order is in decreasing electron donor ability, as described by para-substituted Hammett parameter (Table 3.1).[32] This trend is reflected in the reduction potentials of the complexes: the more electron donating, the farther negative the complex gets reduced. The difference between the most electron donating **OCH$_3$** (σ_p = –0.27) and electron-withdrawing **CN** (σ_p = +0.66) is about 700 mV. As has been detailed previously,[11, 33-35] each complex displays one reversible one-electron wave followed by an irreversible or quasi-reversible one-electron reductive wave at a more negative potential (Figure 3.2). These have been confirmed spectroscopically and crystallographically as a reversible bpy centered reduction proceeded by a metal based reduction ($Re^{I/0}$) that results in the loss of the labile ligand, which in this case is chloride.[36] At more negative potentials (600-810 mV farther from the second reduction) is a third well defined irreversible reductive wave. This has been assigned as bpy centered reduction for mono-substituted Re(4-cyano-2,2′-bipyridine)$(CO)_3Cl$,[22] however this is most likely the case for the other five complexes as well.

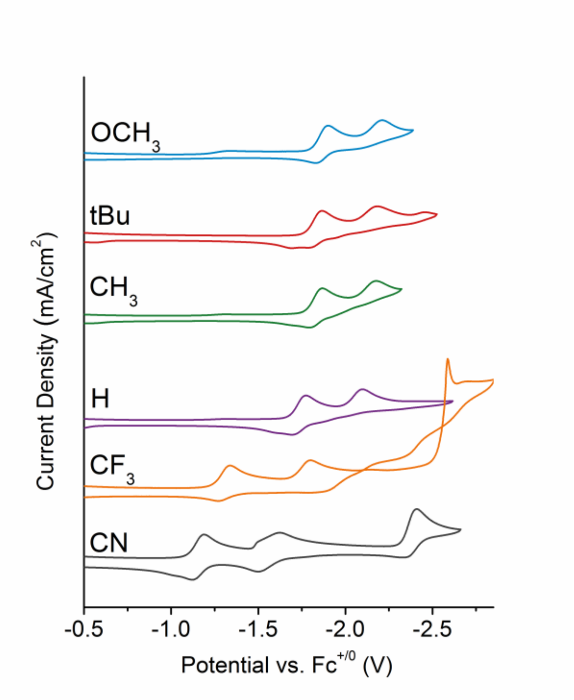

Figure 3.2 Cyclic voltammograms under Ar of the six 4,4′-substituted complexes (labeled with their substituent). All voltammograms recorded in 0.1M $TBAPF_6$ CH_3CN solution with 1 mM complex. Reduction potentials are listed in Table 3.8.

The effect of the donating ability of the substituents is seen both in the potentials of the complex’s reductions as well as in the number of features (Figure 3.2). The electron donating substituted complexes **OCH_3**, ***t*Bu-Cl**, and **CH_3** have slightly more negative reduction potentials than **bpy-H** (–120 mV, –80 mV, and –110 mV respectively) reflecting increased difficulty in reducing the more electron rich compounds. Counter to the electron donating case, the complexes with electron withdrawing substituents, **CF$_3$** and **CN**, have much more positive reduction potentials than **bpy-H** by 44 mV and 59 mV, respectively. There are also no additional reductive features seen, indicating there is no balance between the reduction of 5- and 6-coordinate singly reduced species. A previously reported crystal structure of the singly reduced **CF$_3$** compound showed a 6-coordinate complex, unlike reduced structures of ***t*Bu-Cl** which are 5-coordinate.[36] The electron withdrawing nature of the CF$_3$ groups prevent LMCT, thus the chloride cannot dissociate until a second reduction takes place. This trend was also noted in the IR-SEC of **CN**.[22] The three main reductive features for **CF$_3$** and **CN** can be attributed to bpy, metal (with chloride loss), then bpy based reductions.

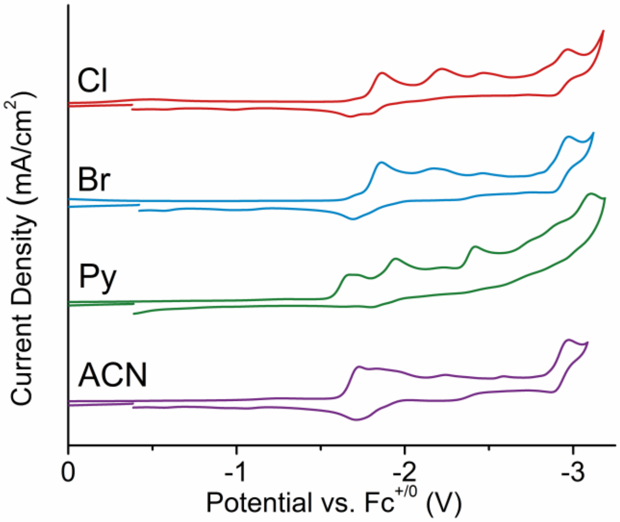

Figure 3.3 Cyclic voltammograms of the four Re(bpy-*t*Bu)(CO)X complexes, labeled by the labile ligand (X). All voltammograms recorded in 0.1M TBAPF$_6$ CH$_3$CN solution with 1 mM complex. Reduction potentials are listed in Table 3.6.

The identity of the labile ligand also has an effect on the reduction potentials of the complex, although much more minor than the substituent effects (Figure 3.3). ***t*****Bu-Cl** and ***t*****Bu-Br** have almost an identical CV response, with ***t*****Bu-Br** having a slightly more positive second reduction potential than ***t*****Bu-Cl** since bromide is a more labile ligand than Cl. The more neutral ligands of ***t*****Bu-CH_3CN** and ***t*****Bu-PY** create a bpy ligand that is easier to reduce (–1.73 V and –1.68 V, respectively, compared to ***t*****Bu-Cl** at –1.86 V). The second reduction is also more positive. Of note is that the reductions of ***t*****Bu-CH_3CN** are not at the same potentials of any of the other complexes, ruling out a coordination of CH_3CN after halide loss.

Cyclic Voltammetry under CO_2. To investigate the effect of ligand and substituent on the catalytic current response without and added proton source, each complex was measured under saturated CO_2 conditions (0.28 M in CH_3CN). In the case of the electron donating substituents (**OCH_3, CH_3,** and ***t*****Bu-Cl**), a current enhancement upon the onset of the second reduction potential is observed (Figure 3.4). A rough measure of the catalytic response can be taken by comparing the peak current response under CO_2 (i_{cat}) versus that under inert conditions (i_p). These i_{cat}/i_p values can be seen in Table 3.1, where previously reported values are in parentheses. In this work, higher values are measured than previously reported for all catalysts, likely due to using a freshly polished working electrode for each scan. Of note is **OCH_3**, which had been previously reported as non-catalytic[11] but has the highest i_{cat}/i_p value in this study (36.2). To determine the activity and selectivity of **OCH_3**, controlled potential electrolysis (CPE) was run. Over 1 hr (3.9

turnovers), analysis of the headspace corresponded to Faradaic efficiencies (FE) of 58% for CO, with no H_2 detected. The complexes ***t*Bu**, **CH_3**, and **bpy-H** are all previously reported as selective for the reduction of CO_2 to CO with near 100% Faradaic efficiency.[11]

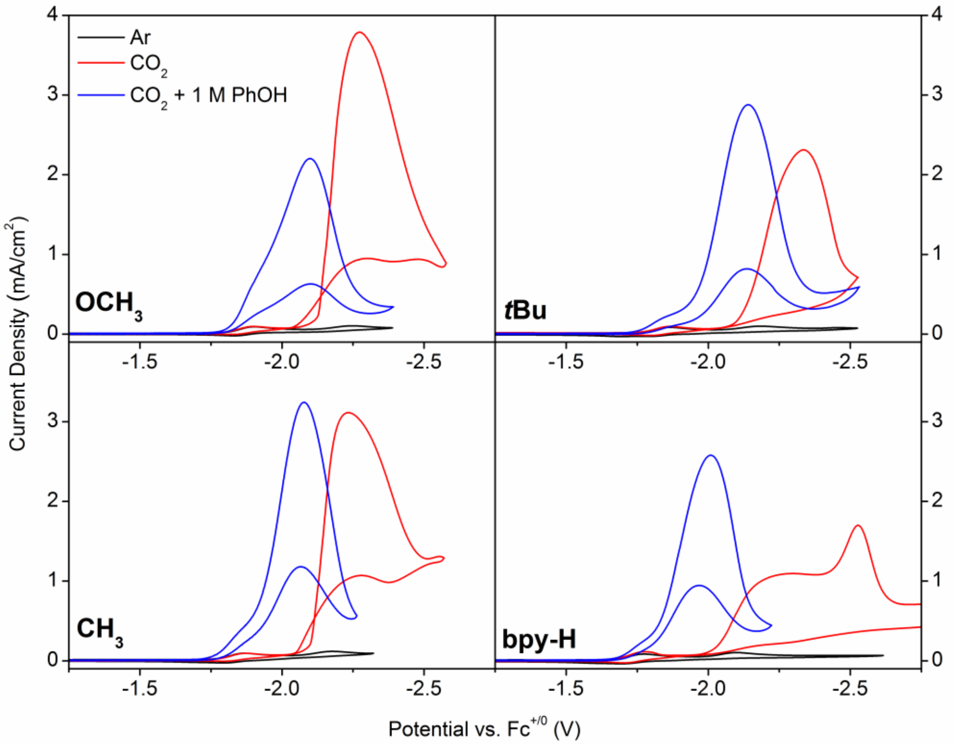

Figure 3.4 CVs of the four electron-donating Re(4,4′-R-bpy)(CO)Cl complexes, labeled by R substituent. Black: Ar atmosphere, red: CO_2 atmosphere, blue, CO_2 atmosphere with 1 M PhOH. All voltammograms recorded in 0.1M $TBAPF_6$ CH_3CN solution with 1 mM complex at 0.1 V/s.

The catalytic current response for electron-withdrawing **CN** and **CF_3** does not occur until the second bpy reduction (third overall reduction), Figure 3.5. This is due to the inability of the doubly reduced species to favorably bind CO_2 (*vide infra*).

The i_{cat}/i_p values are also much lower than the electron donating cases (i_{cat}/i_p **CF_3** = 2.7, **CN** = 5.6). **CN** was found to have an 18% FE for CO, owing partly to evidence that the cyano groups react with CO_2 to form carboxylamides.[22] **CF_3** was previously reported as non-catalytic because of the lack of catalytic current at the second reduction potential.[36] The modest current enhancement at the third reduction was investigated via CPE, where analysis of the headspace corresponded to Faradaic efficiencies (FE) of 29% for CO, with 2% H_2 detected.

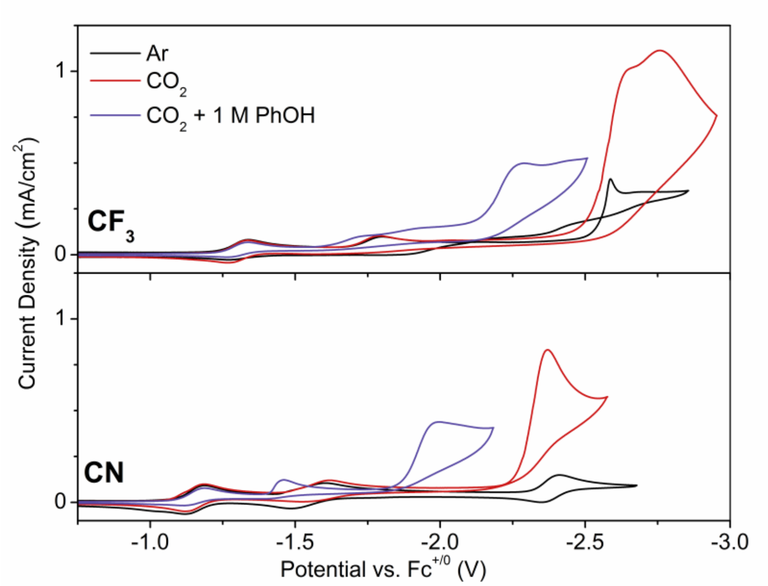

Figure 3.5 CVs of the two electron-withdrawing Re(4,4′-R-bpy)(CO)Cl complexes, labeled by R substituent. Black: Ar atmosphere, red: CO_2 atmosphere, blue, CO_2 atmosphere with 1 M PhOH added. All voltammograms recorded in 0.1M $TBAPF_6$ CH_3CN solution with 1 mM complex at 0.1 V/s.

While the labile ligand effected the reductions of the complexes under Ar, this is not the case under catalytic conditions. The catalytic onset potential and peak catalytic wave are almost identical to each other, as well as the i_{cat}/i_p values (Figure 3.11 Table 3.7). This is of note for both ***t*Bu-CH_3CN** and ***t*Bu-PY**, whose second reductions are more positive than the onset of the catalytic wave. This reveals that ligand loss is not a hindering factor to catalysis. Since the catalytic activity is the same, ***t*****Bu-CH_3CN**, ***t*****Bu-PY**, and ***t*****Bu-Br** were not included in the catalytic comparisons.

Determination of TOF_{max}. While consideration of i_{cat}/i_p is a useful tool in first identifying catalysis by CV, it does not convey intrinsic catalytic properties. This is because when a peak shape is seen in a catalytic wave, side-phenomena (substrate consumption, deactivation of the catalyst, etc.) are inhibiting the full catalytic response.[26-27] An ideal catalytic CV response is S-shaped, where the forward and return sweep are identical to each other and the catalytic current is independent of scan rate. For an EC′ catalytic mechanism, a catalytic rate constant can be determined from the plateau current by Equation E3.1[28]

$$\frac{i_{cat}}{i_p} = 2.24\sqrt{\frac{RT}{F}\frac{2k_{cat}}{v}} \qquad \textbf{(E3.1)}$$

where R is the universal gas constant, T is temperature, F is Faraday’s constant, v is the scan rate, and k_{cat} is the catalytic rate constant. In this case k_{cat} is equal to the maximum turnover frequency (TOF_{max}, Equation E3.2).[37]

$$TOF_{max} = k_{cat} \qquad \textbf{(E3.2)}$$

The rate of CO_2 to CO by Re-bpy catalysts has been found to be a third order,[16] and thus k_{cat} can also be used to determine the overall intrinsic rate of the catalyst through Equations E3.3 and E3.4.

$$\text{rate} = k_{obs}[\text{Rebpy}] \qquad \textbf{(E3.3)}$$

$$k_{obs} = k_{cat}[CO_2][H^+]^2 \qquad \textbf{(E3.4)}$$

If an S-shaped wave cannot be achieved, FOWA can also be used to determine k_{cat}. This method utilizes the current at the onset of the catalytic wave, where “side phenomenon” have not yet taken place. For a 2-electron, EC′ catalytic process FOWA is governed by Equation E3.5,[26-27]

$$\frac{i_{cat}}{i_p} = \frac{2.24 n_{cat}\sqrt{\left(\frac{RT}{Fv}\right)k_{cat}}}{1+\exp\left[\left(\frac{F}{RT}\right)(E-E°_{cat})\right]} \qquad \textbf{(E3.5)}$$

where n_{cat} is the number of electrons involved in the catalytic process, E the potential (V) corresponding to i_{cat}, and $E°_{cat}$ the standard potential of the active catalyst recorded under non-catalytic conditions. K_{cat} is obtained by plotting i_{cat}/i_p vs. $1/(1+\exp[(F/RT)(E – E°_{cat}])$, where the slope is defined by $2.24n_{cat}[(Fv/RT)\ k_{cat}]^{1/2}$ (see Appendix for details).

To garner which method would be most applicable to the Re-bpy system, both were applied to each complex and the resulting k_{cat} values compared. All catalysts had a catalytic current that was scan rate dependent at 100 mV/s, which was the scan rate used to determine the original i_{cat}/i_p values. To attempt to achieve an S-shaped wave the scan rate was increased, however it was found that even at 25 V/s (the maximum for our instrument) the catalytic current was not an ideal S-shape, particularly on the return sweep. For most of the complexes there was a limit to the increase in catalytic current, which was the CVs used to determine k_{cat}. Variable scan rate CV for all six compounds can be seen in Figure 3.6 and values in Table 3.1. The k_{cat} values for the electron donating substituted complexes are **OCH_3** = 966 s^{-1}, **tBu** = 526 s^{-1}, and **CH_3** = 815 s^{-1}. **Bpy-H** had the lowest k_{cat} at 46

s^{-1} whilst the electron withdrawing substituted complexes had larger rate constants at **CF_3** = 1933 s^{-1} and **CN** = 1819 s^{-1}.

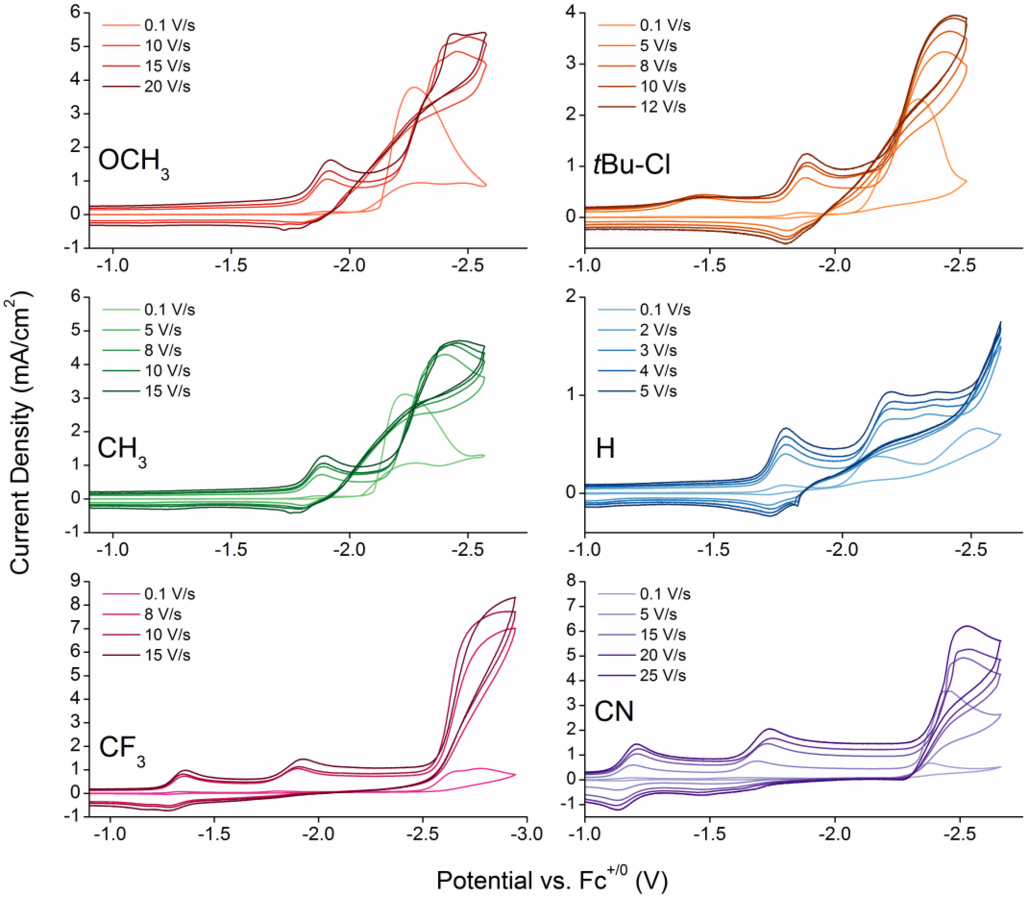

Figure 3.6 Catalytic scan rate dependence CVs for the six substituted complexes.

Table 3.1 Catalytic information for Re(4,4′-R-bpy)$(CO)_3Cl$ under CO_2.

R	**OCH_3**	***t*Bu-Cl**	**CH_3**	**H**	**CF_3**	**CN**
σ_p[a]	–0.27	–0.20	–0.17	0	+0.54	+0.66
E^o_{cat} (V)[b]	–2.20	–2.12	–2.12	–2.10	–2.62	–2.38
FE[e]	58%CO	100%CO[c]	100%CO[c]	100%CO[c]	29%CO	18%CO[d]
i_{cat}/i_p[f]	36.2	29.0	32.6	14.9	2.7	5.6
$E_{cat/2}$[g]	–2.18	–2.20	–2.14	–2.09	–2.57	–2.31
η[h]	–1.64	–1.66	–1.60	–1.55	–2.03	–1.77
k_{cat} (FOWA, s^{-1})		406		62	1933	1819
k_{cat}[i]	966 (15)	593 (8)	815 (20)	46 (5)	-	-

Reduction potentials reported vs. $Fc^{+/0}$. [a]para-substituted Hammett parameter for benzene.[32] [b]Determined by DPV. [c]Reported by Smieja *et al*.[11] [d]Reported by Clark *et al.*[22] [e]Faradaic efficiencies determined by CPE. [f]Determined at 100 mV/s. [g]Potential relating to $i_{cat/2}$.[38] [h]Using $E^o_{CO2/CO}$(CH_3CN) of –0.541 V vs. $Fc^{+/0}$.[39] [i]Value in parentheses is the scan rate (V/s) used to determine k_{cat}.

FOWA allowed for the use of the CV scans at 100 mV/s and could be used for all 6 complexes. One obstacle was the fact that a true E°_{cat} could not be determined since the catalytic reduction is irreversible (due to labile ligand loss). This value was estimated using DPV (Figure 3.13), as has been done for the comparison of water oxidation catalysts with the same issue.[40] The values obtained are similar, and the deviations are most likely due to interference from side phenomena during catalysis, affecting the current response.

Addition of Proton Source. The increase in catalysis due to the addition of a Brønsted acid for Re-bpy species has been well documented since the first report by Hawecker, Lehn, and Ziessel, where increase in current was seen when 10% water was added to a DMF solution of the catalyst.[13] Water however is a weak proton donor (pKa = 38-41 in CH_3CN)[41] and severely limits the solvent window of CH_3CN. Thus we first looked to study the effects of four different Brønsted acids of varying strength on the catalytic behavior and selectivity of ***t*Bu-Cl**: 2,2,2-trifluoroethanol (TFE) pK_a(CH_3CN) 35.4, phenol (PhOH) pK_a(CH_3CN) 29.1, and acetic acid (AcOH) $pK_a(CH_3CN)$ 23.5.[41-44] The most favorable of these acids would then be used to study the effects on the rest of the complexes.

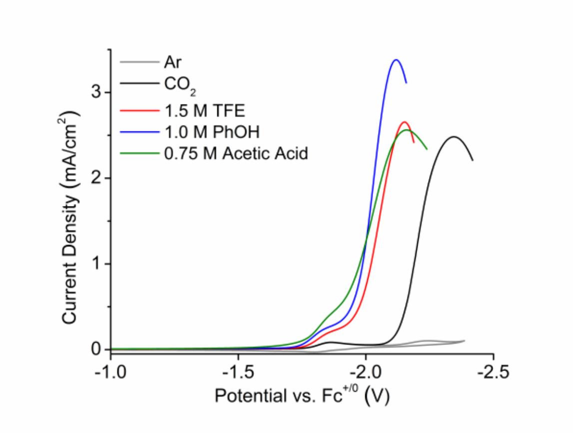

Figure 3.7 CVs of Re(*t*Bu-bpy)$(CO)_3$Cl (***t*Bu-Cl**) under CO_2 with different acids added. All voltammograms recorded in 0.1M $TBAPF_6$ CH_3CN solution with 1 mM complex.

The optimum amount acid was found by increasing the concentration until catalytic current plateaued. The stronger the acid, the less was needed (0.75 M AcOH, 1 M PhOH, and 1.5 M TFE). All acids decreased the solvent window for catalysis (Figure 3.12), with acetic acid having the shortest window (ca. –2.2 V vs. $Fc^{+/0}$). Catalytic current response of ***t*Bu-Cl** with each acid seen in Figure 3.7, where all acids are seen to shift the current response more positive by ~170 mV (–2.32 V to ca. –2.15 V). TFE and acetic matches the peak height of that without a proton source (i_{cat}/i_p (0.1 V/s) = 29.0) and PhOH gave a slight increase in current (i_{cat}/i_p = 33.4). CPE experiments revealed that both TFE and PhOH did not change the selectivity of the catalyst for CO production, the addition of 0.75 M AcOH resulted in 104% H_2 production with 2% CO (Table 3.8).

Determination of k_{cat} was not as straightforward with the added Brønsted acids. For one, FOWA could not be used because the foot of the catalytic wave overlapped with a slight increase in current at the first reduction potential of the catalyst. When the scan rate was increased to achieve an S-shaped wave, catalytic current still increased through 25 V/s. Due to these limitations, scans at 25 V/s were used to estimate k_{cat} using Equation E3.1 and we note that this is most likely an underreporting of the intrinsic rate constant under these conditions. Values can be found in Table 3.8, where the magnitude of k_{cat} trends with increasing acid strength.

Phenol gave the largest enhancement in k_{cat} without effecting selectivity and was therefore used as the proton source for the remainder of the complexes. Again, for the complexes with electron donating substituents, **OCH_3**, **CH_3** and **bpy-H**, the foot of the catalytic wave is more positive with added acid and overlaps with the first reduction potential. The catalytic current also continued to increase through 25 V/s when striving for an S-shaped current response. While the k_{cat} values from this method are most likely underreported, they are still comparable to those taken without a proton source added. These values are in Table 3.2, where it is seen that the addition of PhOH for the electron donating substituents increase k_{cat} by 2-fold. **Bpy-H** rate constant increases by almost 17-fold (46 s^{-1} to 770 s^{-1}), but its activity is still lower than the other electron-donating substituted catalysts. In contrast, the rate for **CF_3** and **CN** drastically decreases by over 12-fold. There is a much larger shift in catalytic reduction potential between that of no added acid to 1 M PhOH (0.40 V vs. 0.2 V for **bpy-H**), suggesting that a different reaction is happening (*vide infra*). CPE of **CN** and **CF_3** with 1 M PhOH give FE of 3% CO and 0% H_2 for **CN** and 5%CO and 34% H_2 for **CF_3**.

Table 3.2 Catalytic information for Re(4,4′-R-bpy)$(CO)_3$Cl complexes under CO_2 saturation with 1 M PhOH.

R	**OCH_3**	***t*Bu-Cl**	**CH_3**	**H**	**CF_3**	**CN**
$E_{cat/2}$ (V)^a	–1.97	–2.03	–1.98	–1.89	–2.17	–1.91
$\Delta E_{cat}{}^a$	0.21	0.17	0.16	0.20	0.40	0.40
$i_{cat}/i_p{}^b$	21.0	36.0	33.9	24.8	6.1	3.0
k_{cat} (s^{-1})^c	1931	1099	1848	770	-	-
Δk_{cat}	×2.0	×2.0	×2.3	×16.8	-	-

Reduction potentials reported vs. $Fc^{+/0}$. [a]Difference between the reduction potential under CO_2 and CO_2 + 1 M PhOH. [b]Determined at 0.1 V/s. [c]Determined at 25 V/s.

DFT Calculations. To further understand the effect of the 4,4′-substituents on the reactivity of the Re-bpy complexes towards CO_2, thermodynamic binding energies of catalytically relevant species were computationally determined (Table 3). Previous studies have shown that the Re-bpy catalysts have a thermodynamic preference for the binding of protons over CO_2, however the catalyst reacts almost 10 times faster with CO_2 than protons.[16] This thermodynamic preference is again noted in this work, where H^+ binding is much more favorable than CO_2. To garner a more complete comparison, the binding of a hydroxycarbonyl (CO_2H) was also considered. Previous computational work has shown that there is almost no barrier for the addition of a proton to the activated bound CO_2,[45] and experimentally the bound CO_2 radial has yet to be observed, unlike the CO_2H species.[46]

The favorability of binding for all three species (H^+, CO_2, and CO_2H) trends with the electron donating ability of the complexes. **OCH_3** has the most favorable binding energies, while **CN** has the least favorable. The positive binding energy towards CO_2 for **CN** (+8.7 kcal/mol) is congruent with the CV, where there is no catalytic activity at the second reduction potential. The strong correlation between binding energies and activity could lend this method to be a powerful tool to help predict reactivity of other potential catalysts.

Table 3.3 Thermodynamic binding energies (ΔG) to the Re^0bpy^{-1} catalytically active state for five of the 4,4′-substituted complex.

R	H^+ (kcal/mol)	CO_2 (kcal/mol)	COOH (kcal/mol)
OCH_3	–46.2	–10.9	–38.2
***t*Bu-Cl**	–41.8	–5.3	–34.9
CH_3	–43.8	–6.4	–36.1
H	–39.4	–2.7	–35.3
CN	–24.5	+8.7	–16.8

3.3 Discussion

Labile Ligand. The effect of the labile ligand on the spectroscopic properties of Re-bpy systems was first characterized by Kurz and co-workers, where they studied $Re(R\text{-}bpy)(CO)_3Cl$ (R = Cl, Br, H_2O, SCN, and CN) with respect to the photochemical reduction of CO_2.[19] Congruent with their results, the cationic complexes ***t*Bu-CH_3CN** and ***t*Bu-PY** are easier to reduce than the neutral complexes due to the lower electron density on Re^I. Both the ligand-centered and metal-centered reductions are affected. This is congruent with the calculated lowest unoccupied molecular orbital (LUMO) of Re-bpy which has the electron density distributed throughout the complex.[47] In all cases a catalytically active Re^0bpy^{-1} state is expected after the second reduction, where subsequent CH_3CN ligation is not expected to occur at these potentials.[48]

The identity of the labile ligand does not affect the activity or overpotential of the catalyst. That is, even for ***t*****Bu-PY** and ***t*****Bu-CH_3CN**, where the reduction potential corresponding to ligand loss occurs at more positive potentials (*ca.* –1.70 V vs. $Fc^{+/0}$), the catalytic wave does not begin until *ca.* –2.10 V vs. $Fc^{+/0}$. This illustrates that is it not the loss of ligand and the presence of the Re^0bpy^{-1} state that dictates the catalytic potential, but rather an actual overpotential required for electrocatalysis to occur. Only in the case of electrocatalysis is turnover independent of labile ligand loss; photocatalysis using Re-bpy complexes utilize a singly reduced species, thus the identity of the labile ligand strongly effects CO_2 reduction (for example, using CN in this case renders the complexes photocatalytically inactive).[49]

Bpy-Substituents. The electronic nature of the 4,4′-substituent on the bpy ligand greatly effects LMCT, both in initial reductions of the complex and during catalysis. The reduction potentials of the Re-bpy complexes trend linearly with the electron donating ability of the substituents, OCH_3 > *t*Bu > CH_3 > H > CF_3 > CN (Figure 3.8). Previous structural studies have shown that the carbonyl stretching frequencies of the Re^0bpy^{-1} anions of **bpy-H**, **CH_3**, and ***t*****Bu-Cl** are all within 1 cm^{-1} of each other, suggesting very similar electron density on the metal center.[36] However, the calculated molecular orbital of the anion shows that the electron density in the highest occupied molecular orbital (HOMO) is spread throughout the molecule, where both metal and bpy ligand are involved in activating CO_2.[47] Thus the availability of the electron density on the bpy ligand is crucial for the selectivity of these complexes. Clearly the substituents have a large effect on the electronic nature of the bpy ligand considering the reduction potentials of the Re complexes shift by 700 mV from **OCH_3** to **CN**.

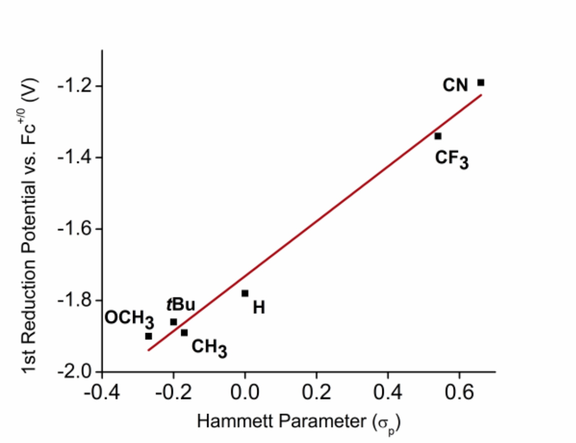

Figure 3.8 Relationship between corresponding para-substituted Hammett parameter and the bpy based reduction potential of the corresponding Re-bpy complex.

The identity of the substituent has a large effect on the activity and selectivity of the catalyst. The electron donating substituents CH_3 and *t*Bu increase the catalytic activity over Re-bpy without sacrificing selectivity. Previous reports have attributed the difference to steric bulk of ***t*Bu-Cl** over **bpy-H**, where the bulky *tert*-butyl groups prevent a dimerization deactivation pathway.[11] **CH_3** does form dimer, but much more slowly than **bpy-H**.[50] Dimer formation is not even possible for **CN** or **CF_3**, which do not have access to the LMCT state to form the neutral 5-coordinate species. These electron-withdrawing substituted complexes also are poor CO_2 reduction electrocatalysts, with Faradaic efficiencies for CO at 18% and 30% for **CN** and **CF_3**, respectively. The controlled potential electrolysis experiments for **CN**, **CF_3**, and **OCH_3** show a rapidly decreasing amount of current over time (monitored over one hour), suggesting that the catalyst quickly deactivates. We ruled out the reductive disproportionation of CO_2 to CO and carbonate since it involves a bimetallic mechanism,[51] which would not be present for these complexes. It is more likely that the extra electron density on the bpy ligand (due to the third reduction of **CN** and **CF_3** to achieve a catalytically active state and the highly electron donating nature of **OCH_3**) is highly destabilizing, leading to a catalyst that quickly degrades over time.

Acid Co-substrate. Re-bpy complexes have a second order dependence on protons for the overall electrocatalytic reduction of CO_2 to CO and H_2O.[16] The effect of proton source was first investigated with $[Re(bpy)(CO)_3(py)]OTf$, where TFE, MeOH, PhOH and water were compared.[31] Congruent with this study, the efficiency of the acid follows the acidity, i.e. the lower the pK_a, the higher the catalytic current. As verified with ***t*Bu-Cl**, PhOH and TFE did not effect the selectivity of the catalyst, but AcOH changed the selectivity to almost exclusively H_2 production. The loss of selectivity for CO_2 reduction toward proton reduction in the presence of acetic acid has also been observed with iron(0) tetraphenylporphyrin.[53]

Computational studies have elucidated the effect of acid and Brønsted acid pK_a on the mechanism of CO_2 reduction by Re-bpy. First, the strength of the proton donor dictates the selectivity of the catalyst. It has been both experimentally and computationally observed that H^+ binding to the catalytically active state is more thermodynamically favorable, however CO_2 reacts much faster,[16] lending to the product selectivity of these complexes. The strength of the proton donor can affect this, however. A too strong of a proton donor would result in H^+ favorability,[45] however the presence of a proton donor helps to achieve the stable intermediate of the catalytic cycle, Re-CO_2H. Thus a balance must be found between a proton donor strong enough to facilitate protonation of a bound CO_2, but weak enough to not shift to favorability of catalyst protonation.[44]

The addition of a proton donor also effects the catalytic mechanism, as observed from the consistent shift of the catalytic potential by 200 mV that is independent of proton source, labile ligand, and bpy substituent. As described by previous studies of the Re-bpy mechanism, once a CO_2 molecule is activated on the metal center, another proton and electron is needed in order for the rate limiting step to occur (breakage of a CO bond coupled with a proton to create H_2O and bound CO).[12, 45, 54] The order of these two steps had not previously been probed experimentally, however this question was addressed computationally in 2015 by Riplinger and Carter.[44] They found that without an explicitly added proton source, additional driving force was needed to be able to abstract protons from the solvent, CH_3CN. This is manifested both in a higher overpotential for catalysis as well as an “electron first” mechanism. This is congruent with the results seen in this study, and the computationally determined catalytic potentials for without added acid for **bpy-H** match within error to our experimental results (experimental: –2.10 V vs. computational: –2.25 V vs. $Fc^{+/0}$). When an explicit proton donor is added, a “proton first” mechanism can be achieved, where protonation of the bound CO_2 can occur before further reduction of the complex. This leads to lower overpotential of the catalyst, and again our experimental results match the computational findings for **bpy-H** (experimental: –1.89 V vs. computational: –1.94 V vs. $Fc^{+/0}$).

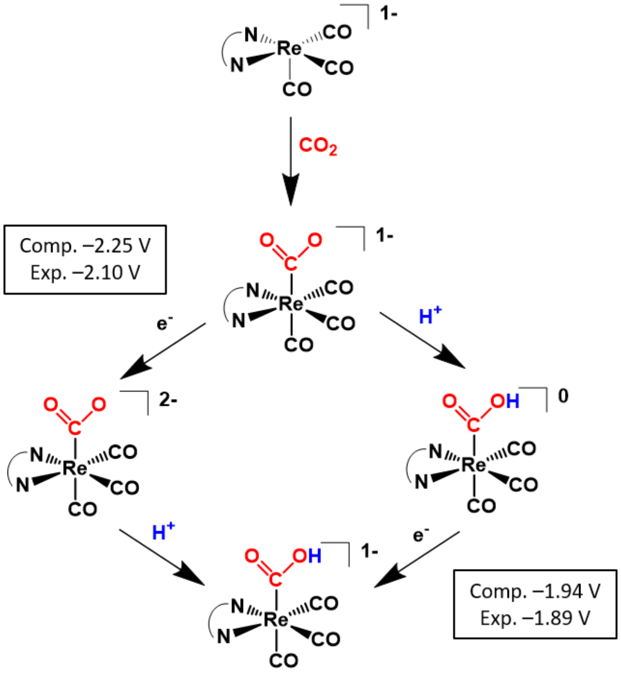

Figure 3.9 Difference in the first step of the Re-bpy electrocatalytic mechanism due to presense or absense of a proton donor (Brønsted acid co-substrate). Reduction potentials are for **bpy-H** and are reported versus Fc$^{+/0}$ at 100 mV/s. Computational values from Reference 44.

Comparing Catalysis. The intrinsic rate constants (k_{cat}) for the four complexes **OCH₃**, ***t*Bu-Cl**, **CH₃**, and **bpy-H** were able to be calculated by both achieving an S-shaped wave by increasing the scan rate as well as using FOWA. Comparable values were achieved from each method, although each has its limitations when applied to the Re-bpy system. A perfect S-shape could not be achieved for any complex, as the return wave never matched the forward wave in the CV. When phenol was added, a plateau current could not be achieved within the limits of our potentiostat. In both of these cases, the k_{cat} values obtained are most likely underreporting catalysis.

The use of FOWA also had its challenges. Catalysis occurs at an irreversible EC wave, thus the standard reduction potential for catalysis had to be estimated. We also note that the overlap between the 1st and 2nd reduction potentials with added phenol prevented the use of FOWA under these conditions. Finally, both methods are based on first knowing the catalytic mechanism, which is not always the case when first studying new catalytic systems. These methods also do not apply to poor catalytic systems, where deactivation pathways and slow catalysis are major factors that cannot be separated out from the pure catalytic response.

We do note the need for more standard and rigorous approaches to reporting catalysis. The values determined in this work were difficult to compare to previously reported rate constants for Re-bpy complexes due to the variety of methods used and values reported. The k_{cat} equivalent value determined by stopped-flow UV-vis spectroscopy for $[Re(tBu\text{-}bpy)(CO)_3]^-$ is 2,800 s^{-1}, which is 4 times larger than the value determined in this work (526 s^{-1} using the plateau current and 406 s^{-1} using FOWA with no added acid). Our rate constants are however larger than those reported previously by CV (131 s^{-1}), where S-shaped currents had not been achieved to determine k_{cat}.[11] More rigorous tandem comparisons between spectroscopic studies and CV are needed to verify the validity of either CV approach to determining k_{cat} for the Re-bpy system.

Catalytic Tafel plots can be used to help benchmark molecular catalysts based on the relationship between their overpotential and TOF_{max}. In Figure 3.10 and Table 3.4, molecular CO_2 reduction electrocatalysts are compared, for the cases where the highest TOF$_{max}$ was achieved with the addition of a Brønsted acid while maintaining selectivity for CO production.[33, 55-57] Overall, **bpy-H** with 1 M PhOH has the lowest overpotential, while FeTPP (and derivatives thereof)[37, 39] still have the highest logTOF for molecular CO$_2$ reduction electrocatalysts.

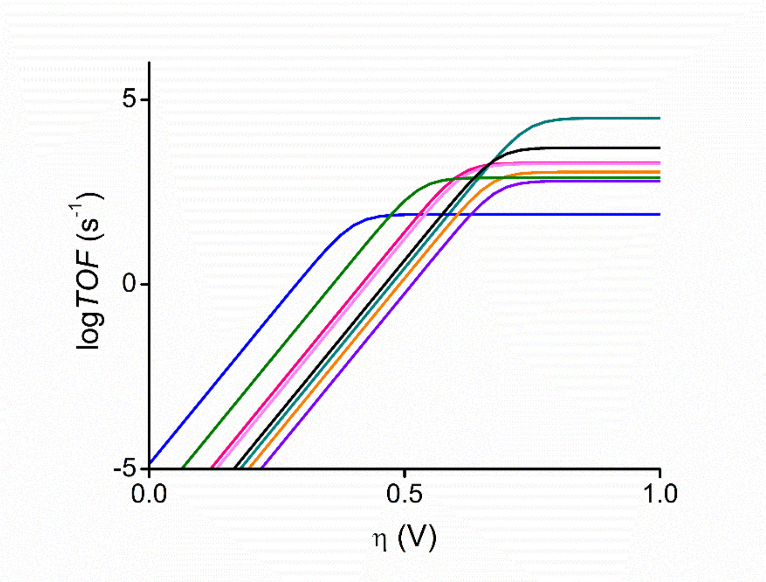

Figure 3.10 Catalytic Tafel plot comparing catalysts in this work with 1M PhOH with other molecular CO$_2$ electrocatalysts under similar conditions (Table 3.4).

Table 3.4 Complexes and values used for the catalytic Tafel plot in Figure 3.10.

Complex	**Color**	**Conditions**	**η (V)[a]**	**logTOF**
Re(OCH$_3$-bpy)(CO)$_3$Cl	pink	CH$_3$CN, 1 M PhOH	0.61	3.3
Re(tBu-bpy)(CO)$_3$Cl	gold	CH$_3$CN, 1 M PhOH	0.67	2.7
Re(CH$_3$-bpy)(CO)$_3$Cl	light pink	CH$_3$CN, 1 M PhOH	0.62	3.3
Re(bpy)(CO)$_3$Cl	green	CH$_3$CN, 1 M PhOH	0.53	2.9
[Mn(mes-bpy)(CO)$_3$(CH$_3$CN)](OTf)[c]	black	CH$_3$CN, 1.4 M TFE	0.68	3.7
FeTPP[d]	cyan	DMF, 3 M PhOH	0.76	4.5
Ni(cyclam)[e]	blue	1:4 H$_2$O:CH$_3$CN	0.58	1.9

[a] Overpotential from E° for CO$_2$ reduction with added Brønsted acid, –1.36 V vs. Fc$^{+/0}$.[39] [b] Ref. 32. [c] Ref 55. [d] Ref. 56. [e] Ref. 57.

3.4 Conclusions

A systematic study of the effect of labile ligand, 4,4′-bpy substituent, and Brønsted acid was conducted to determine the effects of each variable. The labile ligands moved the reduction potentials of Re(*t*Bu-bpy) more positive (py > CH_3CN > Br >Cl), but did not affect the overpotential or activity of catalysis. The 4,4′-substituents affected both overpotential and activity for catalysis, with **bpy-H** having the lowest overpotential and **CH_3** with the highest $TOF_{max,}$ while electron withdrawing substituents (CN and CF_3) deactivated the catalyst. The addition of Brønsted acids decreased the overpotential for catalysis by 200 mV, where PhOH and TFE did not affect selectivity for CO production while AcOH changed selectivity towards H_2. The addition of 1 M PhOH to the complexes with electron donating substituents (OCH_3, CH_3, and *t*Bu), increased TOF_{max} by twofold and changed the mechanism to “proton first”, further demonstrating the influence of available protons during catalysis.

Utilizing more rigorous approaches to determine catalytic rate constants from CV allows for a more accurate and direct comparison of Re-bpy based complexes to other molecular CO_2 reduction electrocatalysts. Both FOWA and use of S-shaped catalytic waves had not been previously utilized for Re-bpy, and the results show increased rates over previous CV studies. The effects of acid with Re-bpy catalysts with electron donating substituents had not been investigated previously, and it was found that all three electron donating groups had increased TOF_{max} over **bpy-H**.

This study highlights the importance in considering the effects on the electronic communication throughout a molecule when making structural changes to a molecular electrocatalyst. The ease of transfer of electron density between the ligand and mental center is of paramount importance, which should be the first factor considered with modifying or designing multi-electron catalysts. The interplay between the overpotential and the activity is also a focal point, where changes that increase activity often increase overpotential. These fundamental principles should be considered in the design of more effective electrocatalysts for CO_2 reduction, which are critical in helping to mitigate the negative effects of climate change due to anthropogenic CO_2 emissions.

3.5 Experimental

General Experimental Considerations. Solvents were obtained from Fisher Scientific and were degassed with argon, dried over alumina, and dispensed by a custom made solvent dispensing system. Reagents were obtained from commercially available sources and used as received: pentacarbonylchlororhenium(I) (Acros), 4,4′-dicyano-2,2′-bipyridine (Carbosynth), 4,4′-di-tert-butyl-2,2′-bipyridine (Sigma Aldrich), 4,4′-dimethoxy-2,2′-bipyridine and 2,2′-bipyridyl (Aldrich), 4,4′-dimethyl-2,2′-bipyridine (Alfa Aesar), phenol (Sigma Aldrich, >99% unstabilized), and 2,2,2-trifluoroethanol (Alfa Aesar, 99+%). Tetrabutylammonium hexafluorophosphate ($TBAPF_6$, Aldrich, 98%) was recrystallized twice from methanol and dried at 90°C overnight before use in electrochemistry experiments. Acetic acid (Acros 99.5%) was stored over 3Å sieves and degassed prior to use. Complexes were synthesized according to literature procedure: Re(4,4′-R-2,2′-bipyridine)$(CO)_3$Cl (R = OCH_3, *t*Bu, CH_3, and H,[11] CF_3,[36] CN[22]), Re(4,4′-R-2,2′-bipyridine)$(CO)_3$L (L = Br, MeCN(OTf) and Py(OTf)[16]). Identity and purity was confirmed by FT-IR (Thermo Scientific Nicolet 6700) and NMR (Varian Mercury 400).

Cyclic Voltammetry. Electrochemical experiments were performed on a BASi Epsilon potentiostat. Experiments were typically run in 0.1 M $TBAPF_6$ in 5 mL of MeCN with 1 mM catalyst. Ferrocene was used as an internal standard (~1 mM) for all scans. A 20 mL scintillation vial with a custom fitted top was used for all CV and DPV experiments, utilizing a 3 mm diameter glassy carbon working electrode and bare Pt wire counter electrode. A Ag/AgCl reference electrode was used and separated from solution in by a glass tube filled with 0.1 M $TBAPF_6$ solution in MeCN fitted with a CoralPor tip. The platinum wire was flame treated with a butane torch prior to use. The glassy carbon working electrode was polished with 15, 3, and 1 micron diamond paste successively, thoroughly rinsed with methanol and dried under a stream of nitrogen prior to experiments and polished with 1 micron diamond polishing paste between scans. To minimize the amount of adventitious water in our set up and prevent solvent loss via sparging the solution, Ar and “bone dry” CO_2 gas were first run through their own Drierite columns and secondly through a sealed vial of dry MeCN filled with 3Å sieves. An oven-dried cannula was then used to transfer the MeCN saturated dry gas to the electrochemical set-up. Electrochemical solutions were sparged for at least 5 minutes prior to the start of data collection, and were kept under a blanket of the gas during measurements. Ohmic drop of the cell was corrected for by using the potentiostat's iR-compensation tool, correcting for 80-90% of the measured resistance. This resulted in a ferrocene peak splitting typically between 61-67 mV. Differential pulse voltammetry was scanned from positive to negative potentials with a step of 4 mV, pulse width 50 ms, pulse period of 200 ms, pulse amplitude of 50 mV, sample period of 1 line period to result in a scan rate of 20 mV/s.

Controlled Potential Electrolysis. Controlled potential electrolysis (CPE) experiments were carried out in a 60 mL Gamry five-neck cell equipped with three Ace-thread ports to hold the electrodes and two joints capable of being sealed by septa for gas sparging. All joints were sealed with electrical tape and threaded ports were additionally sealed with clay to prevent leakage of gaseous products. The setup included a glassy carbon rod working electrode, platinum wire counter electrode (separated from solution by a porous glass frit), and a Ag/AgCl reference electrode (BASi, separated from solution by a glass sheath filled with 0.1 M $TBAPF_6$ in CH_3CN and capped with a CoralPor tip). Experimental conditions included 30 mL of dry CH_3CN with 0.1 M $TBAPF_6$, 1 mM complex and the appropriate amount of acid. Solutions were sparged with dry Ar or CO_2 (dried via method described above) for 10 minutes prior to electrolysis. During the experiment the solution was constantly stirred and wrapped in aluminum foil to protect from light. Gas analysis were performed using 1 mL sample injections on a Hewlett-Packard 7890A Series gas chromatograph with two molsieve columns (30m × 0.53mm i.d. × 25μm film). The 1 mL injection was split between two columns, one with N_2 as the carrier gas and one with He (g) to quantify both H_2

and CO simultaneously in each run. The amount of CO and H_2 gas produced was quantified by utilizing experimentally recorded calibration curves.

3.6 Acknowledgements

This chapter, in part, is currently being prepared for submission for publication of the material, entitled "Kinetic and Mechanistic Effects of Substituent, Labile Ligand, and Brønsted Acid on Electrocatalytic CO_2 Reduction by Re(bpy) Complexes" by Melissa L. Clark, Martina Lessio, Po Ling Cheung, Emily A. Carter, and Clifford P. Kubiak. The dissertation author is the primary author of this manuscript.

This work was supported by the Air Force Office of Scientific Research through the MURI program under AFOSR Award No. FA9550-10-1-0572. Dr. Mark Reineke, Dr. Matthew D. Sampson, Prof. Cyrille Costentin, Prof. Charles Machan, and Dr. Jonathan M. Smieja are acknowledged for valuable discussions and assistance.

3.7 References

(1) Alberico, E.; Nielsen, M., *Chem. Commun.* **2015**, *51*, 6714.

(2) Costentin, C.; Robert, M.; Savéant, J.-M.; Tatin, A., *Proc. Nat. Acad. Sci. USA* **2015**, *112*, 6882.

(3) Aresta, M.; Dibenedetto, A.; Quaranta, E., One- and Multi-electron Pathways for the Reduction of CO_2 into C1 and C1+ Energy-Richer Molecules: Some Thermodynamic and Kinetic Facts. In *Reaction Mechanisms in Carbon Dioxide Conversion*, 2016; 311-345.

(4) Grice, K. A., *Coord. Chem. Rev.* **2017**, *336*, 78.

(5) Wang, W. H.; Himeda, Y.; Muckerman, J. T.; Manbeck, G. F.; Fujita, E., *Chem. Rev.* **2015**.

(6) Porosoff, M. D.; Yan, B.; Chen, J. G., *Energy Environ. Sci.* **2015**.

(7) Qiao, J.; Liu, Y.; Hong, F.; Zhang, J., *Chem. Soc. Rev.* **2014**, *43*, 631.

(8) Windle, C. D.; Perutz, R. N., *Coord. Chem. Rev.* **2012**, *256*, 2562.

(9) Benson, E. E.; Kubiak, C. P.; Sathrum, A. J.; Smieja, J. M., *Chem. Soc. Rev.* **2009**, *38*, 89.

(10) Dry, M. E., *Catal. Today* **2002**, *71*, 227.

(11) Smieja, J. M.; Kubiak, C. P., *Inorg. Chem.* **2010**, *49*, 9283.

(12) Grice, K. A.; Kubiak, C. P., Chapter five - Recent studies of rhenium and manganese bipyridine carbonyl catalysts for the electrochemical reduction of CO_2. In *Advances in Inorganic Chemistry*, Michele, A.; Rudi van, E., Eds. Academic Press: 2014; Vol. 66, 163-188.

(13) Hawecker, J.; Lehn, J.-M.; Ziessel, R., *J. Chem. Soc., Chem. Commun.* **1984**, 328.

(14) Hawecker, J.; Lehn, J.-M.; Ziessel, R., *Helvetica Chimica Acta* **1986**, *69*, 1990.

(15) Elgrishi, N.; Chambers, M. B.; Wang, X.; Fontecave, M., *Chem. Soc. Rev.* **2017**, *46*, 761.

(16) Smieja, J. M.; Benson, E. E.; Kumar, B.; Grice, K. A.; Seu, C. S.; Miller, A. J.; Mayer, J. M.; Kubiak, C. P., *Proc. Nat. Acad. Sci. USA* **2012**, *109*, 15646.

(17) Hawecker, J.; Lehn, J.-M.; Ziessel, R., *J. Chem. Soc., Chem. Commun.* **1983**, 536.

(18) Agarwal, J.; Fujita, E.; Schaefer, H. F., 3rd; Muckerman, J. T., *J. Am. Chem. Soc.* **2012**, *134*, 5180.

(19) Kurz, P.; Probst, B.; Spingler, B.; Alberto, R., *Eur. J. Inorg. Chem.* **2006**, *2006*, 2966.

(20) Cabrera, C. R.; Abruña, H. D., *J. Electroanal. Chem.* **1986**, *209*, 101.

(21) O'Toole, T. R.; Sullivan, B. P.; Bruce, M. R. M.; Margerum, L. D.; Murray, R. W.; Meyer, T. J., *J. Electroanal. Chem.* **1989**, *259*, 217.

(22) Clark, M. L.; Rudshteyn, B.; Ge, A.; Chabolla, S. A.; Machan, C. W.; Psciuk, B. T.; Song, J.; Canzi, G.; Lian, T.; Batista, V. S.; Kubiak, C. P., *J. Phys. Chem. C* **2016**, *120*, 1657.

(23) Anfuso, C. L.; Xiao, D. Q.; Ricks, A. M.; Negre, C. F. A.; Batista, V. S.; Lian, T. Q., *J. Phys. Chem. C* **2012**, *116*, 24107.

(24) Machan, C. W.; Yin, J.; Chabolla, S. A.; Gilson, M. K.; Kubiak, C. P., *J. Am. Chem. Soc.* **2016**, *138*, 8184.

(25) Bligaard, T.; Bullock, R. M.; Campbell, C. T.; Chen, J. G.; Gates, B. C.; Gorte, R. J.; Jones, C. W.; Jones, W. D.; Kitchin, J. R.; Scott, S. L., *ACS Catal.* **2016**, *6*, 2590.

(26) Costentin, C.; Drouet, S.; Robert, M.; Savéant, J.-M., *J. Am. Chem. Soc.* **2012**, *134*, 11235.

(27) Costentin, C.; Drouet, S.; Robert, M.; Savéant, J.-M., *J. Am. Chem. Soc.* **2012**, *134*, 19949.

(28) Rountree, E. S.; McCarthy, B. D.; Eisenhart, T. T.; Dempsey, J. L., *Inorg. Chem.* **2014**, *53*, 9983.

(29) Costentin, C.; Drouet, S.; Robert, M.; Saveant, J. M., *Science* **2012**, *338*, 90.

(30) Wasylenko, D. J.; Rodriguez, C.; Pegis, M. L.; Mayer, J. M., *J. Am. Chem. Soc.* **2014**, *136*, 12544.

(31) Wong, K.-Y.; Chung, W.-H.; Lau, C.-P., *J. Electroanal. Chem.* **1998**, *453*, 161.

(32) Hansch, C.; Leo, A.; Taft, R. W., *Chem. Rev.* **1991**, *91*, 165.

(33) Smieja, J. M.; Sampson, M. D.; Grice, K. A.; Benson, E. E.; Froehlich, J. D.; Kubiak, C. P., *Inorg. Chem.* **2013**, *52*, 2484.

(34) Johnson, F. P. A.; George, M. W.; Hartl, F.; Turner, J. J., *Organometallics* **1996**, *15*, 3374.

(35) Machan, C. W.; Sampson, M. D.; Chabolla, S. A.; Dang, T.; Kubiak, C. P., *Organometallics* **2014**, *33*, 4550.

(36) Benson, E. E.; Grice, K. A.; Smieja, J. M.; Kubiak, C. P., *Polyhedron* **2013**, *58*, 229.

(37) Azcarate, I.; Costentin, C.; Robert, M.; Savéant, J.-M., *J. Phys. Chem. C* **2016**, *120*, 28951.

(38) Appel, A. M.; Helm, M. L., *ACS Catal.* **2014**, *4*, 630.

(39) Azcarate, I.; Costentin, C.; Robert, M.; Savéant, J.-M., *J. Am. Chem. Soc.* **2016**, *138*, 16639.

(40) Matheu, R.; Neudeck, S.; Meyer, F.; Sala, X.; Llobet, A., *ChemSusChem* **2016**, *9*, 3361.

(41) McCarthy, B. D.; Martin, D. J.; Rountree, E. S.; Ullman, A. C.; Dempsey, J. L., *Inorg. Chem.* **2014**, *53*, 8350.

(42) Ngo, K. T.; McKinnon, M.; Mahanti, B.; Narayanan, R.; Grills, D. C.; Ertem, M. Z.; Rochford, J., *J. Am. Chem. Soc.* **2017**, *139*, 2604.

(43) Lam, Y. C.; Nielsen, R. J.; Gray, H. B.; Goddard, W. A., *ACS Catal.* **2015**, *5*, 2521.

(44) Riplinger, C.; Carter, E. A., *ACS Catal.* **2015**, *5*, 900.

(45) Keith, J. A.; Grice, K. A.; Kubiak, C. P.; Carter, E. A., *J. Am. Chem. Soc.* **2013**, *135*, 15823.

(46) Sampson, M. D.; Froehlich, J. D.; Smieja, J. M.; Benson, E. E.; Sharp, I. D.; Kubiak, C. P., *Energy Environ. Sci.* **2013**, *6*, 3748.

(47) Benson, E. E.; Sampson, M. D.; Grice, K. A.; Smieja, J. M.; Froehlich, J. D.; Friebel, D.; Keith, J. A.; Carter, E. A.; Nilsson, A.; Kubiak, C. P., *Angew. Chem. Intl. Ed.* **2013**, *52*, 4841.

(48) Christensen, P.; Hamnett, A.; Muir, A. V. G.; Timney, J. A., *J. Chem. Soc., Dalton Trans.* **1992**, 1455.

(49) Takeda, H.; Ishitani, O., *Coord. Chem. Rev.* **2010**, *254*, 346.

(50) Hayashi, Y.; Kita, S.; Brunschwig, B. S.; Fujita, E., *J. Am. Chem. Soc.* **2003**, *125*, 11976.

(51) Machan, C. W.; Chabolla, S. A.; Yin, J.; Gilson, M. K.; Tezcan, F. A.; Kubiak, C. P., *J. Am. Chem. Soc.* **2014**, *136*, 14598.

(52) Manbeck, G. F.; Muckerman, J. T.; Szalda, D. J.; Himeda, Y.; Fujita, E., *J Phys Chem B* **2015**, *119*, 7457.

(53) Costentin, C.; Robert, M.; Saveant, J. M., *Acc. Chem. Res.* **2015**.

(54) Riplinger, C.; Sampson, M. D.; Ritzmann, A. M.; Kubiak, C. P.; Carter, E. A., *J. Am. Chem. Soc.* **2014**, *136*, 16285.

(55) Sampson, M. D.; Nguyen, A. D.; Grice, K. A.; Moore, C. E.; Rheingold, A. L.; Kubiak, C. P., *J. Am. Chem. Soc.* **2014**, *136*, 5460.

(56) Costentin, C.; Passard, G.; Robert, M.; Saveant, J. M., *Proc. Nat. Acad. Sci. USA* **2014**, *111*, 14990.

(57) Costentin, C.; Robert, M.; Savéant, J.-M., *Chem. Soc. Rev.* **2013**, *42*, 2423.

(58) Costentin, C.; Savéant, J.-M., *ChemElectroChem* **2014**, *1*, 1226.

3.8 Appendix

Table 3.5 Reduction Potentials vs. $Fc^{+/0}$ (V) for each 4,4′-substitued complex under Ar corresponding to Figure 3.2.

Substituent	1st Reduction	2nd Reduction	3rd Reduction
OCH_3	–1.90	–2.21	–2.83
***t*Bu**	–1.86	–2.17	–2.92
CH_3	–1.89	–2.18	–2.91
H	–1.78	–2.16	–2.90
CF_3	–1.34	–1.79	–2.59
CN	–1.19	–1.60	–2.41

Table 3.6 Reduction Potentials vs. $Fc^{+/0}$ (V) for each labile ligand substituted complex under Ar corresponding to Figure 3.3.

Labile Ligand	1st Reduction	2nd Reduction	3rd Reduction
Br	–1.86	–2.19	–2.98
Cl	–1.86	–2.32	–2.92
CH_3CN	–1.73	–2.11	–2.97
Pyridine	–1.68	–1.94	–3.11

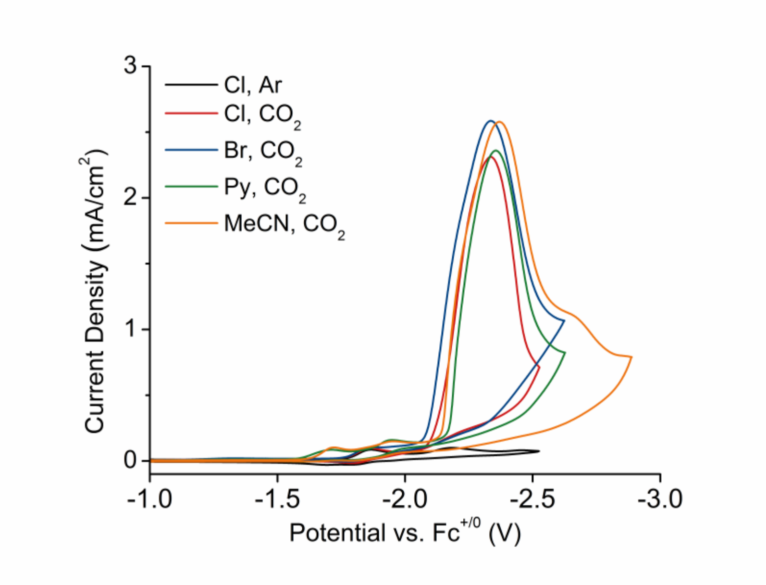

Figure 3.11 CVs under CO_2 atmosphere, showing that the labile ligand (L) does not affect the catalytic current response of Re(tBu-bpy)$(CO)_3$L. All voltammograms recorded in 0.1M $TBAPF_6$ CH_3CN solution with 1 mM complex at 0.1 V/s.

Table 3.7 Comparison of the reduction potentials (V vs. Fc$^{+/0}$) and catalytic descriptors for labile ligand complexes Re(tBu-bpy)$(CO)_3$L corresponding to Figure 3.10.

Labile Ligand	**Br**	**Cl**	**Py**	**ACN**
$E_{cat/2}$	–2.17	–2.20	–2.22	–2.20
$E_{cat,onset}$	–2.03	–2.03	–2.08	–2.06
i_{cat}/i_p	31.7	29.0	24.6	28.6

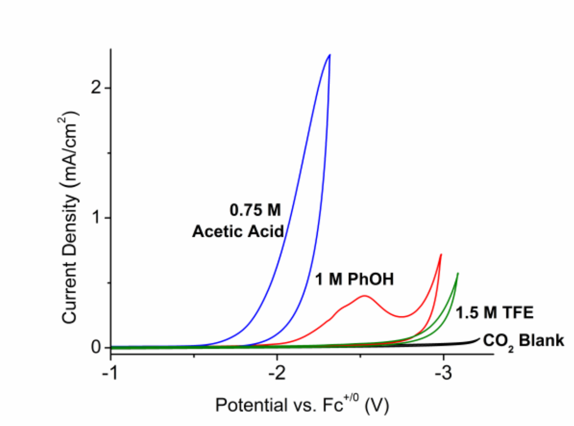

Figure 3.12 CVs under CO_2 atmosphere, showing solvent window for each acid tested with ***t*Bu-Cl**. All voltammograms recorded in 0.1M $TBAPF_6$ CH_3CN solution with 1 mM complex at 0.1 V/s.

Table 3.8 Comparison of the activity of Re(*t*Bu-bpy)$(CO)_3Cl$ (***t*Bu-Cl**) with different acids under CO_2.

Acid	**None**	**TFE**	**PhOH**	**Acetic**
Concentration (M)	N/A	1.5 M	1.0 M	0.75 M
E_{cat} (V vs. Fc$^{+/0}$)	–2.32	–2.15	–2.11	–2.16
%FE	100%CO	102%CO	100%CO	112%H_2
i_{cat}/i_p (0.1 V/s)	29.0	29.0	33.4	29.0
k_{cat} (SRD, s^{-1})	526	800	1026	4378

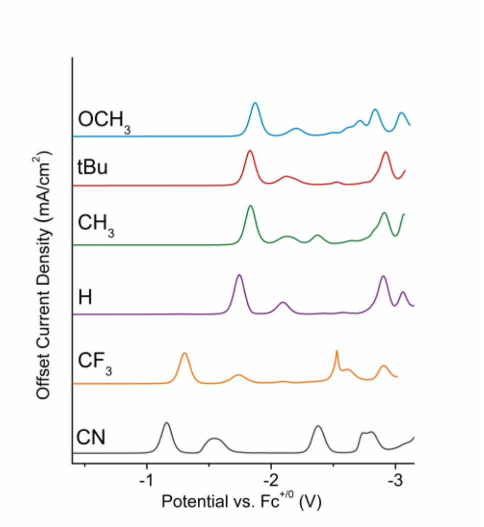

Figure 3.13 Differential pulse voltammograms (DPV) of the six 4,4′-substituted complexes.

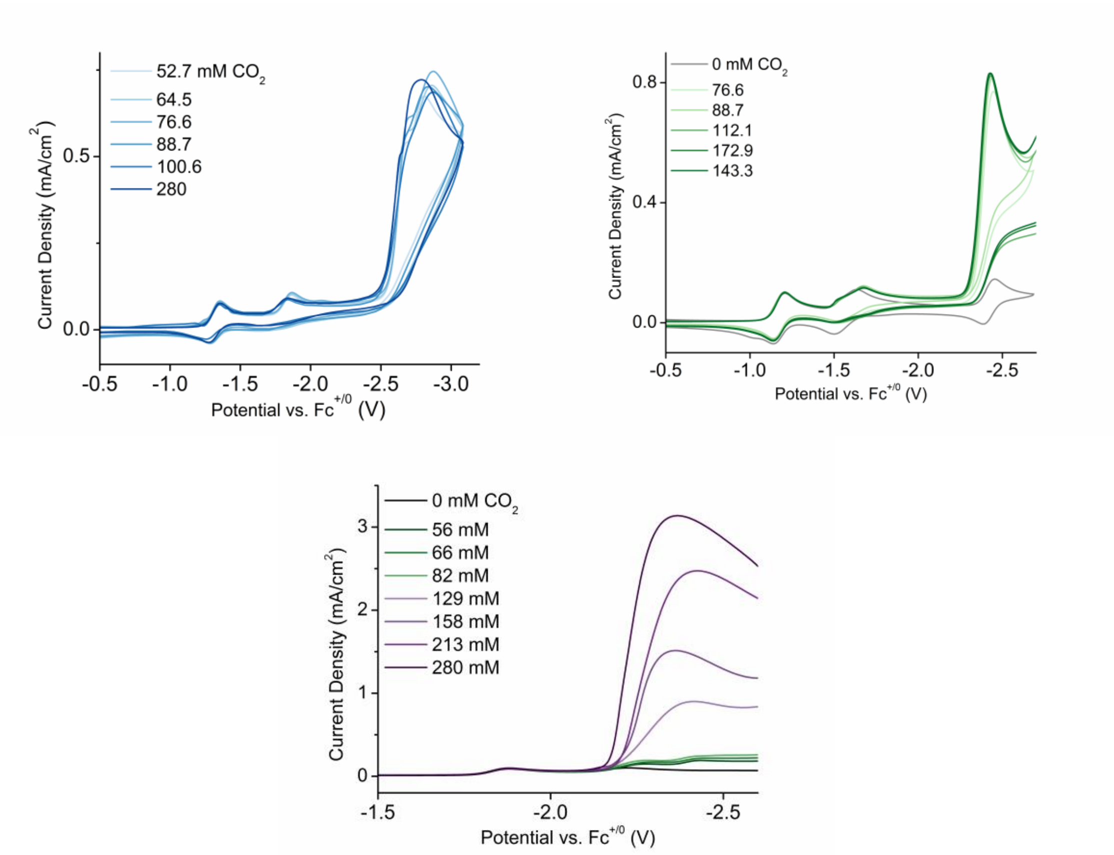

Figure 3.14 CV [CO_2] Dependence Studies for **CF_3** (left), **CN** (right) and ***t*Bu-Cl** (bottom). Return wave of *t*Bu-Cl is removed for clarity.

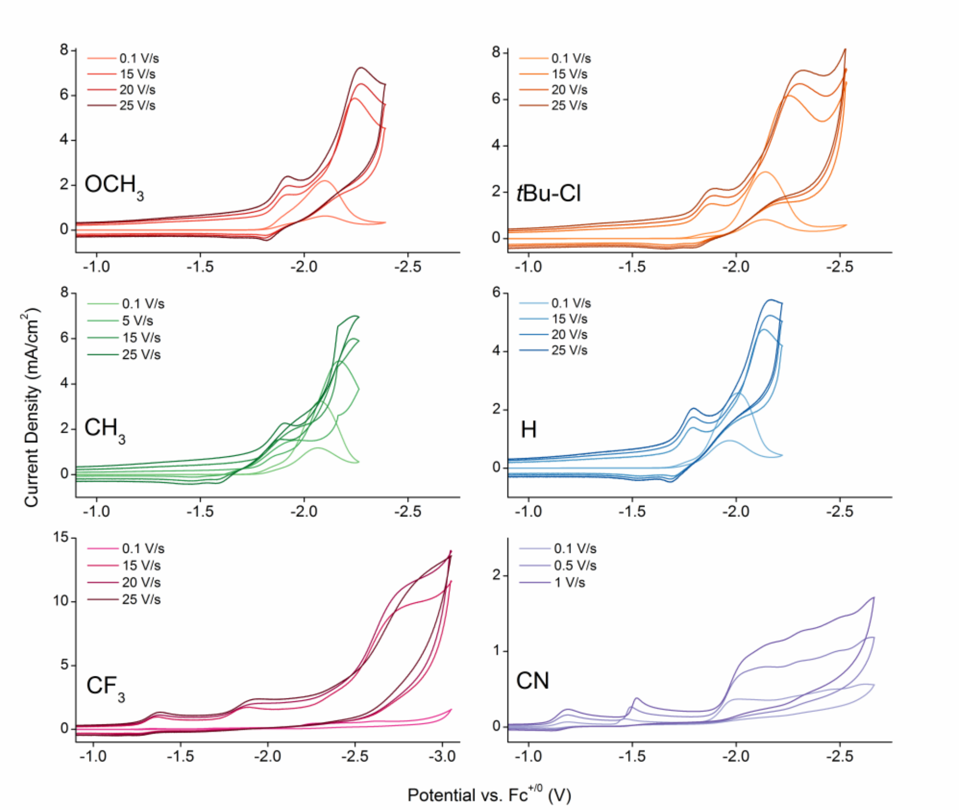

Figure 3.15 Scan rate dependence CVs for the 6 substituted Re-bpy complexes with 1 M PhOH added. Scans at 25 V/s were used to estimate k_{cat}.

Foot of the Wave Analysis (FOWA). FOWA was conducted using previously reported methods.[30, 58] The steps for using FOWA are as follows:

1. CV under Ar to determine:
    a. Peak current when no catalysis is occurring (i_p)
    b. Standard Reduction Potential for the catalytic wave (E_{cat})
        i. For **Re(tBu-bpy)** this is currently being taken from DPV
    c. Capacitive current (i_c)
2. Subtract i_c from the foot of the wave area of catalysis and from i_p
3. Plot i_{cat}/i_p vs. $1/(1+\exp[(F/RT)(E - E°_{cat}])$
4. Use the slope linear region of the graph to determine k_{obs} from $2.24(n_{cat})[(RT/Fv)(k_{cat})]^{1/2}$

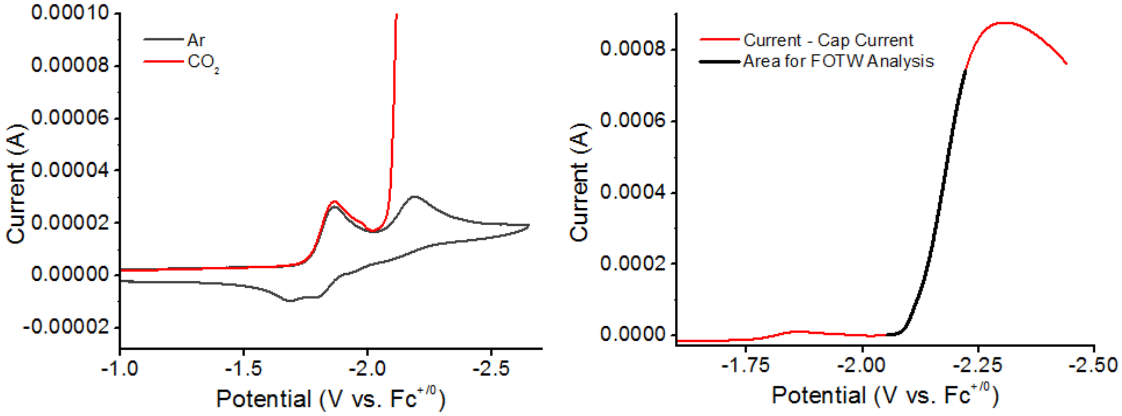

Figure 3.16 Left: Zoom in of the Ar CV of ***t*Bu-Cl** under Ar and CO_2. i_c = 1.73037x10^{-5} A and uncorrected peak current i_{p*} = 2.63614x10^{-5} A to give i_p = 9.0577x10^{-6} A. Right: Catalytic CO_2 forward scan of ***t*Bu-Cl** where i_c has been correction for. The region used for FOWA is shaded in black.

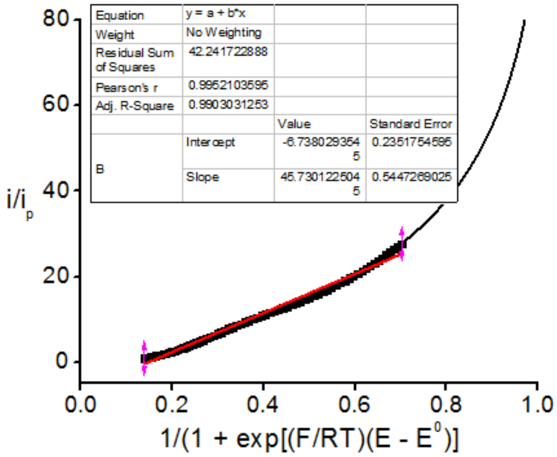

Equation	y = a + b*x		
Weight	No Weighting		
Residual Sum of Squares	42.241722888		
Pearson's r	0.9952103595		
Adj. R-Square	0.9903031253		
		Value	Standard Error
B	Intercept	-6.7380293545	0.2351754595
	Slope	45.7301225045	0.5447269025

Figure 3.17 FOWA plot using E^o_{cat} = –2.128 V vs. $Fc^{+/0}$ and the data points from Figure 3.15 starting at a i_{cat}/i_p of 1 (indicating the start of a catalytic response). The fit included data points only up to R^2 > 0.99.[30]

Chapter 4

Electrocatalytic CO_2 Reduction by $M(bpy\text{-}R)(CO)_4$ (M = Mo, W; R = H, *t*Bu) Complexes. Electrochemical, Spectroscopic, and Computational Studies and Comparison with Group 7 Catalysts

4.1 Introduction

The electrocatalytic reduction of CO_2 to value-added products and fuels is an area that has seen significant progress over the last several decades.[1-5] In particular, the use of homogeneous electrocatalysts is an attractive approach because they can be studied with a variety of techniques and modified via synthesis to affect reactivity. Previous work from our group focused on the study of complexes of the type M(bpy-R)$(CO)_3$X (M = Re, Mn; R = H, *t*Bu, etc.), based on the 2,2′-bipyridine system originally reported by Lehn[6]. Our more recent studies have shown that the 4,4′-di-*tert*-butyl-2,2′-bipyridine (bpy-*t*Bu) ligand is effective in increasing the activity of rhenium-based CO_2 reduction catalysts compared to the complexes of their 2,2′-bipyridine counterparts.[7-9]

Many homogeneous electrocatalysts for CO_2 reduction are based on expensive and rare metals such as Ru and Re. The cost of these metals makes it difficult to envision their use in large-scale deployment of systems for the synthesis of renewable chemicals and fuels from CO_2. Significant progress has been made towards developing electrocatalysts based on more abundant metals (for example: Mn,[10-11] Ni,[12] Fe,[13-14] and Cu[15]). Notably, there are very few reports of electrocatalytic CO_2 reduction catalysts based on complexes of group 6 metals (Cr, Mo, W),[16-17] even though this group contains the metals commonly found in the active sites of formate dehydrogenase (FDH) enzymes, which interconvert CO_2 and formate.[18] Aerobic bacteria also utilize molybdenum in the active site of carbon monoxide dehydrogenase (CODH) enzymes that are capable of oxidizing CO to CO_2.[19]

Stoichiometric reactions of dianionic Cr, Mo and W pentacarbonyl complexes with CO_2 lead to the formation of coordinated CO (Figure 4.1),[20] and there are other examples of stoichiometric CO_2 reduction at homogeneous group 6 metal complexes.[21,22,23] The coupling of CO_2 with olefins,[24] as well as hydrogenation of CO_2 to formic acid[25] or alkyl formates[26] have been observed at group 6 complexes. Given the precedent for CO_2 reactivity with group 6 complexes, we were curious to see if 2,2′-bipyridine complexes of these group 6 metals could be used as *electrocatalysts* for the reduction of CO_2 to produce value-added products such as CO.

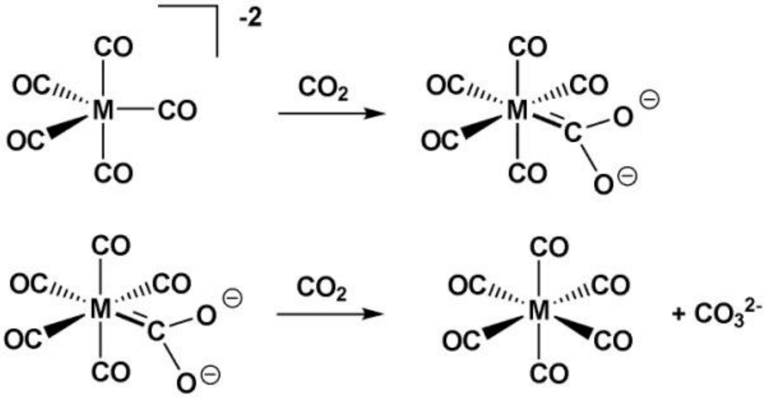

Figure 4.1 Reactions of group 6 dianions with CO_2 (M = Cr, Mo, W).

The spectroscopic, photochemical, and electrochemical properties of group 6 complexes of the type $M(L)(CO)_4$ (M = Cr, Mo, W, L = diimine ligand) are well known.[27] It has been proposed that the reduction of these metal complexes by two electrons leads to the loss of a CO ligand and generation of a five-coordinate $[M(L)(CO)_3]^{2-}$ species,[27,28] although spectroscopic characterization of such species has not been reported. We note the parallel between this postulated $[M(L)(CO)_3]^{2-}$ species and the dianionic $[M(CO)_5]^{2-}$ complexes reported by Cooper and co-workers to react with CO_2 to form $M(CO)_6$,[20] thus reducing CO_2 to CO. The group 6 dianionic $[M(bpy\text{-}R)(CO)_3]^{2-}$ complexes are also formally isoelectronic to the five-coordinate $[Re(bpy\text{-}t\text{Bu})(CO)_3]^-$ and $[Mn(bpy\text{-}t\text{Bu})(CO)_3]^-$ anions, the critical transition states that react with CO_2 in electrocatalytic reduction of CO_2 by Re(bpy-*t*Bu)$(CO)_3$X and Mn(bpy-*t*Bu)$(CO)_3$X.[11]

Herein we report electrochemical studies of the group 6 complexes M(bpy-R)$(CO)_4$ (R = H, M = Mo (**1**), W (**2**); R = *t*Bu, M = Mo (**3**), W(**4**)). We find that these complexes are electrocatalysts for the reduction of CO_2. Particular focus is placed on complex **4**, as it is isoelectronic with previously published highly active rhenium and manganese systems. NMR spectroscopy, X-ray crystallography, and Density Functional Theory (DFT) studies are also used to examine the species relevant to catalytic CO_2 reduction. The comparisons between the group 6 and group 7 complexes contribute to a clearer understanding of the specific characteristics that lead to more active CO_2 reduction catalysts.

4.2 Results and Discussion

Synthesis and Characterization. The known complexes M(bpy-R)$(CO)_4$ (M = W, Mo; R = H, *t*Bu, **1**–**4**, Figure 4.2), were synthesized similar to literature procedures.[29] These complexes were isolated as bright orange-red (M = Mo) or dark red (M = W) air-stable solids. Although complex **4** has been mentioned in the literature,[30-32] it's ^{1}H and ^{13}C NMR spectra had not been previously reported. The FT-IR spectra of these complexes display the standard four-signal pattern ($2A_1$, B_1, and B_2) in the ν(CO) region (1700–2100 cm^{-1}, Figure 4.9) for tetracarbonyl complexes of this type with values that are in agreement with the literature (Table 4.3).[33-34] The addition of the *t*Bu groups increases the solubility of **3** and **4** in organic solvents compared to **1** and **2**.

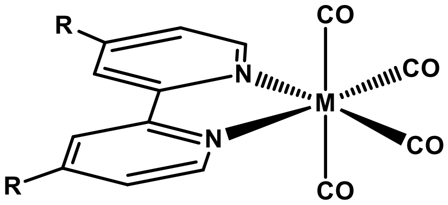

(**1**) M = Mo, R = H
(**2**) M = W, R = H
(**3**) M = Mo, R = *t*Bu
(**4**) M = W, R = *t*Bu

Figure 4.2 Complexes **1**–**4** studied in this work.

In order to compare with the reported X-ray structures of M(bpy)(CO)$_4$ (M = Mo (**1**)[35], W (**2**)[36-37]), X-ray quality crystals were grown of the *tert*-butyl derivatives M(bpy-*t*Bu)(CO)$_4$ (M = Mo (**3**), W (**4**); Figure 4.3) by vapor diffusion of pentane into concentrated toluene solutions of the complexes. The molecular geometries of **3** and **4** are similar to the corresponding complexes with the parent bipyridine ligand (**1** and **2**), with slightly shorter M–N bonds (Table 4.4), indicating slightly stronger donation from the *tert*-butyl ligand and slightly stronger back donation to the M–CO groups. This is also observed in the FT-IR data for complexes **1**–**4**, in which the ν(CO) frequencies are shifted to lower wavenumbers on the *t*Bu-substituted complexes compared to the parent complexes. The C–C bond lengths between the two pyridyl rings (C9–C10) for all of the complexes are consistent with a neutral bipyridine ligand.[38]

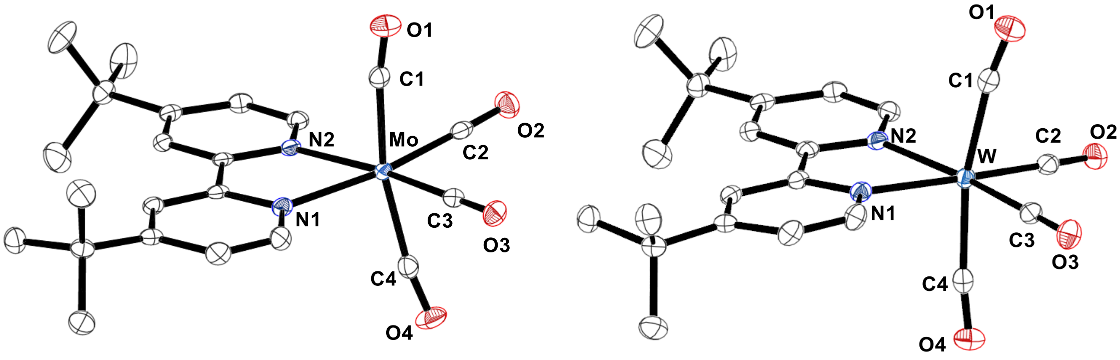

Figure 4.3 Molecular structures of **3** (left) and **4** (right), with ellipsoids shown at 50% probability and hydrogen atoms excluded for clarity. Selected bond lengths and angles are listed in Table 4.4.

A search of the Cambridge Crystallographic Database did not yield any other tetracarbonyl tungsten or molybdenum complexes with 4,4′-disubstituted bipyridine ligands.[39] However, a comparison of the structures of **1**–**4** with previously reported isoelectronic [Re(bpy-R)(CO)$_4$](OTf) complexes reveals interesting similarities and differences. The bending of the axial CO ligands away from the bipyridine ligands in complexes **1**–**4** (as seen in the M–C1–O1 and M–C4–O4 angles of *ca.* 171–172°) is a common feature of group 6 tetracarbonyl complexes, and has been explained in terms of back donation from a π* orbital on the bidentate diimine ligand.[40] This structural deviation of the metal carbonyls from linearity is also apparent in the structure of the d^6 [Re(bpy-R)(CO)$_4$](OTf) complexes (R = H, *t*Bu).[41-42] Notably, complex **4** has significantly longer C–O bond lengths compared to [Re(bpy-*t*Bu)(CO)$_4$](OTf), which is evidence of stronger back donation from the tungsten metal center. This is also reflected in the FT-IR spectra of **4** and the corresponding rhenium complex. They have similar patterns for the ν(CO) stretches in their FT-IR spectra, but the stretches for the tungsten complex **4** are 116–138 cm^{-1} lower in energy than the rhenium complex in acetonitrile.

Electrochemical Studies. The cyclic voltammograms of complexes **1**–**4** in acetonitrile are very similar, displaying one reversible reduction at ca. –1.6 V vs. SCE followed by an irreversible reduction at ca. –2.1 V vs. SCE (voltammogram for **1** shown in Figure 4.4, reduction potentials for **1**–**4** are listed in Table 4.1 and voltammograms of **2**–**4** Figure 4.10). This data is similar to previously reported electrochemistry for **1** and **2** that was obtained in THF,[43-44] acetonitrile (1st reduction only),[45] and dimethoxyethane.[46-47] The first reduction of **3** has also been reported in multiple solvents.[48] The first reduction of these complexes is primarily localized on the bipyridyl ligand, forming stable 19-electron $[M(bpy\text{-}R)(CO)_4]^{\bullet-}$ species that have been previously characterized for the parent bipyridine complexes **1** and **2** by FT-IR,[46] UV-Vis,[28] and EPR spectroscopies.[28, 49]

Table 4.1 Reduction potentials vs. SCE for complexes **1**–**4**. All complexes were studied under the same conditions as stated for **1**.

Complex	$E_{1/2}$ (V)	2nd (V)[a]
1	–1.58	–2.14
2	–1.49	–2.08
3	–1.66	–2.20
4	–1.58	–2.15

[a]Irreversible; reported as the location of the peak of the irreversible wave vs. SCE during the reductive sweep in the cyclic voltammogram at 100 mV/s.

When acetonitrile solutions containing complexes **1**–**4** are exposed to a CO_2 atmosphere, the first reduction in the cyclic voltammograms is similar to the reduction under inert atmosphere. However, at the second reduction potential, a current increase is observed (i_{cat}/i_p = 2.3, 3.4, 3.1, and 3.9 for **1**, **2**, **3**, and **4**, respectively, Figure 4.4), which is attributed to catalytic reduction of CO_2. These current enhancements occur at potentials that are similar to the peak potential of CO_2 reduction by Re(bpy-*t*Bu)$(CO)_3$Cl (–2.1 V vs SCE).[7] The i_{cat}/i_p and the corresponding turnover frequency (TOF, Table 4.2) show that the tungsten complexes are more active than the molybdenum complexes, and the *tert*-butyl groups enhance the activity for both metals. Complex **4** was selected for further study as it was the most active catalyst based on cyclic voltammetry (i_{cat}/i_p of 3.9), but more importantly because it is isoelectronic with the well-studied fac-Re(bpy-tBu)$(CO)_3$X species so that the most appropriate comparison can be made.

Scan-rate dependence studies for complex **4** (Figure 4.11) show that the second reduction remains irreversible even at high scan rates (ca. 10 V s^{-1}). The irreversibility of the second reduction indicates that a chemical reaction occurs following this reduction. This can be postulated as a loss of one CO ligand, although there is only brief mention of this in the literature, and full characterization for the dianions has not been previously reported.[28,27] The small oxidation wave observed at ca. –700 mV only appears after the second reduction is reached.

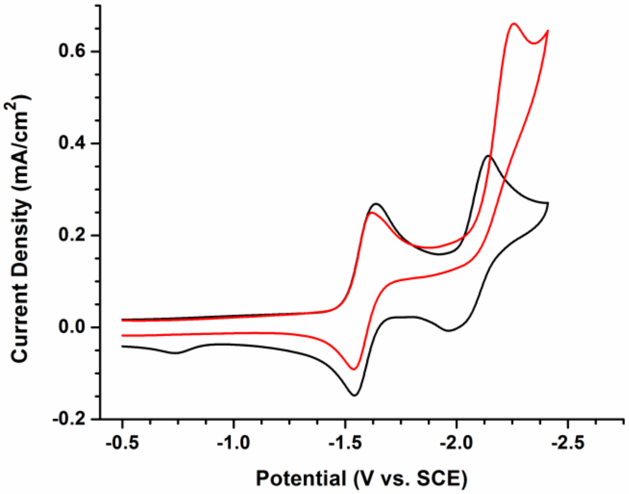

Figure 4.4 Representative cyclic voltammogram of **1** at a scan rate of 100 mV/s under N_2 (black line) and CO_2 (red). Conditions: 1 mm diameter glassy carbon working electrode, platinum wire counter electrode, Ag/AgCl reference, decamethylferrocene ($FeCp_2$*) internal reference, 1 mM 1, 0.1 M tetrabutylammonium hexafluorophosphate ($TBAPF_6$), room temperature. Complexes **2**, **3**, and **4** exhibit similar behavior.

Controlled Potential Electrolysis. In order to study the catalytic reduction of CO_2, controlled potential electrolysis experiments were carried out with complex **4**. Care was taken to separate the counter electrode from the solution with a glass tube packed with a plug of glass wool during bulk electrolysis, because it has been shown that electrochemical oxidation of group 6 $M(L)(CO)_4$ complexes leads to the liberation of CO.[34] Bulk electrochemical reduction at –2.3 V under a CO_2 atmosphere led to formation of CO with a 109 ± 7% faradaic efficiency, as detected by gas chromatography (Figure 4.12). Carbon monoxide was also observed by gas chromatography when the same experiment was performed under inert atmosphere, due to the loss of a carbonyl ligand that occurs after the second reduction. The current density under CO_2 initially decreased after the start of the bulk electrolysis but stabilized at 0.66 mA/cm^2, whereas under N_2 it stabilized at 0.44 mA/cm^2 (Figure 4.12). This verifies the catalytic activity observed in the cyclic voltammograms, and also indicates that the catalyst is highly selective for CO formation. There was no evidence of carbonate, formate, or other CO_2-derived products by NMR or FT-IR measurements of complex **4**, and therefore the reaction is likely of the form $CO_2 + 2e^- + 2H^+ \rightarrow CO + H_2O$, similar to the group 7 catalysts. The catalytic activity was observed to be stable over the course of several hours (Figure 4.13), indicating that the compound remains active over time. Hydrogen was observed only in small quantities (less than 3% faradaic efficiency).

Chemical Reduction and Characterization of the Reduced Species. Crystallographic characterization of the mono or di-reduced forms of M(bpy-R)$(CO)_4$ have not been reported, nor have the di-reduced species been characterized by spectroscopy. While the oxygen and proton sensitivity of these highly reduced forms makes isolation challenging, the anions and dianions of **2** and **4** were produced in yields of 40%–70% and characterized by FT-IR and NMR. After many attempts, crystal structures of the anion $[W(bpy)(CO)_4]^-$ (**5**) and dianion [W(bpy-*t*Bu)$(CO)_3]^{2-}$ (**6**) were obtained. Addition of 1 equivalent of KC_8 to a solution of **2** and 18-crown-6 in THF led to the formation of a dark orange solution of the new species **5**. Vapor diffusion of pentane into a solution of **5** in THF led to black-orange crystals suitable for X-ray diffraction. Consistent with analogous anionic complexes,[7-8, 11] the anionic tungsten complex crystallizes with the potassium cation enclosed in the crown ether, seen in Figure 4.5. The potassium is both associated with an axial carbonyl (K–O bond length of 2.813(3) Å) and a THF solvent molecule. The bond length alteration in the 2,2′-bipyridine ring of **5** is suggestive of substantial electron density on the ligand, supporting the assignment of the first electrochemical reduction as being ligand based.[50]

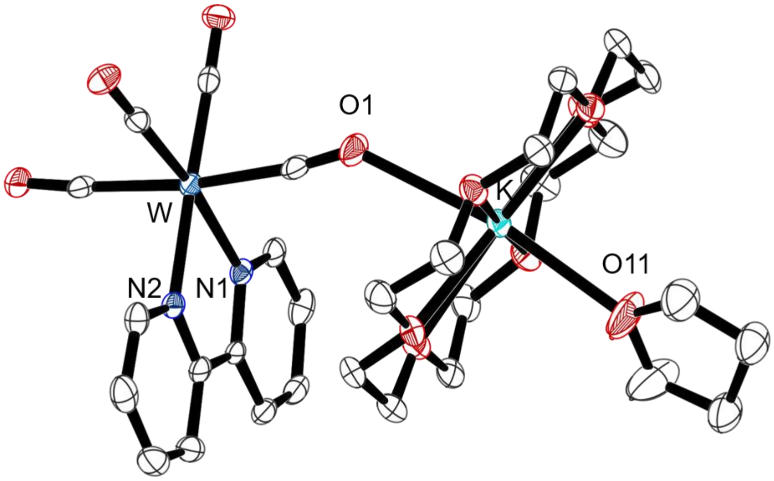

Figure 4.5 Molecular structure of [W(bpy)(CO)$_4$][K(18-crown-6)•THF] (**5**). Ellipsoids are shown at 50% probability. Hydrogen atoms are omitted for clarity.

Dianionic species **6** was formed by the addition of 2.2 equivalents of KC$_8$ to a THF solution of **4** in the presence of 18-crown-6. The ^{1}H NMR spectrum of the black-purple solution of complex **6** in THF-*d*$_8$ (Figure 4.16) showed signals for a diamagnetic compound, with bipyridine ligands that were significantly shifted upfield from the starting material (4.80, 6.60, and 8.47 ppm for **6** vs. 7.58, 8.40, and 9.10 ppm for **4**). This upfield shift in the C–H protons on the bipyridine ligand has also been observed in the [Al(bpy-H)$_2$]$^-$ anion, which has been assigned as possessing two (bpy-H)$^{2-}$ ligands.[51]

A diffracting crystal of **6** was obtained after multiple crystallization attempts. Although several issues exist with the structure, it was found to be the [W(bpy-

*t*Bu)$(CO)_3$][K(18-crown-6)$]_2$ species. The dianion crystallizes between two layers of the 18-crown-6 ligands, which display significant disorder (Figure 4.14). The C9–C10 distance in **6** is significantly shorter than the corresponding bond in **4** (1.483 Å). The C–O distances in the carbonyl ligands of **6** are also significantly longer than those in **4**.

The lengthening of the metal-carbonyl bonds in **5** and **6** due to the increased back bonding from the metal is consistent with the FT-IR spectra of these complexes. The carbonyl stretching frequencies of complex **4** shift to a lower frequency by roughly 30 cm^{-1} upon the first chemical reduction, and the subsequent reduction leads to the dianion **6**, which exhibits a band at 1837 cm^{-1} and a broad band at 1713 cm^{-1} as shown in Figure 4.6 (the IR spectra of **5** and of the dianion $[W(bpy)(CO)_3]^{2-}$ are shown in Figure 4.15). These ν(CO) bands are observed at much lower frequencies than [Re(bpy-*t*Bu)$(CO)_3]^-$ (1940 cm^{-1} and 1835 cm^{-1}) and Mn(bpy-*t*Bu)$(CO)_3]^-$ (1911 cm^{-1} and 1813 cm^{-1}) anions that are isoelectronic with **6**. This indicates that the anion **6** has much stronger back donation to the antibonding π* orbitals of the CO ligands than the corresponding Re or Mn monoanions with the same ligand sets.

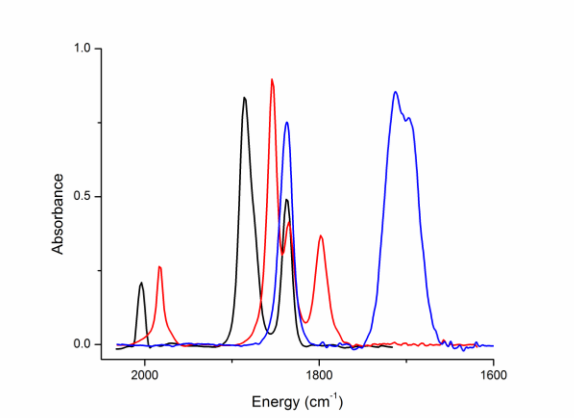

Figure 4.6 FT-IR spectra of the chemically reduced species of W(bpy-*t*Bu)(CO)$_4$ (**4**) in THF under N$_2$. The neutral species **4** (black) has ν(CO) stretches of 2004 cm^{-1}, 1886 cm^{-1}, and 1837 cm^{-1}. The chemically reduced anion (red) ν(CO) stretches are 1982 cm^{-1}, 1854 cm^{-1}, 1835 cm^{-1}, and 1798 cm^{-1}; the doubly reduced species **6** (blue) ν(CO) stretches are 1837 cm^{-1} and 1713 cm^{-1}.

DFT Calculations of Catalytically Relevant Complexes. In order to obtain a deeper insight into the species formed upon electrochemical reduction of **4**, the DFT-optimized structures of the reduced species obtained from **4** were calculated. Geometry optimized structures were obtained by using the X-ray coordinates of **4** and **6** as the initial inputs to obtain the structures of the neutral form (**A**) and the five-coordinate dianion (**D**). The geometry of the mono-reduced species [W(bpy-*t*Bu(CO)$_4$]$^{-1}$ (**B**) and the doubly-reduced species structure [W(bpy-*t*Bu)(CO)$_4$]$^{-2}$ (**C**) were then optimized from **A** (Figure 4.7). Frequency calculations were used to establish that the optimized structures were not intermediates. The crystal structure for **6** and the DFT-optimized structure of **D** are intermediate between a square pyramid and a trigonal bipyramid (τ_5 = 0.44 and 0.46, respectively)[52] (Figure 4.8). Pertinent bond distances for the calculated structures and coordinates for the optimized structures are included Table 4.7. The calculated v(CO) stretching frequencies for species **D** (1822, 1734, and 1724 cm^{-1}) agree well with the v(CO) band energies observed in IR for the reduced species **6** in THF (1837 cm^{-1} and a broad band at 1713 cm^{-1}). A comparison of the calculated and experimental v(CO) stretching frequencies for species **A**–**D** is included in Table 4.8). The central C–C bonds in the bipyridine ligands in the dianions **C** and **D** are significantly shortened compared to **A** and **B**, with C–C bond lengths of 1.390 and 1.398 Å for the central C–C bond in the bipyridine ligand in the octahedral (**C**) and five-coordinate (**D**) complexes. The bond lengths for **C** and **D** are shorter than the bond lengths in the neutral complex (1.463 and 1.481 Å for geometry optimization (**A**) and X-ray structure of **4**), and the monoanion (**B**) (1.423 Å). These results are consistent with our understanding of the system from the electrochemical and structural studies, indicating that the bipyridine accepts a significant amount of the electron density from both $1e^-$ reductions observed in the electrochemistry of **1**–**4**.

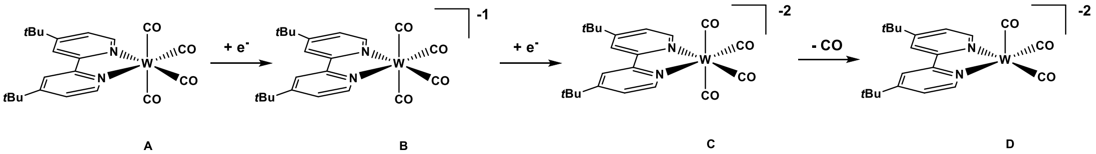

Figure 4.7 Complexes based on complex **4** that were studied using DFT calculations.

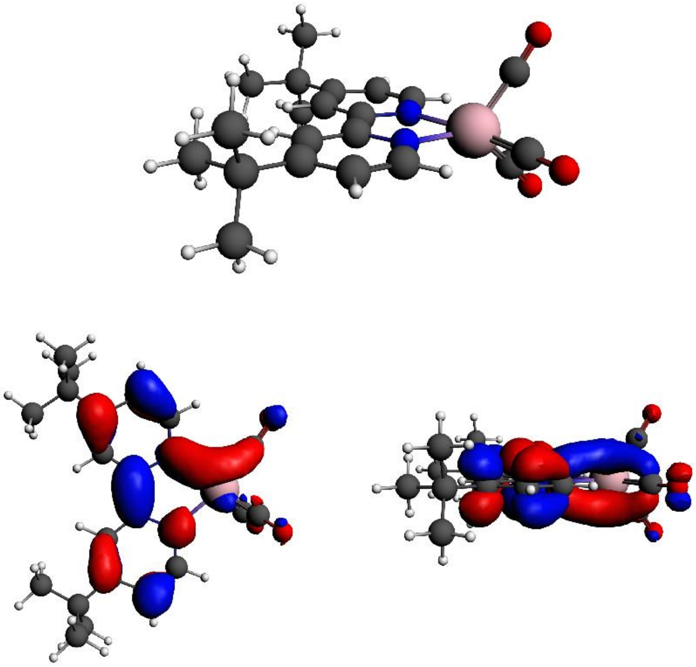

Figure 4.8 Ball and stick representation of the geometry optimized structure (top) and the DFT-calculated HOMO (bottom left: top view; right: side view) of the five-coordinate dianionic species **D**.

Examination of the calculated highest occupied molecular orbitals (HOMOs) and lowest unoccupied molecular orbitals (LUMOs) of complexes **A**–**D** provides further insights about these complexes. The calculated HOMO of the dianion **D** is delocalized over the bipyridine and somewhat over the tungsten center (Figure 4.8). In comparison, the LUMO, singly occupied molecular orbital (SOMO) and HOMO of **A**, **B**, and **C** are primarily localized on the bipyridine with some electron density on the CO ligands (see Appendix). The calculated HOMO for species **D** is qualitatively similar to the calculated HOMO for the [Re(bpy-*t*Bu)(CO)$_3$]$^{-1}$ anion, which is the reactive species in catalysis with Re(bpy-*t*Bu)(CO)$_3$X catalysts.[8] Calculations on a related species, [Mn(bpy-H)(CO)$_3$]$^{-1}$ also showed that the HOMO of this species is delocalized over the bipyridine ligand as well as the metal center.[53]

Comparison with Group 7 Catalysts. A comparison of the catalytic activities of **1**–**4** with analogous group 7 complexes is shown in Table 4.2. The group 6 species are similar in activity to $[Re(bpy\text{-}tBu)(CO)_3(CH_3CN)](OTf)$ and more active than the corresponding Mn species under the same conditions (Mn complexes do not exhibit catalysis without added protons). Upon the addition of a proton source, the group 7 catalysts greatly outperform the W and Mo species. The effect of adding a Brönsted acid could not be quantified for the group 6 species due to the negative potentials of the second reductions being too close to the direct reduction of the acids at the electrodes in the cyclic voltammetry experiments.

Table 4.2 Comparison of the catalytic activity of complexes **1**–**4** to relevant group 7 complexes.[11]

Complex	i_{cat}/i_p	TOF (s^{-1})[a]
$Mo(bpy)(CO)_4$ (**1**)	2.3	1.0
$W(bpy)(CO)_4$ (**2**)	3.4	2.2
$Mo(bpy\text{-}tBu)(CO)_4$ (**3**)	3.1	1.9
$W(bpy\text{-}tBu)(CO)_4$ (**4**)	3.9	2.9
$[Re(bpy\text{-}tBu)(CO)_3(CH_3CN)](OTf)$[b]	3.3	2.1
$Mn(bpy\text{-}tBu)(CO)_3Br$[b]	1.0	0.0
$[Re(bpy\text{-}tBu)(CO)_3(CH_3CN)](OTf)$[c]	54	570
$Mn(bpy\text{-}tBu)(CO)_3Br$[d]	42	340

[a]TOF for **1**–**4** obtained using method described by Smieja et al.[11] [b]Activity under similar conditions to those used for **1**–**4**. [c]1.4 M 2,2,2-trifluoroethanol (TFE) added. [d]1.6 M TFE added.

While the Mo and W complexes reported herein are not exceptional electrocatalysts for CO_2 reduction, their study is very valuable because it provides a framework in which to understand similar electrocatalysts, such as the group 7 species. Through comparisons of the structurally similar and isoelectronic group 6 M(bpy-R)$(CO)_4$ species and the group 7 M(bpy-R)$(CO)_3$X species, we can understand what characteristics lead to efficient and active catalysts.

The first electrochemical reduction of both the group 6 (**1**–**4**) and group 7 M(bpy-R)$(CO)_3$X (M = Re, Mn) electrocatalysts proceeds through reduction of the bipyridine ligand. In the rhenium system, ligand loss (dissociation of the chloride or other X ligand) subsequently occurs from $[Re(bpy\text{-}R)(CO)_3X]^-$ leading to a species that can be assigned as a Re(0) center and a neutral bipyridine ligand. Ultimately, a Re(0)–Re(0) dimer is formed, and characterization of the dimer gives clear indication that the reduction has occurred at the metal center.[54] For manganese, reduction of a Mn(bpy-R)$(CO)_3$X species leads to extremely rapid dimerization such that monomeric $[Mn(bpy\text{-}R)(CO)_3X]^-$ species have not been observed spectroscopically. In stark comparison, the group 6 complexes do not lose a ligand or dimerize upon reduction, but rather the axial carbonyl becomes somewhat more susceptible to substitution.[43] However, the electron density remains primarily over the bipyridine ligand, and the carbonyl ligand remains strongly coordinated enough that we were able to crystallize the $[W(bpy)(CO)_4]^-$ anion (complex **5**), wherein the bipyridine ligand is clearly reduced. Notably, reduction of a $[Re(bpy\text{-}R)(CO)_4]^+$ cation does not lead to an observable Re(bpy-R)$(CO)_4$ species,[42] indicating that the group 6 complexes bind CO more strongly than the group 7 complexes.

A second reduction in both the group 6 and the group 7 systems leads to a diamagnetic complex with five-coordinate geometry and a similar HOMO delocalized over the metal and the bipyridine. For the rhenium complexes, XANES data suggests that these species are best described as $M^0(bpy^{-1})$. The second reduction in the $Re(bpy\text{-}R)(CO)_3Cl$ systems is 300–400 mV more negative than the first, however the second reduction potentials of **1**–**4** are 540–590 mV more negative than their first reduction. This is similar to the separation observed between the 2,2′-bipyridine monoanion and dianion.[55] Thus it seems reasonable that they are described as $M^0(bpy^{-2})$ species, rather than $M^{-1}(bpy^{-1})$ or $M^{-2}(bpy^0)$ complexes. Further studies are needed to unambiguously assign these ground states.

These comparisons lead to two important conclusions about electrocatalysts for CO_2 reduction. The first is that having catalytically relevant electrons stored in both the bipyridine ligand and the metal center leads to a lower overpotential compared to having two electrons stored on the bipyridine ligand. The second conclusion about these electrocatalysts is that having a complex that strongly back-donates to CO is undesirable because it will hinder release of the product and slow overall catalysis, i.e. CO poisoning of the catalyst.

4.3 Conclusions

Electrochemical experiments on groups 6 complexes **1**–**4** $M(bpy\text{-}R)(CO)_4$ (R = H, M = Mo (**1**), W (**2**); R = *t*Bu, M = Mo (**3**), W (**4**)) have shown that these complexes are competent catalysts for CO_2 reduction through a two-electron reduction process to generate a diamagnetic dianionic complex. The reduced species have been studied using X-ray crystallography, IR spectroscopy and DFT calculations. These catalysts display stronger back donation to CO than group 7 catalysts, which may explain why they operate at slower rates. Future studies will include studying the stoichiometric reactions of the reduced species with CO_2 and H^+ sources, as well as attempting to elucidate the full catalytic cycle. The catalytic cycle of CO_2 reduction by $Re(bpy)(CO)_3Cl$ has recently been elucidated by computational methods, and similar study of group 6 catalysts would be very informative.[56] Complexes **1–4** are rare examples of group 6 electrocatalysts for CO_2 reduction and future work will focus on developing more efficient and selective catalysts based on these relatively abundant metals.

4.4 Experimental

Materials and Methods. Unless otherwise noted, all transformations and manipulations were performed under an atmosphere of N_2 or Ar using standard Schlenk and glovebox techniques. Acetonitrile, pentane, toluene, and tetrahydrofuran (THF) were dried on a custom solvent purification system and stored over 3Å molecular sieves. Complexes **1**, **2**, and **3** were synthesized according to literature methods and spectroscopic data matched literature values.[29, 57] Potassium graphite (KC_8) was synthesized according to literature procedures and stored in the glovebox freezer prior to use.[58] Tetrabutylammonium hexafluorophosphate ($TBAPF_6$) was recrystallized from methanol and dried under vacuum. All other reagents and solvents were purchased from commercial suppliers and used as received. FT-IR data was collected on a Thermo Nicolet 6700. ^1H and ^{13}C NMR spectra were collected on a Varian 400 MHz spectrometer or Bruker Avance III 300 MHz spectrometer equipped with a broad band probe. NMR data was referenced against residual solvent peaks and reported downfield of tetramethylsilane (δ = 0 ppm). Elemental analyses were performed by Midwest Microlab, LLC in Indianapolis, IN.

Synthesis of W(4,4′-di-*tert*-butyl-2,2′-bipyridine)(CO)$_4$ (4). A stirring 15 mL toluene solution of 4,4′-di-*tert*-butyl-2,2′-bipyridine (352 mg, 1.31 mmol) and W(CO)$_6$ (404 mg, 1.15 mmol) was refluxed for 17 h. The solution was filtered through a plug of basic alumina, which was rinsed 3 times with 30 mL dichloromethane. The combined solvent was removed under vacuum and the solid was collected on a filter and rinsed 3 times with 20 mL of pentane to yield a dark red solid (488 mg, 75.3% yield). ^{1}H NMR (400 MHz, CDCl$_3$): δ = 1.44 (s, 18H), 7.37 (dd, *J* = 2.2 Hz, *J* = 5.9 Hz, 2H), 8.07 (br d, *J* = 1.1 Hz, 2H), 9.09 (d, *J* = 5.9 Hz, 2H).^{1}H NMR (400 MHz, THF-*d*$_8$): δ = 1.45 (s, 18H), 7.58 (dd, *J* = 2.0 Hz, *J* = 6.0 Hz, 2H), 8.40 (br d, *J* = 2.2 Hz, 2H), 9.10 (d, *J* = 5.9 Hz, 2H).^{13}C{^{1}H} NMR (100.6 MHz, CDCl$_3$): 30.52, 35.56, 119.09, 123.44, 152.68, 155.84, 162.05, 201.53, 215.85.^{13}C{^{1}H} NMR (100.6 MHz, THF-*d*$_8$): 30.25, 36.01, 120.54, 124.22, 153.14, 156.72, 162.93, 202.39, 215.40.Anal Calc. for $C_{22}H_{24}WN_2O_4$: C, 46.81; H, 4.29; H, 4.97. Found: C, 46.78; H, 4.44; N, 4.81.

Synthesis of [W(2,2′-bipyridine)(CO)$_4$][K(18-crown-6)] (5). Similar to the analogous reductions of Re(bpy-*t*Bu)(CO)$_3$Cl in THF,[59] 20 mL of 3 mM **2** and 18-crown-6 (1.1 equiv.) in THF was cooled to –35 ºC. KC$_8$ (1.1 equiv.) was then added to the solution and shaken, in which the solution turned from red to dark orange. The solution was allowed to warm to room temperature (~30 minutes) upon which it was filtered to afford a dark orange solution of the anion. The solvent was removed under reduced pressure, rinsed twice with 1 mL of pentane, then dried under vacuum to yield a black orange solid in 45% yield. X-ray quality crystals were grown from the vapor diffusion of pentane into a portion of a 3 mM THF solution of **5**. IR (THF) υ(CO): 1984 cm^{-1}, 1857 cm^{-1}, 1838 cm^{-1}, 1800 cm^{-1}.

Synthesis of [W(4,4′-di-*tert*-butyl-2,2′-bipyridine)$(CO)_3$][K(18-crown-6)$]_2$ (6). Complex **6** was synthesized and characterized in a similar fashion to **5**, using a 3 mM of **4** in THF, 2.2 equivalents 18-crown-6 (for X-ray and FTIR) and 2.2 equivalents of KC_8 to yield a dark purple solution of **6**. Upon drying a black purple solid was obtained with a yield of 73%. ^1H NMR (300 MHz, THF-d_8): δ = 1.12 (s, 18H), 4.80 (d, J = 6.0 Hz, 2H), 6.60 (d, 2H), 8.47 (d, J = 6.0 Hz, 2H). IR (THF) υ(CO): 1837 cm^{-1}, 1713 cm^{-1}.

Synthesis of [W(4,4′-di-*tert*-butyl-2,2′-bipyridine)$(CO)_3$][K(18-crown-6)]. The di-*tert*-butyl monoanion was synthesized and characterized in a similar fashion to **5**, using 10 mL of 2 mM **4** in THF, 1.1 equivalents 18-crown-6 and 1.1 equivalents of KC_8 to yield a dark orange solution. The black orange solid was collected with a yield of 43%. IR (THF) ν(CO): 1982 cm^{-1}, 1854 cm^{-1}, 1835 cm^{-1}, and 1798 cm^{-1}.

Synthesis of [W(2,2′-bipyridine)$(CO)_3$][K(18-crown-6)$]_2$. The tungsten bipyridine dianion was synthesized and characterized in a similar fashion to **5**, using a 2 mM of **2** in THF, 2.5 equivalents 18-crown-6 and 2.2 equivalents of KC_8 to yield a dark purple solution. The black purple solid was collected with a yield of

55%. ^{1}H NMR (300 MHz, THF-d_8): δ = 4.69 (br, 2H), 5.46 (br, 2H), 6.67 (br, 2H), 8.44 (br, 2H). IR (THF) ν(CO): 1840 cm^{-1} and 1711 cm^{-1}.

Electrochemistry. Electrochemical experiments were performed with a BASi CV-50W or BASi Epsilon potentiostat using a single-compartment cell. A 1 mm diameter glassy carbon electrode, Pt wire counter electrode, and Ag/AgCl reference electrode (separated from the solution by a vycor tip) were used for all experiments. Cyclic voltammograms were performed at room temperature under N_2 or CO_2 in an acetonitrile solution of 0.1 M $TBAPF_6$ as the electrolyte, which was purged with N_2 or CO_2 before each experiment. The scan rate for cyclic voltammetry was 100 mV·s^{-1} unless otherwise noted. Decamethylferrocene (Fc*) was used as the internal reference, which was then used to reference to SCE.

Bulk Electrolysis. Bulk electrolysis experiments were performed using a BASi Epsilon potentiostat connected to a 60 mL single-compartment cell designed on our laboratory. A 1 mm glassy carbon working electrode, Pt wire counter electrode surrounded by a glass rod (open at the end), and a Ag/AgCl reference electrode protected by a vycor tip was used in the setup. The bulk reductions were performed on a 30 mL scale with a catalyst concentration (**4**) of 1 mM and 0.1 M $TBAPF_6$. The solution before each experiment was purged with either dry N_2 or CO_2 gas. Gas analyses were performed on a Hewlett-Packard 7890A Series gas chromatograph with two molsieve columns (30 m × 0.53 mm ID × 25 μm film). The injected 1 mL sample of the cell's head was split between the two columns which differed by their carrier gas (N_2 and He) and allowed for quantification of both CO and H_2 in each run. The volume of CO or H_2 was elucidated from the peak area, correlated by gas chromatography calibration curves.

X-Ray Crystallography. Single crystal X-ray diffraction studies were carried out on a Bruker Kappa APEX-II CCD diffractometer equipped with Mo Kα radiation (λ = 0.71073 Å) or a Bruker Kappa APEX CCD diffractometer equipped with Cu Kα radiation (λ = 1.54184 Å). The crystals were mounted on a Cryoloop with Paratone oil and data were collected under a nitrogen gas stream at 100(2) K using ω and ϕ scans. Data were integrated using the Bruker SAINT software program and scaled using the SADABS software program. Solution by direct methods (SHELXS) produced a complete phasing model consistent with the proposed structure. All non-hydrogen atoms were refined anisotropically by full-matrix least-squares (SHELXL-97).[60] All hydrogen atoms were placed using a riding model. Their positions were constrained relative to their parent atom using the appropriate HFIX command in SHELXL-97. Crystallographic data for complexes **3**, **4**, **5**, and **6** are summarized in Table 4.5 and Table 4.6.

Density Functional Theory Calculations. Density functional theory (DFT) calculations were performed with the Amsterdam Density Functional (ADF) program suite,[61-62] version 2012.01.[63] The triple-ζ Slater-type orbital TZ2P ADF basis set was utilized without frozen cores. Relativistic effects were included through use of the zeroth-order regular approximation (ZORA).[64-65] The functional used was BP86, and the local density approximation (LDA) of Vosko, Wilk and Nusair[66] (VWN) was coupled with the generalized gradient approximation (GGA) corrections described by Becke[67] and Perdew[68-69] for electron exchange and correlation. Single point frequency calculations were performed to verify that the calculated geometries were at their minima. Molecular orbitals and final geometries were visualized with the ADF-GUI.

4.5 Acknowledgements

This chapter, in full, comes directly from a manuscript entitled: "Electrocatalytic CO_2 Reduction by M(bpy-R)$(CO)_4$ (M = Mo, W; R = H, *t*Bu) Complexes. Electrochemical, Spectroscopic, and Computational Studies and Comparison with Group 7 Catalysts." by Melissa L. Clark, Kyle A. Grice, Curtis E. Moore, Arnold L. Rheingold, and Clifford P. Kubiak, which has been published in *Chem. Sci.*, **2014**, 5, 1894-1900. http://dx.doi.org/10.1039/c3sc53470g. The dissertation author is a primary co-author of this manuscript.

This material is based upon work supported by the Air Force Office of Scientific Research through the MURI program under AFOSR Award No. FA9550-10-1-0572. Dr. Jonathan M. Smieja, Dr. Eric E. Benson, Dr. Jesse Froehlich, and Dr. Matthew D. Sampson are acknowledged for valuable discussions and assistance with electrochemistry, chemical reductions, and crystallography. Professor Joshua Figueroa, Professor John A. Keith, Dr. Steve George, and Dr. Alissa F. Sasayama are acknowledged for assistance with DFT calculations.

4.6 References

(1) Benson, E. E.; Kubiak, C. P.; Sathrum, A. J.; Smieja, J. M., *Chem. Soc. Rev.* **2009**, *38*, 89.

(2) Savéant, J.-M., *Chem. Rev.* **2008**, *108*, 2348.

(3) Windle, C. D.; Perutz, R. N., *Coord. Chem. Rev.* **2012**, *256*, 2562.

(4) Costentin, C.; Robert, M.; Savéant, J.-M., *Chem. Soc. Rev.* **2013**, *42*, 2423.

(5) Appel, A. M.; Bercaw, J. E.; Bocarsly, A. B.; Dobbek, H.; DuBois, D. L.; Dupuis, M.; Ferry, J. G.; Fujita, E.; Hille, R.; Kenis, P. J. A.; Kerfeld, C. A.; Morris, R. H.; Peden, C. H. F.; Portis, A. R.; Ragsdale, S. W.; Rauchfuss, T. B.; Reek, J. N. H.; Seefeldt, L. C.; Thauer, R. K.; Waldrop, G. L., *Chem. Rev.* **2013**, *113*, 6621.

(6) Hawecker, J.; Lehn, J. M.; Ziessel, R., *J. Chem. Soc., Chem. Commun.* **1984**, 328.

(7) Smieja, J. M.; Kubiak, C. P., *Inorg. Chem.* **2010**, *49*, 9283.

(8) Smieja, J. M.; Benson, E. E.; Kumar, B.; Grice, K. A.; Seu, C. S.; Miller, A. J.; Mayer, J. M.; Kubiak, C. P., *Proc. Natl. Acad. Sci. USA* **2012**, *109*, 15646.

(9) Grice, K. A.; Kubiak, C. P., Chapter five - Recent studies of rhenium and manganese bipyridine carbonyl catalysts for the electrochemical reduction of CO_2. In *Advances in Inorganic Chemistry*, Michele, A.; Rudi van, E., Eds. Academic Press: 2014; Vol. 66, 163-188.

(10) Bourrez, M.; Molton, F.; Chardon-Noblat, S.; Deronzier, A., *Angew. Chem. Intl. Ed.* **2011**, *50*, 9903.

(11) Smieja, J. M.; Sampson, M. D.; Grice, K. A.; Benson, E. E.; Froehlich, J. D.; Kubiak, C. P., *Inorg. Chem.* **2013**, *52*, 2484.

(12) Froehlich, J. D.; Kubiak, C. P., *Inorg. Chem.* **2012**, *51*, 3932.

(13) Bhugun, I.; Lexa, D.; Savéant, J.-M., *J. Phys. Chem.* **1996**, *100*, 19981.

(14) Costentin, C.; Drouet, S.; Robert, M.; Savéant, J.-M., *Science* **2012**, *338*, 90.

(15) Lilio, A. M.; Grice, K. A.; Kubiak, C. P., *Eur. J. Inorg. Chem.* **2013**, *2013*, 4016.

(16) Ramos Sende, J. A.; Arana, C. R.; Hernandez, L.; Potts, K. T.; Keshevarz-K, M.; Abruna, H. D., *Inorg. Chem.* **1995**, *34*, 3339.

(17) Pickett, C. J.; Pletcher, D., *J. Chem. Soc., Dalton Trans.* **1976**, 749.

(18) Reda, T.; Plugge, C. M.; Abram, N. J.; Hirst, J., *Proc. Natl. Acad. Sci. USA* **2008**, *105*, 10654.

(19) Dobbek, H.; Gremer, L.; Kiefersauer, R.; Huber, R.; Meyer, O., *Proc. Natl. Acad. Sci. USA* **2002**, *99*, 15971.

(20) Lee, G. R.; Maher, J. M.; Cooper, N. J., *J. Am. Chem. Soc.* **1987**, *109*, 2956.

(21) Jayarathne, U.; Chandrasekaran, P.; Jacobsen, H.; Mague, J. T.; Donahue, J. P., *Dalton Trans.* **2010**, *39*, 9662.

(22) Contreras, L.; Paneque, M.; Sellin, M.; Carmona, E.; Perez, P. J.; Gutierrez-Puebla, E.; Monge, A.; Ruiz, C., *New J. Chem.* **2005**, *29*, 109.

(23) Yonke, B. L.; Reeds, J. P.; Zavalij, P. Y.; Sita, L. R., *Angew. Chem. Int. Ed.* **2011**, *50*, 12342.

(24) Bernskoetter, W. H.; Tyler, B. T., *Organometallics* **2011**, *30*, 520.

(25) Tai, C.-C.; Chang, T.; Roller, B.; Jessop, P. G., *Inorg. Chem.* **2003**, *42*, 7340.

(26) Darensbourg, D. J.; Ovalles, C., *J. Am. Chem. Soc.* **1984**, *106*, 3750.

(27) Vlček Jr, A. n., *Coord. Chem. Rev.* **2002**, *230*, 225.

(28) Kaizu, Y.; Kobayashi, H., *Bull. Chem. Soc. Jpn.* **1972**, *45*, 470.

(29) Hor, T. S. A.; Chee, S.-M., *J. Organomet. Chem.* **1987**, *331*, 23.

(30) Tolun, E.; Proctor, C. J.; Todd, J. F. J.; Walshe, J. M. A.; Connor, J. A., *Org. Mass Spectrom.* **1984**, *19*, 294.

(31) Schadt, M. J.; Lees, A. J., *Inorg. Chem.* **1986**, *25*, 672.

(32) Cao, S.; Bal Reddy, K.; Eyring, E. M.; van Eldik, R., *Organometallics* **1994**, *13*, 91.

(33) Connor, J. A.; Overton, C., *J. Organomet. Chem.* **1983**, *249*, 165.

(34) Johnson, R.; Madhani, H.; Bullock, J. P., *Inorg. Chim. Acta* **2007**, *360*, 3414.

(35) Braga, S. S.; Coelho, A. C.; Goncalves, I. S.; Almeida Paz, F. A., *Acta Crystallogr., Sect. E* **2007**, *63*, m780.

(36) Ye, Q.; Wu, Q.; Zhao, H.; Song, Y.-M.; Xue, X.; Xiong, R.-G.; Pang, S.-M.; Lee, G.-H., *J. Organomet. Chem.* **2005**, *690*, 286.

(37) Chapman, J.; Kolawole, G.; Long, N.; White, A. J. P.; Williams, D. J.; O'Brien, P., *S. Afr. J. Sci.* **2005**, *101*, 454.

(38) Scarborough, C. C.; Wieghardt, K., *Inorg. Chem.* **2011**, *50*, 9773.

(39) Allen, F., *Acta Crystallographica Section B* **2002**, *58*, 380.

(40) Makedonas, C.; Mitsopoulou, C. A., *Eur. J. Inorg. Chem.* **2007**, *2007*, 110.

(41) Scheiring, T.; Kaim, W.; Fiedler, J., *J. Organomet. Chem.* **2000**, *598*, 136.

(42) Grice, K. A.; Gu, N. X.; Sampson, M. D.; Kubiak, C. P., *Dalton Trans.* **2013**, *42*, 8498.

(43) Miholová, D.; Vlček, A. A., *J. Organomet. Chem.* **1985**, *279*, 317.

(44) Miholová, D.; Gaš, B.; Záliš, S.; Klíma, J.; Vlček, A. A., *J. Organomet. Chem.* **1987**, *330*, 75.

(45) Crutchley, R. J.; Lever, A. B. P., *Inorg. Chem.* **1982**, *21*, 2276.

(46) Dessy, R. E.; Wieczorek, L., *J. Am. Chem. Soc.* **1969**, *91*, 4963.

(47) Dessy, R. E.; Stary, F. E.; King, R. B.; Waldrop, M., *J. Am. Chem. Soc.* **1966**, *88*, 471.

(48) Connor, J. A.; Overton, C.; El Murr, N., *J. Organomet. Chem.* **1984**, *277*, 277.

(49) Vlček Jr, A.; Baumann, F.; Kaim, W.; Grevels, F.-W.; Hartl, F., *J. Chem. Soc., Dalton Trans.* **1998**, 215.

(50) Gore-Randall, E.; Irwin, M.; Denning, M. S.; Goicoechea, J. M., *Inorg. Chem.* **2009**, *48*, 8304.

(51) Nikiforov, G. B.; Roesky, H. W.; Noltemeyer, M.; Schmidt, H. G., *Polyhedron* **2004**, *23*, 561.

(52) Addison, A. W.; Rao, T. N.; Reedijk, J.; van Rijn, J.; Verschoor, G. C., *J. Chem. Soc., Dalton Trans.* **1984**, 1349.

(53) Hartl, F.; Rosa, P.; Ricard, L.; Le Floch, P.; Záliš, S., *Coord. Chem. Rev.* **2007**, *251*, 557.

(54) Benson, E. E.; Kubiak, C. P., *Chem. Commun.* **2012**, *48*, 7374.

(55) Krejčik, M.; Viček, A. A., *J. Eletroanal. Chem.* **1991**, *313*, 243.

(56) Keith, J. A.; Grice, K. A.; Kubiak, C. P.; Carter, E. A., *J. Am. Chem. Soc.* **2013**, *135*, 15823.

(57) Daniel, T.; Suzuki, N.; Tanaka, K.; Nakamura, A., *J. Organomet. Chem.* **1995**, *505*, 109.

(58) Schwindt, M. A.; Lejon, T.; Hegedus, L. S., *Organometallics* **1990**, *9*, 2814.

(59) Smieja, J. M.; Benson, E. E.; Kumar, B.; Grice, K. A.; Seu, C. S.; Miller, A. J. M.; Mayer, J. M.; Kubiak, C. P., *Proc. Natl. Acad. Sci. USA* **2012**, *109*, 15646.

(60) Sheldrick, G., *Acta Crystallogr., Sect. A* **2008**, *64*, 112.

(61) te Velde, G.; Bickelhaupt, F. M.; Baerends, E. J.; Fonseca Guerra, C.; van Gisbergen, S. J. A.; Snijders, J. G.; Ziegler, T., *J. Comput. Chem.* **2001**, *22*, 931.

(62) Fonseca Guerra, C.; Snijders, J. G.; te Velde, G.; Baerends, E., *J. Theor. Chem. Acc.* **1998**, *99*, 391.

(63) Kallane, S. I.; van Gastel, M., *J. Phys. Chem. A* **2016**, *120*, 7465.

(64) van Lenthe, E.; Baerends, E. J.; Snijders, J. G., *J. Chem. Phys.* **1993**, *99*, 4597.

(65) van Lenthe, E.; Snijders, J. G.; Baerends, E. J., *J. Chem. Phys.* **1996**, *105*, 1200.

(66) Vosko, S. H.; Wilk, L.; Nusair, M., *Can. J. Phys.* **1980**, *58*, 1200.

(67) Becke, A. D., *Phys. Rev. A* **1988**, *38*, 3098.

(68) Perdew, J. P., *Phys. Rev. B* **1986**, *33*, 8822.

(69) Perdew, J. P., *Phys. Rev. B* **1986**, *34*, 7406.

4.7 Appendix

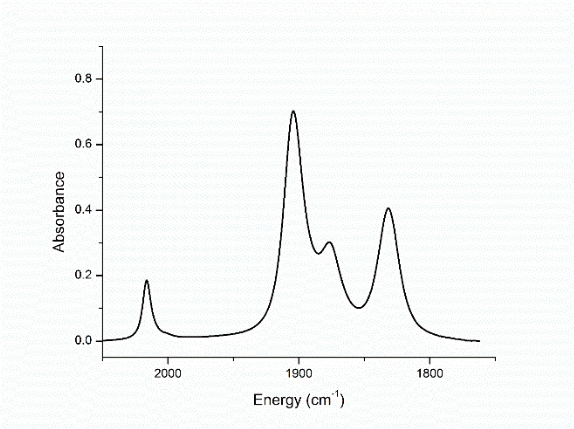

Figure 4.9 Carbonyl stretching region of the FT-IR spectrum of complex **1** in acetonitrile solution. Complexes **2**–**4** display similar patterns in this region (Table 4.3). Complex **1** has ν(CO) stretches at 2016 cm^{-1}, 1904 cm^{-1}, 1877 cm^{-1}, and 1832 cm^{-1}.

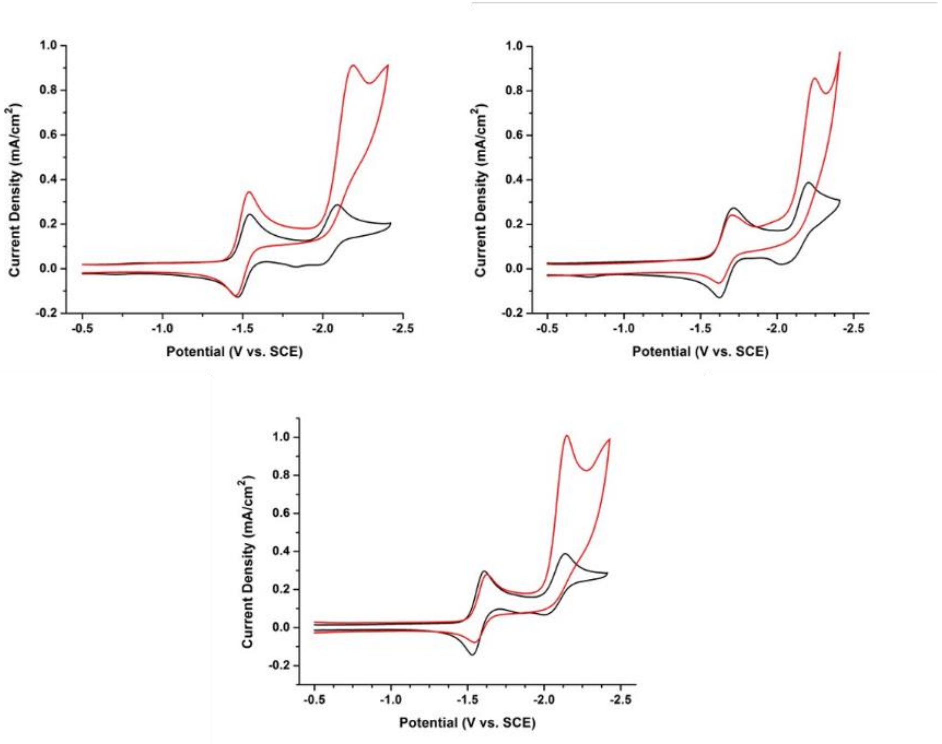

Figure 4.10 Cyclic voltammograms of complexes **2** (left), **3** (right), and **4** (bottom) at 100 mV/s.

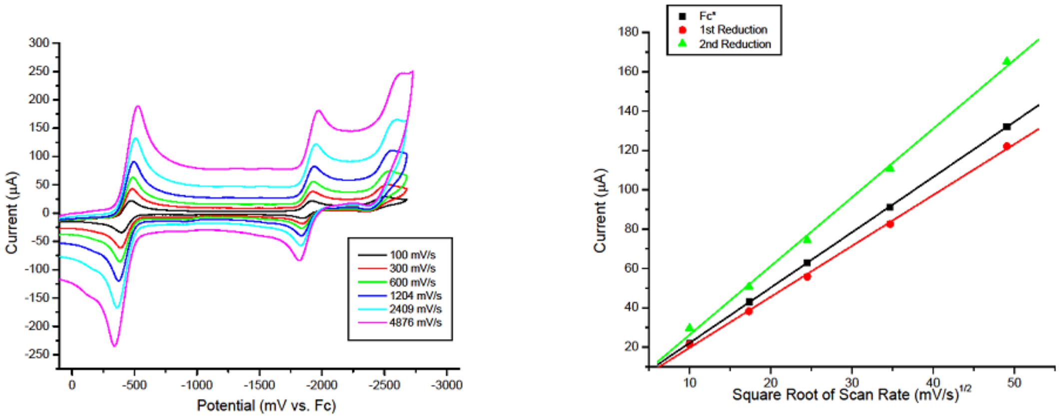

Figure 4.11 Left: Scan-rate dependence of complex **4** showing $\mathrm{FeCp_2}$* along with the first and second reductions at various scan rates. Right: Plot of peak current versus square root of scan rate from scan-rate dependence studies of complex **4**.

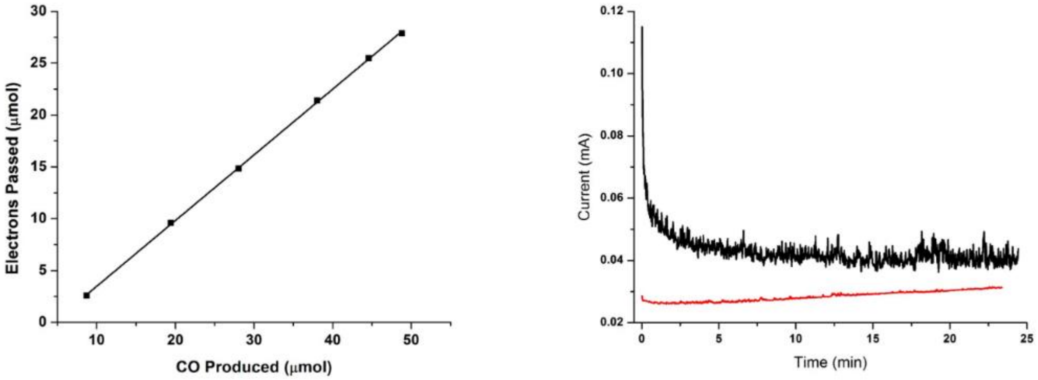

Figure 4.12 (left) Faradaic efficiency study of W(bpy-*t*Bu)$(CO)_4$ (**4**) in dry acetonitrile with carbon dioxide at –2.3 V. Slope corresponds to 109 ± 7% Faradaic efficiency for the conversion of CO_2 to N_2. This is uncorrected for the amount of CO produced for the loss of a carbonyl ligand upon the second reduction. (right) Comparison of current versus time graphs from bulk electrolyses of **4** under N_2 (red) and CO_2 (black) over 24 minutes.

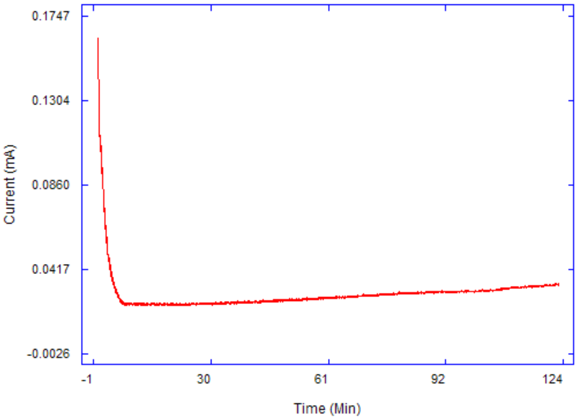

Figure 4.13 Current versus time graph for the bulk electrolysis of complex **4** under CO_2. The total charge passed was 0.2128 C and the lowest current passed was 0.023 mA at ca. 7 min into the two hour experiment. Experiments of up to 12 hours have been performed and show similar behaviour.

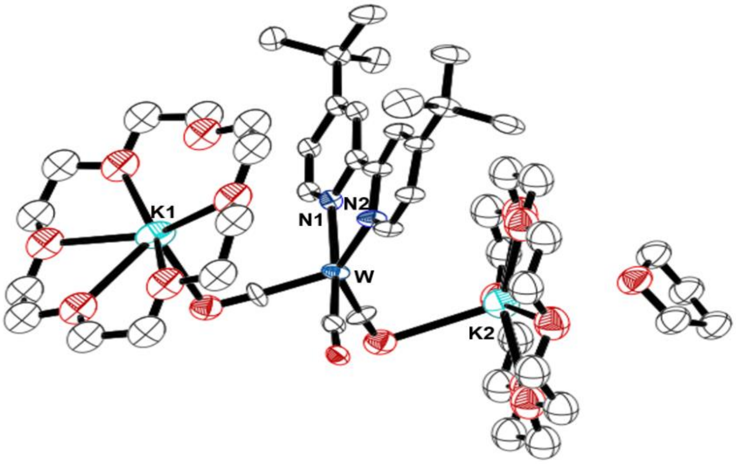

Figure 4.14 Molecular structure of [W(bpy-*t*Bu)$(CO)_3$][K(18-crown-6)$]_2$•THF (**6**) with hydrogen atoms and disorder omitted for clarity. Ellipsoids are shown at 50% probability. The crystal exhibits two-positional disorder across a mirror plane.

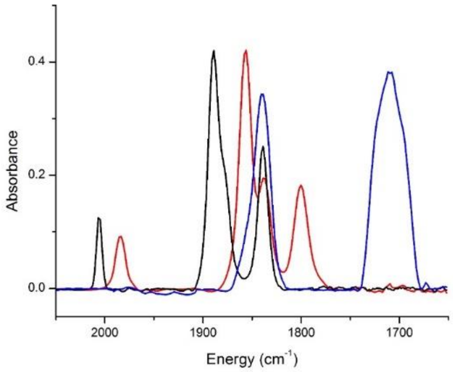

Figure 4.15 The v(CO) stretches in the infrared spectra of W(bpy)(CO)$_4$ (**2**) (black), chemically reduced anionic [W(bpy)(CO)$_4$][K(18-crown-6)] (**5**) (red), and chemically reduced dianionic [W(bpy)(CO)$_3$][K(18-crown-6)]$_2$ (blue). Spectra taken in THF under N$_2$. Neutral species **2** has v(CO) stretches at 2005 cm^{-1}, 1889 cm^{-1}, and 1839 cm^{-1}. Complex **5** has v(CO) stretches at 1984 cm^{-1}, 1857 cm^{-1}, 1838 cm^{-1}, and 1800 cm^{-1}. The dianion has stretching frequencies at 1840 cm^{-1} and 1711 cm^{-1}.

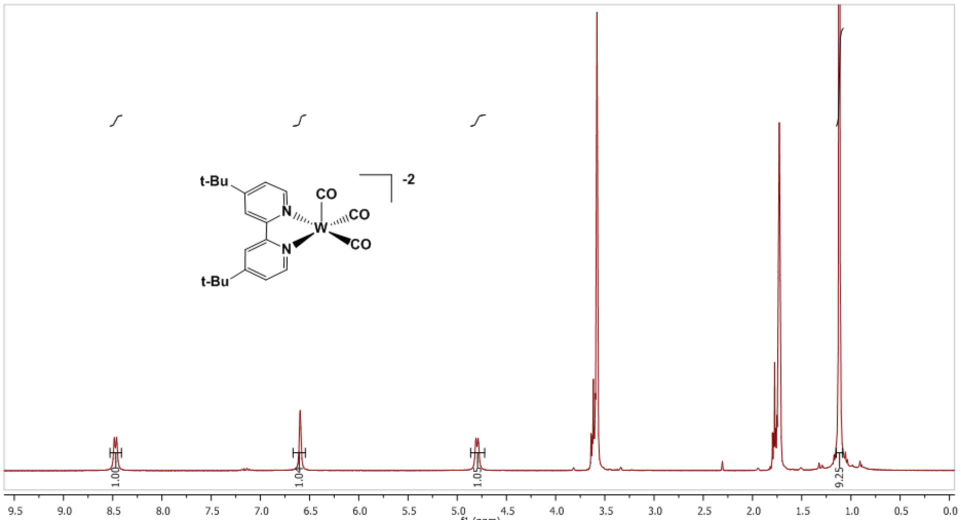

Figure 4.16 ^{1}H NMR spectrum of [W(4,4′-di-tert-butyl-2,2′-bipyridine)(CO)$_3$][K(18-crown-6)]$_2$ (**6**) in THF-d_8. Solvent residual signals at 1.72 and 3.58 ppm.

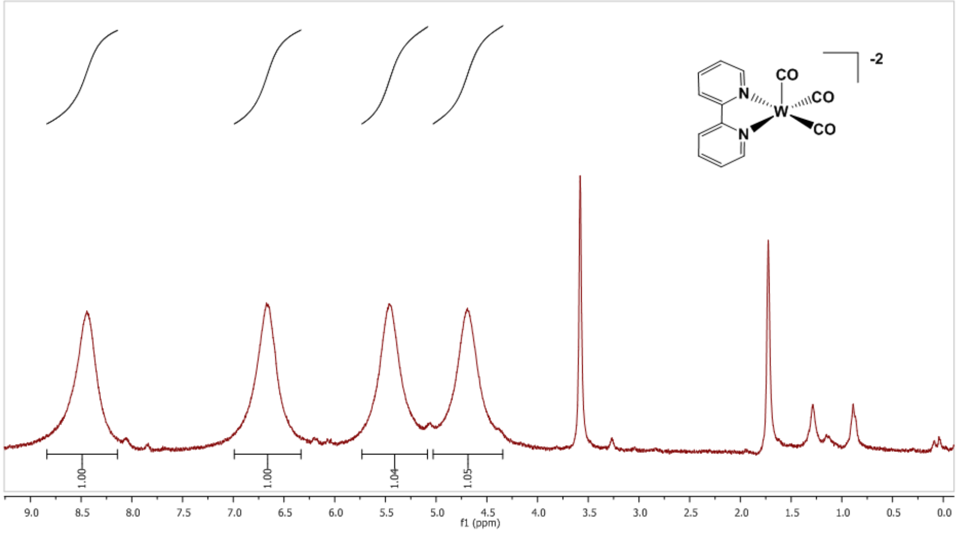

Figure 4.17 ^{1}H NMR spectrum of [W(2,2′-bipyridine)(CO)$_3$][K(18-crown-6)]$_2$ in THF-d_8. Solvent residual signals at 1.72 ppm and 3.58 ppm for THF- d_8 and peaks at 0.89 ppm and 1.29 ppm are from residual pentane. Peak broadening is likely due to decomposition of the sample (observed by a color change of the solution from dark purple to orange as the signals disappeared).

Table 4.3 Carbonyl ligand stretching frequencies (cm^{-1}) of M(L)(CO)$_4$ complexes **1–4** in acetonitrile solution.

1	**2**	**3**	**4**
2016	2009	2015	2007
1904	1892	1901	1888
1877	1873[a]	1875	1870[a]
1832	1828	1830	1826

[a] This signal overlaps with the larger signal at higher wavenumbers

Table 4.4 Selected bond lengths (Å) and angles (deg) for complexes **1**–**6**.

Bond/Angle	**3**	**1**[35]	**4**	**2**[36-37]	**5**	**6**
M–N1	2.232(2)	2.249(3)	2.2208(19)	2.272(8)	2.215(3)	2.154(9)
M–N2	2.242(2)	2.241(2)	2.230(2)	2.261(8)	2.212(3)	2.133(9)
M–C1	2.041(3)	2.022(4)	2.041(3)	2.032(11)	2.025(4)	1.892(2)
M–C2	1.964(3)	1.952(4)	1.969(2)	1.938(10)	1.975(4)	1.947(13)
M–C3	1.953(3)	1.962(3)	1.955(3)	1.933(11)	1.961(4)	1.892(7)
M–C4	2.052(3)	2.056(4)	2.037(3)	2.000(11)	2.023(4)	-
C9–C10	1.483(4)	1.483(5)	1.481(3)	1.48(1)	1.396(6)	1.369(14)
N1–M–N2	71.99(8)	72.34(9)	72.12(7)	71.4(3)	73.3(1)	73.1(3)
N1–M–C3	99.93(9)	98.4(1)	99.28(4)	97.1(4)	99.1(1)	98.1(7)
C3–M–C2	89.1(1)	90.1(1)	90.18(10)	93.3(5)	84.6(2)	84.6(6)
C2–M–N2	99.02(9)	99.1(1)	98.46(9)	98.2(4)	103.0(1)	93.6(5)
C1–M–C4	168.3(1)	167.8(1)	168.28(9)	171.5(4)	172.3(2)	-
M–C1–O1	171.8(2)	170.7(3)	171.6(2)	171(1)	173.5(4)	177.0(7)
M–C2–O2	178.7(2)	178.5(3)	178.0(2)	176(1)	176.5(3)	174.0(14)
M–C3–O3	178.9(2)	178.4(3)	178.6(2)	179(1)	176.8(3)	152(3)
M–C4–O4	170.9(2)	171.9(3)	172.2(2)	171(1)	174.2(3)	-

Table 4.5 Crystallographic data and refinement information of neutral compounds.

Compound	**Mo(bpy-*t*Bu)(CO)$_4$**	**W(bpy-*t*Bu)(CO)$_4$**
Empirical Formula	$C_{22}H_{24}MoN_2O_4$	$C_{22}H_{24}N_2O_4W$
Formula Weight	476.37	564.28
Temperature (K)	100(2)	100(2)
Crystal System	orthorhombic	orthorhombic
Space Group	Pbca	Pbca
a (Å)	17.9132(6)	17.8251(9)
b (Å)	11.6738(4)	11.6986(6)
c (Å)	21.3034(8)	21.3193(11)
α (deg)	90	90
β (deg)	90	90
γ (deg)	90	90
V (Å^3)	4454.9(3)	4445.7(4)
Z Value	8	8
ρ *calc* (g/cm^3)	1.421	1.686
m (mm^{-1})	0.617	5.225
Theta range for Data Collection (deg)	5.654 to 50.804	3.82 to 50.76
Independent Reflections	4,099 [R(int) = 0.0386]	4,091 [R(int) = 0.0374]
Data/restraints/parameters	4099/0/268	4091/0/268
Goodness of Fit on F^2	1.060	1.071
R indices (all data) R1, wR2	0.0315, 0.0647	0.0198, 0.0408
Largest diff. peak and hole	0.66 to -0.51	0.76 to -0.46

Table 4.6 Crystallographic data and refinement information of reduced compounds.

Compound	**[W(bpy)(CO)$_4$][K(18-crown-6)]**	**[W(bpy-*t*Bu)(CO)$_3$][K(18-crown-6)]$_2$**
Empirical Formula	$C_{30}H_{40}KN_2O_{11}W$	$C_{49}H_{80}K_2N_2O_{16}W$
Formula Weight	827.60	1213.01
Temperature (K)	100(2)	100(2)
Crystal System	monoclinic	orthorhombic
Space Group	$P2_1/c$	Pnma
a (Å)	12.2130(3)	29.9821(16)
b (Å)	18.7469(5)	15.8708(9)
c (Å)	15.4880(4)	11.8370(6)
α (deg)	90	90
β (deg)	107.674(1)	90
γ (deg)	90	90
V (Å^3)	3378.69(15)	5632.5(5)
Z Value	4	4
ρ *calc* (g/cm^3)	1.6269	1.430
m (mm^{-1})	3.601	5.622
Theta range for Data Collection (deg)	3.5 to 50.82	5.896 to 138.088
Independent Reflections	6,209 [R(int) = 0.0336]	5,372 [R(int) = 0.1648]
Data/restraints/parameters	6209/0/405	5372/75/311
Goodness of Fit on F^2	0.731	1.061
R indices (all data) R1, wR2	0.0317; 0.0898	0.0968; 0.1980
Largest diff. peak and hole	1.08 and -0.59	2.145 and -1.172

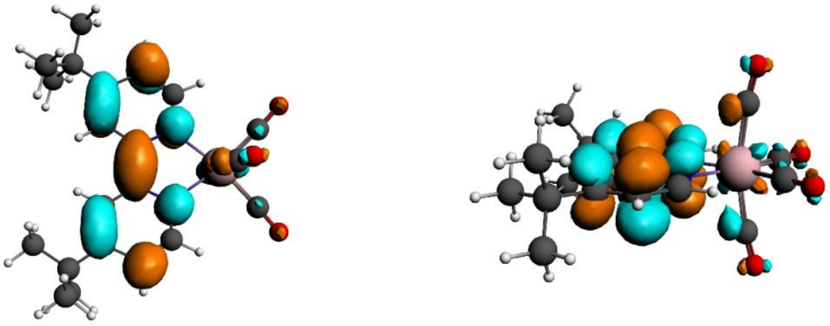

Figure 4.18 Top and side view of DFT-calculated Lowest Unoccupied Molecular Orbital (LUMO) of W(bpy-*t*Bu)(CO)$_4$ (**A**).

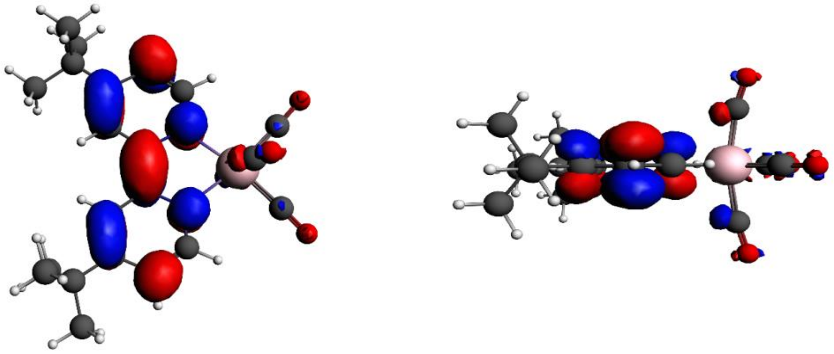

Figure 4.19 Top and side view of DFT-calculated Singly Occupied Molecular Orbital (SOMO) of [W(bpy-*t*Bu)(CO)$_4$]$^{–1}$ (**B**).

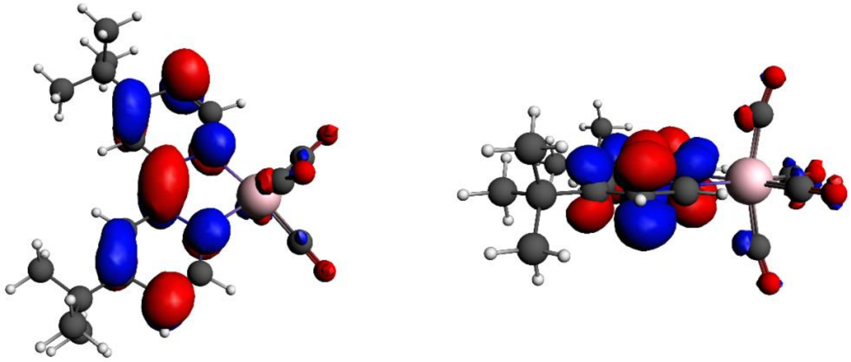

Figure 4.20 Top and side view of DFT-calculated Highest Occupied Molecular Orbital (HOMO) of [W(bpy-*t*Bu)(CO)$_4$]$^{–2}$ (**C**).

Table 4.7 Pertinent bond lengths (Å) in the DFT-optimized structures of **A**–**D**.

Bond	A	B	C	D
M–N	2.223	2.234	2.220	2.195
M–N	2.222	2.234	2.220	2.165
M–C_{ax}	2.041	2.037	2.037	1.936
M–C_{ax}	2.041	2.036	2.037	1.930
M–C_{eq}	1.978	1.971	1.972	1.954
M–C_{eq}	1.974	1.971	1.971	–
C–O_{ax}	1.163	1.170	1.177	1.200
C–O_{ax}	1.163	1.170	1.177	1.200
C–O_{eq}	1.172	1.181	1.190	1.200
C–O_{eq}	1.172	1.181	1.190	–
C_{py}–C_{py}	1.463	1.423	1.390	1.398
C–N	1.368	1.396	1.432	1.434
C–N	1.364	1.395	1.432	1.422

Table 4.8 Comparison of the experimental and computational v(CO) stretching frequencies (in cm^{-1}).

Complex	Experimental (THF)	DFT (gas phase)
W(bpy-*t*Bu)$(CO)_4$	2004, 1886, 1837	1995, 1912, 1903, 1878
[W(bpy-*t*Bu)$(CO)_4]^{-}$	1982, 1854, 1835, 1798	1962, 1864, 1852, 1827
[W(bpy-*t*Bu)$(CO)_4]^{2-}$	Not observed	1925, 1814, 1798, 1775
[W(bpy-*t*Bu)$(CO)_3]^{2-}$	1837, 1713	1822, 1734, 1724

Table 4.9 Geometry optimized xyz coordinates for W(bpy-tBu)(CO)$_4$ (**A**) from DFT calculations.

Atom	X	Y	Z
1.W	0.790379	11.179751	7.741391
2.O	-0.704886	8.861315	9.356582
3.O	1.948957	11.855555	10.590981
4.O	2.908110	8.931325	7.126820
5.O	3.111638	13.150460	6.766189
6.N	-0.311931	11.010845	5.819370
7.N	-0.858977	12.669510	7.772876
8.C	-0.245550	9.719468	8.720640
9.C	1.543084	11.581177	9.526710
10.C	2.135586	9.772762	7.387842
11.C	2.208586	12.478475	7.056967
12.C	0.004079	10.130028	4.838517
13.H	0.853193	9.484839	5.045238
14.C	-0.689760	10.035306	3.646784
15.H	-0.362247	9.294848	2.919040
16.C	-1.789027	10.879673	3.388372
17.C	-2.106679	11.783206	4.400230
18.H	-2.940952	12.465143	4.271183
19.C	-1.373310	11.837454	5.593885
20.C	-1.681173	12.763776	6.683851
21.C	-2.732946	13.683558	6.641840
22.H	-3.358290	13.722141	5.753248
23.C	-2.997274	14.547712	7.707981
24.C	-2.141065	14.427881	8.815761
25.H	-2.262795	15.051899	9.697472
26.C	-1.109719	13.501381	8.808416
27.H	-0.441965	13.403715	9.659949
28.C	-2.570847	10.783159	2.073427
29.C	-3.711261	11.813125	2.002194
30.H	-4.447936	11.663227	2.803827
31.H	-4.240715	11.708400	1.045538
32.H	-3.335598	12.844351	2.060692
33.C	-3.179637	9.367424	1.948915
34.H	-2.403738	8.590676	1.957210
35.H	-3.732887	9.281113	1.002330
36.H	-3.875309	9.161088	2.774127
37.C	-1.610955	11.029161	0.886535
38.H	-1.164085	12.031644	0.939373
39.H	-2.161298	10.947634	-0.062138
40.H	-0.795390	10.294622	0.864655
41.C	-4.153811	15.553309	7.634532

Table 4.9 Geometry optimized xyz coordinates for W(bpy-tBu)$(CO)_4$ (**A**) from DFT calculations, continued.

Atom	X	Y	Z
42.C	-5.483382	14.795505	7.412816
43.H	-5.472062	14.217892	6.478836
44.H	-6.316102	15.511370	7.352673
45.H	-5.686777	14.100576	8.238962
46.C	-3.918708	16.516408	6.447976
47.H	-2.982347	17.077735	6.571374
48.H	-4.746572	17.237630	6.382490
49.H	-3.867206	15.977900	5.492048
50.C	-4.271110	16.383639	8.923697
51.H	-4.465418	15.750485	9.800227
52.H	-5.108269	17.088811	8.831086
53.H	-3.362690	16.971200	9.114411

Table 4.10 Geometry optimized *xyz* coordinates for $[W(bpy\text{-}t\text{Bu})(CO)_4]^-$ (**B**) from DFT calculations.

Atom	X	Y	Z
1.W	0.798782	11.179772	7.746514
2.O	-0.713630	8.852339	9.333812
3.O	1.974205	11.806692	10.603045
4.O	2.927328	8.923412	7.190520
5.O	3.147095	13.122251	6.780394
6.N	-0.291653	11.002230	5.805580
7.N	-0.848285	12.688002	7.784914
8.C	-0.262054	9.725672	8.699747
9.C	1.550182	11.557857	9.529513
10.C	2.139832	9.772446	7.420614
11.C	2.218484	12.468471	7.061513
12.C	0.021034	10.149144	4.810810
13.H	0.885751	9.516255	5.000758
14.C	-0.674105	10.043444	3.617111
15.H	-0.335741	9.320274	2.877275
16.C	-1.815937	10.876088	3.395019
17.C	-2.142106	11.754802	4.407532
18.H	-3.000797	12.411477	4.299035
19.C	-1.390072	11.839601	5.613369
20.C	-1.685423	12.746412	6.669269
21.C	-2.752964	13.684338	6.643191
22.H	-3.386675	13.712741	5.758301
23.C	-3.003496	14.552921	7.689831
24.C	-2.129650	14.466273	8.812127
25.H	-2.241725	15.102299	9.685959
26.C	-1.098209	13.536957	8.796870
27.H	-0.421897	13.456266	9.645839
28.C	-2.604534	10.777268	2.082938

Table 4.10 Geometry optimized *xyz* coordinates for [W(bpy-*t*Bu)(CO)$_4$]$^{–}$ (**B**) from DFT calculations, continued.

Atom	X	Y	Z
29.C	-3.822646	11.716776	2.058918
30.H	-4.527165	11.482324	2.869290
31.H	-4.357786	11.608736	1.103755
32.H	-3.523702	12.769530	2.158179
33.C	-3.109885	9.329564	1.883540
34.H	-2.277865	8.613422	1.864944
35.H	-3.657451	9.242182	0.931250
36.H	-3.785225	9.036708	2.700007
37.C	-1.681341	11.152040	0.900391
38.H	-1.323355	12.186667	0.999822
39.H	-2.222684	11.060845	-0.055279
40.H	-0.801287	10.496333	0.859570
41.C	-4.160228	15.565309	7.608053
42.C	-5.491242	14.831483	7.326721
43.H	-5.451970	14.275355	6.381038
44.H	-6.321371	15.553645	7.261150
45.H	-5.718928	14.113077	8.126533
46.C	-3.891451	16.567639	6.461446
47.H	-2.953101	17.113603	6.632685
48.H	-4.712145	17.300296	6.387517
49.H	-3.805337	16.051055	5.496169
50.C	-4.318613	16.361342	8.916103
51.H	-4.515740	15.697708	9.769196
52.H	-5.163434	17.060863	8.827345
53.H	-3.418311	16.948981	9.141948

Table 4.11 Geometry optimized *xyz* coordinates for [W(bpy-*t*Bu)(CO)$_4$]$^{2–}$ (**C**) from DFT calculations.

Atom	X	Y	Z
1.W	0.794239	11.204635	7.728628
2.O	-0.579831	8.880287	9.447818
3.O	2.055196	11.908638	10.541024
4.O	2.927102	8.928007	7.221305
5.O	3.206857	13.032674	6.688890
6.N	-0.314469	10.960232	5.821107
7.N	-0.835877	12.712138	7.770736
8.C	-0.205449	9.759726	8.760092
9.C	1.587571	11.637077	9.481234
10.C	2.129827	9.787791	7.422444
11.C	2.234748	12.438224	6.985406
12.C	-0.035954	10.074122	4.850969
13.H	0.821175	9.430595	5.054322
14.C	-0.731892	9.926441	3.659771

Table 4.11 Geometry optimized *xyz* coordinates for $[W(bpy\text{-}t\text{Bu})(CO)_4]^{2-}$ (**C**) from DFT calculations, continued.

Atom	**X**	**Y**	**Z**
15.H	-0.410248	9.168043	2.947097
16.C	-1.863717	10.801653	3.410093
17.C	-2.172068	11.717080	4.385447
18.H	-3.008666	12.399749	4.244645
19.C	-1.429700	11.834392	5.615974
20.C	-1.704683	12.741014	6.632661
21.C	-2.787611	13.692711	6.624412
22.H	-3.447049	13.684961	5.757874
23.C	-3.010166	14.582154	7.645843
24.C	-2.095316	14.535508	8.773201
25.H	-2.187107	15.202453	9.629885
26.C	-1.074782	13.595688	8.753798
27.H	-0.383297	13.538245	9.595499
28.C	-2.644703	10.665469	2.097864
29.C	-3.795807	11.678438	1.978037
30.H	-4.523980	11.550185	2.791659
31.H	-4.323367	11.541448	1.019538
32.H	-3.421827	12.711407	2.020801
33.C	-3.247998	9.242681	1.993458
34.H	-2.463610	8.479381	2.090591
35.H	-3.760723	9.098252	1.024974
36.H	-3.973042	9.075074	2.803454
37.C	-1.691479	10.881204	0.896146
38.H	-1.287923	11.904461	0.907623
39.H	-2.217431	10.719999	-0.062450
40.H	-0.838272	10.191055	0.946206
41.C	-4.154005	15.603263	7.645291
42.C	-5.051867	15.496295	6.401065
43.H	-4.477761	15.672102	5.480110
44.H	-5.859388	16.245555	6.450653
45.H	-5.510426	14.499822	6.326810
46.C	-3.573373	17.038521	7.692429
47.H	-2.909263	17.161474	8.559175
48.H	-4.379735	17.791682	7.758113
49.H	-2.977860	17.238853	6.789594
50.C	-5.044441	15.394732	8.895438
51.H	-5.520203	14.403420	8.864624
52.H	-5.835877	16.164110	8.952443
53.H	-4.444752	15.442777	9.814530

Table 4.12 Geometry optimized *xyz* coordinates for $[\mathrm{W(bpy\text{-}}t\mathrm{Bu)(CO)_3}]^{2-}$ (**D**) from DFT calculations.

Atom	X	Y	Z
1.W	25.364167	4.045685	2.713676
2.O	23.329082	1.700844	2.325860
3.C	24.081466	2.621903	2.485752
4.O	24.755090	4.074856	5.807524
5.C	24.957760	4.060553	4.624590
6.N	26.250394	4.102924	0.706320
7.N	27.513368	4.105378	2.971538
8.C	25.547637	4.112090	-0.455152
9.H	24.466312	4.103083	-0.321234
10.C	26.094116	4.128471	-1.720567
11.H	25.425081	4.134082	-2.581812
12.C	27.533443	4.131426	-1.869150
13.C	28.270477	4.130900	-0.705621
14.H	29.358954	4.130606	-0.748830
15.C	27.668072	4.124713	0.591474
16.C	28.353777	4.134139	1.809936
17.C	29.772194	4.177327	1.961988
18.H	30.366864	4.202974	1.048873
19.C	30.396033	4.190865	3.188828
20.C	29.520395	4.156736	4.351368
21.H	29.915142	4.161684	5.368451
22.C	28.161334	4.118670	4.177194
23.H	27.498620	4.093881	5.041467
24.C	28.150311	4.126812	-3.271484
25.C	27.700829	5.387664	-4.050410
26.H	26.604907	5.450176	-4.095504
27.H	28.062732	6.297209	-3.548975
28.H	28.091422	5.375360	-5.084136
29.C	29.688026	4.109075	-3.241747
30.H	30.086152	4.992623	-2.722910
31.H	30.065287	3.215891	-2.723768
32.H	30.087466	4.105042	-4.269241
33.C	27.671421	2.876201	-4.050043
34.H	28.012785	1.959233	-3.547806
35.H	26.574377	2.838660	-4.093270
36.H	28.060880	2.878438	-5.084258
37.C	31.911396	4.234260	3.385894
38.C	32.299869	5.480782	4.221328
39.H	33.385316	5.500208	4.429117
40.H	32.028271	6.401067	3.683749
41.H	31.765024	5.490373	5.180919
42.C	32.380651	2.970873	4.151466

Table 4.12 Geometry optimized *xyz* coordinates for [W(bpy-*t*Bu)(CO)$_3$]$^{2-}$ (**D**) from DFT calculations, continued.

Atom	X	Y	Z
43.H	33.466149	3.008516	4.357028
44.H	31.851046	2.876004	5.109547
45.H	32.164822	2.066086	3.564678
46.C	23.865226	5.235569	2.424033
47.C	32.679574	4.295743	2.055125
48.H	33.765136	4.330383	2.244141
49.H	32.468562	3.414066	1.433270
50.H	32.402610	5.189367	1.477775
51.O	22.974622	6.016971	2.232190

Chapter 5

Orientation of Cyano-Substituted Bipyridine Re(I) *fac*-Tricarbonyl Electrocatalysts Bound to Conducting Au Surfaces

5.1 Introduction

As global anthropogenic carbon dioxide (CO_2) emissions continue to rise, there is a need not only to reduce production of CO_2, but also to use it as a substrate for value-added products. One solution would be to utilize this CO_2 to synthesize liquid fuels, which would help create a carbon neutral cycle.[1] The first step of the cycle can be done by electrocatalytically reducing CO_2, and both heterogeneous[2-3] and homogeneous[4-5] systems have been employed for this purpose.[6-8] While homogeneous systems are favored for their selectivity and tunability, heterogeneous catalysts have the advantages of stability, low catalyst loading, and straightforward product separation. Linking molecular catalysts to conductive surfaces provides an opportunity to combine the advantages of both systems.[9]

It is important to understand the nature of catalyst-to-surface binding as orientation can greatly affect electron transfer and substrate access to the active site.[10] In recent years, infrared-visible sum frequency generation (SFG) spectroscopy has emerged as a useful tool for determining the average molecular orientation at surfaces and interfaces.[11-14] As a second-order nonlinear technique, it is only allowed at interfaces that lack an inversion symmetry and is therefore a useful technique for probing complexes adsorbed to solid surfaces. Previously, we have investigated the molecular orientation and vibrational relaxation dynamics of a series of *fac*-Re(dcbpy)$(CO)_3$Cl (dcbpy = 4,4′-dicarboxy-2,2′-bipyridine) CO_2 reduction catalysts on single crystal TiO_2 and gold surfaces.[15-17] These studies indicated that the catalytically active site of the rhenium favorably oriented outwards from the surface and that longer alkyl anchoring chains increased the tilt angle of the catalyst towards the TiO_2 surface.

Considering the great potential and interest in attaching molecular catalysts to electrode surfaces, more attachment strategies need to be investigated. Re-bpy based catalysts are excellent model systems because of their high activity for CO_2 reduction, the wealth of mechanistic information known, and the easy synthetic tunability of the bpy ligand.[18-19] A non-covalent attachment of a Re-bpy catalyst to graphitic carbon demonstrated that strong binding was not necessary for immobilizing an active catalyst[20] and this attachment strategy was successfully employed towards other molecular catalysts as well.[21] However, little is known about how these types of non-covalent attachment strategies affect the orientation of the complexes. This can be investigated using Au electrodes, as Au is well known for its ability to form air-stable self-assembled monolayers (SAMs)[22] with multiple substituents of differing binding strengths.[23] Au is furthermore ideal for our purposes as a commonly used metal surface for SFG spectroscopy.[24] Herein we report spectroscopic and molecular electrochemical studies of Re(R-bpy)$(CO)_3Cl$ (R-bpy = 4,4′-dicyano-2,2′-bipyridine (**1**) 4-cyano-2,2′-bipyridine (**2**)) and characterization of their adsorption onto an Au surface by SFG spectroscopy coupled with DFT simulations.

5.2 Results and Discussion

Synthesis and Characterization of Molecular Catalysis. The ligand 4-cyano-2,2′-bipyridine (CN-bpy) was synthesized as previously reported by the Negishi coupling of 2-pyridylzinc bromide and 2-bromo-4-cyanopyridine.[25] The two complexes Re(diCN-bpy)$(CO)_3Cl$ (**1**) and Re(CN-bpy)$(CO)_3Cl$ (**2**) (Figure 5.1) were synthesized similarly to analogous compounds[26] and characterized by NMR, FTIR, UV-Vis, and elemental analysis. Single crystals suitable for X-ray diffraction studies were grown by slow evaporation of a super-saturated solution of **1** or **2** in dichloromethane (Figure 5.5). A crystallographic data summary and key bond lengths and angles are presented in the Appendix. Previous studies of the

Re(bpy)(CO)$_3$Cl catalysts suggest that electron-withdrawing groups on the bipyridine ligands generally lower the activity of CO$_2$ reduction for catalysis.[27] Thus, we note that **1** and **2** were not expected to be optimal catalysts, but they do represent two of the very few options for catalyst attachment to Au surfaces, namely cyanide,[28] isocyanide,[29] and thiol[30-31] linkages.

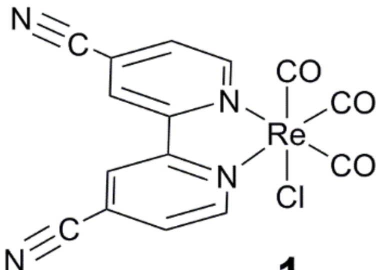

1

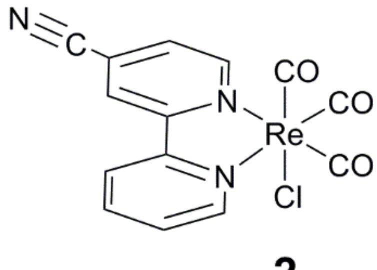

2

Figure 5.1 Re(diCN-bpy)(CO)$_3$Cl (**1**) and Re(CN-bpy)(CO)$_3$Cl (**2**)

Electrochemical experiments in acetonitrile (ACN) solution were conducted to probe the catalytic activity of the unsupported complexes. The cyclic voltammograms (CV) of both **1** and **2** show three one-electron reductive features (Figure 5.2): a quasi-reversible wave followed by two irreversible reductions. At higher scan rates, the second reduction becomes more reversible for **1** (–1.63 V; all potentials vs. Fc/Fc$^+$) indicative of a slow chemical step on the CV time scale. The second reduction for **2** (–1.87 V) as well as the third reductive wave for both complexes (**1**: –2.43 V, **2**: –2.80 V) remain irreversible even at high scan rates (Figures 5.6 and 5.7). Under saturated CO$_2$ conditions (~0.28 M in ACN), current enhancement is observed only at the third reduction. This is in contrast to most previous reported Re-bpy based catalysts, which are catalytically active in their doubly reduced state,[26] although not unprecedented when electron-withdrawing substituents are employed.[32] Comparing the peak current under Ar and CO_2 saturated conditions, **1** is more active than **2** with i_{cat}/i_p values of 8.3 and 6.1 and turn over frequencies (TOF)[33] of 13.3 s^{-1} and 7.2 s^{-1} for **1** and **2**, respectively.

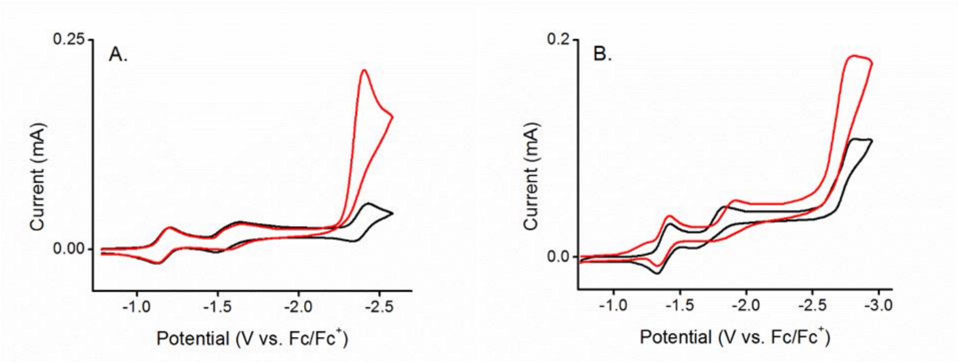

Figure 5.2 Cyclic voltammograms of **1** (a) and **2** (b) under Argon (black) and CO_2 (red).Reductive waves for **1** occur at –1.20 V, –1.63 V, and –2.43 V vs. Fc/Fc^+ and for **2** at –1.41 V, –1.87 V, and –2.80 V vs. Fc/Fc^+. Conditions: 1 mM analyte, 0.1 M $TBAPF_6$ in ACN with a glassy carbon working, Pt counter, and Ag/AgCl pseudo reference electrodes at 100 mV/sec with 1 mM ferrocene added as an internal reference. The current increase of the third reduction under CO_2 is indicative of catalysis.

Controlled potential electrolysis (CPE) with sampling of the headspace for gas chromatography identified the production of CO. Gaseous products were not detected in CPE experiments under inert gas, indicating the CO is a product of catalysis. An FT-IR spectrum was taken of the CPE solution after the experiment, which in addition to showing stretches akin to an intermediate species of the catalyst (as compared to IR-SEC spectra, *vide infra*), a peak at 1684 cm^{-1} was also observed (Figure 5.9). This can be assigned to a carboxyamide stretch, which is most likely a decomposition product from the hydrolysis of the cyano groups. This has also been observed for Re(4-methyl-4′-cyano-2,2′-bipyridine)$(CO)_3Cl$.[34]

Infrared spectroelectrochemistry (IR-SEC) experiments[35] were performed to further characterize the products of catalysis. Under inert (N_2) and catalytic conditions (CO_2 saturation), similar reduced states were observed through the carbonyl and cyano region of the IR spectra for both complexes (Figures 5.10-12). New bands however were observed at 1672 and 1282 cm^{-1}, which correspond with the formation of carbonate (CO_3^{2-}). To confirm the production of CO_3^{2-} as a product of catalysis, the experiment was repeated with $^{13}CO_2$. In the IR-SEC of **2** under these conditions (Figure 5.13) the carbonate bands shifted to lower in energy by 41 and 17 cm^{-1}, respectively, which is close to the shift expected by the harmonic oscillator model (~15 cm^{-1} per bond).[36-37] This indicates CO_3^{2-} is being formed from CO_2 and not labile carbonyl ligands. Due to the weak strength of the expected CO (g) stretch and its possibility to overlap with that of the cyano group (v(CO) 2137 cm^{-1}), carbon monoxide was not definitively detected in these measurements. These results from CPE and IR-SEC experiments indicate the reaction catalyzed is the disproportionation of two equivalents of gaseous CO_2 to CO and CO_3^{2-}.[38] To the best of our knowledge, the thermodynamic potential for the reaction of $2CO_2 + 2e^- \rightarrow CO + CO_3^{2-}$ has not been determined in ACN, most likely due to the unavailable free energy thermodynamic values for carbonate in ACN. The closest approximation for a thermodynamic potential would be for the reaction of $2CO_2 + 2H_2O + 2e^- \rightarrow CO + H_2O + HCO_3^{2-}$ (where $E° = -0.65$ vs. NHE or approximately –1.3 V vs. Fc/Fc$^+$),[39] which is likely occurring due to our electrochemical solutions inescapably having small amounts of H_2O. With this consideration and by using the half wave potential method,[40] these complexes have overpotentials of –1.0 V for **1** and – 1.3 V for **2**.

Further electrochemical studies were performed to access the interactions of **1** and **2** with gold electrodes. As molecular (non-immobilized) catalysts, **1** and **2** behave similarly using an Au electrode as they did using a glassy carbon electrode with almost identical reduction potentials (Figure 5.14), however catalysis could not be observed due to the potential window of Au being more positive than the third reduction of the complexes (ca. –2.3 V vs. Fc/Fc^+ under an atmosphere of CO_2, Figure 5.15). Even at slow scan rates (25 mV/sec) there was no discernible catalyst/surface interaction on the CV time scale. These scans were repeated using a gold coated slide where the complex was adsorbed onto the surface as determined by SFG. No current response for either catalyst was observed in aqueous or organic solvents. This is most likely due to the weak nature of the Au-NC interaction and the large overpotential of the complexes, such that the adsorbed complexes dissociate from the Au surface before any redox features can be observed. We further probed the ability for the SAM to stay on the gold surface in different solvents by gently rinsing a coated slide with various solvents before taking surface measurements. It was found that ACN, ethanol, tetrahydrofuran, water, acetone, chloroform, and dichloromethane all removed the complexes from the surface, thus no further electrochemical measurements were made.

Catalyst Orientation on Au surface by DFT Calculation. Cyano groups have been found to bind weakly with gold,[23] thus a particular geometry of the complexes **1** and **2** on gold surfaces could not be assumed. To determine the lowest energy binding modes to the surface, Density Functional Theory (DFT) with the PW91 functional was used to find optimized geometries of the complexes on an Au(111) model cluster. Several possible binding orientations were investigated under restrictions of at least one cyano group bound to a gold atom.

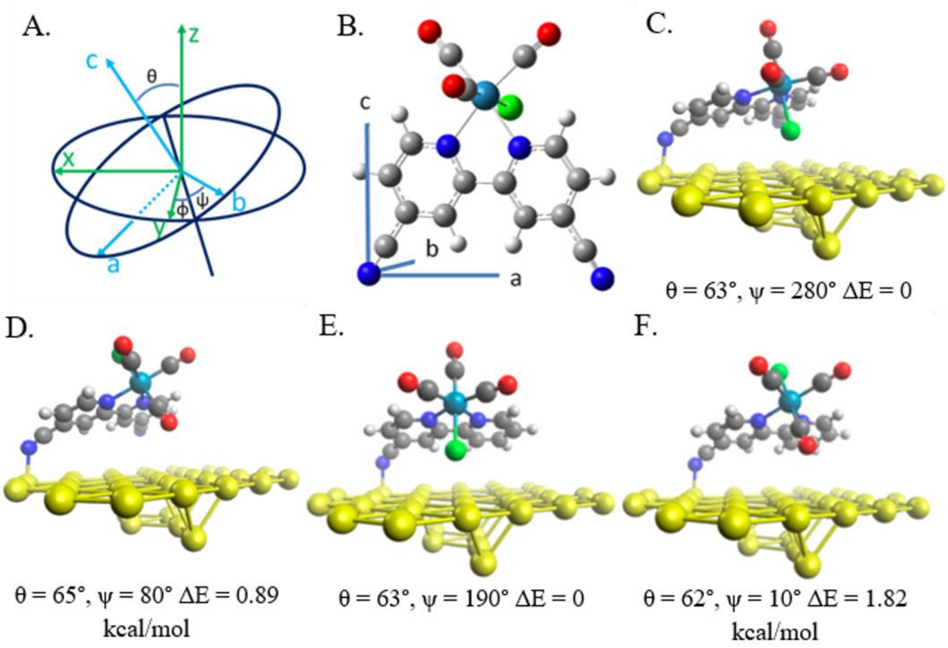

Figure 5.3 (a) Schematic illustration of the orientation angles used to model the complex on the gold thin film surface. Axes x, y and z represent the laboratory coordinates of the gold surface, while a, b and c represents the molecular coordinates of the complex. Orientation angles θ, ψ, and ϕ are the Euler transformation angles between the two Cartesian coordinates in the ZYZ rotation matrix formalism. (b) Molecular axis system for complex **1**. The same axis system is used for complex **2**. (c-f) DFT optimized monodentate geometries for **1** for either Cl facing the surface (c) or CO facing the surface (d). DFT optimized geometries for **2** with Cl facing the surface (e) and CO facing the surface (f). Values indicated are the tilt angle (θ), twist angle (ψ), and the energy (ΔE) relative to the geometry labeled with “ΔE = 0” of that complex.

The DFT-optimized geometries for complexes **1** and **2** are depicted in Figure 5.3. Orientation of the complex is described using angles corresponding to the tilt (θ), twist (ψ), and rotation (ϕ) of the molecule relative to the Au surface (Figure 5.3a). Throughout, the tilt angles (θ) are found to be close to 63°, however the energetic analysis shows that there is no significant preference for which axial ligand faces the surface (CO or Cl) for either complex. This computational tilt angle is in agreement with previous reports of the preference of CN groups to orient parallel to metal surfaces.[41] In the case of complex **1**, both mono- and bidentate (Figure 5.16) cyano binding modes were explored. Starting from the bidentate structure with only one cyano group computationally bound to the surface, letting the N-Au bond relax leads to spontaneous dissociation of the second cyano group. This suggests that monodentate binding is more stable than bidentate binding even though the cyano groups span a similar distance to that between two Au atoms separated by 2 other Au atoms (8.6 Å). The preference for monodentate binding may be due to the added flexibility it offers in getting the axial CO ligand closer to the surface and thus interacting with the Au surface. In the monodentate structure of **1**, the distance between the CO and the nearest Au atom is 3.3 Å while in the bidentate structure it is 3.5 Å, slightly farther. These are similar to recent results obtained of **2** using infrared reflection absorption spectroscopy (IRRAS).[42] In the monodentate structures of **1**, the unattached arm is found tilted about 10° from being in a bidentate configuration (Figure 5.3c-d). To compare to similar complexes that have carboxy linkages to TiO_2,[16] orientations of **1** and **2** were simulated where the bpy ligand is perpendicular to the surface (Figure 5.17). These structures were found to be less stable than the CO facing monodentate structures (Figues 5.3b and 5.3d) by 9.64 and 7.56 kcal/mol for **1** and **2**, respectively, indicating a strong relationship between the binding strength of the anchoring group and the molecular orientation of the complex on the surface.

Orientation Confirmation by SFG Spectroscopy. To determine which of the calculated orientations most likely exist on the surface, SFG measurements were performed to compare to simulated SFG spectra from the DFT optimized structures. The efficacy of using SFG to determine molecular orientation comes from the technique's capability to use the dependencies of the polarization of SFG signal on the vibrational transition moments of the adsorbed species.[11-16] That is, the SFG signal comes from the sum of a constant frequency visible beam and a tunable infrared beam (tunable to the vibrational resonance of the molecule) overlapping at the surface of the material. This creates an output beam, the sum frequency signal, which is the sum of these two input beams. A resonant SFG signal can only be obtained from vibrational modes that are both Raman and IR active, and the intensity of the resulting SFG signals of different normal modes can be used to determine molecular geometry by simulation. Self-assembled monolayers of complexes **1** and **2** were prepared by soaking a cleaned Au coated glass slide in a 1 mM solution of the complex in chloroform for three days. The sample was then washed with ethanol and dried under N_2 before being used for SFG measurements.

The normalized experimental SFG spectra and matching simulated DFT spectra of **1** and **2** are displayed in Figure 5.4. Both experimental spectra were collected under PPP polarization combination (P-polarized SFG, P-polarized visible, P-polarized IR). The resonant signals of the complexes are greatly affected by the strong non-resonant signals from the Au surface, resulting in an “s-shaped” signal.[43] The overlap and differing amplitudes of the carbonyl stretches as well as interference with Au signal in the SFG prevents direct comparisons to the IR spectra, both in shape and band energy assignment. Simulated SFG spectra were found by using the B3LYP functional with the orientation angles from the optimized geometries. Plotting the simulated SFG spectrum (Figure 5.18) with the non-resonant contribution removed against the corresponding experimental IR spectrum shows that there is a significant loss of features in the simulated spectrum as well as a red-shift. Figure 5.19 shows that the SFG amplitudes are highly sensitive to these orientation angles, especially to θ. For example, the symmetric a″(1) stretch loses half of its intensity in going from θ = 0° to θ = 30° (ψ fixed at 80°). The same kind change would require a change of ψ to change from 0° to 60° (θ fixed at 65°).

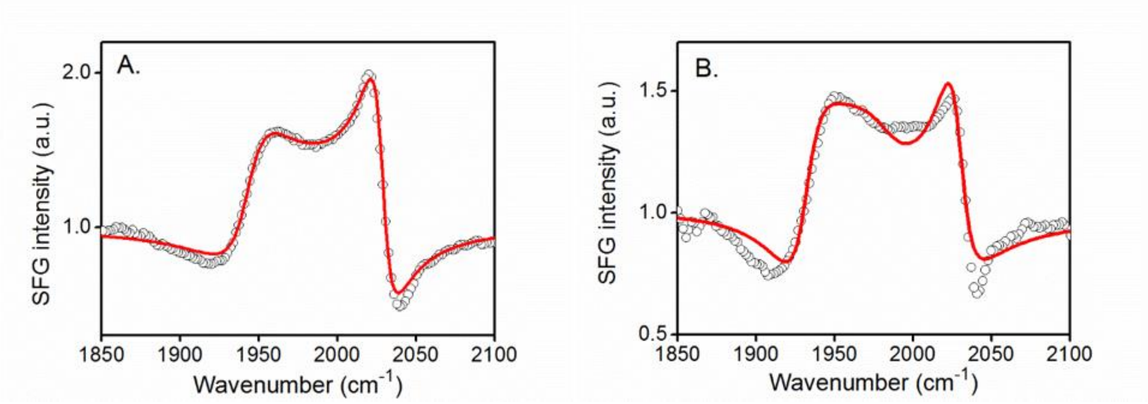

Figure 5.4 Representative PPP-polarized SFG spectra of (a) **1** and (b) **2** monolayers adsorbed onto gold thin films (black circles) with DFT simulations of the SFG spectra (red).

The geometry that most closely related to the experimental SFG data was that of the CO ligand facing the surface for both complexes with monodentate binding (Figure 5.18 and Table 5.3). In order to achieve a more accurate spectral fit, the calculated frequencies were allowed to relax by ± 20 cm^{-1} (Figure 5.4, red line). This corresponds to a 1% error (20 cm^{-1} relative to 2000 cm^{-1}) in the calculated frequency while not changing the expected orientation. The fitted frequencies for complex **1** give an in-phase symmetric a'(1) stretch around 2028 cm^{-1}, an anti-symmetric a'' stretch around 1948 cm^{-1} and an out-of-phase symmetric a'(2) stretch around 1946 cm^{-1}. For complex **2** these stretches are around 2028 cm^{-1}, 1981 cm^{-1} and 1931 cm^{-1}, respectively (other fitting parameters are given in Table 5.4 and spectral data in Table 5.5). According to the spectral shape and the DFT simulations, the a'' and a'(1) modes have amplitudes opposite in sign relative to the a'(2) mode. The a'' mode has an intensity about three times smaller compared to the other two modes, thus the peak near 1960 cm^{-1} originates mostly from the a'(2) mode. As a result, the contribution of the a″ mode in the SFG spectra and the resulting fitted frequency is not as well defined. We found that the non-resonant amplitude (and phase) was about 1.83 (–6°) for complex **1** and 1.02 (17°) for complex **2** indicating the two molecules interact slightly differently with the gold surface.

The calculated SFG spectra from the other optimized geometries had clear differences to rule them out as possible orientations (Figure 5.19). Those with the Cl facing towards the Au surface led to SFG spectra with a strong intensity a'(2) stretch and almost no intensity from the other two modes. Bidentate binding of complex **1** was ruled out based on the mismatched intensities. The SFG spectra also rule out bidentate binding as the non-zero value of the a'' stretch indicates a twist relative to the surface that could not be achieved if both cyano groups adsorbed onto Au. The differences in the spectra in Figure 5.4 for **1** and **2** despite their similar binding modes are due to the sensitivity of SFG to slight differences in orientations. Figure 5.20 shows that using the orientation angles for **2** makes the SFG spectrum for **1** resemble that of **2**.

It is important to note that in this calculation we have used the hyperpolarizability calculated for isolated molecules. If there exists strong intermolecular interaction due to close proximity of molecules on surface, the hyperpolarizability tensor elements may change, which would affect the orientations determined from fitting the SFG spectra. This possibility cannot be excluded, although it is not very likely according to the preferred binding geometry shown in Figure 5.3.

5.3 Conclusions

We have determined the binding geometries of a pair of molecular electrocatalysts bound to Au(111) by combining SFG spectroscopy and DFT calculations of SFG spectra. The complexes Re(diCN-bpy)$(CO)_3Cl$ and Re(CN-bpy)$(CO)_3Cl$ were found to be catalytically active towards CO_2 in their triply reduced states, generating equimolar amounts of carbon monoxide and carbonate. No electrochemical behavior was observed from immobilized **1** or **2** on an Au surface, as the weak binding nature of the Au-NC interaction coupled with the large overpotential of the catalysts led to dissociation of the complexes from the surface before any redox features could be observed. Under no applied potential, both complexes orient into an adsorbed monolayer on Au surfaces as characterized by SFG. Based on DFT optimized geometries, the weak binding of the cyano groups to Au surfaces lends to a large tilt angle, orienting the bpy ligand more parallel to the surface with the axial chloride facing up, a favorable orientation for redox state transitions and catalysis. The similar binding orientation of both complexes and the lack of bidentate binding of Re(diCN-bpy)$(CO)_3Cl$ (**1**) demonstrates that only one anchoring group may be needed for the attachment of molecular catalysts to conductive surfaces. These conclusions highlight the strength of the methodology coupling DFT with SFG spectroscopy to determine and verify the binding modes and orientations of transition metal electrocatalysts on metallic electrodes, demonstrating the careful balance between active molecular catalysts and attachment strategies, both of which are needed to create a deployable CO_2 reduction system.

5.4 Experimental

General Experimental Considerations. ^1H and ^{13}C NMR spectra were recorded at 298K on a Varian 500 MHz spectrometer. ^1H chemical shifts are reported relative to TMS ($\delta = 0$) by referencing to deuterated solvent shifts. FT-IR spectra were performed on a Thermo Scientific Nicolet 6700 and UV-Vis-NIR data were collected on a Shimadzu UV 3600 spectrophotometer using Starna Standard open top 10 mm path length cuvettes. Microanalyses were performed by NuMega Resonance Labs, San Diego, CA for C, H, and N.

Reagents. Solvents were obtained from Fisher Scientific (and used as received) unless otherwise noted and deuterated solvents and $^{13}CO_2$ (g) were obtained from Cambridge Isotope Laboratories. Electrochemistry and spectroscopy solvents were degassed with argon, dried over alumina, and dispensed by a custom made solvent dispensing system. Reagents were obtained from commercially available sources; pentacarbonylchlororhenium(I) from Sigma Aldrich, 2-pyridylzinc bromide solution 0.5 M in THF from Acros Organics, tetrakis(triphenylphosphine)palladium(0) from Strem Chemicals, 4,4′-dicyano-2,2′-bipyridine was from Carbosynth Limited, and 2-bromoisonicotinonitrile from Matrix Scientific. Tetrabutylammonium hexafluorophosphate (TBAPF$_6$, Aldrich, 98%) was recrystallized twice from methanol and dried at 90°C overnight before use in electrochemistry experiments. The ligand 4-cyano-2,2′-bipyridine was synthesized according to literature procedure.[25]

Synthesis of Re(bpy-R)(CO)$_3$Cl complexes. Analogous to similar previously reported complexes,[26] an oven-dried round-bottom flask was charged with equal molar equivalents of Re(CO)$_5$Cl and bipyridine ligand. Dry toluene (20 mL) was then added and the solution was heated to reflux for three hours under a nitrogen atmosphere. The mixture was cooled in the freezer before filtering and washing with cold pentane to collect the desired solid product, which was dried overnight in a vacuum oven at ~80°C.

Re(4,4′-dicyano-2,2′-bipyridine)(CO)$_3$Cl (1) Reaction of Re(CO)$_5$Cl (177mg, 0.489 mmol) with 4,4′-dicyano-2,2′-bipyridine (101 mg, 0.489 mmol) to yield a bright red-orange powder (236mg, 94% yield). ^{1}H NMR (CD$_3$CN) δ = 9.22 (sh d, J = 6, 2H), 8.76 (sh s, 2H), 7.95 (sh d, J = 6, 2H). ^{13}C{H} NMR (CD$_3$CN) 156.54, 155.18, 130.82, 128.17, 124.36, 116.15 . IR (ACN) ν(CO) 2027 cm^{-1}, 1927 cm^{-1}, and 1911 cm^{-1}. IR (KBr pellet) ν(CO) 2027 cm^{-1}, 1926 cm^{-1}, 1889 cm^{-1}, ν(CN) 2245 cm^{-1}. UV-Vis (ACN) λ_{max}/nm = 221, 246, 312, 435. ESI-MS (*m/z*) [M – H]$^-$: calcd: 511.0; found: 511.1. Elemental analysis for complex with one DCM molecule $C_{16}H_8Cl_3N_4O_3Re$ calcd: C 32.20, H 1.35, N 9.39; found: C 32.16; H 1.55; N 9.48. Single crystals suitable for X-ray diffraction were grown by slow evaporation of a super saturated solution of **1** in dichloromethane. Faradaic efficiency during bulk electrolysis for CO was 18% ± 5% over three runs.

Re(4-cyano-2,2′-bipyridine)(CO)$_3$Cl (2) Reaction of Re(CO)$_5$Cl (260mg, 0.719 mmol) with 4-cyano-2,2′-bipyridine (130 mg, 0.719 mmol) to yield a bright orange powder (257mg, 73% yield). ^{1}H NMR (CD$_3$CN) δ = 9.19 (d, 1H), 9.04 (d, 1H), 8.77 (s, 1H), 8.45 (d, 1H), 8.25 (t, 1H), 7.89 (d, 1H), 7.69 (t, 1H). ^{13}C{H} NMR (CD$_3$CN) 157.84, 155.13, 154.81, 154.17, 141.16, 129.87, 129.27, 127.54, 125.53, 124.02, 116.24. IR (ACN) ν(CO) 2025 cm^{-1}, 1922 cm^{-1}, and 1905 cm^{-1}. IR (KBr pellet) ν(CO) 2024 cm^{-1}, 1913 cm^{-1}, 1894 cm^{-1}, ν(CN) 2240 cm^{-1}. UV-Vis (ACN) λ_{max}/nm = 243, 305, 403. ESI-MS (*m/z*) [M – H]$^-$: calcd: 486.0; found: 486.1. Elemental analysis for $C_{14}H_7ClN_3O_3Re$ calcd: C 34.54, H 1.45, N 8.63; found: C 34.47, H 1.50, N 8.53; Single crystals suitable for X-ray diffraction were grown from vapor diffusion of diethyl ether into a saturated solution of **2** in dichloromethane. Faradaic efficiency during bulk electrolysis for CO was 41% ± 2% over three runs.

X-Ray Crystallography. Single crystal X-ray diffraction studies were carried out on a Bruker Kappa APEX-II CCD diffractometer equipped with Mo Kα radiation (λ = 0.71073 Å) or a Bruker Kappa APEX CCD diffractometer equipped with Cu Kα radiation (λ = 1.54184 Å). The crystals were mounted on a Cryoloop with Paratone oil and data were collected under a nitrogen gas stream at 100(2) K using ω and ϕ scans. Data were integrated using the Bruker SAINT software program and scaled using the SADABS software program. Solution by direct methods (SHELXS) produced a complete phasing model consistent with the proposed structure. All non-hydrogen atoms were refined anisotropically by full-matrix least-squares (SHELXL-97).[44]

Homogeneous Electrochemistry. Electrochemical experiments were performed on a BASi Epsilon potentiostat. A single compartment cell was used consisting of a 1 mm glassy carbon electrode or 1 mm gold electrode, Pt wire counter electrode, and an Ag/AgCl reference electrode (separated from the solution by a CoralPor tip). Cyclic voltammograms were performed at room temperature using a 5 mL acetonitrile solution of 1 mM of the complex, 0.1 M TBAPF$_6$ as the electrolyte, and 1 mM ferrocene as the internal reference. The solutions were purged with dried Ar or CO$_2$ and stirred before each experiment. Cyclic voltammograms are reported at a scan rate of 100 mV/sec and referenced to ferrocene unless otherwise noted. Uncompensated resistance between the working and reference electrodes was corrected by using iR compensation on the potentiostat. Scan-rate dependence studies for each complex were carried out to ensure the homogeneity of the system (see supporting information). To determine i_{cat}/i_p, the i_p is determined as the peak current under Ar of a reversible electron transfer, which in this case is the 1st reduction. The peak catalytic current (i_{cat}) is determined by the highest point of the catalytic wave (under CO_2 atmosphere).

Bulk Electrolysis. Bulk electrolysis was performed in a custom threaded 60 mL single-compartment cell with a custom air-tight Teflon top. The setup consists of a carbon rod working electrode, coiled Pt wire counter electrode (protected from the bulk solution by fritted glass), and an Ag/AgCl pseudoreference electrode (separated from solution by a CoralPor tip). The ACN solution (~40 mL) consisted of 0.1 $TBAPF_6$ and 1 mM complex, sparged with either Ar or CO_2. Solutions were constantly stirred and protected from light during the experiment. The voltage chosen for electrolysis was that of slightly past the third reduction in cyclic voltammetry. Experiments were set to have the catalyst undergo four turnovers, each passing roughly 33 Coulombs. Gas analysis was performed by sampling 1 mL of the headspace of the cell at the end of each experiment and injecting on a Hewlett-Packard 7890A series gas chromatograph with two molsieve columns (30 m × 0.53 mm i.d. × 25 μm film). The 1 mL injection was split between two columns, one with N_2 carrier gas and the other He to quantify both CO and H_2, respectively. Instrument specific calibration curves were used to determine amount of each gas produced.

Infrared Spectroelectrochemistry (IR-SEC). IR-SEC experiments were carried out in a custom made cell[35] with a glassy carbon working, platinum counter, and pseudoreference silver electrode. A N_2 sparged solution of 0.3 mM complex in 0.1 M $TBAPF_6$ in ACN was used and a blank solution of 0.1 M $TBAPF_6$ in ACN was used for the FTIR solvent subtractions. For experiments under CO_2 or $^{13}CO_2$, the solution was saturated with the gas (~0.28 M) directly before use. A Pine Instrument Company model AFCBP1 bipotentiostat was used to apply potential to the system.

Preparation of Au Slides and Surface Attachment. Optically flat Au substrates consisting of a layer of Cr (1-4 nm) and Au (200-300 nm) evaporated onto borosilicate glass slides were used. For surface attachment of the catalysts, all Au substrates were cleaned using a Bunsen burner method.[45] The Au slide was then cooled under a stream of N_2 before being immediately submersed in a 1 mM solution of **1** or **2** in chloroform and stored in the dark for one to three days. The slide was then removed from solution, washed with pentane, and dried under N_2 before immediate use. The samples were stored overnight in the dark before SFG measurements.

SFG Spectroscopy. The broadband vibrational SFG setup is based on a 1 kHz Spitfire Ti:Sapphire regenerative amplifier system (Spectra Physics) producing 150 fs pulses at 800 nm (12,500 cm^{-1}) with a pulse energy of 4 mJ. Half of the fundamental was used to pump a TOPAS-COPA (Light Conversion) producing tunable IR pulses, centered near 2000 cm^{-1}, with energies of ~10-15 μJ and a bandwidth of ~150 cm^{-1}. The remaining 2 mJ of 800 nm output was spectrally narrowed to ~10 cm^{-1} by using a home-built pulse shaper. The visible pulses were filtered to 2 μJ and combined with the IR at the sample surface. The angle of incidence of visible and IR are 65° and 50° with respect to the surface normal, respectively. The reflected sum frequency signal was collimated and filtered to remove any residual IR and fundamental visible photons before being refocused onto the slit of an 300 mm monochromator (Acton Spectra-Pro 300i) and detected with an liquid nitrogen-cooled CCD (Princeton Instruments, PyLoN, 1340 × 100 pixels) operating at –120 °C. All spectra were collected under PPP polarization combination (P-polarized SFG, P-polarized visible, P-polarized IR). The SFG intensity $I_{SFG,N}$ can be expressed as[43, 46-47]

$$I_{SFG}\propto\left|\chi^{(2)}_{NR}+\chi^{(2)}_{R}\right|^2 I_{IR}I_{vis}=\left|A^{(2)}_{NR}e^{i\delta}+\sum_q A^{(2)}_{q,eff}\frac{1}{\omega_{IR}-\omega_q+i\Gamma_q}\right|^2 I_{IR}I_{vis} \qquad (\mathbf{E5.1})$$

Where $\chi^{(2)}_{R}$ and $\chi^{(2)}_{NR}$ are the effective resonant and non-resonant nonlinear susceptibility tensors, respectively, I_{IR} (I_{vis}) the intensity of IR (visible) beam, δ and A_{NR} the phase and amplitude of the non-resonant signal, A_q ω_q and Γ_q the amplitude of effective resonant susceptibility, frequency and damping constant of the *q*th vibrational mode, respectively, and ω_{IR} the frequency of the incident tunable infrared beam. To remove the contribution of frequency dependence of the incident beam, we have defined a normalized SFG spectra (S_{SFG}) according to equation (E5.2), in which the sample SFG spectra was normalized by the SFG spectra of a bare gold thin film (I_{Au}) measured under the same condition.

$$S_{SFG}=\frac{I_{SFG}}{I_{Au}}=\frac{\left|A^{(2)}_{NR}e^{i\delta}+\sum_q A^{(2)}_{q,eff}\frac{1}{\omega_{IR}-\omega_q+i\Gamma_q}\right|^2}{\left|A^{(2)}_{NR}\right|^2} \qquad (\mathbf{E5.2})$$

It was observed that the non-resonant signals from gold thin films decrease with complexes **1** or **2** adsorbed on the surfaces. The reason for this change is unclear;

we speculate that it likely reflects an adsorption-induced change of the surface electronic density of states in gold. For convenience, the intensity of SFG spectra of bare gold have been rescaled to yield a normalized SFG signal such that the normalized the S_{SFG}=1 when the signal is dominated by nonresonant Au response. In the discussion below, only these normalized SFG spectra are shown and analyzed.

DFT Geometry Optimization. Density functional theory (DFT) calculations were carried out with the local PW91[48-52] functional using the Gaussian 2009 software package[53] and its default integration grid and optimization criteria. The 6-31G(d) basis set[54-55] was used on nonmetal atoms i.e. C, H. N, Cl, and O. The LANL2DZ[56-58] pseudo-potential and basis set was used on metal atoms i.e. Re and Au. Automated density fitting[59-60] was used to quicken the calculations. The system was treated as a restricted neutral singlet with Re(I) and an even number of Au atoms. Images for these calculations were generated using Avogadro 1.1.1.[61]

The Au(111) surface, an approximate model for the bulk Au used in the experiments, was prepared as follows using the gradient-corrected PBE level of theory with a single zeta quality basis set within the plane-wave pseudopotential scheme as implemented in the SIESTA software package. As a first step, bulk Au was optimized starting with a four-atom bulk Au cell and calculating minimum energy lattice parameters and fractal atomic coordinates. The optimized bulk cell parameters were used to construct a supercell containing an Au(111) slab with four layers of Au atoms in a 4 × 6 (11.8 Å × 17.8 Å) supercell. Periodic boundary constraints were used with Gamma point sampling corresponding to a single k-point for the supercell. Plane-waves were given a kinetic energy cut-off of 200 Ry. Geometry optimization was with a force tolerance of 0.004 eV/Å while freezing all Au atoms. This slab was then carved into a cluster of 32 atoms (27 below the complex and 5 below more below that) ensuring that the axial ligand can face the surface without passing the edge of the cluster.

For the geometry optimizations, all gold atoms were frozen to closer approximate surface conditions. Additionally, the N atom of the cyano N-Au bond was arbitrarily frozen around 2.134 Å (complex **1**) or 2.083 Å (complex **2**) from the Au atom for monodentate binding. Similarly, two N atoms were frozen around 2.134 Å and 2.165 Å from the Au atoms for bidentate binding. These restrictions were needed to prevent unrealistic edge effects from occurring due to the small size of the cluster.

Theoretical Simulation of SFG. The macroscopic second order susceptibility can be separated into specific tensor components for each normal mode, *q*, with corresponding Fresnel factors as shown in Equation E5.3.

$$\chi^{(2)}_{ppp} = \sum_q \left(-L_{xxz}\chi^{(2)}_{xxz,q} - L_{xzx}\chi^{(2)}_{xzx,q} + L_{zxx}\chi^{(2)}_{zxx,q} + L_{zzz}\chi^{(2)}_{zzz,q}\right) \qquad \textbf{(E5.3)}$$

Here, L_{ijk} (i,j,k=x,y,z) are products of the Fresnel factors of the IR, visible and SFG beam at the experimental incident angles, which can be calculated from the known complex reflective index of Au (see Table 5.6).

The microscopic molecular tensor components are determined by Equation E5.4,

$$\chi^{(2)}_{ijk,q} = \sum_{l,m,n} \langle R_{il} R_{jm} R_{kn} \rangle A_{lmn,q} \qquad \textbf{(E5.4)}$$

where $A_{lmn,q}$ is the molecular hyperpolarizability tensor element for each normal mode, *q*, and $\langle R_{il}R_{jm}R_{kn}\rangle$ is the average product of the Euler transformation matrix components. Molecular reference frame Cartesian axes (*l,m,n*) for **1** and **2** are depicted in Figure 5.3a and b. Molecular rotation is performed via the $Z_{\phi}Y_{\theta}Z_{\psi}$ rotation matrix, where the θ angle is the tilt angle, the ψ angle is the twist angle, and the ϕ angle is the final spin angle. Complexes in a laboratory setting are assumed to be distributed isotropically on the surface of Au, therefore, χ is averaged of all ϕ angles 0° –359° in increments of 5° in the simulated SFG polarized spectra.

Molecular hyperpolarizability tensor elements are determined by the partial derivatives of the polarizabilities α_{lm} and dipole moments μ_n with respect to the coordinate, Q, of a given normal mode, *q*, as shown in Equation E5.5.

$$A_{lmn,q}= \frac{\partial\alpha_{lm}}{\partial Q_q}\frac{\partial\mu_n}{\partial Q_q} \qquad \textbf{(E5.5)}$$

Polarizability derivatives and dipole moment derivatives with respect to normal mode coordinates were obtained from *ab initio* molecular orbital calculations. Geometry optimization, energy minimization and vibrational normal mode analysis were performed for gas phase complexes using DFT. These were carried out with the hybrid B3LYP[62-65] functional using Gaussian 2009[53] and its default integration grid and optimization criteria. The 6-311+G(d) basis set[54-55] was used on nonmetal atoms i.e. C, H. N, Cl, and O. The SDD pseudopotential and basis set[66] was used on the Re atom. Images for these calculations were generated using GaussView.[67] Theoretical frequencies were scaled by 0.975.

The SFG spectra of the sample have been fitted according to Equation E5.2-4 with theoretically derived amplitudes ($A_{lmn,q}$) from the PW91 cluster geometries. A_{NR}, Γ_q, and orientation angles (θ and ψ) are fitting parameters. Γ_q determines the width of the resonant peaks. A_{NR} is used as a scaling factor to ensure that the overall amplitude of computed SFG spectra match the experimental values. The relative SFG amplitudes of the three CO stretching modes are determined by the relative values of computed $A_{lmn,q}$ and orientation angles (θ and ψ). The angular dependence enables us to determine molecular orientation by comparing the measured and computed SFG spectra.

The fitting parameters listed in Table 5.4 were obtained allowing frequencies to relax (Figure 5.4) while parameters obtained for fixed frequencies are listed in Table 5.3 (Figure 5.18). For complex **2**, the frequencies relaxed within ± 20 cm^{-1}. The nonresonant amplitudes were restricted to be positive and the damping constants were restricted to be between 0 and 25.

5.5 Acknowledgements

This chapter, in full, comes directly from a manuscript entitled: "Orientation of Cyano-Substituted Bipyridine Re(I) *fac*-Tricarbonyl Electrocatalysts Bound to Conducting Au Surfaces" by Melissa L. Clark, Benjamin Rudshteyn, Aimin Ge, Steven A. Chabolla, Charles W. Machan, Brain T. Psciuk, Jia Song, Gabriele Canzi, Tianquan Lian, Victor S. Batista, and Clifford P. Kubiak, which has been published in *The Journal of Physical Chemistry C*, **2016**, *120(3)*, 1657-1665.

http://dx.doi.org/10. 1021/acs.jpcc.5b10912. The dissertation author is the primary author of this manuscript.

This material is based upon work supported by AFOSR Grant #FA9550-13-1-0020. S.C. acknowledges support from a NSF GRFP award. B.R. acknowledges support from the National Science Foundation Graduate Research Fellowship under Grant No. DGE-1122492. V.S.B. acknowledges computer time from the supercomputing facilities at Yale as well as at NERSC. M.L.C. thanks Tram Dang for assistance with gold sample preparation. The authors would also like to thank Dr. Arnold Rheingold and Dr. Curtis Moore for their assistance with X-ray crystallography, the UCSD Chemistry & Biochemistry Molecular MS Facility for mass spectrometry analyses, and Dr. Wendu Ding and Dr. Ke R. Yang for their advice on the calculations.

5.6 References

(1) Whipple, D. T.; Kenis, P. J. A., *J. Phys. Chem. Lett.* **2010**, *1*, 3451.

(2) Hori, Y.; Kikuchi, K.; Suzuki, S., *Chem. Lett.* **1985**, 1695.

(3) Hori, Y., *Mod. Asp. Electrochem.* **2008**, *42*, 89.

(4) Benson, E. E.; Kubiak, C. P.; Sathrum, A. J.; Smieja, J. M., *Chem. Soc. Rev.* **2009**, *38*, 89.

(5) Windle, C. D.; Perutz, R. N., *Coord. Chem. Rev.* **2012**, *256*, 2562.

(6) Qiao, J.; Liu, Y.; Hong, F.; Zhang, J., *Chem. Soc. Rev.* **2014**, *43*, 631.

(7) Kumar, B.; Llorente, M.; Froehlich, J.; Dang, T.; Sathrum, A.; Kubiak, C. P., *Ann. Rev. Phys. Chem.* **2012**, *63*, 541.

(8) Appel, A. M.; Bercaw, J. E.; Bocarsly, A. B.; Dobbek, H.; DuBois, D. L.; Dupuis, M.; Ferry, J. G.; Fujita, E.; Hille, R.; Kenis, P. J.; Kerfeld, C. A.; Morris, R. H.;

Peden, C. H.; Portis, A. R.; Ragsdale, S. W.; Rauchfuss, T. B.; Reek, J. N.; Seefeldt, L. C.; Thauer, R. K.; Waldrop, G. L., *Chem. Rev.* **2013**, *113*, 6621.

(9) Wrighton, M. S., *Science* **1986**, *231*, 32.

(10) Prezhdo, O. V.; Duncan, W. R.; Prezhdo, V. V., *Acc. Chem. Res.* **2008**, *41*, 339.

(11) Chen, Z.; Shen, Y. R.; Somorjai, G. A., *Ann. Rev. Phys. Chem.* **2002**, *53*, 437.

(12) Shen, Y. R., *Ann. Rev. Phys. Chem.* **2013**, *64*, 129.

(13) Johnson, C. M.; Baldelli, S., *Chem. Rev.* **2014**, *114*, 8416.

(14) Wang, H. F.; Velarde, L.; Gan, W.; Fu, L., *Ann. Rev. Phys. Chem.* **2015**, *66*, 189.

(15) Anfuso, C. L.; Xiao, D. Q.; Ricks, A. M.; Negre, C. F. A.; Batista, V. S.; Lian, T. Q., *J. Phys. Chem. C* **2012**, *116*, 24107.

(16) Anfuso, C. L.; Snoeberger, R. C., 3rd; Ricks, A. M.; Liu, W.; Xiao, D.; Batista, V. S.; Lian, T., *J. Am. Chem. Soc.* **2011**, *133*, 6922.

(17) Anfuso, C. L.; Ricks, A. M.; Rodríguez-Córdoba, W.; Lian, T., *J. Phys. Chem. C* **2012**, *116*, 26377.

(18) Grice, K. A.; Kubiak, C. P., Chapter five - Recent studies of rhenium and manganese bipyridine carbonyl catalysts for the electrochemical reduction of CO_2. In *Advances in Inorganic Chemistry*, Michele, A.; Rudi van, E., Eds. Academic Press: 2014; Vol. 66, 163-188.

(19) Keith, J. A.; Grice, K. A.; Kubiak, C. P.; Carter, E. A., *J. Am. Chem. Soc.* **2013**, *135*, 15823.

(20) Blakemore, J. D.; Gupta, A.; Warren, J. J.; Brunschwig, B. S.; Gray, H. B., *J. Am. Chem. Soc.* **2013**, *135*, 18288.

(21) Kang, P.; Zhang, S.; Meyer, T. J.; Brookhart, M., *Angew. Chem. Intl. Ed.* **2014**, *53*, 8709.

(22) Dubois, L. H.; Nuzzo, R. G., *Ann. Rev. Phys. Chem.* **1992**, *43*, 437.

(23) Kiguchi, M.; Miura, S.; Hara, K.; Sawamura, M.; Murakoshi, K., *Appl. Phys. Lett.* **2006**, *89*, 213104.

(24) Bain, C. D., *J. Chem. Soc., Faraday Trans.* **1995**, *91*, 1281.

(25) Fang, Y.-Q.; Hanan, G. S., *Synlett* **2003**, *2003*, 0852.

(26) Smieja, J. M.; Kubiak, C. P., *Inorg. Chem.* **2010**, *49*, 9283.

(27) Benson, E. E.; Grice, K. A.; Smieja, J. M.; Kubiak, C. P., *Polyhedron* **2013**, *58*, 229.

(28) Mishchenko, A.; Zotti, L. A.; Vonlanthen, D.; Burkle, M.; Pauly, F.; Cuevas, J. C.; Mayor, M.; Wandlowski, T., *J. Am. Chem. Soc.* **2011**, *133*, 184.

(29) Angelici, R. J.; Lazar, M., *Inorg. Chem.* **2008**, *47*, 9155.

(30) de la Llave, E.; Herrera, S. E.; Méndez De Leo, L. P.; Williams, F. J., *J. Phys. Chem. C* **2014**, *118*, 21420.

(31) Ferrence, G. M.; Henderson, J. I.; Kurth, D. G.; Morgenstern, D. A.; Bein, T.; Kubiak, C. P., *Langmuir* **1996**, *12*, 3075.

(32) Cosnier, S.; Deronzier, A.; Moutet, J. C., *New J. Chem.* **1990**, *14*, 831.

(33) Smieja, J. M.; Sampson, M. D.; Grice, K. A.; Benson, E. E.; Froehlich, J. D.; Kubiak, C. P., *Inorg. Chem.* **2013**, *52*, 2484.

(34) Mecchia Ortiz, J. H.; Morán Vieyra, F. E.; Borsarelli, C. D.; Romero, I.; Fontrodona, X.; Parella, T.; Lis de Katz, N. D.; Fagalde, F.; Katz, N. E., *Eur. J. Inorg. Chem.* **2014**, *2014*, 3359.

(35) Machan, C. W.; Sampson, M. D.; Chabolla, S. A.; Dang, T.; Kubiak, C. P., *Organometallics* **2014**, *33*, 4550.

(36) Machan, C. W.; Chabolla, S. A.; Yin, J.; Gilson, M. K.; Tezcan, F. A.; Kubiak, C. P., *J. Am. Chem. Soc.* **2014**, *136*, 14598.

(37) Simón-Manso, E.; Kubiak, C. P., *Organometallics* **2005**, *24*, 96.

(38) Sullivan, B. P.; Bolinger, C. M.; Conrad, D.; Vining, W. J.; Meyer, T. J., *J. Chem. Soc., Chem. Commun.* **1985**, 1414.

(39) Costentin, C.; Drouet, S.; Robert, M.; Saveant, J. M., *Science* **2012**, *338*, 90.

(40) Appel, A. M.; Helm, M. L., *ACS Catal.* **2014**, *4*, 630.

(41) Parker, G. K.; Hope, G. A., *ECS Transactions* **2010**, *28*, 223.

(42) Wang, J.; Clark, M. L.; Li, Y.; Kaslan, C. L.; Kubiak, C. P.; Xiong, W., *J. Phys. Chem. Lett.* **2015**, *6*, 4204.

(43) Lambert, A. G.; Davies, P. B.; Neivandt, D. J., *Appl. Spectrosc. Rev.* **2005**, *40*, 103.

(44) Sheldrick, G., *Acta Cryst. A* **2008**, *64*, 112.

(45) Nogues, C.; Wanunu, M., *Surf. Sci.* **2004**, *573*, L383.

(46) Wang, H.-F.; Gan, W.; Lu, R.; Rao, Y.; Wu, B.-H., *Int. Rev. Phys. Chem.* **2005**, *24*, 191.

(47) Zhuang, X.; Miranda, P.; Kim, D.; Shen, Y., *Phys. Rev. B* **1999**, *59*, 12632.

(48) Burke, K.; Perdew, J. P.; Y. Wang, Y., In *Electronic Density Functional Theory: Recent Progress and New Directions*, Dobson, J. F.; Vignale, G.; Das., M. P., Eds. Plenum: Berlin, 1998; 11-20.

(49) Perdew, J. P.; Chevary, J. A.; Vosko, S. H.; Jackson, K. A.; Pederson, M. R.; Singh, D. J.; Fiolhais, C., *Phys. Rev. B: Condens. Matter* **1993**, *48*, 4978.

(50) Perdew, J. P.; Chevary, J. A.; Vosko, S. H.; Jackson, K. A.; Pederson, M. R.; Singh, D. J.; Fiolhais, C., *Phys. Rev. B: Condens. Matter* **1992**, *46*, 6671.

(51) Perdew, J. P.; Burke, K.; Ernzerhof, M., *Phys. Rev. Lett.* **1997**, *78*, 1396.

(52) Perdew, J. P.; Burke, K.; Ernzerhof, M., *Phys. Rev. Lett.* **1996**, *77*, 3865.

(53) Frisch, M. J.; Trucks, G. W.; Schlegel, H. B.; Scuseria, G. E.; Robb, M. A.; Cheeseman, J. R.; Scalmani, G.; Barone, V.; Mennucci, B.; Petersson, G. A.; Nakatsuji, H.; Caricato, M.; Li, X.; Hratchian, H. P.; Izmaylov, A. F.; Bloino, J.; Zheng, G.; Sonnenberg, J. L.; Hada, M.; Ehara, M.; Toyota, K.; Fukuda, R.; Hasegawa, J.; Ishida, M.; Nakajima, T.; Honda, Y.; Kitao, O.; Nakai, H.; Vreven, T.; Montgomery, J. A., Jr.; ; Peralta, J. E.; Ogliaro, F.; Bearpark, M.; Heyd, J. J.; Brothers, E.; Kudin, K. N.; Staroverov, V. N.; Kobayashi, R.; Normand, J.; Raghavachari, K.; Rendell, A.; Burant, J. C.; Iyengar, S. S.; Tomasi, J.; Cossi, M.; Rega, N.; Millam, N. J.; Klene, M.; Knox, J. E.; Cross, J. B.; Bakken, V.; Adamo, C.; Jaramillo, J.; Gomperts, R.; Stratmann, R. E.; Yazyev, O.; Austin, A. J.; Cammi, R.; Pomelli, C.; Ochterski, J. W.; Martin, R. L.; Morokuma, K.; Zakrzewski, V. G.; Voth, G. A.; Salvador, P.; Dannenberg, J. J.; Dapprich, S.; Daniels, A. D.; Farkas, Ö.; Foresman, J. B.; Ortiz, J. V.; Cioslowski, J.; Fox, D. J. *Gaussian 09*, Gaussian, Inc.: Wallingford, CT, 2009.

(54) McLean, A. D.; Chandler, G. S., *J. Chem. Phys.* **1980**, *72*, 5639.

(55) Krishnan, R.; Binkley, J. S.; Seeger, R.; Pople, J. A., *J. Chem. Phys.* **1980**, *72*, 650.

(56) Hay, P. J.; Wadt, W. R., *J. Chem. Phys.* **1985**, *82*, 270.

(57) Hay, P. J.; Wadt, W. R., *J. Chem. Phys.* **1985**, *82*, 299.

(58) Wadt, W. R.; Hay, P. J., *J. Chem. Phys.* **1985**, *82*, 284.

(59) Dunlap, B., *J. Chem. Phys.* **1983**, *78*, 3140.

(60) Dunlap, B., *J. Mol. Struct.* **2000**, *529*, 37.

(61) Hanwell, M. D.; Curtis, D. E.; Lonie, D. C.; Vandermeersch, T.; Zurek, E.; Hutchison, G. R., *J. Cheminform.* **2012**, *4*, 17.

(62) Stephens, P. J.; Devlin, F. J.; Chabalowski, C. F.; Frisch, M. J., *J. Phys. Chem.* **1994**, *98*, 11623.

(63) Becke, A. D., *J. Chem. Phys.* **1993**, *98*, 5648.

(64) Lee, C. T.; Yang, W. T.; Parr, R. G., *Phys. Rev. B: Condens. Matter* **1988**, *37*, 785.

(65) Vosko, S. H.; Wilk, L.; Nusair, M., *Can. J. Phys.* **1980**, *58*, 1200.

(66) Dolg, M.; Wedig, U.; Stoll, H.; Preuss, H., *J. Chem. Phys.* **1987**, *86*, 866.

(67) Dennington, R.; Keith, T.; Millam, J. *GaussView, Version 5*, Semichem Inc.: Shawnee Mission, KS, 2009.

(68) Olmon, R. L.; Slovick, B.; Johnson, T. W.; Shelton, D.; Oh, S.-H.; Boreman, G. D.; Raschke, M. B., *Physical Review B: Condensed Matter* **2012**, *86*, 235147.

5.7 Appendix

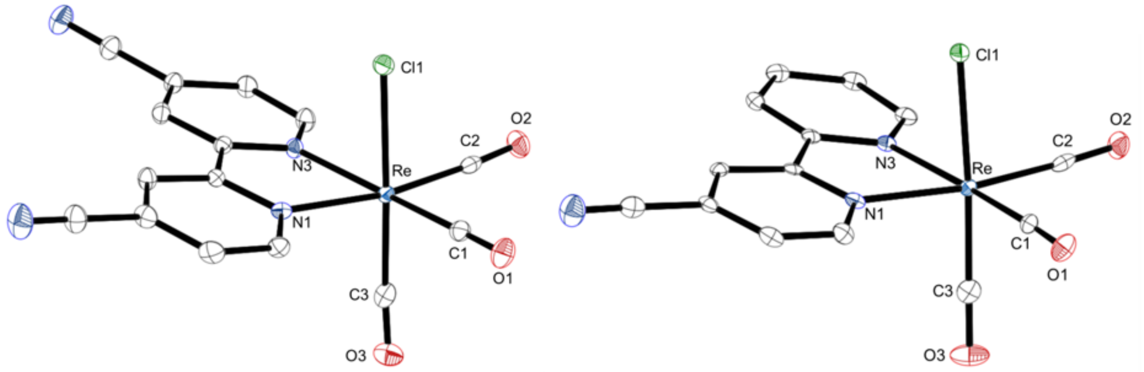

Figure 5.5 X-ray crystallographically determined molecular structure of [Re(4,4′-cyano-2,2′-bipyridine)$(CO)_3Cl$] (**1**) and [Re(4-cyano-2,2′-bipyridine)$(CO)_3Cl$] (**2**). H atoms and incorporated solvent molecules were omitted for clarity; ellipsoids are at 50% probability.

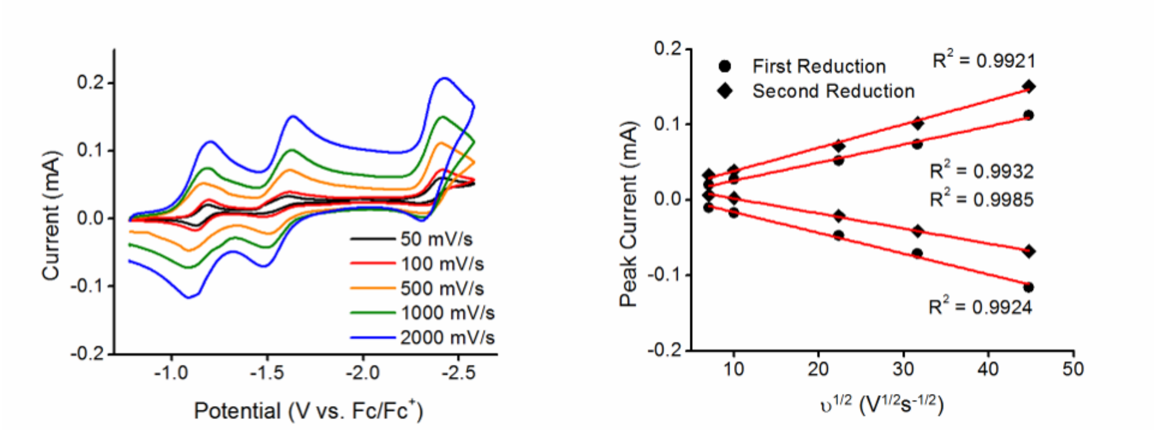

Figure 5.6 Left: Cyclic voltammograms of complex **1** during homogeneous electrochemistry showing the three reductions at various scan rates. Right: Plot of peak current versus square root of the scan rate.

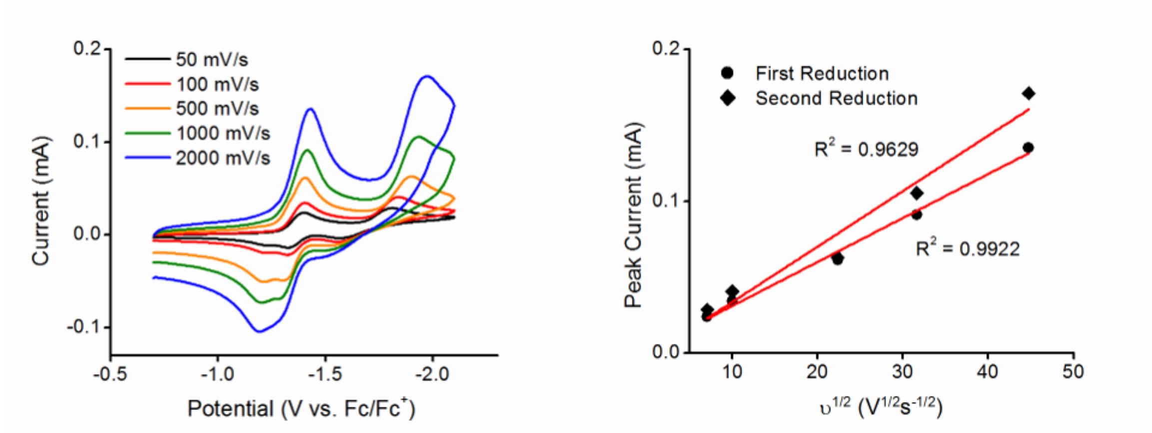

Figure 5.7 Left: Cyclic voltammograms of complex **2** during homogeneous electrochemistry showing the two reductions at various scan rates. Right: Plot of peak current versus square root of the scan rate for the two reductions.

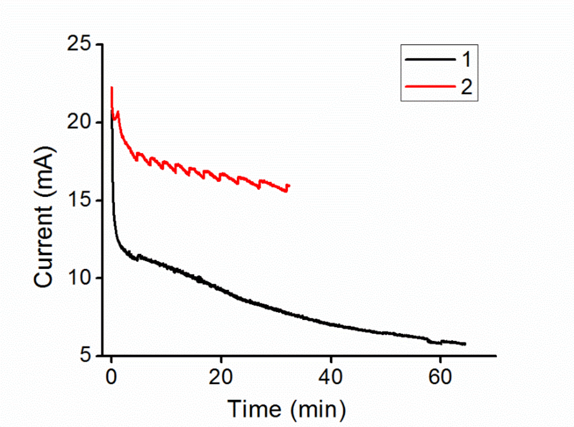

Figure 5.8 Sample bulk electrolysis traces of complexes **1** (black) and **2** (red). During the experiment, the amount of charge passed was equivalent to four turnovers of the catalyst.

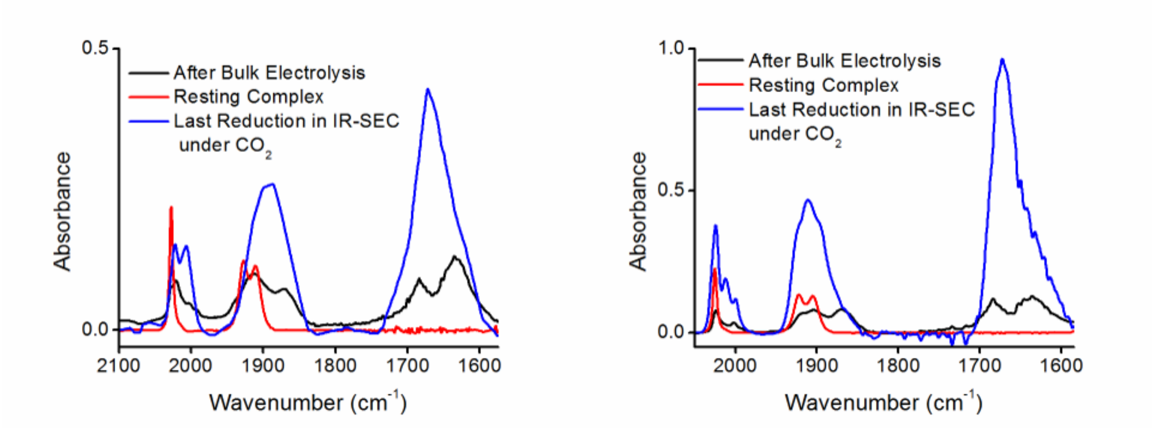

Figure 5.9 FT-IR spectra taken after bulk electrolysis (black) of **1** (left) and **2** (right) compared to the resting spectra of the complex (red) and the last state observed in IR-SEC (blue). For **1**: (black) 2021, 1911, 1869, 1684, 1635 cm^{-1}; (red) 2027, 1928, 1911 cm^{-1}; (blue) 2022, 2007, 1887, 1672 cm^{-1}. For **2**: (black) 2024, 2002, 1903, 1870, 1684, 1635 cm^{-1}; (red) 2025, 1922, 1905 cm^{-1}; (blue) 2024, 2012, 2000, 1911, 1672 cm^{-1}.

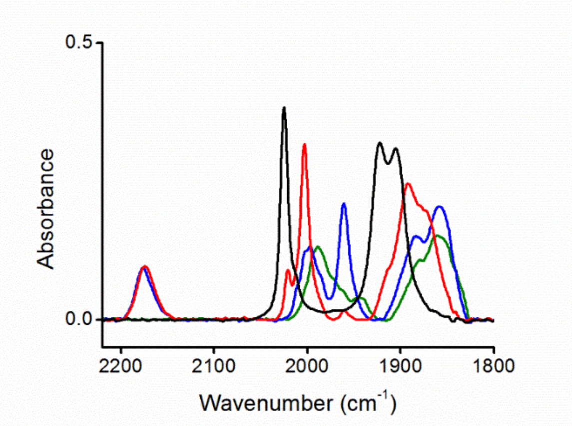

Figure 5.10 IR-SEC of Re(CN-bpy)(CO)$_3$Cl (**2**) under an atmosphere of N$_2$. Resting species (black) v(CO) 2025, 1922, and 1905 cm^{-1}. First reduced species (red) v(CO) 2022, 2003, 1892, 1874 cm^{-1}; v(CN) 2174 cm^{-1}. Second reduction (blue) v(CO) 1994, 1960, 1859 cm^{-1}; v(CN) 2174 cm^{-1}. Third reduced state (green) v(CO) 1989 and 1860 cm^{-1}.

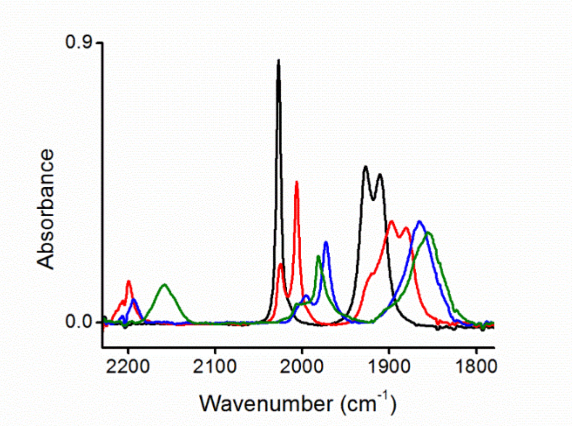

Figure 5.11 IR-SEC of Re(diCN-bpy)(CO)$_3$Cl (**1**).Resting species (black) v(CO) 2027, 1927, and 1910 cm^{-1}. First reduced species (red) v(CN) 2199, v(CO) 2024, 2006, 1897, and 1880 cm^{-1}. Second reduction (blue) v(CN) 2193, v(CO) 1995, 1972, 1865 cm^{-1}. Third reduction v(CN) 2159, v(CO) 1981 and 1855 cm^{-1} (green).

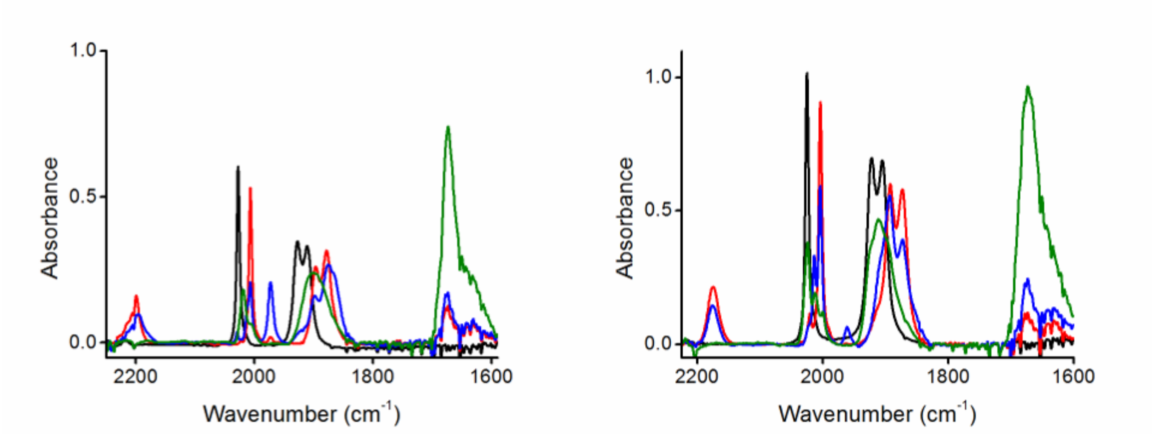

Figure 5.12 IR-SEC of complex **1** (left) and **2** (right) under an atmosphere of CO$_2$. For **1** (left): Resting species (black) v(CO) 2027, 1927, 1911 cm^{-1}. First reduction (red) v(CO) 2006, 1987, 1977 cm^{-1}; v(CN) 2199 cm^{-1}. Second reduction (blue) v(CO) 2006, 1972, 1897, 1874 cm^{-1}; v(CN) 2196 cm^{-1}. Third reduction (green) v(CO) 2018, 1901 cm^{-1}. For **2** (right): Resting species (black) v(CO) 2025, 1921, 1905 cm^{-1}. First reduction (red) v(CO) 2003, 1892, 1873 cm^{-1}; v(CN) 2175 cm^{-1}. Second reduction (blue) v(CO) 2003, 1960, 1893, 1872 cm^{-1}; v(CN) 2176 cm^{-1}. Third reduction (green) v(CO) 2023, 2012, 1911 cm^{-1}.

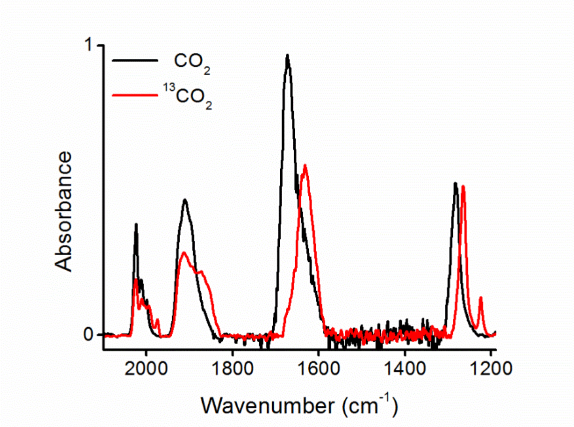

Figure 5.13 IR-SEC of Re(CN-bpy)(CO)$_3$Cl (**2**) with CO$_2$ (black) and ^{13}CO$_2$ (red) atmosphere at a potential corresponding to the third reduction of the complex (ca. –2.80 V vs. Fc/Fc$^+$). An isotope shift is observed for the peaks corresponding to the formation of carbonate (1672 and 1282 cm^{-1}).

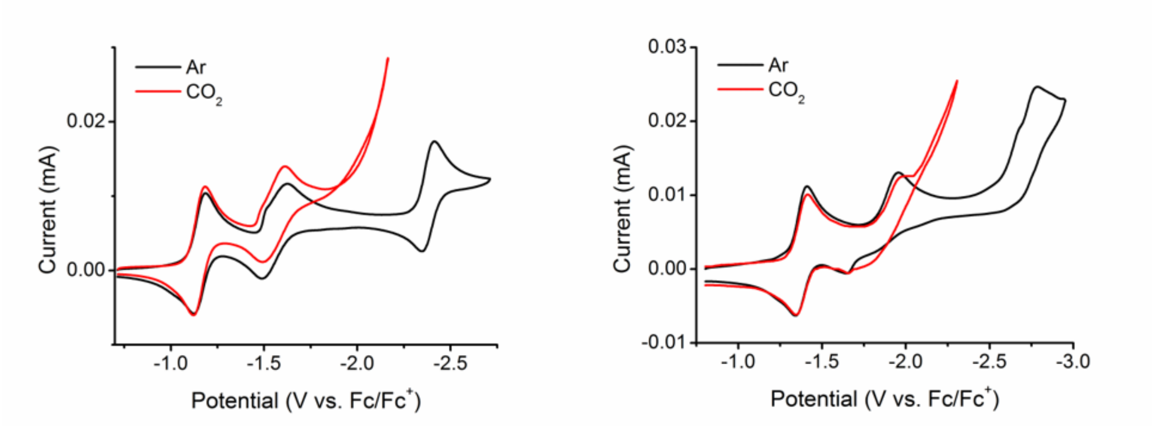

Figure 5.14 Cyclic voltammograms of **1** (left) and **2** (right) under Ar (black) and CO$_2$ (red) atmosphere using a gold electrode. Reductive waves for **1** occur at –1.18 V, –1.63 V, and –2.41 V vs. Fc/Fc$^+$. Reductive waves for **2** occur at –1.41 V, –2.00 V, and –2.79 V vs. Fc/Fc$^+$.

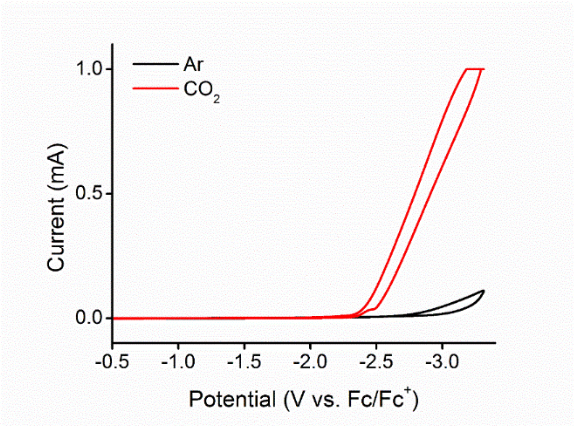

Figure 5.15 Potential window for an Au electrode under Ar (black) and CO_2 (red) atmosphere in 0.1 M $TBAPF_6$ in ACN, occurring at –2.3 V vs. Fc/Fc$^+$ under CO_2 and –2.7 V vs. Fc/Fc$^+$ under Ar.

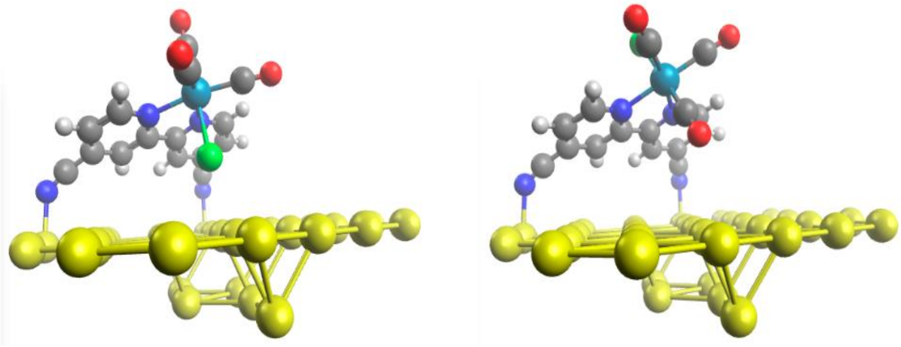

θ = 60°, ψ = 270°, ΔE = 0θ = 60°, ψ = 90°, ΔE = 0.38 kcal/mol

Figure 5.16 DFT optimized geometry with bidentate binding of complex **1** with axial Cl (left) or CO (right) ligand close to the Au surface. Values indicated are the tilt angle (θ), twist angle (ψ), and the energy (ΔE) relative to the geometry labeled with “ΔE = 0”.

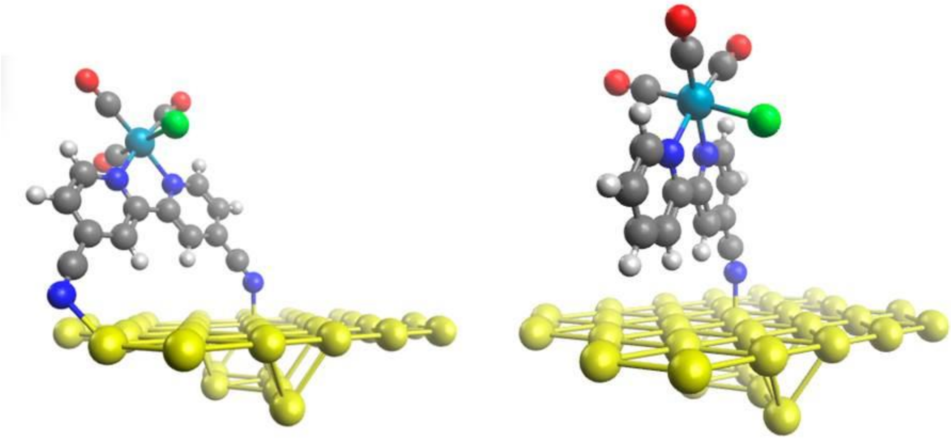

Figure 5.17 DFT optimized geometry with the bpy ring perpendicular to the surface for complex **1** (left) and complex **2** (right).

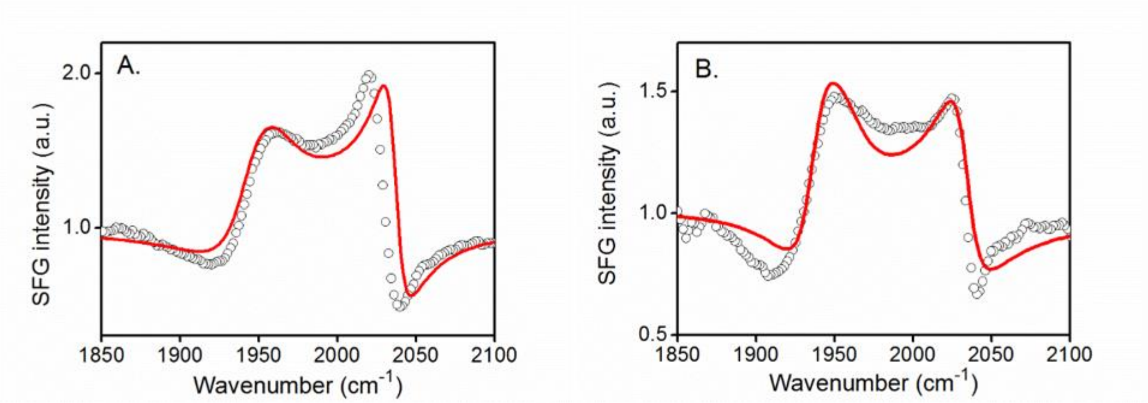

Figure 5.18 B3LYP simulated SFG spectra based on the DFT PW91 optimized geometries for each complex without letting frequencies relax for complex **1** (A) and complex **2** (B)with experimental spectra shown with black circles and the fit shown with red solid.

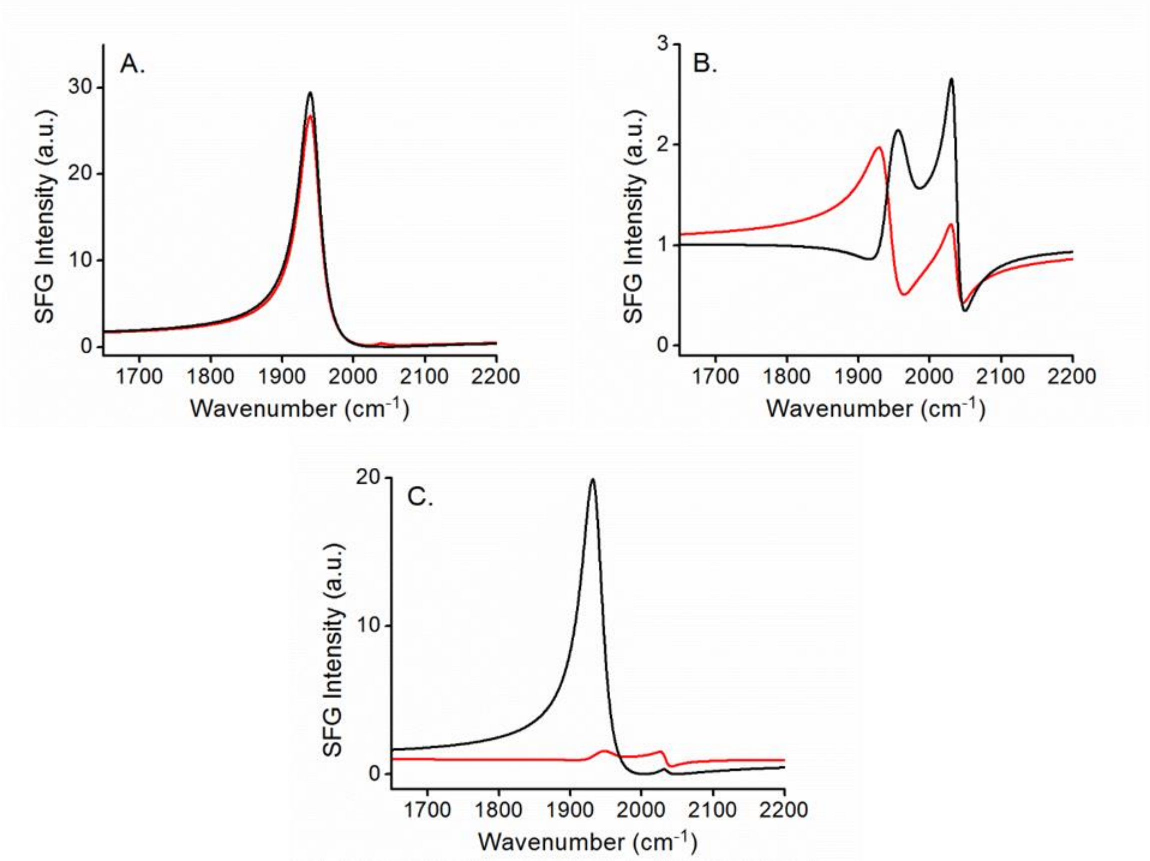

Figure 5.19 B3LYP simulated SFG Spectra based on the DFT PW91 optimized geometries (non-optimized parameters) for each complex. Complex **1** structures of Cl (A) or axial CO ligand (B) facing towards surface with monodentate (black) and bidentate (red) binding. Complex **2** (C) with Cl (black) or axial CO (red) ligand facing towards surface. Specifically, the non-optimized parameters used were, for complex **1**, $\delta = -6°$ and Γ_q = 18.0 cm^{-1}, 18.0 cm^{-1}, and 8.7 cm^{-1} for the out-of-phase symmetric, antisymmetric, and symmetric stretches respectively. For complex **2**, $\delta = -13°$ and Γ_q = 18.2 cm^{-1}, 19.0 cm^{-1}, and 8.2 cm^{-1} for the out-of-phase symmetric, antisymmetric, and symmetric stretches respectively were used.

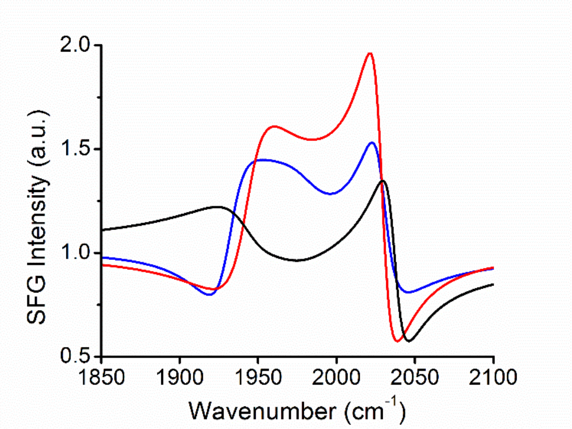

Figure 5.20 Simulated SFG spectra using orientation angles of **2** (blue) are applied to **1** (red) to show that using the orientation angles for **2** makes the SFG spectrum for **1** resemble that of **2** (resulting spectra, black).

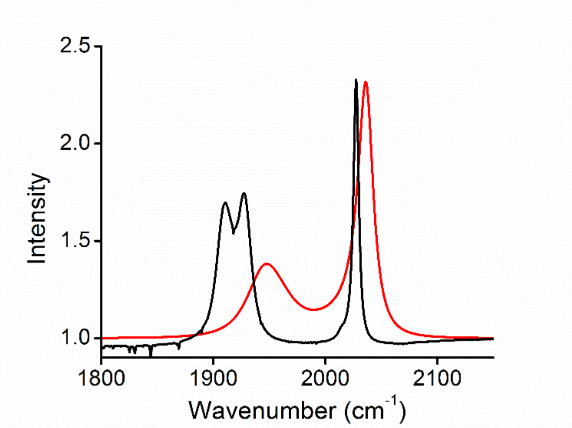

Figure 5.21 Simulated SFG spectrum of **1** (red, Θ = 66°, Ψ = 80°, Phase angle = 354°) without nonresonant contributions with parameters of Table 5.3 compared with the experimental FTIR spectrum (black, in ACN).

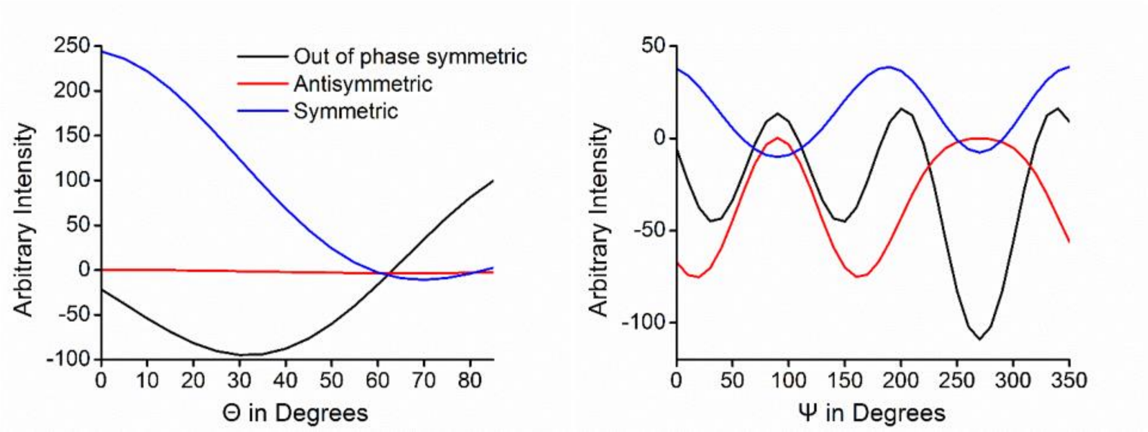

Figure 5.22 (left) The dependence of the amplitudes of each vibration of **1** as a function of θ while keeping ψ fixed at 80°, where blue is symmetric, red is antisymmetric, and black is the out of phase symmetric vibration. (right) The dependence of the amplitudes of each vibration of **1** as a function of ψ while keeping θ fixed at 65°, where blue is symmetric, red is antisymmetric, and black is the out-of-phase symmetric vibration.

Table 5.1 Crystallographic data and refinement information.

Compound	**Re(diCN-bpy)(CO)$_3$Cl**	**Re(CN-bpy)(CO)$_3$Cl**
Empirical Formula	$C_{15}H_6ClN_4O_3Re,CH_2Cl_2$	$C_{14}H_7ClN_3O_3Re$, CH_2Cl_2
Formula Weight	596.83	571.82
Temperature (K)	100(2)	100(2)
Crystal System	monoclinic	monoclinic
Space Group	$P2_1/n$	$P2_1/n$
a (Å)	8.3755(10)	10.7568(8)
b (Å)	11.7615(14)	11.9888(9)
c (Å)	19.164(2)	14.3677(12)
α (deg)	90	90
β (deg)	100.728(5)	108.538(3)
γ (deg)	90	90
V (Å^3)	1854.8(4)	1756.7(2)
Z Value	4	4
ρ *calc* (g/cm^3)	2.1371	2.1619
mu (mm^{-1})	7.009	7.393
Independent Reflections	4,099 [R(int) = 0.0468]	4,091 [R(int) = 0.0458]
Data/restraints/parameters	5661/0/243	3221/0/225
Goodness of Fit on F^2	1.0383	1.0388
R indices (all data) R1, wR2	0.0279, 0.0518	0.0190, 0.0287
Largest diff. peak and hole	0.8592 to –0.8421	0.5997 to –0.7117

Table 5.2 Selected bond lengths (Å) and angles (deg) for x-ray crystallographic structures of complexes **1** and **2**.

Bond/Angle	**1 (di)**	**2 (mono)**
Re–N1	2.170(2)	2.157(2)
Re–N3	2.173(3)	2.167(2)
Re–C1	1.928(3)	1.917(2)
Re–C2	1.936(2)	1.928(3)
Re–C3	1.928(3)	1.899(3)
Re–Cl1	2.4698(7)	2.4783(7)
C8–C9	1.477(4)	1.473(3)
N1–Re–N3	74.84(9)	74.87(8)
N1–Re–C3	94.9(1)	93.0(1)
N1–Re–Cl1	83.64(6)	83.92(6)
Cl1–Re–C1	92.37(8)	93.68(7)
Cl1–Re–C3	178.36(8)	176.75(9)
Re–C1–O1	178.7(2)	177.3(2)
Re–C2–O2	176.3(2)	177.4(2)
Re–C3–O3	176.4(2)	177.7(2)

Table 5.3 Fitting parameters of the SFG spectra for orientation angles derived from DFT for complexes **1** and **2** while not allowing frequencies to relax.

Complex	**Mode**	**Amplitude**	**ω_q (cm^{-1})**	**Γ_q (cm^{-1})**	**(θ, ψ)**	**δ**	$A_{NR}^{(2)}$
1	a'(1)	–9.7	2037	8.4	(66°, 80°)	–6°	1.83
	a''	–3.4	1969	25.0			
	a'(2)	14.2	1943	21.7			
2	a'(1)	–4.1	2033	12.3	(62°, 82°)	17°	1.02
	a''	–2.8	1962	25.0			
	a'(2)	4.7	1936	14.9			

Table 5.4 Fitting parameters of the SFG spectra for orientation angles derived from DFT for complexes **1** and **2** while allowing other parameters, including frequencies, to relax.

Complex	Mode	Amplitude	ω_q (cm^{-1})	Γ_q (cm^{-1})	(θ, ψ)	δ	$A_{NR}^{(2)}$
1	a'(1)	–9.7	2028	8.4	(66°, 80°)	–6°	1.83
	a''	–3.4	1948	14.0			
	a'(2)	14.2	1946	16.7			
2	a'(1)	–4.1	2029	14.1	(62°, 82°)	6°	1.19
	a''	–2.8	1981	25.0			
	a'(2)	4.7	1931	10.3			

Table 5.5 Theoretical SFG Spectral Data Using B3LYP/(SDD,6-311+G(d)).

Complex	Mode	Freq. (cm^{-1})* 1.00	Freq. (cm^{-1})* 0.975	SFG Intensity (a.u.)			
				Monodentate (Cl down)	Monodentate (CO down)	Bidentate (Cl down)	Bidendate (CO down)
1	a'(2)	1992.67	1942.85	–96.15	–9.7	–92.28	–12.76
	a''	2018.99	1968.52	–0.54	–3.4	0.06	0.27
	a'(1)	2088.92	2036.69	–0.94	14.2	6.16	–4.06
2	a'(2)	1985.63	1935.99	–81.46	–4.11	--	--
	a''	2011.85	1961.55	1.55	–2.84	--	--
	a'(1)	2085.67	2033.53	–4.92	4.71	--	--

Table 5.6 Refractive indices and Fresnel factors.*

<table>
<tr><th colspan="4">Refractive Indices</th></tr>
<tr><td></td><td colspan="2">*Gold Thin Film*$^{(a)}$</td><td>*Air*</td></tr>
<tr><td>**Visible (800 nm)**</td><td colspan="2">0.124 + 5.00*i*</td><td>1</td></tr>
<tr><td>**IR (center: 5000 nm)**</td><td colspan="2">3.00 + 34.3*i*</td><td>1</td></tr>
<tr><td>**SFG (690 nm)**</td><td colspan="2">0.136 + 4.03*i*</td><td>1</td></tr>
<tr><th colspan="4">Fresnel factors</th></tr>
<tr><td>$|L_{xxz}|$</td><td>$|L_{xzx}|$</td><td>$|L_{zxx}|$</td><td>$|L_{zzz}|$</td></tr>
<tr><td>0.17</td><td>0.03</td><td>0.02</td><td>1.27</td></tr>
</table>

*The refractive index of the interfacial layer is assumed to be 1.20. The angles of incidence for visible and IR are 65° and 50°, respectively. The calculated Fresnel factors show that the $\chi_{ppp}^{(2)}$ is dominated by the $\chi_{zzz}^{(2)}$ component. (a)Optical dielectric function of gold.[68]

Chapter 6

Re and Mn 4′-mercapto-2,2′-bipyridine CO_2 reduction catalysts and their interactions with Au electrodes

6.1 Introduction

The utilization of anthropogenic carbon dioxide emissions as a reagent to recreate commercially usable energy products would help to decrease both our society’s dependence on non-renewable energy sources as well as greenhouse gas emissions. The difficultly lies in the stability of the CO_2 molecule, leading to high activation barriers for any chemical transformation.[1-2] The use of organometal catalysts have been employed to help lower these barriers through proton-assisted processes to produce products such as CO and formate.[3-5] The selectivity, synthetic tunability, and ease of characterization have allowed significant progress to be made in developing molecular CO_2 reduction catalysts.[6-7]

A growing field within molecular CO_2 reduction electrocatalysis is the functionalization of electrodes to incorporate catalysts into heterogeneous systems.[8-9] Anchoring molecular catalysts onto electrodes would increase catalyst stability and electron transfer while capitalizing on the molecular system’s selectivity and activity. One catalyst that has received a lot of attention is the Re(2,2′-bipyridine)$(CO)_3$Cl (Re-bpy) and Mn-bpy family of catalysts, which are some of the most active and selective electrocatalysts for the reduction of CO_2 to CO.[10-13] Re-bpy and its derivatives have been incorporated into membranes[14] and polymerized onto electrodes,[15-19] as well as extensively studied when surface bound to TiO_2.[20-24] Mn-bpy has also more recently been incorporated into photochemical devices on TiO_2[25], Nafion membranes,[26] and multi-walled carbon nanotubes[27] and nanowires.[28]

The diverse interest in incorporating Re-bpy into heterogeneous systems calls for fundamental understanding of the surface effects on molecular catalysts to help guide the design of heterogenized systems. Recently, we studied the structural and electronic effects of the adsorption of cyano functionalized Re-bpy catalysts onto gold electrodes.[29] It was found that the cyano groups deactivated the catalyst, however the cyano-Au interaction led to a geometry where the would-be catalytically active site was pointing away from the electrode surface. Additional sum frequency generation spectroscopy (SFG) experiments found that the proximity to the surface caused faster vibrational excited state decay times.[30-31]

To build upon the knowledge gained from this previous work, Re-bpy and Mn-bpy catalysts substituted with thiols are investigated both as molecular catalysts and characterized when covalently bound to an Au surface (Figure 6.1). Mono-substituted complexes were chosen since two anchoring groups had not been needed in the cyano substituted complexes.[29] Thiols form strong S-Au bonds, which will give insights on how the strength of the attachment effects orientation of the catalyst on the surface as well as electron transfer between the complex and substrate.

6.2 Results and Discussion

Synthesis and Characterization. Complexes *fac*-Re(4-mercaptomethyl-2,2′-bipyridine)$(CO)_3Cl$ (**1**) and *fac*-Mn(4-mercaptomethyl-2,2′-bipyridine)$(CO)_3Br$ (**2**).were synthesized following well-established protocols[11, 32] and were obtained in good yields (> 68%). Mercaptomethyl substituents were chosen to preclude any thiol reactivity during molecular catalysis. For surface attachment, disulfide complexes were chosen because of their stability and ease of handling, as thiols are known to easily oxidize and polymerize.[33] Synthesis started with formation of 4-thione-2,2′-bipyridine (**bpy=S**) by coupling 4-bromo-2,2′-bipyridine with sodium hydrogen sulfide under basic conditions,[34] which was then immediately oxidized to the disulfide (**bpySSbpy**) using hydrogen peroxide.[35] Dimers **3** and **4** were obtained by refluxing **bpySSbpy** with the appropriate metal salt to yield orange solids, which are only soluble in DMF and DMSO. The manganese complexes **2** and **4** are light sensitive and thus manipulations were done with as little light exposure as possible.

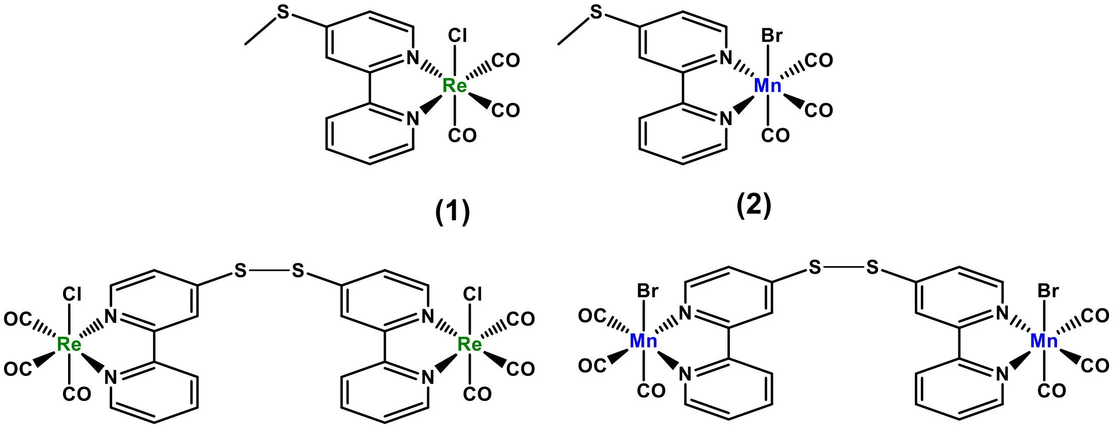

(1) **(2)**

(3) **(4)**

Figure 6.1 Complexes **1–4** studied in this work.

Crystal structures of **1**, **2**, **bpy=S**, and **bpySSbpy** were obtained (Figures 6.5 and 6.6). Complexes **1** and **2** show octahedral coordination geometries around the metal center, with bond lengths similar to analogous complexes.[29] Both have a facial arrangement of the three carbonyl ligands, which is also evidenced by characteristic ν(CO) stretching modes in FT-IR spectroscopy. The bond distance and between the 4-carbon of the bipyridine ring and the sulfur atom is 1.732 Å for **1** and 1.760 Å for **2**, which is typical for a C-S partial double bond.[36] In contrast, the C-S bond in **bpy=S** (Figure 6.6) is shorter and even more double bond in character at 1.697 Å. Thione-thiol tautomerism of 4-mercaptopyridines has previously been observed in solution, where the thione form is favored in polar solvents.[37] Crystals of **bpy=S** were grown from ethanol, thus the thione version was expected. Once oxidized, this bond elongates back to a single bond at 1.774 Å as observed in the structure of **bpySSbpy**, which has C_2 symmetry with a typical S-S bond distance of 2.029 Å.[38]

Homogeneous Electrochemistry. Complexes **1** and **2** were synthesized as homogeneous analogues to characterize catalysis without interference from possible thiol-electrode interactions. Under inert atmosphere (Ar) using a glassy carbon working electrode and dry acetonitrile (MeCN), complex **1** shows two reductions at –1.76 V and –2.04 V vs. $Fc^{+/0}$ (Figure 6.2). The first reduction is reversible when scanning is stopped before the second reduction, and is attributed to the reduction of the bipyridine ligand. The second reduction is irreversible and corresponds to reduction of the metal center to Re^0, coupled with the loss of $Cl^–$.[39] These features remain steady at increasing scan rates, showing that the complexes freely diffuse from the surface as defined by the Randles-Sevcik equation.[40] A small oxidation peak can be seen at –0.5 V at slower scan rates, corresponding to breakage of a Re-Re dimer that is known to be a deactivation pathway for Re-bpy complexes that do not have bulky bpy substituents.[41] These reduction potentials are slightly more positive than $Re(bpy)(CO)_3Cl$ by 20 mV and 80 mV for the first and second reductions, respectively.[11]

Manganese complex **2** also exhibits an electrochemical response like other substituted Mn-bpy complexes.[32, 42] Under Ar on a glassy carbon working electrode, two irreversible reductions are seen at –1.62 V and –1.86 V vs. $Fc^{+/0}$, which are 140 mV and 180 mV more positive than the reductions of **1** (Figure 6.2).

Based on previous studies,[32] the first reduction can be assigned as the reduction of the metal center, followed by the loss of Br^- and rapid dimerization. This Mn-Mn dimer is then reduced to form the catalytically active $[Mn(bpy\text{-}SMe)(CO)_3]^-$ anion. Oxidative cleavage of the dimer can be seen at –0.65 V. Complex **2** is also freely diffusing.

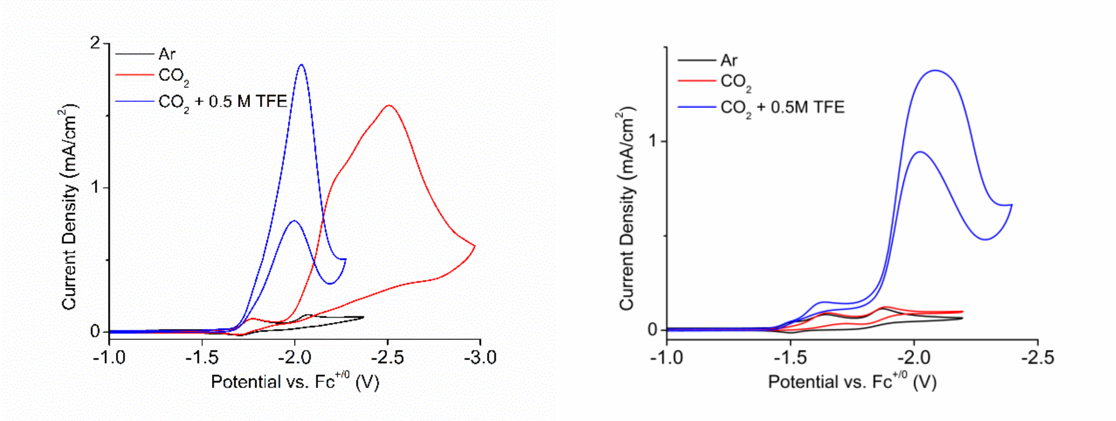

Figure 6.2 Cyclic voltammograms of **1** (Re, left) and **2** (Mn, right) under the same conditions: 1 mM complex, 5 mL of 0.1 M $TBAPF_6$ in CH_3CN; glassy carbon working, platinum counter, and Ag/AgCl reference electrode. Scan at 100 mV/s.

Under an atmosphere of CO_2, only **1** exhibits catalytic current at the second reduction. This corresponds to an i_{cat}/i_p of 13 (at 0.1 V/s), and by increasing the scan rate to achieve a plateau current, a TOF_{max} of 93 s^{-1} (10 V/s) was determined (see Appendix for details). Bulk electrolysis experiments showed 99% ± 2% Faradaic efficiency for the formation of CO with less than 0.1% Faradaic efficiency for hydrogen formation. 2,2,2-trifluoroethanol (TFE, $pK_{a(CH3CN)}$ = 35.4)[43] was then added as a proton source until maximum current was achieved. At 0.5 M TFE, the peak current shifted more positive by 470 mV to –2.04 V (from –2.51 V vs. $Fc^{+/0}$), and corresponded to TOF_{max} of 646 s^{-1} (25 V/s). These TOF_{max} values are very similar to Re(bpy)$(CO)_3$Cl, which has a TOF_{max} of 46 s^{-1} and 770 s^{-1} under CO_2 and CO_2 with 1 M phenol, respectively.

Complex **2** was catalytically active only after addition of a proton source,[42] and with 0.5 M TFE there was a 12-fold increase in current and a TOF_{max} of 396 s^{-1}. Bulk electrolysis experiments with 0.5 M TFE showed 100% ± 5% efficiency for CO and H_2 < 0.4% over three runs. The activity of complex **2** is very similar to that of Mn(4,4′-di-*tert*-butyl-2,2′-bipyridine)$(CO)_3$Br, which has a TOF_{max} of 340 s^{-1}.

Since these complexes are meant to be analogues to those covalently attached to Au electrodes, electrochemistry was also done using a gold working electrode. Scans of **1** and **2** under Ar were almost identical compared to those taken on glassy carbon, with an exception of more dimer oxidation (–0.5 V) observed for **1** at higher scan rates (Figures 6.7). Both complexes were freely diffusing. Under an atmosphere of CO_2, **1** showed an increase in current corresponding to an i_{cat}/i_p of 15.3. This slight increase in activity compared to using a glassy carbon working electrode has also been observed for Mo(bpy)$(CO)_4$, contributed to the affinity of Au for CO, helping product dissociation during catalysis.[44] Again, no increase in current was seen under CO_2 for **2**, and TFE was not added as a proton source due to its small electrochemical window for gold electrodes.

Surface Attachment. A self-assembled monolayer (SAM) of the monomers of complexes **3** or **4** (**3m** and **4m**) were made by soaking a freshly cleaned gold-coated slide in a 1 mM solution of the complex in DMF for 24 hr. The slide was rinsed copiously with organic solvents and dried under a stream of nitrogen before taking any measurements. Polarization modulation infrared reflection absorption spectroscopy (PM-IRRAS) was performed as an initial means of characterizing the complexes on the surface. The PM-IRRAS shows all three v(CO) stretching frequencies for both **3m** and **4m** (Figure 6.3). Compared to their solution FT-IR spectra, the carbonyl modes are shifted to higher energy by ca. 12 cm^{-1}. The broadening of the peaks is most likely due to surface roughness of the Au slide.[24, 45] Additional characterization by density functional theory (DFT) and complimentary spectroscopy measurements such as sum frequency generation spectroscopy (SFG) are needed in order to carefully study the orientation and electrochemical properties of these SAMs.

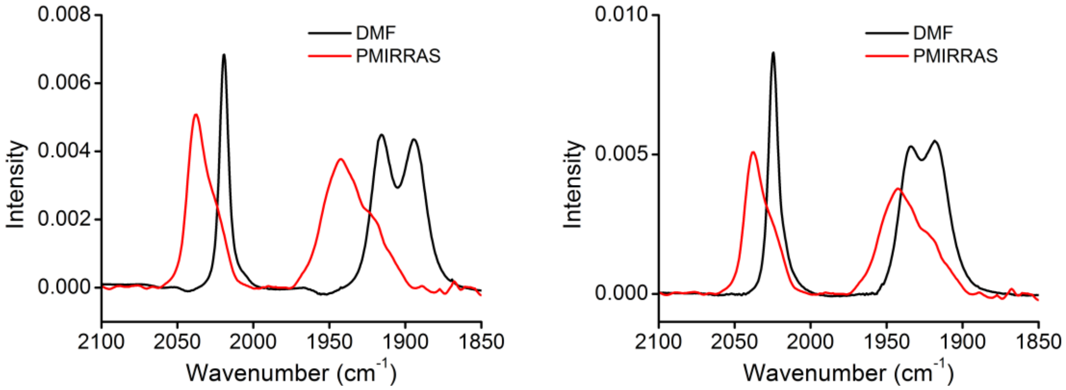

Figure 6.3 Comparison between v(CO) frequencies in FTIR solution phase spectra (DMF, black) and PM-IRRAS spectra (red) for complexes **3m** (left) and **4m** (right).

6.3 Conclusions & Future Experiments

Molecular complexes **1** and **2** have been synthesized and characterized for the selective electrochemical reduction of CO_2 to CO. Both Re and Mn complexes show reactivity similar to that of the unsubstituted Re and Mn-bpy complexes, with

TOF_{max} values with 0.5 M TFE of 646 s^{-1} and 396 s^{-1} for Re (**1**) and Mn (**2**), respectively. Disulfide complexes **3** and **4** where synthesized and covalently attached onto Au surfaces. PM-IRRAS characterization of the monolayers show a broadening of the carbonyl stretching frequencies, suggesting inhomogeneous molecular packing of the complexes on the surface.

Additional experiments will help to fully characterize the interactions between complexes **3m** and **4m** and the gold surface. The use of density functional theory (DFT) coupled with sum frequency generation spectroscopy (SFG) will help to elucidate the most probable binding orientation to the surface. Preliminary work of the monomer of **3m** on Au (Figure 6.4) shows an optimized geometry where the chloride is facing away from the surface and the complex is tilted by a 74º angle with respect to the bpy ligand. This is a larger tilt angle than when a cyano anchoring group is used, in which a 63º tilt angle was determined.[29] Electrochemical SFG will also elucidate any structural changes to the bound complexes under potential as well as stripping potentials, which normally occur around –1.0 V ± 0.25 V with respect to aqueous Ag/AgCl in a saturated KCl solution.[33] Together these studies will help to fully characterize both molecular and surface bound thiol-substituted bipyridine complexes, which are important steps towards fully understanding attached catalysis.

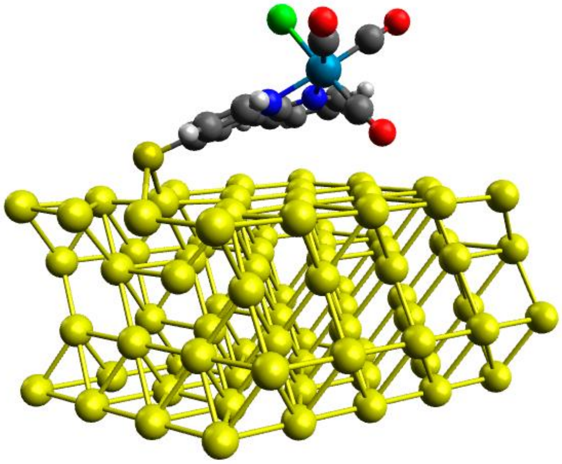

Figure 6.4 DFT optimized geometry of the monomer of Re monomer **3m** on an Au slab, corresponding to a 74º tilt of the bpy ring towards the surface and the chloride facing away from the surface.

6.4 Experimental

General Experimental Considerations. ^{1}H and ^{13}C NMR spectra were recorded at 298K on a Varian 500 MHz spectrometer. Chemical shifts are reported relative to TMS (δ = 0) by referencing to deuterated solvent signals. FT-IR spectra were performed on a Thermo Scientific Nicolet 6700. Electrochemical experiments were performed on a BASi Epsilon potentiostat. Microanalyses were performed by NuMega Resonance Labs, San Diego, CA for C, H, and N. Solvents were received from Fisher Scientific and were dried either on a custom solvent system (degassed with Argon and dried over alumina columns) or over 3Å sieves and degassed prior to use. Deuterated solvents were obtained from Cambridge Isotope Laboratories. Reagents were obtained from commercial sources; pentacarbonylchlororhenium(I) and sodium hydrogen sulfide from Sigma Aldrich, bromopentacarbonylmanganese(I) from Alfa Aesar, and 4-methylthio-2,2′-

bipridine and 4-chloro-2,2′-bipyridine from HetCat. Tetrabutylammonium hexafluorophosphate (TBAPF$_6$, Aldrich, 98%) was recrystallized twice from methanol and dried at 90°C overnight before use in electrochemistry experiments. Reactions were performed sheltered from light using standard Schlenk-line and Glove Box techniques under an atmosphere of nitrogen.

Synthesis of *fac*-Re(4-mercaptomethyl-2,2′-bipyridine)(CO)$_3$Cl (1). To an oven dried round bottom flask, Re(CO)$_5$Cl (0.392 mmol, 142 mg), dry toluene (10 mL), and 4-methylthio-2,2′-bipridine (0.395 mmol, 80 mg) was added. The solution stirred in the dark under refluxing conditions for three hours, upon which an orange precipitate was observed. The solution was cooled to –8°C before the solid was collected by filtration and washed with copious amounts of cold pentane. The solid was dried under reduced pressure at ~50°C overnight to yield a yellow solid (175 mg, 88% yield). Crystals suitable for X-ray diffraction were grown by the slow evaporation of pentane into a solution of the complex in dichloromethane. ^{1}H NMR (CD$_3$CN) δ = 9.01 (d, 1H), 8.71 (d, 1H), 8.43 (d, 1H), 8.18 (t, 1H), 8.17 (s, 1H), 7.62 (t, 1H), 7.41 (d, 1H), 2.66 (s, 3H). 13C{H} NMR (CD$_3$CN) δ = 157.86, 156.83, 155.96, 152.73, 141.15, 128.88, 125.35, 123.82, 121.07, 14.80. IR (CHCl$_3$) v(CO) 2025, 1926, 1899 cm^{-1}. UV-Vis (ACN) $\lambda_{max/nm}$ = 255, 293, 367. ESI-MS (m/z) [M – Cl + MeOH]+: calcd: 505.02; found: 505.13. Elemental analysis $C_{14}H_{10}ClN_2O_3ReS$ calcd: C 33.10, H 1.98, N 5.51 S 6.31; found: C 32.94; H 1.87; N 5.51; S 6.38. CCDC 1477731. Faradaic efficiency during bulk electrolysis with 1 mM catalyst under saturated CO$_2$ conditions (~0.28 M in ACN) for production of CO was 99 ± 2% and H$_2$ < 0.1% over three runs.

Synthesis of *fac*-Mn(4-mercaptomethyl-2,2′-bipyridine)(CO)$_3$Br (2). To an oven dried round bottom flask, 4-methylthio-2,2′-bipridine (0.473 mmol, 96 mg) was added to a stirring solution of Mn(CO)$_5$Br (0.473 mmol, 109 mg) in diethyl ether (10 mL). The mixture was heated to 50°C under nitrogen in the dark for four hours, during which an orange precipitate was observed. The solution was cooled to –8°C before the solid was collected by filtration and washed with copious amounts of cold diethyl ether. The solid was dried under reduced pressure at ~50°C overnight to yield a yellow solid (136 mg, 68% yield). Crystals suitable for X-ray diffraction were grown by the slow evaporation of pentane into a solution of the complex in tetrahydrofuran. ^{1}H NMR (CD$_3$CN) δ = 9.21 (d, 1H), 8.90 (d, 1H), 8.34 (d, 1H), 8.11 (t, 1H), 8.10 (s, 1H), 7.60 (t, 1H), 7.40 (d, 1H), 2.65 (s, 3H). ^{13}C{H} NMR (CD$_3$CN) δ = 156.79, 156.59, 155.94, 154.98, 153.36, 140.27, 127.94, 124.34, 123.28, 120.22, 14.74. IR (CHCl$_3$) ν(CO) 2030, 1942, 1922 cm^{-1}. UV-Vis (ACN) $\lambda_{max/nm}$ = 273, 289, 419. Elemental analysis $C_{14}H_{10}BrMnN_2O_3S$ calcd: C 39.93, H 2.39, N 6.65; S 7.61; found: C 39.94; H 2.33; N 6.70; S 7.64. CCDC 1477732. Faradaic efficiency during bulk electrolysis with 1 mM catalyst and 0.5 M TFE under saturated CO$_2$ conditions (~0.28 M in ACN) for production of CO was 100 ± 5% and H$_2$ < 0.4% over three runs.

Synthesis of 4-thione-2,2′-bipyridine (bpy=S). Made using a modified literature procedure,[34] sodium hydrogen sulfide (0.88 g, 15.69 mmol) was added to dry and degassed DMF (10 mL), and to it was added 4-chloro-2,2′-bipyridine (300 mg, 1.57 mmol) and solid KOH (0.26 g, 4.63 mmol), respectively. The reaction was refluxed under nitrogen overnight. After cooling, the reaction was filtered to remove the white precipitate and the filtrate was reduced under pressure to yield a yellow solid. To this 10 mL of water was added to dissolve the product and the pH was adjusted to neutral with 2 M HCl solution. The product was extracted from an aqueous layer by washing 3x10 mL of DCM. The organic phase was collected, washed once with brine, and dried over $MgSO_4$. Removal of solvent afforded a light orange solid (0.208 g 70% yield). ^{1}H NMR (CD_3CN) δ = 9.14 (s, 1H, NH), 8.71 (d, 1H), 8.09 (d, 1H), 7.98 (s, 1H), 7.95 (m, 1H), 7.51 (m, 2H), 7.34 (d, 1H). ESI-MS $[M-H]^-$ (m/z) calcd: 187.03; found: 187.32. Crystals suitable for X-ray diffraction were grown from recrystallization in ethanol. CCDC 1540832.

Synthesis of di(2,2'-bipyridine)-4-disulfide (bpySSbpy). Similarly to previously reported thiol oxidation procedures,[35] to a stirred solution 4-mercapto-2,2′-bipyridine (273 mg, 1.45 mmol) in dichloromethane (10 mL) was added 1mol% NaI and H2O2 (30% w/w solution, 0.15 mL, 1.45 mmol). The mixture was stirred at room temperature for 24 hours. The solvent was removed to afford a white powder that was washed and filtered from diethyl ether. The resulting solid was collected dried under vacuum at ~40ºC overnight to afford off-white product (103 mg, 38%). Crystals suitable for X-ray diffraction were grown by the slow evaporation of diethyl ether into a solution of the complex in dichloromethane. ^{1}H NMR ($CDCl_3$) δ = 8.68 (d, 2H), 8.56 (s, 2H), 8.55 (d, 2H), 8.37 (d, 2H), 7.82 (td, 2H), 7.44 (dd, 2H), 7.33 (m, 2H). ^{13}C{H} NMR ($CDCl_3$) δ = 156.50, 155.33, 149.62, 149.39, 148.09, 137.15, 124.29, 121.56, 119.78, 117.95. ESI-MS (m/z) [M + H]: calcd: 375.07; found: 375.12. CCDC 1540831.

Synthesis of [Re(4-disulfide-2,2′-bipyridine)(CO)$_3$Cl]$_2$ (3). To a stirred solution of Re(CO)$_5$Cl (194 mg, 0.54 mmol) in toluene (10 mL) was added di(2,2'-bipyridine)-4-disulfide (100 mg, 0.27 mmol). The solution was heated under a N$_2$ atmosphere for 3.5 hours. Once cooled, the solution was filtered and the resulting solid was washed with chloroform and diethyl ether. The solid was dried overnight under vacuum at ~40ºC overnight to afford a bright orange product (160 mg, 61% yield). ^{1}H NMR (*d6*-DMSO) δ = 9.02 (m, 4H), 8.90 (d, 2H), 8.79 (d, 2H), 8.36 (t, 2H), 7.90 (m, 2H), 7.77 (m, 2H). ^{13}C{H} NMR (*d6*-DMSO) 197.34, 189.614, 154.86, 154.24, 152.89, 152.74, 140.14, 128.05, 124.45, 121.06. IR (DMF) v(CO) 2019, 1916, 1894 cm^{-1}. ESI-MS (m/z) [M – Cl]: calcd: 950.92; found: 950.96. Elemental analysis $C_{26}H_{14}Cl_2N_4O_6Re_2S_2$ calcd: C 31.68, H 1.43, N 5.68, S 6.50; found: C 31.35, H 1.80, N 5.58.

Synthesis of [Mn(4-sulfide-2,2′-bipyridine)(CO)$_3$Br]$_2$ (4). To a stirred solution of Mn(CO)$_5$Br (45 mg, 0.195 mmol) in diethyl ether (5 mL) was added 2,2'-bipyridine-4-disulfide (35 mg, 0.09 mmol). The solution was heated to a light reflux under a N2 atmosphere overnight. Once cooled, the solution was filtered and the resulting solid was washed with diethyl ether. The solid was dried under vacuum at ~40ºC overnight to afford a bright orange product (68 mg, 91%). ^{1}H NMR (*d6*-DMSO) δ = 9.12 (d, 2H), 9.09 (d, 2H), 8.93 (s, 2H), 8.69 (d, 2H), 8.26 (td, 2H), 7.90 (dd, 2H), 7.74 (m, 2H). ^{13}C{H} NMR (*d6*-DMSO) 154.67, 154.16, 153.28, 139.07, 126.98, 123.38, 122.17, 120.57, 120.27, 119.94. IR (DMF) v(CO) 2024, 1934, 1918 cm^{-1}.

X-Ray Crystallography. Single crystal X-ray diffraction studies were carried out on a Bruker Kappa APEX-II CCD diffractometer equipped with Mo Kα radiation (λ = 0.71073 Å) or a Bruker Kappa APEX CCD diffractometer equipped with Cu Kα radiation (λ = 1.54184 Å). The crystals were mounted on a Cryoloop with Paratone oil and data were collected under a nitrogen gas stream at 100(2) K using ω and ϕ scans. Data were integrated using the Bruker SAINT software program and scaled using the SADABS software program. Solution by direct methods (SHELXS) produced a complete phasing model consistent with the proposed structure. All non-hydrogen atoms were refined anisotropically by full-matrix least-squares (SHELXL-97).[46]

Preparation of Au Slides and Surface Attachment. Optically flat Au substrates consisting of a layer of Cr (1-4 nm) and Au (200-300 nm) evaporated onto borosilicate glass slides were used. For surface attachment of the catalysts, all Au substrates were cleaned by dipping in piranha solution (3:1 sulfuric acid:30% H_2O_2) for 1-2 minutes. *Caution: Piranha solutions are extremely energetic and may result in explosion if not handled with extreme caution.* The slides were washed with copious amounts of ultra-pure water before being washed with ethanol and dried under a stream of N_2. Prior to use, the slides were flame treated[47] to remove any surface water and were immediately submerged in a 1 mM solution of the compound in dry and N_2 degassed DMF. This solution was kept under nitrogen in the dark, and slides were submerged for 12-24 hours. Slides were then washed with DMF, dried under a stream of nitrogen and immediately analyzed.

Homogeneous Electrochemistry. Electrochemical experiments were performed using a BASi Epsilon potentiostat. A 20 mL scintillation vial with a custom fitted top was used for all CV and DPV experiments, utilizing a 3 mm diameter glassy carbon working electrode, Pt wire counter electrode, and a Ag/AgCl reference electrode (separated from solution in by a glass sheath and CoralPor tip). The glassy carbon working electrode was polished with 15, 3, and 1micron diamond paste successively, thoroughly rinsed with methanol and dried under a stream of nitrogen prior to experiments and polished with 1 micron diamond polishing paste between scans. The platinum wire was flame treated with a butane torch prior to use. To minimize the amount of adventitious water in our set up and prevent solvent loss via sparging the solution, Ar and “bone dry” CO_2 gas were first run through their own Drierite columns and secondly through a sealed vial of dry CH_3CN filled with 3Å sieves. An oven-dried cannula was then used to transfer the CH_3CN saturated dry gas to the electrochemical set-up. Electrochemical solutions were sparged for at least 5 minutes prior to the start of data collection, and were kept under a blanket of the gas during measurements. Experimental conditions, unless otherwise noted, consisted of 5 mL of a 0.1 M $TBAPF_6$ solution of CH_3CN, 1 mM complex, and 1 mM ferrocene to use as an internal standard with a typical scan rate of 0.1 V/s. Ohmic drop of the cell was corrected for by using the potentiostat’s iR-compensation tool, correcting for 80-90% of the measured resistance. This resulted in a ferrocene peak splitting typically between 61-67 mV.

Bulk Electrolysis. Bulk electrolysis was performed in a custom threaded 60 mL single-compartment cell (ChemGlass) with a custom air-tight polyether ether ketone (PEEK) top. The setup consists of a carbon rod working electrode, coiled Pt wire counter electrode (protected from the bulk solution by fritted glass), and an Ag/AgCl pseudo-reference electrode (separated from solution by a CoralPor tip). The setup is tested for airtightness before each run. The CH_3CN solution (~40 mL) consisted of 0.1 $TBAPF_6$, 1 mM complex, and sparged with either Ar or CO_2 before each experiment. Solutions were constantly stirred and protected from light during the experiment. The voltage chosen for electrolysis was that of slightly past the catalytic potential in cyclic voltammetry. Experiments were set to run for four turnovers (approx. 33 Coulombs). Gas analysis was performed by sampling 1 mL of the headspace of the cell at the end of each experiment and injecting on a Hewlett-Packard 7890A series gas chromatograph with two molsieve columns (30 m × 0.53 mm i.d. × 25 µm film). The 1 mL injection was split between two columns, one with N_2 carrier gas and the other He to quantify both CO and H_2, respectively. Instrument specific calibration curves were used to determine amount of each gas produced.

Phase-Modulated Infrared Reflection Adsorption Spectroscopy (PM-IRRAS). PM-IRRAS spectra were acquired on a Bruker Equinox 55 FT-IR with a Bruker PMA 37 accessory. Polarization modulation was achieved using a PEM-90-D ZnSe Photoelastic Modulator (Hinds Instruments) operating at 50 kHz and half-wave retardation coupled with a Synchronous Sampling Demodulator (GWC Instruments). The reflected light was detected with a liquid nitrogen cooled mercury cadmium telluride detector equipped with BaF_2 window and set at an incidence angle of 88º with respect to surface normal. Spectra collected were an average of 60 scans of each sum and difference with 4 cm^{-1} resolution and maximum dephasing at 2000 cm^{-1}. Baseline was established by subtracting the spectrum of a bare gold slide which treated identically to the samples. All spectra were collected in a dry air atmosphere using a Parker Balston Purge Gas Generator.

6.5 Acknowledgements

This chapter, in part, is currently being prepared for submission for publication of the material, entitled "Re and Mn 4′-mercapto-2,2′-bipyridine CO_2 reduction catalysts and their electrochemical interactions with Au electrodes as determined by SFG spectroscopy″ by Melissa L. Clark, Aimin Ge, Benjamin Rudshteyn, Christopher Miller, Tianquan Lian, Victor S. Batista, and Clifford P. Kubiak. The dissertation author is the primary author of this manuscript.

This work was supported by the Air Force Office of Scientific Research Grant No. FA9550-17-0198 Gwendolynne Lee and Alma Zhanaidarova are acknowledged for their support and helpful discussions.

6.6 References

(1) Aresta, M.; Dibenedetto, A.; Quaranta, E., One- and Multi-electron Pathways for the Reduction of CO_2 into C1 and C1+ Energy-Richer Molecules: Some Thermodynamic and Kinetic Facts. In *Reaction Mechanisms in Carbon Dioxide Conversion*, 2016; 311-345.

(2) Aresta, M.; Dibenedetto, A.; Angelini, A., *Chem. Rev.* **2014**, *114*, 1709.

(3) Benson, E. E.; Kubiak, C. P.; Sathrum, A. J.; Smieja, J. M., *Chem. Soc. Rev.* **2009**, *38*, 89.

(4) Grice, K. A., *Coord. Chem. Rev.* **2017**, *336*, 78.

(5) Morris, A. J.; Meyer, G. J.; Fujita, E., *Acc. Chem. Res.* **2009**, *42*, 1983.

(6) Arakawa, H.; Aresta, M.; Armor, J. N.; Barteau, M. A.; Beckman, E. J.; Bell, A. T.; Bercaw, J. E.; Creutz, C.; Dinjus, E.; Dixon, D. A.; Domen, K.; DuBois, D. L.; Eckert, J.; Fujita, E.; Gibson, D. H.; Goddard, W. A.; Goodman, D. W.; Keller, J.; Kubas, G. J.; Kung, H. H.; Lyons, J. E.; Manzer, L. E.; Marks, T. J.; Morokuma, K.; Nicholas, K. M.; Periana, R.; Que, L.; Rostrup-Nielson, J.; Sachtler, W. M. H.; Schmidt, L. D.; Sen, A.; Somorjai, G. A.; Stair, P. C.; Stults, B. R.; Tumas, W., *Chem. Rev.* **2001**, *101*, 953.

(7) Maeda, C.; Miyazaki, Y.; Ema, T., *Catal. Sci. Tech.* **2014**, *4*, 1482.

(8) Serna, P.; Gates, B. C., *Acc. Chem. Res.* **2014**, *47*, 2612.

(9) Sun, C.; Gobetto, R.; Nervi, C., *New J. Chem.* **2016**.

(10) Grice, K. A.; Kubiak, C. P., Chapter five - Recent studies of rhenium and manganese bipyridine carbonyl catalysts for the electrochemical reduction of CO_2. In *Advances in Inorganic Chemistry*, Michele, A.; Rudi van, E., Eds. Academic Press: 2014; Vol. 66, 163-188.

(11) Smieja, J. M.; Kubiak, C. P., *Inorg. Chem.* **2010**, *49*, 9283.

(12) Hawecker, J.; Lehn, J.-M.; Ziessel, R., *Helvetica Chimica Acta* **1986**, *69*, 1990.

(13) Hawecker, J.; Lehn, J.-M.; Ziessel, R., *J. Chem. Soc., Chem. Commun.* **1984**, 328.

(14) Yoshida, T.; Tsutsumida, K.; Teratani, S.; Yasufuku, K.; Kaneko, M., *J. Chem. Soc., Chem. Commun.* **1993**, 631.

(15) O'Toole, T. R.; Sullivan, B. P.; Bruce, M. R. M.; Margerum, L. D.; Murray, R. W.; Meyer, T. J., *J. Electroanal. Chem.* **1989**, *259*, 217.

(16) Cosnier, S.; Deronzier, A.; Moutet, J.-C., *J. Mol. Catal.* **1988**, *45*, 381.

(17) Cabrera, C. R.; Abruña, H. D., *J. Electroanal. Chem.* **1986**, *209*, 101.

(18) Cosnier, S.; Deronzier, A.; Moutet, J.-C., *J. Electroanal. Chem.* **1986**, *207*, 315.

(19) Cecchet, F.; Alebbi, M.; Bignozzi, C. A.; Paolucci, F., *Inorg. Chim. Acta* **2006**, *359*, 3871.

(20) Ge, A.; Rudshteyn, B.; Psciuk, B. T.; Xiao, D.; Song, J.; Anfuso, C. L.; Ricks, A. M.; Batista, V. S.; Lian, T., *J. Phys. Chem. C* **2016**, *120*, 20970.

(21) Windle, C. D.; Pastor, E.; Reynal, A.; Whitwood, A. C.; Vaynzof, Y.; Durrant, J. R.; Perutz, R. N.; Reisner, E., *Chem. Eur. J.* **2015**, *21*, 3746.

(22) Anfuso, C. L.; Xiao, D. Q.; Ricks, A. M.; Negre, C. F. A.; Batista, V. S.; Lian, T. Q., *J. Phys. Chem. C* **2012**, *116*, 24107.

(23) Anfuso, C. L.; Snoeberger, R. C., 3rd; Ricks, A. M.; Liu, W.; Xiao, D.; Batista, V. S.; Lian, T., *J. Am. Chem. Soc.* **2011**, *133*, 6922.

(24) Vanselous, H.; Stingel, A. M.; Petersen, P. B., *J. Phys. Chem. Lett.* **2017**, 825.

(25) Rosser, T. E.; Windle, C. D.; Reisner, E., *Angew. Chem. Intl. Ed.* **2016**.

(26) Walsh, J. J.; Neri, G.; Smith, C. L.; Cowan, A. J., *Chem. Commun.* **2014**, *50*, 12698.

(27) Walsh, J. J.; Smith, C. L.; Neri, G.; Whitehead, G. F.; Robertson, C. M.; Cowan, A. J., *Faraday Discuss* **2015**, *183*, 147.

(28) Torralba-Peñalver, E.; Luo, Y.; Compain, J.-D.; Chardon-Noblat, S.; Fabre, B., *ACS Catal.* **2015**, 6138.

(29) Clark, M. L.; Rudshteyn, B.; Ge, A.; Chabolla, S. A.; Machan, C. W.; Psciuk, B. T.; Song, J.; Canzi, G.; Lian, T.; Batista, V. S.; Kubiak, C. P., *J. Phys. Chem. C* **2016**, *120*, 1657.

(30) Li, Y.; Wang, J.; Clark, M. L.; Kubiak, C. P.; Xiong, W., *Chem. Phys. Lett.* **2016**, *650*, 1.

(31) Wang, J.; Clark, M. L.; Li, Y.; Kaslan, C. L.; Kubiak, C. P.; Xiong, W., *J. Phys. Chem. Lett.* **2015**, *6*, 4204.

(32) Smieja, J. M.; Sampson, M. D.; Grice, K. A.; Benson, E. E.; Froehlich, J. D.; Kubiak, C. P., *Inorg. Chem.* **2013**, *52*, 2484.

(33) Love, J. C.; Estroff, L. A.; Kriebel, J. K.; Nuzzo, R. G.; Whitesides, G. M., *Chem. Rev.* **2005**, *105*, 1103.

(34) Wang, Q.; Day, P.; Griffiths, J.-P.; Nie, H.; Wallis, J. D., *New J. Chem.* **2006**, *30*, 1790.

(35) Kirihara, M.; Asai, Y.; Ogawa, S.; Noguchi, T.; Hatano, A.; Hirai, Y., *Synthesis* **2007**, *2007*, 3286.

(36) *CRC Handbook of Chemistry and Physics, 97th Edition*. CRC Press: Online, 2016.

(37) Stoyanov, S.; Petkov, I.; Antonov, L.; Stoyanova, T.; Karagiannidis, P.; Aslanidis, P., *Can. J. Chem.* **1990**, *68*, 1482.

(38) Constable, E. C.; Housecroft, C. E.; Neuburger, M.; Price, J. R.; Zampese, J. A., *Australian Journal of Chemistry* **2010**, *63*, 1334.

(39) Keith, J. A.; Grice, K. A.; Kubiak, C. P.; Carter, E. A., *J. Am. Chem. Soc.* **2013**, *135*, 15823.

(40) Wang, J., *Analytical Electrochemistry*. 3rd ed.; Wiley-VCH: Hoboken, N.J., 2006; 1-41.

(41) Benson, E. E.; Kubiak, C. P., *Chem. Commun.* **2012**, *48*, 7374.

(42) Bourrez, M.; Molton, F.; Chardon-Noblat, S.; Deronzier, A., *Angew. Chem. Intl. Ed.* **2011**, *50*, 9903.

(43) Lam, Y. C.; Nielsen, R. J.; Gray, H. B.; Goddard, W. A., *ACS Catal.* **2015**, *5*, 2521.

(44) Tory, J.; Setterfield-Price, B.; Dryfe, R. A. W.; Hartl, F., *ChemElectroChem* **2015**, *2*, 213.

(45) Blaudez, D.; Bonnier, M.; Desbat, B.; Rondelez, F., *Langmuir* **2002**, *18*, 9158.

(46) Sheldrick, G., *Acta Cryst. A* **2008**, *64*, 112.

(47) Nogues, C.; Wanunu, M., *Surf. Sci.* **2004**, *573*, L383.

(48) Savéant, J.-M., *Elements of molecular and biomolecular electrochemistry : an electrochemical approach to electron transfer chemistry*. Wiley-Interscience: Hoboken, N.J., 2006.

(49) Azcarate, I.; Costentin, C.; Robert, M.; Savéant, J.-M., *J. Phys. Chem. C* **2016**, *120*, 28951.

6.7 Appendix

Calculation of $\mathrm{TOF}_{\mathrm{max}}$. The maximum turnover frequency can be determined from a plateaued catalytic CV response that is independent of scan rate.[48] In a 2-electron EC′ mechanism, the catalytic rate constant (k_{cat}) can be determined from the plateau current using the relationship between the plateau current under catalytic conditions (i_{cat}, Equation E6.1) and the peak current under non-catalytic conditions (i_p, Equation E6.2). Dividing Equation E6.1 by E6.2 (assuming the diffusion coefficient does not change dramatically under Ar versus CO_2) yields Equation E6.3.

$$i_{cat}=n_{cat}FAC^{\circ}_{cat}(Dk_{cat})^{1/2} \tag{\textbf{E6.1}}$$

$$i_p=0.4463n_p^{3/2}FAC^{\circ}_{cat}\left(\frac{F}{RT}\right)^{1/2}\nu^{1/2}D^{1/2} \tag{\textbf{E6.2}}$$

$$\frac{i_{cat}}{i_p}=2.24\sqrt{\frac{RT}{F}\frac{2k_{cat}}{\nu}} \tag{\textbf{E6.3}}$$

Where n_{cat} is the number of electrons in the catalytic process, F is Faraday’s constant, A is the electrode area (cm^2), C^{o}_{cat} is the concentration of catalyst (mol/L), and D is the catalyst diffusion coefficient (cm^2/s), n_p is the number of electrons for the non-catalytic process, R is the universal gas constant, and T is temperature. K_{cat} can also be described as the maximum turnover frequency ($\mathrm{TOF}_{\mathrm{max}}$), which is the theoretical number of times a catalyst can convert substrate to product per unit of time (Equation E6.4).[49]

$$\mathrm{TOF}_{\mathrm{max}}=k_{cat} \tag{\textbf{E6.4}}$$

It is noted that k_{cat} is a global rate constant and does not apply to a particular step in the catalytic mechanism.

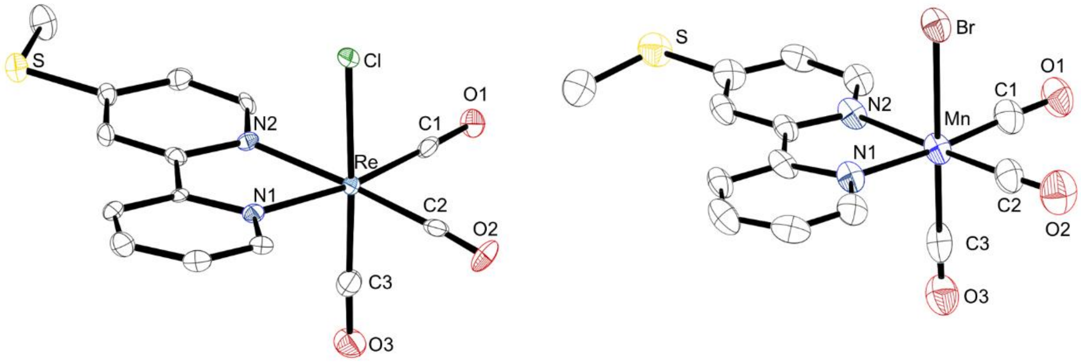

Figure 6.5 X-ray crystallographically determined molecular structure of Re(4-methylthio-2,2′-bipyridine)$(CO)_3$Cl (**1**) and Mn(4-methylthio-2,2′-bipyridine)$(CO)_3$Br (**2**). H atoms omitted for clarity and ellipsoids at 50% probability. CCDC 1477731-1477732.

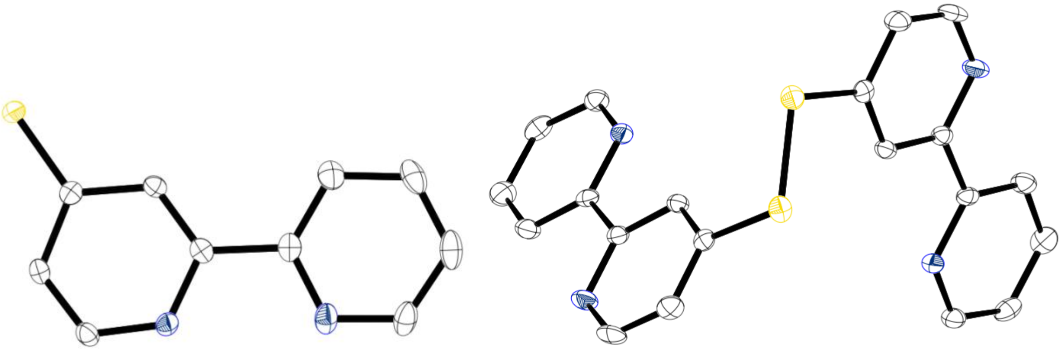

Figure 6.6 X-ray crystallographically determined molecular structure of ligands 4-mercapto-2,2′-bipyridine (left) and [2,2'-bipyridine-4-disulfide]$_2$ (right). H atoms omitted for clarity and ellipsoids at 50% probability. CCDC 1540831-1540832.

Table 6.1 Crystallographic data and refinement information for complexes **1** and **2**.

Compound	**Re(MeS-bpy)(CO)$_3$Cl**	**Mn(MeS-bpy)(CO)$_3$Br**
Empirical Formula	$C_{14}H_{10}ClN_2O_3ReS$	$C_{14}H_{10}BrMnN_2O_3S$
Formula Weight	507.96	421.15
Crystal System	monoclinic	triclinic
Space Group	$P2_1/n$	P-1
***a* (Å)**	10.5295(6)	6.6811(15)
***b* (Å)**	12.7123(8)	8.3367(18)
***c* (Å)**	11.9526(2)	13.932(3)
α (deg)	90	92.589(7)
β (deg)	98.859(2)	97.506(7)
γ (deg)	90	93.047(7)
V (Å^3)	1580.82(17)	767.2(3)
Z Value	4	2
ρ *calc* (g/cm^3)	2.1342	1.8230
mu (mm^{-1})	8.0000	3.612
Independent Reflections	2,894 [R(int) = 0.0491]	2,796 [R(int) = 0.1085]
Data/restraints/parameters	2559/0/199	1850/0/199
Goodness of Fit on F^2	1.0015	1.0619
R indices (all data) R1, wR2	0.0491, 0.1099	0.1211, 0.1370
Largest diff. peak and hole	1.5408 to –1.7422	1.3135 to –1.1900

Table 6.2 Crystallographic data and refinement information for ligands.

Compound	6-mercapto-2,2′-bipyridine	bpySSbpy
Empirical Formula	$C_{10}H_8N_2S$	$C_{20}H_{14}N_4S_2$
Formula Weight	188.25	374.47
Crystal System	monoclinic	monoclinic
Space Group	$P2_1/n$	C 2/c
***a* (Å)**	7.0306(5)	22.281(3)
***b* (Å)**	10.2510(7)	5.4708(8)
***c* (Å)**	12.9104(10)	13.5967(2)
α (deg)	90	90
β (deg)	101.624(4)	100.602(4)
γ (deg)	90	90
V ($Å^3$)	911.38	1709.5(4)
Z Value	4	4
ρ *calc* (g/cm^3)	1.3719	1.455
mu (mm^{-1})	0.303	0.323
Independent Reflections	1,874 [R(int) = 0.0331]	1,365 [R(int) = 0.0490]
Data/restraints/parameters	1874/0/121	1894/0/118
Goodness of Fit on F^2	1.036	1.092
R indices (all data) R1, wR2	0.0526, 0.0893	0.0490, 0.1060
Largest diff. peak and hole	0.34 to –0.35	0.298 to –0.435

Table 6.3 Selected bond lengths (Å) and angles (deg) for X-ray crystallographic structures of complexes, where M stands for metal (Re or Mn) and X stands for halogen (Cl or Br).

Bond/Angle	$Re(MeS\text{-}bpy)(CO)_3Cl$	$Mn(MeS\text{-}bpy)(CO)_3Br$
M–N1	2.179(5)	2.038(6)
M–N2	2.167(5)	2.052(6)
M–X	2.470(2)	2.524(1)
M–C1	1.942(7)	1.795(8)
M–C2	1.904(7)	1.798(9)
M–C3	1.918(7)	1.855(8)
C8–C9	1.483(8)	1.481(1)
N1–M–N2	75.05	78.54
N1–M–C3	95.71	90.07
N1–M–X	83.13	88.25
X–M–C1	94.89	89.20
X–M–C3	178.37	176.64
M–C1–O1	177.00	176.05
M–C2–O2	178.47	174.34
M–C3–O3	178.08	178.02

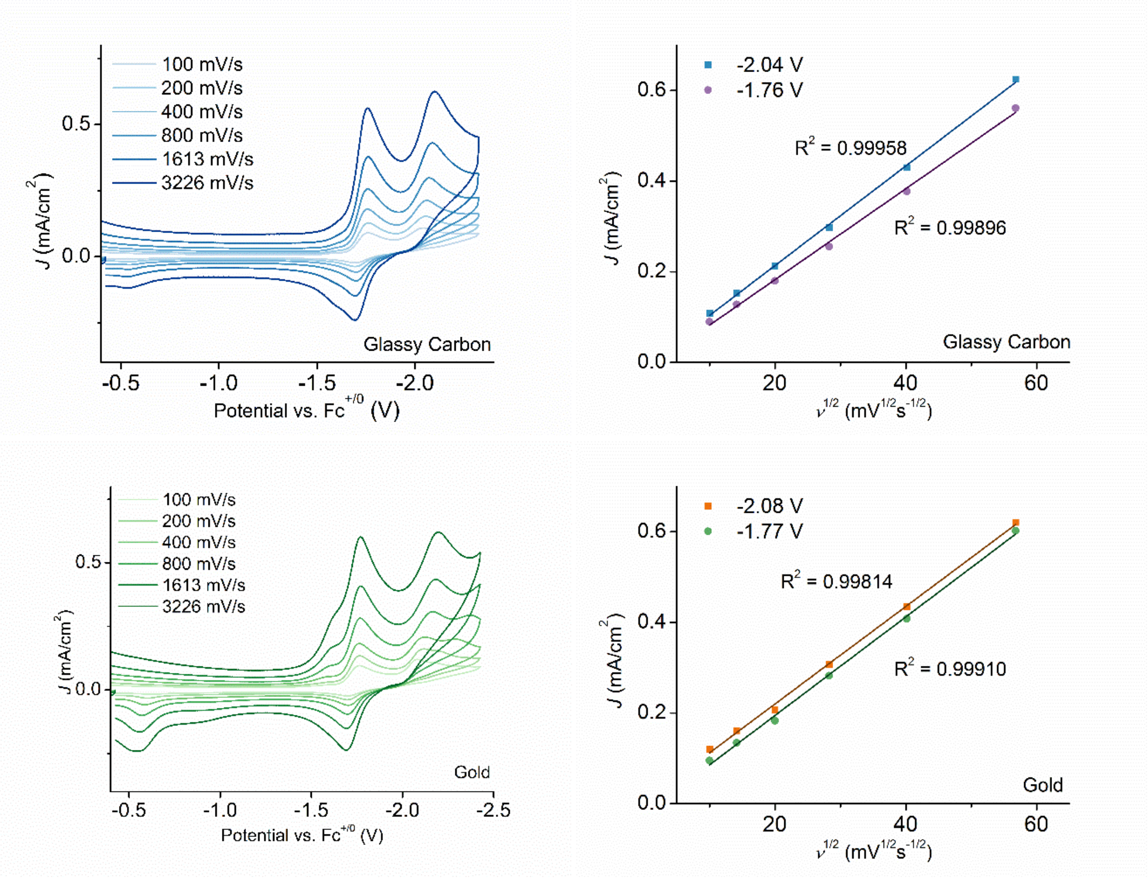

Figure 6.7 Left: Cyclic Voltammograms of Re complex **1** during homogeneous electrochemistry showing the two reductions at various scan rates using a glassy carbon working electrode (top) or gold working electrode (bottom). Right: Plot of peak current density versus the square root of the scan rate for the two electrodes, showing that the complexes are freely diffusing in solution and not affected by the electrode surface.

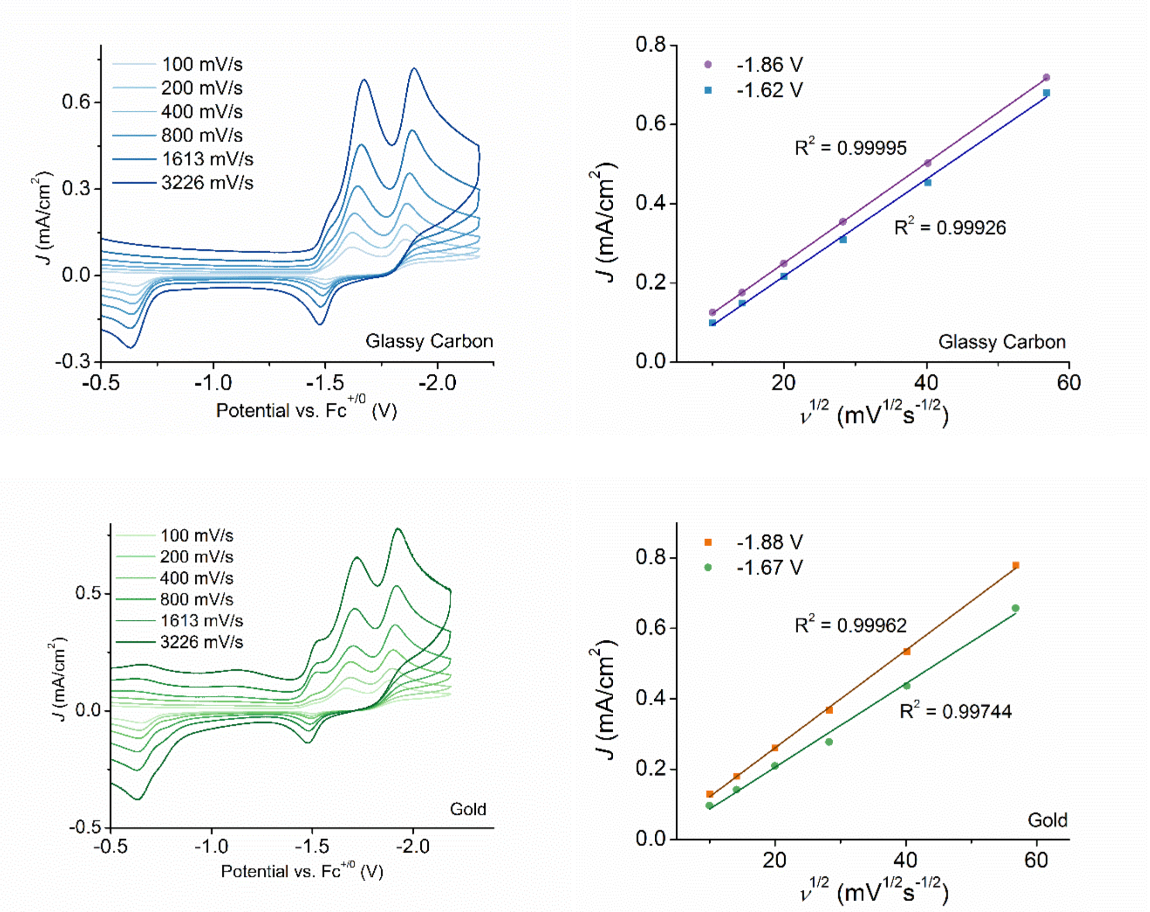

Figure 6.8 Left: Cyclic Voltammograms of Mn complex **2** during homogeneous electrochemistry showing the two reductions at various scan rates using a glassy carbon working electrode (top) or gold working electrode (bottom). Right: Plot of peak current density versus the square root of the scan rate for the two electrodes, showing that the complexes are freely diffusing in solution and not affected by the electrode surface.

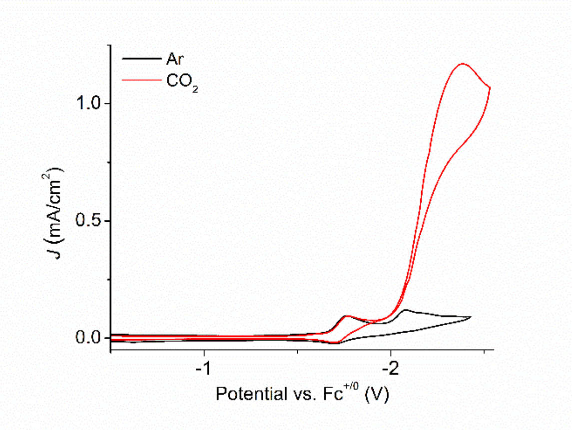

Figure 6.9 Cyclic voltammogram of **1** under Ar (black) and CO_2 (red) using a gold working electrode.

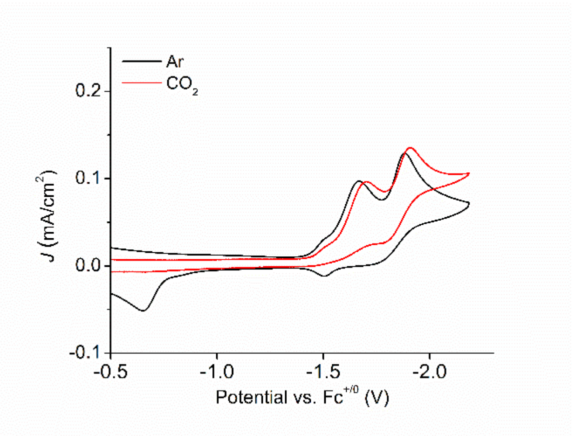

Figure 6.10 Cyclic voltammogram of **2** under Ar (black) and CO_2 (red) using a gold working electrode.

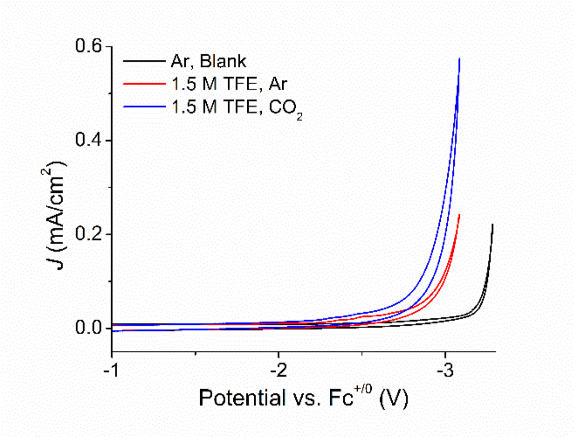

Figure 6.11 Cyclic voltammograms showing the solvent window when using a glassy carbon working electrode under Ar, CO_2 and with added TFE.

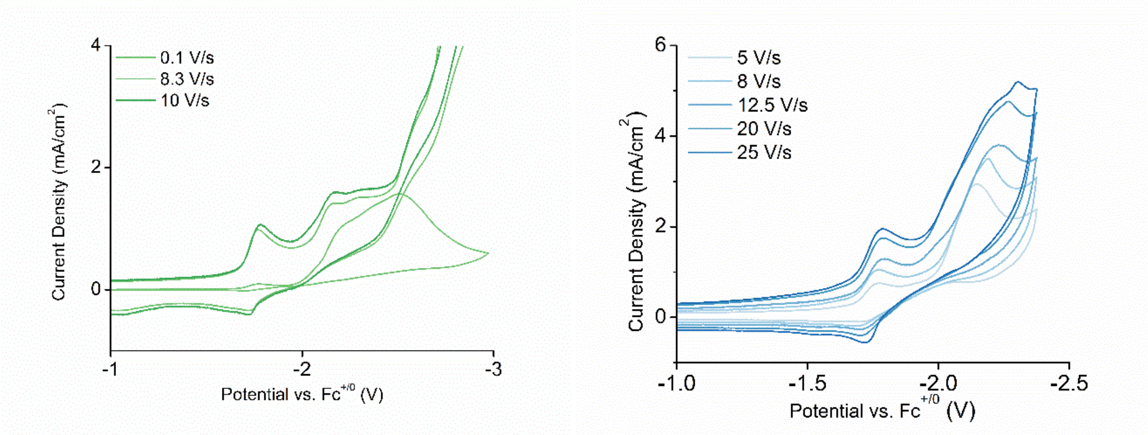

Figure 6.12 CV scan rate dependent studies under catalytic conditions (CO_2) to determine k_{cat} from an S-shaped wave for Re complex **1**. Left: CO_2. Right: CO_2 with 0.5 M TFE.

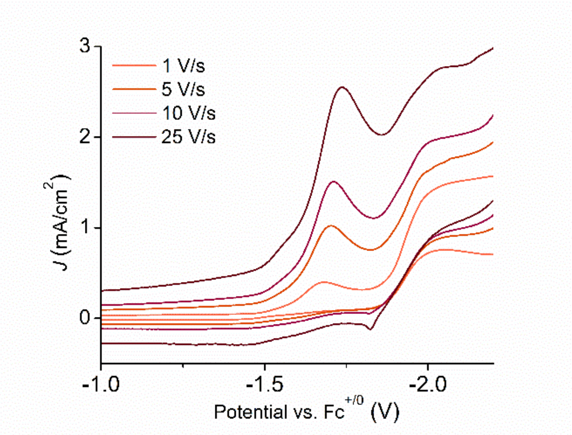

Figure 6.13 CV scan rate dependent studies under catalytic conditions (CO_2 with 1.5 M TFE) to determine k_{cat} from an S-shaped wave for Mn complex **2**.

Chapter 7

Comparing Other α-Diimine Ligands for Electrocatalytic CO_2 Reduction

7.1 Introduction

The activity and selectivity of the Re(bpy)$(CO)_3$Cl (bpy = 2,2′-bipyridine) family of catalysts is largely in part to the electronic properties of the bpy ligand. As a highly conjugated redox active ligand, bpy has a low lying unoccupied π* orbital, perfect for accepting and sharing electron density to the metal center.[1] This orbital lies below that of the Re lowest unoccupied molecular orbital (LUMO) d_{z^2}, and so the reduction of the bpy ligand before the metal center helps to lower overpotential of catalysis. The decentralized highest occupied molecular orbital (HOMO) of the catalytically active state (Re^0bpy^{-1}), which spreads across the metal and bpy, is believed to help with selectivity of the catalyst for CO_2 binding over H^+ since the incoming CO_2 molecule can interact with the bpy π* as well as the Re d_{z^2} orbitals.[2]

The success of using bpy as the redox active interest has sparked interest in many groups to investigate other redox active α-diimines in the same Re framework to test their ability for CO_2 electroreduction.[3-10] Most are met with little success. This chapter will analyze one of these ligands, which is the previously untested α-diimine ligand, dipyrrin. Density functional theory (DFT) calculations will then be used to help elucidate potential differences between bpy, dipyrrin, and other α-diimine ligands recently tried in literature. These comparisons, we hope, will guide others in designing new catalysts for CO_2 reduction.

7.2 Dipyrrin Based Complexes

Introduction. Dipyrrin ligands and their complexes are popular in the photochemistry community due to their luminescent properties.[11-12] Sometimes referred to as "half-porphyrins" and considered an analogue of BODIPY (4,4-difluoro-4-bora-3a,4a-diaza-*s*-indacene), dipyrrins are a highly conjugated ligand (Figure 7.1). This allows for appreciable quantum yields and tunable emission wavelengths that come from the many ways to synthetically modifying the ligand.[13] Due to these properties, dipyrrin based complexes have received attention in areas including organic photovoltaics, luminescent sensors,[11] metal-organic frameworks, and coordination polymers.[14-16] Despite their similarities to bpy and the available literature of easily synthesized Re(α-diimine)$(CO)_3Cl$ complexes, dipyrrins have not been investigated for their reactivity towards CO_2. To probe this question, two Re dipyrrin complexes were made, Re(5-phenyldipyrrin)$(CO)_3$(py) (**1**) and Re(5-mesityldipyrrin)$(CO)_3$(py) (**2**). Pyridine was used in lieu of chloride since dipyrrin is an anionic ligand, and there is literature precedence of pyridine labilization for CO_2 reduction electrocatalysis on Re-bpy.[17]

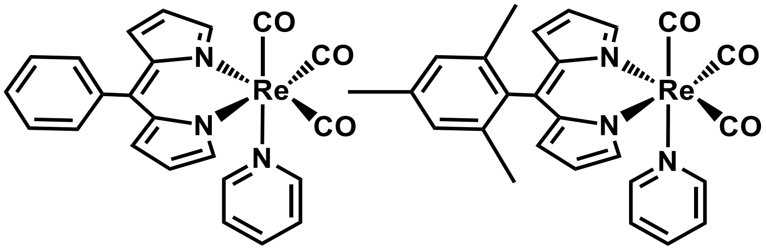

Figure 7.1 Re(5-phenyldipyrrin)$(CO)_3$(py) (left) and Re(5-mesityldipyrrin)$(CO)_3$(py) (right) studied in this work.

Synthesis and Characterization. Synthesis of 5-phenyldipyrrin and 5-mesityldipyrrin was performed by coupling of pyrrole and the corresponding aldehyde,[18] followed by oxidation,[19] to afford the conjugated ligand as previously reported. While the corresponding Re(dipyrrin)$(CO)_3(PPh_3)$ complexes have been previously reported,[20] the pyridyl versions were not found in the literature. These complexes were synthesized in an *in situ* two step procedure where $Re(CO)_5Cl$ and the corresponding dipyrrin were refluxed in toluene for four hours under inert atmosphere followed by exchange of the solvent for pyridine to reflux overnight. The complexes were purified by column chromatography to afford orange powders.

Crystals suitable for X-ray diffraction for the pyridyl substituted complexes were grown from vapor diffusion of pentane into a saturated solution of the complex in dichloromethane (Figure 7.2). X-ray structures of the PPh_3-substituted complexes have been previously reported,[20] however pyridine was chosen because it is a more labile ligand and thus would be more susceptible to dissociation to create an active site for CO_2 binding. Compared to the crystal structure of $Re(bpy)(CO)_3Cl$ (Re-bpy),[21] the dipyrrin has a slightly larger bite angle (N1-Re-N2) at 85.1º for **1** and 84.6º for **2** compared to 74.9º for Re(bpy). In both complexes, the 4-substituent is almost orthogonal to the plane of the dipyrrin with angles of 101.8º and 93.3º for **1** and **2**, respectively.

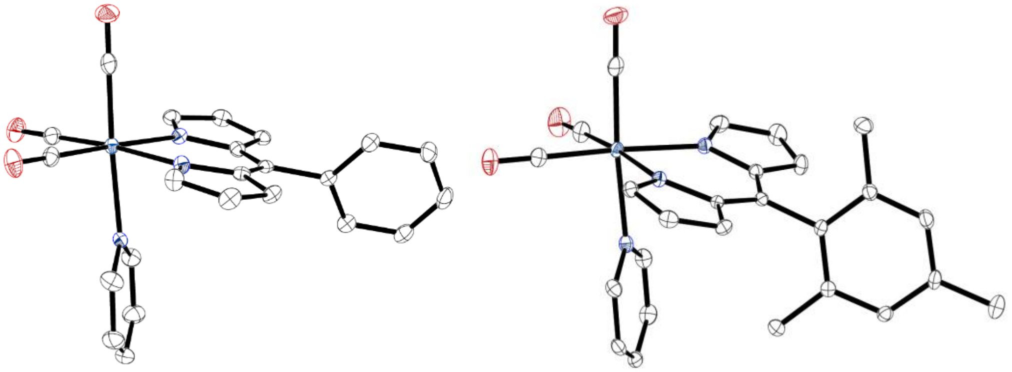

Figure 7.2 Molecular structures of 1 and 2 as determined by X-ray crystallography. White = C, purple = N, red = O, blue = Re. Hydrogen atoms omitted for clarity. Structure information in Tables 7.5 and 7.6.

Electrochemistry. The cyclic voltammograms (CV) of **1** and **2** can be seen in Figure 7.3. Under inert atmosphere (Ar), both complexes show three reductive features. The first is reversible (ca. –1.70 V vs. $Fc^{+/0}$), while the next two are irreversible. Under an atmosphere of CO_2, there is small increase in current at the second reductive feature. However, this increase is quite small, with i_{cat}/i_p values of 2.45 for **1** and 1.23 for **2**. Further experimental analysis is needed to determine product distribution and deactivation pathways, however computational analysis can help us to understand why these complexes are not as good as the Re-bpy system (*vide infra*).

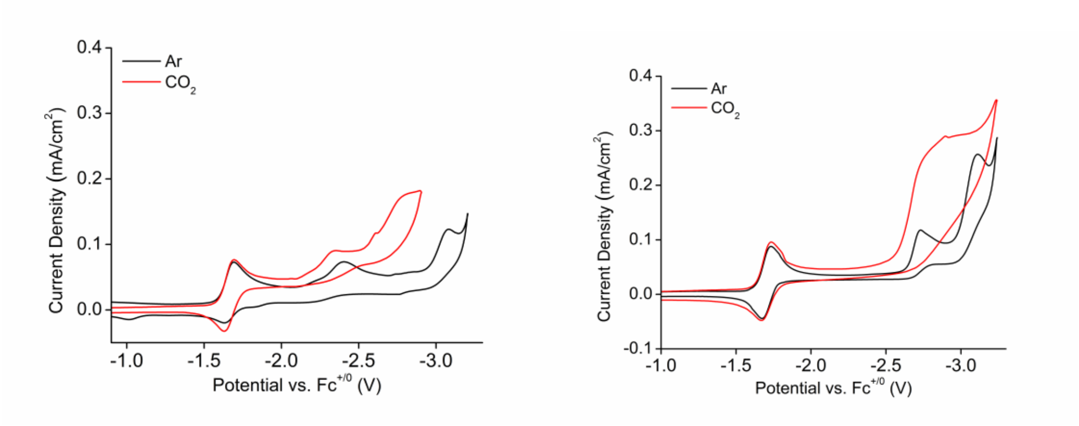

Figure 7.3 CVs of **1** (left) and **2** (right) under Ar and CO_2 atmosphere. Catalytic current is seen upon the second reduction under CO_2.

7.3 Computational Comparisons between α-Diimine Ligands

Introduction. Dipyrrin is the not the only ligand to be tested and found to not be as valuable as bpy towards creating active and selective Re-based CO_2 reduction catalysts. Other α-diimine ligands, such as pyridine monoimine (PMI),[9, 22-23] 1,10-phenanthroline (phen),[21, 24] bis(imino)acenaphthlene (BIAN),[7] and 1,4-diazabutadiene (DAB)[8] have all been used in the Re(α-diimine)$(CO)_3X$ (X = Cl, Br) framework and were found to have very poor catalytic properties (Figure 7.4). To gain a better understanding of why, in a collaboration with Prof. Emily Carter and her student Dr. Martina Lessio at Princeton University, we set out to computationally compare these complexes. We note that each ligand can easily be modified with a variety of substituents, however we chose substituents based on simplicity and literature precedence for electrochemical CO_2 reduction studies.

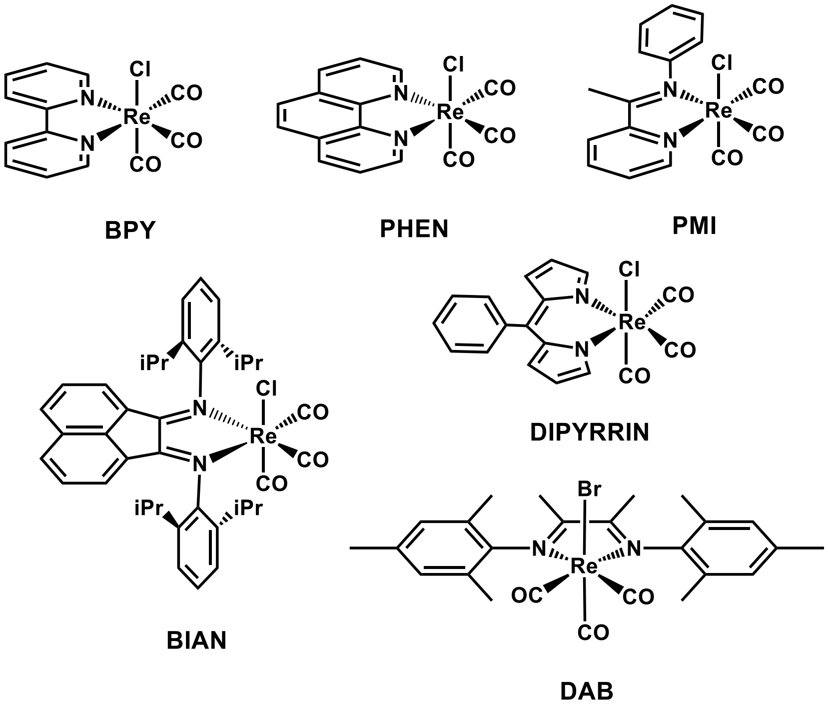

Figure 7.4 The six complexes computationally compared in this work, identified by the α-diimine ligand.

Molecular Orbitals of Reduced Complexes. The delocalized electron density over the entire catalytically active state of Re-bpy is an important factor to its reactivity.[1] Therefore, we first set out to compare the singly occupied molecular orbital (SOMO) and the highest occupied molecular orbital (HOMO) of each of the six compounds (Table 7.1). In comparing the SOMO across the complexes, it is clear that the first reduction is ligand based for each ligand. The bpy and phen complexes look almost identical, where the additional middle aromatic ring on phen does not gain any electron density from the reduction. PMI, where an orthogonal benzyl substituent is in the place of bpy's second pyridyl ring, shows electron density across the α-diimine and remaining pyridyl structure. BIAN and DAB, which do not have a conjugated α-diimine ring structure, show electron density primarily on the α-diimine core. Finally, dipyrrin, which is comprised of pyrrole heterocycles rather than pyridyl, has delocalized electron density on these pyrrole rings, away from the α-diimine structure.

Comparison of the HOMOs of each of the six complexes also reveals subtle differences in the electron density distribution. In each case, electron density is primarily located across the metal and equatorial carbonyls, indicating a metal based reduction. Again, the bpy and phen complex's HOMOs look basically identical, where electron density is delocalized across the α-diimine, Re, and equatorial carbonyls. PMI, BIAN, and DAB complexes are also similar in that the distribution is mainly across the metal center and conjugated α-diimine core. In all three complexes, the phenyl groups not in plane with the α-diimine do not have the orbital symmetry to accept electron density. Different from the rest, the dipyrrin HOMO again shows decreased charge density at the α-diimine core of the ligand. The lack of even delocalized of charge density could be a main reason why the dipyrrin ligand is a poor substitute for bpy for CO_2 reduction catalysis. Due to this, dipyrrin was not included in the remainder of this study.

Table 7.1 Density different plots showing the polarization that occurs upon adding one (SOMO) and two (HOMO) electrons to each Re(α-diimine)$(CO)_3Cl$ complex. Purple represents decreased charge density while orange represents increased charge density. Potassium atoms were used for charge balance. Atoms: C = brown, N = blue, H = white, O = pink, Cl = mint, Re = gold, K = blue.

α-diimine	**$1e^-$ Reduced Complex SOMO**	**$2e^-$ Reduced Complex HOMO**
bpy	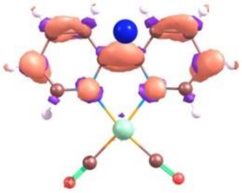	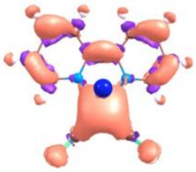
phen	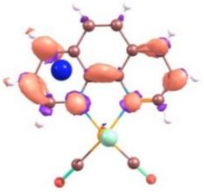	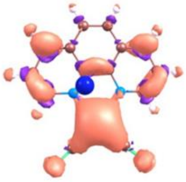
PMI	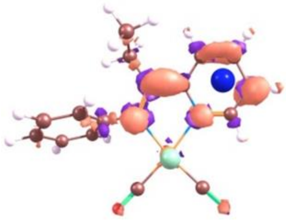	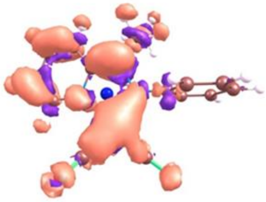
DAB	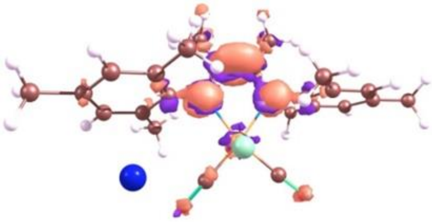	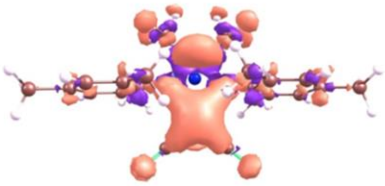
BIAN	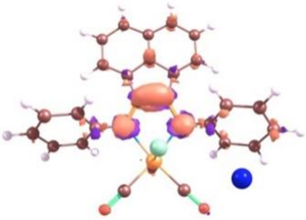	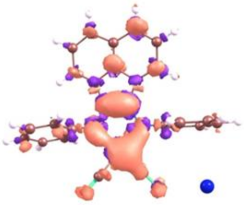
dipyrrin	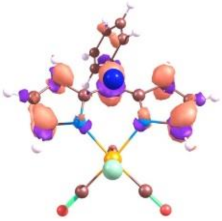	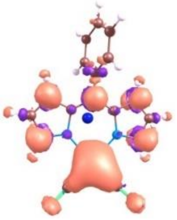

Comparison of Ligand Electron Donating Ability. To assess the electron donating ability of each of the ligands, a comparison was made between ligand pK_a and the reduction potentials of the complex. Since all of the complex's first reduction is ligand based, the more positive the reduction potential, the more electron withdrawing the ligand and the lower the pK_a will be. As seen in Table 7.2, computed and experimental first reduction potentials match fairly well, with the biggest difference being for PMI, where the computational value is 0.36 V more positive. This could be due to PMI being the only asymmetric ligand, leading to the two imines having different σ-donating environments to the metal center. PMI aside, the computed pK_a values for the ligands trend with the first reduction potentials. Bpy, which comprises the most active Re(α-diimine)$(CO)_3X$ catalyst, is also the most electron donating ligand.

Table 7.2 Computed vs. experimentally determined first reduction potentials as well as computed ligand pK_a values to quantitatively determine the electron-donating ability of the ligand.

α-diimine	**Complex 1st reduction potential (V vs SCE)**		**Computed p*K*a**
	Computed	**Experimental**	
bpy	–1.29	–1.34	11.2
phen	–1.26	–1.36	9.6
PMI	–0.94	–1.30	5.3-5.8
DAB	–0.75	–0.83	9.2
BIAN	–0.59	–0.50	5.1

Comparison of Binding Strength. To gain more insight into how these electronic parameters trend with the reactivity of the complexes, the binding energies for three key moieties to the doubly reduced catalytically active state were calculated (Figure 7.5). As CO_2 reduction to CO is a proton coupled process, the binding of protons (H^+), CO_2 and hydroxycarbonyl (COOH) were determined (Table 7.3). The Re-COOH adduct is known to be the most stable intermediate during the catalytic cycle,[25] and the coupling of a proton to the activated CO_2 lowers the overall ΔG of the reaction.[26-27] It has also been previously determined that H^+ binding is more thermodynamically favorable for the bpy complex,[2] however the reaction with CO_2 is ten times faster, indicating a kinetic preference for CO_2 reduction over H^+.[28]

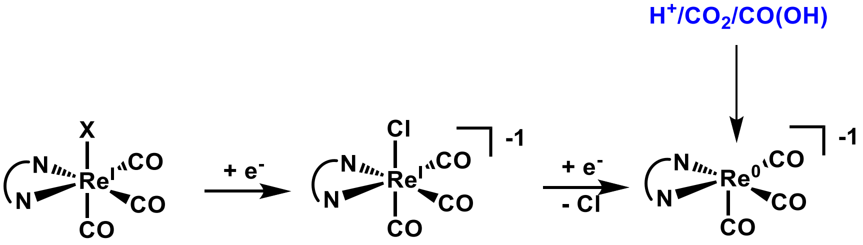

Figure 7.5 Diagram showing the two reductions of the Re(α-diimine)$(CO)_3X$ complexes and the reaction of substrates H^+, CO_2 and COOH with the catalytically active state corresponding to the computed binding energies (ΔG) in Table 7.3.

Just like bpy, all of the ligands show a thermodynamic preference for the binding of H^+ over CO_2. The binding energies trend with the electron donating ability of the ligand, where bpy has the most favorable binding energy for all three substrates. The added stabilization from the addition of a proton to the activated CO_2 is seen in the more favorable energies for COOH binding in all cases. Of note is the endergonic values for the binding energies of CO_2 to PMI, DAB, and BIAN. These results indicate that PMI, DAB, and BIAN based complexes should be poor CO_2 electrocatalysts that need protons to stabilize any reactivity with CO_2.

However, the favorability of proton binding over CO_2 may result in proton reduction if a proton source were to be included during catalysis.

Table 7.3 Computed binding energies (ΔG) for H^+, CO_2, and COOH to the catalytically active state of each Re(α-diimine)$(CO)_3X$ complex (Figure 7.5).

α-diimine	**Binding energy (kcal/mol)**		
	H^+	**CO_2**	**COOH**
bpy	–39.4	–2.7	–35.3
phen	–41.2	–5.4	–33.3
PMI	–24.0	+4.3	–22.2
DAB	–19.9	+14.0	–11.0
BIAN	–14.2	+15.9	–10.1

Catalytic Activity. If electron donating ability of the ligand is the main predictor in catalytic activity for Re(α-diimine)$(CO)_3X$ complexes, the order of activity should trend bpy > phen > PMI > DAB > BIAN. Reported activity and product distribution is listed in Table 7.4. We note that due to differences in reporting catalysis the values may not be directly comparable, hence we support the recent push in the literature for the adoption of more rigorous and standardized benchmarking of catalysis.[29-31]

Table 7.4 Reported catalytic activity of each of the Re(α-diimine)$(CO)_3X$ complexes.

	bpy[a]	**phen[32,b]**	**PMI[9]**	**DAB[8]**	**BIAN[6]**
Computed pK_a	11.2	9.6	5.2-5.8	9.2	5.1
E_{cat} (V vs.$Fc^{+/0}$)	–2.10	–2.09	–2.38	N/A	–2.54
i_{cat}/i_p	14.9	10.1	2.6	<0.5	not reported
Reported %FE for CO	100%	100%	44%	<10%	24%
Other Products	none	none	CO_3^{2-}	CO_3^{2-}	H_2

[a] Reported in Chapter 3. [b] i_{cat}/i_p larger than literature value. See Appendix.

In line with our computational data, Re(phen)$(CO)_3Cl$ has the closest activity to the bpy based complexes. Despite being so similar to bpy, phen has only recently been characterized for electrocatalytic CO_2 reduction.[32] However, substituents to enhance the complex's fluorescence have been more rigorously studied.[33-36] As a photocatalyst for CO_2 reduction, phen has been found to be somewhat active, producing 11.5 equivalents of CO per catalyst after 120 minutes (compared to bpy complex, 26.4 equiv./cat. after 120 minutes).[21]

Complexes of PMI, DAB, and BIAN show very little activity for CO_2 reduction, as is predicted by our calculations. In each case, various deactivation pathways have been cited. In a study using the (2-cyclohexyl-1-methyl)-methylimino-pyridine ligand (MeCyIm), 44% CO was observed by controlled potential electrolysis (CPE) over 1.1 hr.[9] Infrared-spectroelectrochemistry (IR-SEC) experiments confirmed the production of CO and the presence of carbonate (CO_3^{2-}). A main deactivation pathway is the reductive insertion of CO_2 into the backbone of the α-diimine at the methyl substituted carbon, which has been structurally characterized on a Mo complex.[22] In the case of DAB based Re complexes, <10% Faradaic efficiencies for CO were observed from CPE experiments. IR-SEC also confirmed small amounts of CO and CO_3^{2-}, where product inhibition was considered a contributing factor to poor catalysis. With the same α-diimine backbone as PMI, it would not be far-fetched to consider CO_2 insertion into this ligand framework as well. In the case of BIAN complexes, four reductions are seen in the CV, where catalytic current occurs after the fourth irreversible reduction. Faradaic efficiencies for CO were reported as 31% after 6000 s and 24% after 10,000 s of CPE.[6] For complexes of all three ligands (PMI, DAB, and BIAN), when a proton source was added, hydrogen production was recorded. These findings support our computational trends.

The Role of Carbonate. When an electrocatalyst is found to not be selective for the reduction of CO_2 to exclusively CO, the question remains of what other products are being formed. Reduction products such as oxalate, formate, carbonate, and oxalic acid are all considered relatively achievable products. The issue here being that when product distribution is being analyzed for poor catalysts, the small amount of these other products being detected may be coming from other sources. The most common of these is carbonate. Recent literature has seen an increase in describing poor molecular CO_2 reduction electrocatalysts as catalyzing the reductive disproportionation of CO_2 into CO and carbonate.[8-9, 37-39] Before attributing carbonate as the main product of poor catalysis, consideration must be made of possible side reactions, quantity detected, and determination of viable reaction mechanisms.

In the presence of water, CO_2 will form equilibria between carbonate, bicarbonate, and carbonic acid, which is dependent on solution pH (Equations E7.1-7.3).

$$CO_2 + H_2O \leftrightarrow H_2CO_3 \qquad (\mathbf{E7.1})$$

$$H_2CO_3 \leftrightarrow H^+ + HCO_3^- \qquad (\mathbf{E7.2})$$

$$HCO_3^- \leftrightarrow H^+ + CO_3^{2-} \qquad (\mathbf{E7.3})$$

While electrocatalysis is most often reported using “dry” MeCN or dimethylformamide (DMF), it is relatively accepted amongst the scientific community that adventitious water is still present in these solutions.[29, 40-41] An *in* *situ* FT-IR study of CO_2 reduction products off of Pt, Au, and GC working electrodes from solutions of MeCN (freshly distilled over CaH_2) containing tetrabutylammonium fluoride (TBAF) observed over time peaks corresponding to carbonate salts at much lower potentials than the solvent window (the solvent window being the potential at which MeCN gets deprotonated).[42] At a glassy carbon electrode held at –2.58 V vs. $Fc^{+/0}$, bands corresponding to both carbonate (1682, 1645, 1302, and 1275 cm^{-1}) and CO (2140 cm^{-1}) were observed. This has been verified in our experiments, where a glassy carbon IR-SEC cell with "dry" MeCN and tetrabutylammonium hexafluorophosphate ($TBAPF_6$) with ca. 0.14 M CO_2 was stepped from ca. –1.4 V to –2.0 V vs. $Fc^{+/0}$, (Figure 7.11). Over the course of 25 minutes, the band corresponding to CO_2 (2342 cm^{-1}) decreased while bands at 1672 cm^{-1} and 1283 cm^{-1}, corresponding to carbonate, increased over time. Considering this potential is lower than the catalytic potentials for the complexes listed above, it is very possible that any carbonate seen is coming directly from solution and not catalysis.

The other argument against carbonate formation is mechanistic. Mechanistic examples of carbonate formation often involve bimetallic pathways.[43] The photochemical reduction of CO_2 by Re-bpy based complexes is considered a bimolecular mechanism, for example. These mechanisms start with the singly reduced bpy complex or the Re-Re bpy dimer, where a bridge carboxylate forms in between the two metal centers, and the presence of another CO_2 molecule allows for the formation of CO and CO_3^{2-}.[44] The addition of Lewis acids for CO_2 reduction electrocatalysis also infer a bimolecular mechanism, where a cyclic intermediate is envisioned.[45-47] In cases where bpy based complexes have hydrogen bonding capabilities, again a bimolecular pathway is presented.[37] In order for carbonate to be considered an actual product of catalysis for these complexes, which show little reactivity for CO_2 and have endergonic binding energies for CO_2, more careful mechanistic studies need to be performed to show a second order dependence for both catalyst and CO_2.

7.4 Conclusions

This chapter has focused on other α-diimines for electrocatalytic CO_2 reduction within the Re(α-diimine)$(CO)_3$Cl framework. Dipyrrin ligands were found to be much less active than their bpy counterparts, most likely due to the active catalyst state having dispersed electron density away from the metal center. Other ligands tried in the literature, DAB, BIAN, PMI, and phen, were computationally compared. It was found that all of the ligands have similar reduced states to Re-bpy, where the first reduction is ligand based (yielding a ligand centered SOMO) and the second reduction is metal based (delocalized HOMO). All of the ligands, however, are less electron donating than bpy and have lower binding affinities for CO_2 and COOH. The activity reported in the literature trends with the computational findings, showing that predicting a ligand's pK_a may be a good way to screen ligands before being experimentally tried for electrocatalytic CO_2 reduction. More electron donating ligands will be better electrocatalysts than bpy for CO_2 reduction, however that will come at the sacrifice of overpotential.

7.5 Experimental

General Experimental Considerations. ^{1}H and ^{13}C NMR spectra were recorded at 298K on a Varian 500 MHz spectrometer. Chemical shifts are reported relative to TMS (δ = 0) by referencing to deuterated solvent signals. FT-IR spectra were performed on a Thermo Scientific Nicolet 6700. Electrochemical experiments were performed on a BASi Epsilon potentiostat. Microanalyses were performed by NuMega Resonance Labs, San Diego, CA for C, H, and N.

Reagents. Solvents were received from Fisher Scientific and were dried either on a custom solvent system (degassed with Argon and dried over alumina columns) or over 3Å sieves and degassed prior to use. Deuterated solvents were obtained from Cambridge Isotope Laboratories. Synthetic reagents were obtained from commercial suppliers. Benzaldehyde and pyrrole were freshly distilled and stored in the dark prior to use. Tetrabutylammonium hexafluorophosphate ($TBAPF_6$, Aldrich, 98%) was recrystallized twice from methanol and dried at 90°C overnight before use in electrochemistry experiments. Reactions were performed sheltered from light using standard Schlenk-line and Glove Box techniques under an atmosphere of nitrogen. The complexes 5-phenyldipyrromethane and 5-mesityldipyrromethane were made according to literature procedure[18] as recommended.[13] Dipyrromethanes were then oxidized to afford the ligands 5-phenyldipyrrin and 5-mesityldipyrrin, which were used immediately.[19]

Re(5-phenyldipyrrin)$(CO)_3$(py). A 100 mL oven-dried roundbottom flask was charged with $Re(CO)_5Cl$ (100 mg, 0.276 mmol), 5-phenyldipyrrin (61 mg, 0.276 mmol), and 20 mL of toluene. The mixture was brought to a light reflux under an inert atmosphere, upon which triethylamine (0.1 mL, 0.717 mmol) was added. Mixture was refluxed over four hours or until complete consumption of 5-phenyldipyrrin as indicated by TLC analysis. The solvent was removed under reduced pressure. Pyridine was added (10 mL) and the mixture was allowed to reflux overnight. The pyridine was removed via reduced pressure, and the resulting black solid mixture was run through an alumina column (4:1 hexane/DCM) where the bright orange band was collected. The resulting bright orange solid was washed once with cold pentane and dried under vacuum overnight (47 mg, 30% yield). ^{1}H NMR ($CDCl_3$) δ =, 8.15 (2H, m), 8.02 (2H, d), 7.71, (1H, m), 7.41 (2H, m), 7.38 (2H, m), 7.16 (2H, m), 6.74 (1H, m), 6.47 (2H, m), 6.42 (2H, m). IR (MeCN) v(CO) 2014 cm^{-1}, 1904 cm^{-1}, 1891 cm^{-1}. Elemental analysis for $C_{23}H_{16}N_3O_3Re$ calcd: C, 48.58; H, 2.84; N, 7.39; found: C, 48.20; H, 3.02; N, 7.41. X-ray quality crystals were grown by vapor diffusion of pentane into a saturated solution of complex in DCM. CCDC 1551957.

Re(5-mesityldipyrrin)(CO)$_3$(py). Made in the same procedure as Re(5-phenyldipyrrin)(CO)$_3$(py). Reagents 5-mesityldipyrrin (131 mg, 0.503 mmol), $Re(CO)_5Cl$ (0.182 g, 0.503 mmol), chloroform (75 mL), triethylamine (0.4 mL, 2.86 mmol), and pyridine (15 mL) were used to afford bright orange powder (105 mg, 34% yield). ^{1}H NMR ($CDCl_3$) δ = 8.11 (4 H, m), 7.67 (1H, m), 7.15 (2H, m), 6.87 (1H, s), 6.74 (1H, s), 6.38 (4H, m), 2.31 (3H, s), 2.03 (3H, s), 1.28 (3H, s). IR (CH_3CN) v(CO) 2014 cm^{-1}, 1905 cm^{-1}, 1891 cm^{-1}. ESI-MS (m/z) $[M + H]^+$: calcd: 612.12; found: 612.07 . Elemental analysis for $C_{26}H_{22}N_3O_3Re$ calcd: C, 51.14; H, 3.63; N, 6.88; found: C, 50.85; H, 3.79; N 6.94. X-ray quality crystals were grown by vapor diffusion of pentane into a saturated solution of complex in DCM. CCDC 1551958.

X-Ray Crystallography. Single crystal X-ray diffraction studies were carried out on a Bruker Kappa APEX-II CCD diffractometer equipped with Mo Kα radiation (λ = 0.71073 Å) or a Bruker Kappa APEX CCD diffractometer equipped with Cu Kα radiation (λ = 1.54184 Å). The crystals were mounted on a Cryoloop with Paratone oil and data were collected under a nitrogen gas stream at 100(2) K using ω and ϕ scans. Data were integrated using the Bruker SAINT software program and scaled using the SADABS software program. Solution by direct methods (SHELXS) produced a complete phasing model consistent with the proposed structure. All non-hydrogen atoms were refined anisotropically by full-matrix least-squares (SHELXL-97).[48]

Homogeneous Electrochemistry. Electrochemical experiments were performed using a BASi Epsilon potentiostat. A 20 mL scintillation vial with a custom fitted top was used for all CV and DPV experiments, utilizing a 3 mm diameter glassy carbon working electrode, Pt wire counter electrode, and a Ag/AgCl reference electrode (separated from solution in by a glass sheath and CoralPor tip). The glassy carbon working electrode was polished with 15, 3, and 1 micron diamond paste successively, thoroughly rinsed with methanol, and dried under a stream of nitrogen prior to experiments, and polished with 1 micron diamond polishing paste between scans. The platinum wire was flame treated with a butane torch prior to use. To minimize the amount of adventitious water in our set up and prevent solvent loss via sparging the solution, Ar and “bone dry” CO_2

gas were first run through their own Drierite columns and secondly through a sealed vial of dry MeCN filled with 3Å sieves. An oven-dried cannula was then used to transfer the MeCN saturated dry gas to the electrochemical set-up. Electrochemical solutions were sparged for at least five minutes prior to the start of data collection, and were kept under a blanket of the gas during measurements. Experimental conditions, unless otherwise noted, consisted of 5 mL of a 0.1 M $TBAPF_6$ solution of MeCN, 1 mM complex, and 1 mM ferrocene to use as an internal standard with a typical scan rate of 0.1 V/s. Ohmic drop of the cell was corrected for by using the potentiostat's iR-compensation tool, correcting for 80-90% of the measured resistance. This resulted in a ferrocene peak splitting typically between 61-67 mV.

Infrared-Spectroelectrochemistry (IR-SEC). IR-SEC experiments were carried out in a custom-made cell with a glassy carbon working and circular platinum counter and pseudoreference silver electrodes.[49] Gases were dried per the procedure listed for CV experiments. A Pine Instrument Company model AFCBP1 bipotentiostat was used to apply potential to the system.

7.6 Acknowledgements

This chapter, in part, is currently being prepared for submission for publication of the material, entitled "Kinetic and Mechanistic Effects of Substituent, Labile Ligand, and Brønsted Acid on Electrocatalytic CO_2 Reduction by Re(bpy) Complexes" by Melissa L. Clark, Martina Lessio, Po Ling Cheung, Emily A. Carter, and Clifford P. Kubiak, where Dr. Martina Lessio contributed the computational studies for this chapter. The dissertation author is the primary author of this manuscript.This work was supported by the Air Force Office of Scientific Research through the MURI program under AFOSR Award No. FA9550-10-1-0572. Prof. Charles Machan and Prof. Seth Cohen are acknowledged for valuable discussions and assistance.

7.7 References

(1) Benson, E. E.; Sampson, M. D.; Grice, K. A.; Smieja, J. M.; Froehlich, J. D.; Friebel, D.; Keith, J. A.; Carter, E. A.; Nilsson, A.; Kubiak, C. P., *Angew. Chem. Intl. Ed.* **2013**, *52*, 4841.

(2) Keith, J. A.; Grice, K. A.; Kubiak, C. P.; Carter, E. A., *J. Am. Chem. Soc.* **2013**, *135*, 15823.

(3) Spall, S. J. P.; Keane, T.; Tory, J.; Cocker, D. C.; Adams, H.; Fowler, H.; Meijer, A. J. H. M.; Hartl, F.; Weinstein, J. A., *Inorg. Chem.* **2016**.

(4) Zeng, Q.; Tory, J.; Hartl, F., *Organometallics* **2014**, *33*, 5002.

(5) Tory, J.; Gobaille-Shaw, G.; Chippindale, A. M.; Hartl, F., *J. Organomet. Chem.* **2014**, *760*, 30.

(6) Portenkirchner, E.; Kianfar, E.; Sariciftci, N. S.; Knor, G., *ChemSusChem* **2014**, *7*, 1347.

(7) Portenkirchner, E.; Oppelt, K.; Ulbricht, C.; Egbe, D. A. M.; Neugebauer, H.; Knör, G.; Sariciftci, N. S., *J. Organomet. Chem.* **2012**, *716*, 19.

(8) Vollmer, M. V.; Machan, C. W.; Clark, M. L.; Antholine, W. E.; Agarwal, J.; Schaefer III, H. F.; Kubiak, C. P.; Walensky, J. R., *Organometallics* **2015**, *34*, 3.

(9) Machan, C. W.; Chabolla, S. A.; Kubiak, C. P., *Organometallics* **2015**, *34*, 4678.

(10) Elgrishi, N.; Chambers, M. B.; Wang, X.; Fontecave, M., *Chem. Soc. Rev.* **2017**, *46*, 761.

(11) Bessette, A.; Hanan, G. S., *Chem. Soc. Rev.* **2014**, *43*, 3342.

(12) Wood, T. E.; Thompson, A., *Chem. Rev.* **2007**, *107*, 1831.

(13) Gryko, D. T.; Gryko, D.; Lee, C. H., *Chem. Soc. Rev.* **2012**, *41*, 3780.

(14) Halper, S. R.; Cohen, S. M., *Inorg. Chem.* **2005**, *44*, 486.

(15) Halper, S. R.; Do, L.; Stork, J. R.; Cohen, S. M., *J. Am. Chem. Soc.* **2006**, *128*, 15255.

(16) Halper, S. R.; Malachowski, M. R.; Delaney, H. M.; Cohen, S. M., *Inorg. Chem.* **2004**, *43*, 1242.

(17) Wong, K.-Y.; Chung, W.-H.; Lau, C.-P., *J. Electroanal. Chem.* **1998**, *453*, 161.

(18) Laha, J. K.; Dhanalekshmi, S.; Taniguchi, M.; Ambroise, A.; Lindsey, J. S., *Org. Process Res. Dev.* **2003**, *7*, 799.

(19) Yu, L.; Muthukumaran, K.; Sazanovich, I. V.; Kirmaier, C.; Hindin, E.; Diers, J. R.; Boyle, P. D.; Bocian, D. F.; Holten, D.; Lindsey, J. S., *Inorg. Chem.* **2003**, *42*, 6629.

(20) McLean, T. M.; Moody, J. L.; Waterland, M. R.; Telfer, S. G., *Inorg. Chem.* **2012**, *51*, 446.

(21) Kurz, P.; Probst, B.; Spingler, B.; Alberto, R., *Eur. J. Inorg. Chem.* **2006**, *2006*, 2966.

(22) Sieh, D.; Lacy, D. C.; Peters, J. C.; Kubiak, C. P., *Chem. Eur. J.* **2015**, *21*, 8497.

(23) Sieh, D.; Kubiak, C. P., *Chem. Eur. J.* **2016**, *22*, 10638.

(24) Ishida, H.; Fujiki, K.; Ohba, T.; Ohkubo, K.; Tanaka, K.; Terada, T.; Tanaka, T., *J. Chem. Soc., Dalton Trans.* **1990**, 2155.

(25) Sampson, M. D.; Froehlich, J. D.; Smieja, J. M.; Benson, E. E.; Sharp, I. D.; Kubiak, C. P., *Energy Environ. Sci.* **2013**, *6*, 3748.

(26) Riplinger, C.; Sampson, M. D.; Ritzmann, A. M.; Kubiak, C. P.; Carter, E. A., *J. Am. Chem. Soc.* **2014**, *136*, 16285.

(27) Riplinger, C.; Carter, E. A., *ACS Catal.* **2015**, *5*, 900.

(28) Smieja, J. M.; Benson, E. E.; Kumar, B.; Grice, K. A.; Seu, C. S.; Miller, A. J.; Mayer, J. M.; Kubiak, C. P., *Proc. Nat. Acad. Sci. USA* **2012**, *109*, 15646.

(29) Bligaard, T.; Bullock, R. M.; Campbell, C. T.; Chen, J. G.; Gates, B. C.; Gorte, R. J.; Jones, C. W.; Jones, W. D.; Kitchin, J. R.; Scott, S. L., *ACS Catal.* **2016**, *6*, 2590.

(30) Costentin, C.; Passard, G.; Savéant, J.-M., *J. Am. Chem. Soc.* **2015**, *137*, 5461.

(31) Appel, A. M.; Helm, M. L., *ACS Catal.* **2014**, *4*, 630.

(32) Oh, S.; Gallagher, J. R.; Miller, J. T.; Surendranath, Y., *J. Am. Chem. Soc.* **2016**, *138*, 1820.

(33) Franco, F.; Cometto, C.; Garino, C.; Minero, C.; Sordello, F.; Nervi, C.; Gobetto, R., *Eur. J. Inorg. Chem.* **2015**, *2015*, 296.

(34) Yi, X.; Zhao, J.; Wu, W.; Huang, D.; Ji, S.; Sun, J., *Dalton Trans.* **2012**, *41*, 8931.

(35) Ito, A.; Kang, Y.; Saito, S.; Sakuda, E.; Kitamura, N., *Inorg. Chem.* **2012**, *51*, 7722.

(36) Machura, B.; Wolff, M.; Jaworska, M.; Lodowski, P.; Benoist, E.; Carrayon, C.; Saffon, N.; Kruszynski, R.; Mazurak, Z., *J. Organomet. Chem.* **2011**, *696*, 3068.

(37) Machan, C. W.; Chabolla, S. A.; Yin, J.; Gilson, M. K.; Tezcan, F. A.; Kubiak, C. P., *J. Am. Chem. Soc.* **2014**, *136*, 14598.

(38) Machan, C. W.; Sampson, M. D.; Kubiak, C. P., *J. Am. Chem. Soc.* **2015**, *137*, 8564.

(39) Clark, M. L.; Rudshteyn, B.; Ge, A.; Chabolla, S. A.; Machan, C. W.; Psciuk, B. T.; Song, J.; Canzi, G.; Lian, T.; Batista, V. S.; Kubiak, C. P., *J. Phys. Chem. C* **2016**, *120*, 1657.

(40) Rountree, E. S.; McCarthy, B. D.; Eisenhart, T. T.; Dempsey, J. L., *Inorg. Chem.* **2014**, *53*, 9983.

(41) McCarthy, B. D.; Martin, D. J.; Rountree, E. S.; Ullman, A. C.; Dempsey, J. L., *Inorg. Chem.* **2014**, *53*, 8350.

(42) Christensen, P. A.; Hamnett, A.; Muir, A. V. G.; Freeman, N. A., *J. Electroanal. Chem.* **1990**, *288*, 197.

(43) Contreras, L.; Paneque, M.; Sellin, M.; Carmona, E.; Perez, P. J.; Gutierrez-Puebla, E.; Monge, A.; Ruiz, C., *New J. Chem.* **2005**, *29*, 109.

(44) Agarwal, J.; Fujita, E.; Schaefer, H. F., 3rd; Muckerman, J. T., *J. Am. Chem. Soc.* **2012**, *134*, 5180.

(45) Sampson, M. D.; Kubiak, C. P., *J. Am. Chem. Soc.* **2016**, *138*, 1386.

(46) Bhugun, I.; Lexa, D.; Savéant, J.-M., *J. Phys. Chem.* **1996**, *100*, 19981.

(47) Lee, G. R.; Maher, J. M.; Cooper, N. J., *J. Am. Chem. Soc.* **1987**, *109*, 2956.

(48) Sheldrick, G., *Acta Cryst. A* **2008**, *64*, 112.

(49) Machan, C. W.; Sampson, M. D.; Chabolla, S. A.; Dang, T.; Kubiak, C. P., *Organometallics* **2014**, *33*, 4550.

7.8 Appendix

Table 7.5 Crystallographic data and refinement information for complexes **1** and **2**.

Compound	**Re(Ph-dipyrrin)(CO)$_3$(py)**	**Re(Mes-dipyrrin)(CO)$_3$(py)**
Empirical Formula	$C_{23}H_{16}N_3O_3Re$	$C_{26}H_{22}N_3O_3Re$
Formula Weight	568.61	610.69
Crystal System	monoclinic	monoclinic
Space Group	C 2/c	$P2_1/n$
***a* (Å)**	19.3640(13)	14.4899(4)
***b* (Å)**	16.9444(11)	12.0685(3)
***c* (Å)**	15.2185(10)	14.6967(4)
α (deg)	90	90
β (deg)	126.504(2)	114.032(1)
γ (deg)	90	90
V (Å^3)	4013.7(5)	2347.26(11)
Z Value	8	4
ρ *calc* (g/cm^3)	1.8818	1.7280
mu (mm^{-1})	6.085	5.209
Independent Reflections	4,068 [R(int) = 0.0442]	7,218 [R(int) = 0.0453]
Data/restraints/parameters	4068/0/270	7218/0/301
Goodness of Fit on F^2	1.042	1.047
R indices (all data) R1, wR2	0.0266, 0.0631	0.0322, 0.0464
Largest diff. peak and hole	1.37 to –1.52	1.19 to –0.94

Table 7.6 Selected bond lengths (Å) and angles (deg) for X-ray crystallographic structures of complexes.

Bond/Angle	**Re(Ph-dipyrrin)(CO)$_3$(py)**	**Re(Mes-dipyrrin)(CO)$_3$(py)**
Re–N1	2.151(3)	2.152(0)
Re–N2	2.158(3)	2.161(3)
Re–N3	2.228(3)	2.223(4)
Re–C1	1.910(4)	1.926(3)
Re–C2	1.907(4)	1.919(2)
Re–C3	1.924(4)	1.917(2)
N1–Re–N2	85.11	84.60
N1–Re–C3	177.58	176.81
N1–Re–N3	84.63	82.33
N3–Re–C1	176.26	175.21
N3–Re–C3	94.34	95.13
Re–C1–O1	177.8	177.5
Re–C2–O2	178.3	178.1
Re–C3–O3	179.7	179.0
C11-C13-C23	101.87	93.3

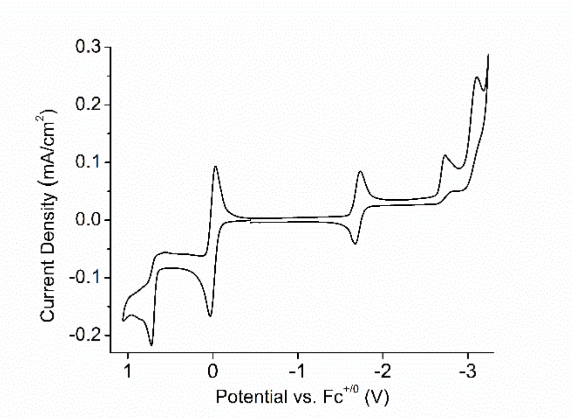

Figure 7.6 Scan of the full CV window to show all accessible redox processes of Re(mesityl-dipyrrin)(CO)$_3$Cl. The reversible redox couple at 0.00 V is the internal reference, ferrocene.

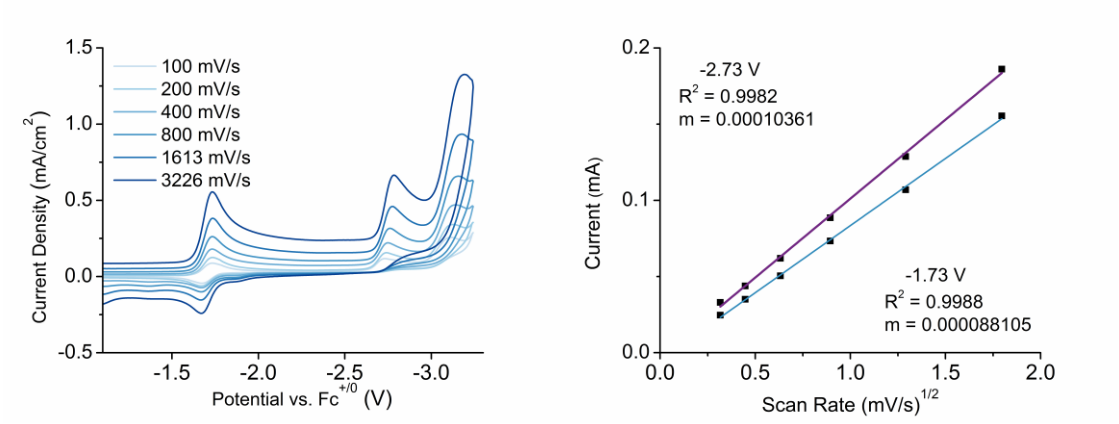

Figure 7.7 Left: CVs at different scan rates of Re(5-mesityldipyrrin)$(CO)_3$(py). Right: Plot indicating a linear dependence of the current on the square root of the scan rate, indicating that the complex is freely diffusing in solution as predicted by the Randles-Sevcik equation.

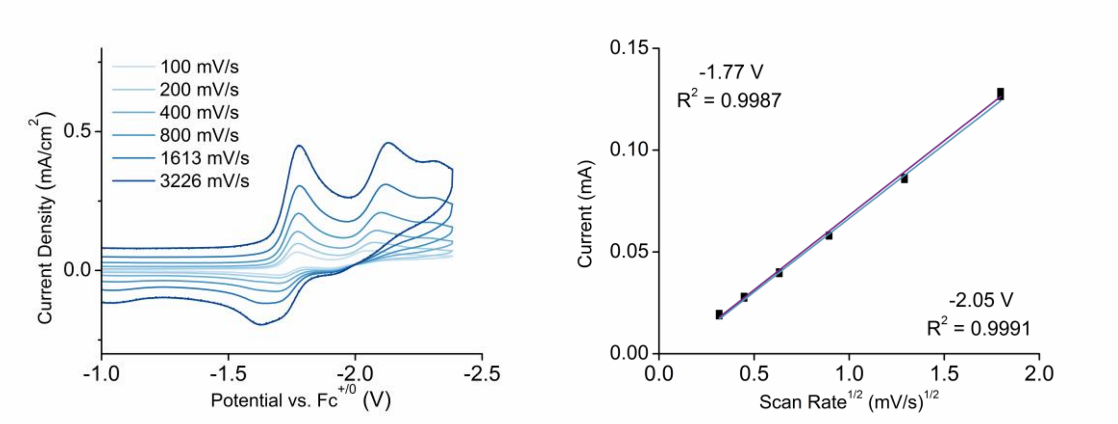

Figure 7.8 Left: CVs at different scan rates of Re(1,10-phenanthroline)$(CO)_3$Cl. Right: Plot indicating a linear dependence of the current on the square root of the scan rate, indicating that the complex is freely diffusing in solution as predicted by the Randles-Sevcik equation.

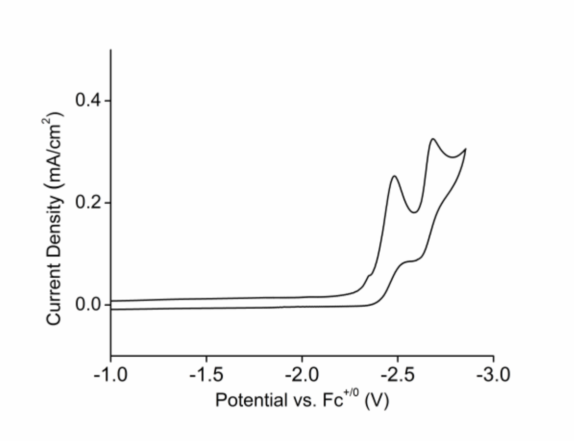

Figure 7.9 CV of 1,10-phenanthroline ligand under Ar.

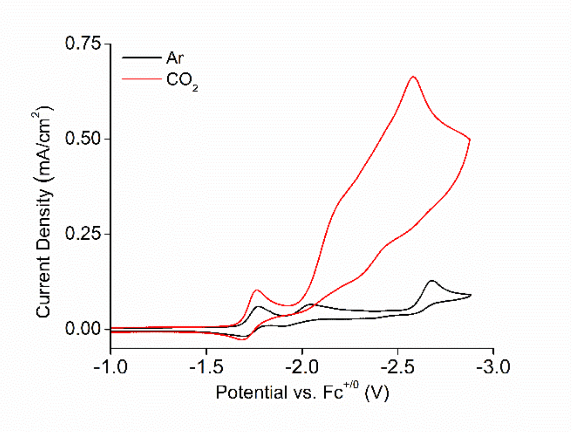

Figure 7.10 CV of Re(phen)(CO)$_3$Cl under Ar (black) and CO$_2$ (red). Conditions: Glassy carbon working, Pt counter, Ag/AgCl reference electrodes with Fc internal reference. 0.1 V/s.

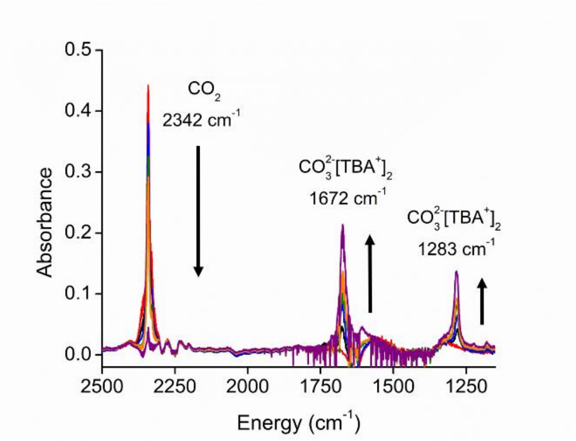

Figure 7.11 IR-SEC of a blank 0.1 M $TBAPF_6$ solution in MeCN that was approximately 0.14 M CO_2. Potential was changed from ca. 1.4 V to 2.0 V vs. $Fc^{+/0}$ over the course of 25 minutes.During this time the band corresponding to CO_2 decreased while those corresponding to carbonate increased. Glassy carbon working, Ag counter and Pt reference electrodes were used.